THÈSE

Préparée et soutenue publiquement le 17 janvier 2020 à

L'UNIVERSITÉ DE LILLE – FACULTÉ DES SCIENCES ET TECHNOLOGIES

Présentée par

Diksha JANI THAVILIGADU

Doctorante du Laboratoire de Spectrochimie Infrarouge et Raman et affiliée à l'Ecole Doctorale des Sciences de la Matière, du Rayonnement et de l'Environnement

Pour obtenir le grade de

DOCTEUR

Mention : Chimie théorique, physique, analytique

RÉACTIVITÉ DE LA MORINE ET PHOTOPHYSIQUE DES HYDROCARBURES AROMATIQUES POLYCYCLIQUES PAR CHIMIE QUANTIQUE ET SPECTROSCOPIE ÉLECTRONIQUE

REACTIVITY OF MORIN AND PHOTOPHYSICS OF POLYCYCLIC AROMATIC HYDROCARBONS BY QUANTUM CHEMISTRY AND ELECTRONIC SPECTROSCOPY

Présidente du jury :	**Dr. Valérie VALLET** (DR CNRS, Université de Lille)
Rapporteurs :	**Dr. Ilaria CIOFINI** (DR CNRS, Chimie ParisTech)
	Dr. Michel MEYER (CR HDR CNRS, Université de Bourgogne)
Examinateurs :	**Pr. Benoît CHAMPAGNE** (PR, Université de Namur)
Directeur de thèse :	**Pr. Jean-Paul CORNARD** (PR, Université de Lille)
Co-encadrant :	**Dr. Aurélien MONCOMBLE** (MCF, Université de Lille)

Acknowledgements/Remerciements

Je tiens tout d'abord à remercier le Docteur Valérie Vallet, Directrice de Recherche au laboratoire de PHysique des Lasers, Atomes et Molecules à l'Université de Lille d'avoir accepté d'être la présidente de mon jury de thèse. Mes remerciements vont aussi au Docteur Ilaria Ciofini, Directrice de Recherche au CNRS, de l'Institute of Chemistry for Life and Health Sciences à Chimie ParisTech, ainsi qu'au Docteur Michel Meyer, Chargé de Recherche au CNRS, de l'Institut de Chimie Moléculaire de l'Université de Bourgogne pour avoir accepté la lourde charge d'être rapporteurs de ce mémoire. J'aimerais également remercier le Professeur Benoît Champagne de l'Unité de chimie physique, théorique et structurale à l'université de Namur d'avoir accepté de juger ce travail.

Je tiens aussi à remercier le LabeX CaPPA d'avoir financé ce projet de recherche.

Un très grand merci à mon Directeur de thèse, le Professeur Jean-Paul Cornard et à mon encadrant, le Docteur Aurélien Moncomble, de m'avoir bien accueillie dans l'équipe, d'avoir été toujours à l'écoute de mes innombrables questions et de m'avoir accompagnée durant ces trois années. J'ai été très heureuse d'avoir eu l'opportunité de travailler avec eux et cela toujours dans la bonne humeur. Ils m'ont aidé à dépasser mes limites et à grandir professionnellement.

Je souhaiterais également remercier toute l'équipe du LASIR ainsi que Hervé Vezin, son Directeur, pour m'avoir accueillie au sein du laboratoire. J'ai eu l'occasion de rencontrer des gens formidables. Merci à Lucie, Jérémy, Samantha, Cécilia, Vincent, Myriam et Matthieu avec qui j'ai travaillé et rigolé au quotidien. Je remercie Alain et Annaïg pour les bons moments passés pendant les pauses et l'enseignement, toute l'équipe PCE pour sa bienveillance ainsi que Catherine, Jean-Pierre et Pascal qui ont toujours été à l'écoute. Enfin, j'ai été heureuse d'avoir pu faire la connaissance de plusieurs doctorants : Yevheniia, avec qui j'ai partagé mon bureau ainsi que Junias, Henry, Guillaume, Pratima, Siewert, Silvère, les deux Thomas, Lucas, Alessandro, Balint, Akos, Luc et tous les autres.

J'aimerais dire un grand merci à mes superbes copines Élodie, Laura, Aurélie et Chloé ainsi que tous mes amis qui ont toujours trouvé les bons mots pour m'encourager ces dernières années. J'ai aussi une pensée très spéciale à Sarvada, ma meilleure amie depuis nos treize ans qui s'est battue jusqu'à la fin contre le lupus. Je sais que même si je n'ai pas pu lui annoncer ma réussite de vive voix, elle est heureuse pour moi.

Enfin, mes remerciements vont à mes parents, mes grands-parents et toute ma famille qui sont à l'Ile Maurice ainsi que ma sœur chérie qui m'ont toujours soutenue et encouragée à travers leurs mots et leurs prières. C'est grâce à eux qu'aujourd'hui je me trouve là. Un grand merci à ma cousine, « ma petite maman », qui me soutient et qui prend soin de moi depuis mon arrivée en France. Finalement, la dernière personne que je voudrais remercier est très importante à mes yeux : toi Sébastien, qui est à mes côtés depuis six ans maintenant. Merci d'avoir été patient surtout pendant mes petits moments de crise et de m'avoir aidée et encouragée pour atteindre mes objectifs.

Table of contents

General Introduction

This PhD work was carried out at the Laboratoire de Spectrochimie Infrarouge et Raman (LASIR - UMR 8516) within the Physico-chemistry of the Environment (PCE) team. The main themes addressed by this research group are related to the study of fundamental processes in the natural environment using laboratory chemical models with the aim of better understanding the reactivity and fate of different pollutants (organic, metals) in the natural systems. The different compartments of the natural environment (water, aerosols, soils and sediments) are concerned by these studies.

This work was carried out within the framework of the LabeX CaPPA (Chemical and Physical Properties of the Atmosphere) which funded 100% this study. The laboratory of excellence brings together 7 laboratories of physicists and chemists with complementary skills and expertise that implement a theoretical as well as experimental approach, in the laboratory and in the field.

My study, presented in this thesis, deals with two very distinct topics related to environmental issues. Although completely independent from each other, these subjects use the same tools like quantum chemistry, more precisely Density Functional Theory (DFT) and time-dependent DFT (TD-DFT) as well as electronic spectroscopies (UV-visible absorption and fluorescence emission).

The first theme is the continuation of a work undertaken for many years within the research group and concerns the complexation of metal cations by model molecules of the organic matter of soils, sediments and organic aerosols. The main objective of this vast study is to obtain a better understanding, at a molecular level, of the process of metal fixing by organic matter and to have a better knowledge of the competition between the main cation binding sites. The complexity of organic matter has led us to study molecules of the plant kingdom, precursors of organic matter. There are mainly polyphenolic compounds in which the complexation sites in competition are the same as those encountered in the macromolecular structure of the compounds of the organic matter. If the chemical systems studied in this

thesis are new, the methodology of the study, the calculation procedures and experimental methods are well established and the obtaining of original results seemed almost assured.

Conversely, the second study deals with a totally new problem within the team and leads to a much higher risk taking. The main objective of this other study is to deepen the knowledge of the photophysics of certain polycyclic aromatic hydrocarbons (PAHs). These compounds are notorious pollutants and were studied a few decades ago, particularly from a physico-chemical point of view. Since then, the published studies mainly concern the detection and quantification of these molecules, especially in the gas phase, in the atmosphere. The optical properties of PAHs have been well known for many years. In particular, some of them have the peculiarity of presenting a dual fluorescence. If this dual emission has been studied experimentally, if the presence of this dual emission is controversial for certain compounds, it turns out that very few theoretical studies relate to this problem. No theoretical study has been carried out to affirm or invalidate this dual fluorescence or to explain its mechanisms. This is the challenge that we have tried to address in this second study which purpose is to shed light on the low energy excited states of some of these compounds, so as to predict the fate of an excited molecule as well as a possible dual fluorescence. While this subject is ground-breaking within the team, it is also innovative in the photophysics community of PAHs. First of all, our ambition is to have a strategy to find some ways to tackle this problem by hoping to open a path towards new more sophisticated and accomplished studies. It is therefore a preliminary study, where only small PAHs will be studied essentially from a theoretical point of view.

The first part of this manuscript deals with the complexation propertries of morin towards three of the period four metal cations (Zn^{II}, Ca^{II} and Mn^{II}).

In the first chapter of this thesis, we expose the state of the art on flavonoids, which are the multisite ligands that were chosen for this study as well as the methodology used. Emphasis was put on morin because it was the principle asset to this work to investigate its complexation ability. As a matter of fact, a fixation site present on the molecule was highlighted as it has never been evoked previously in the literature.

The second chapter evolved around the zinc cation and its interaction with morin. The experimental spectra obtained from electronic spectroscopy were confronted to the electronic transitions computed by TD-DFT to highlight the preferential chelating site among the four present within morin. Molecular orbitals and QT-AIM calculations were carried out. Zn^{II} complexation with quercetin and luteolin were compared to the studied system.

In chapter three, the Mn^{II}-morin and Mn^{II}-quercetin systems were investigated. This study was similar to that involving the zinc cations by combining experiments and quantum chemistry calculations. No fluorescence experiments were performed since the UV-vis data was enough to determine the metal fixation site on the morin and quercetin molecules.

The fourth chapter is the last one which was related to the study of the complexation reactions. It concerns the interaction of calcium cations with morin by following the same steps as zinc and manganese cations. The study was taken a step further compared to chapters two and three, by investigating the various deprotonated species of the complex formed using absorption and fluorescence spectroscopy as well as DFT and TD-DFT computations.

The second topic of this thesis related to polycyclic aromatic hydrocarbons was evoked in a second part.

Chapter one exposes the environmental aspect of PAHs. Then, the principle of dual fluorescence and the three different possible mechanisms that can explain such phenomenon are presented. Pyrene, perylene, benzo[*a*]pyrene, benzo[*e*]pyrene, benzo[*g,h,i*]perylene and coronene were the chosen molecules for this study. The methodology used in this topic is also given.

The aim of the second chapter is to establish the optical properties of the selected PAHs by recording their absorption and emission spectra. The data obtained was used in the setting up of a benchmark to find the adequate functional and basis set.

Finally, the last chapter deals with the identification of the structural changes occurring when the molecules are promoted to the first and second excited states. Following that, a sampling

of the potential energy surfaces was done and energies were calculated with respect to different reaction coordinates to obtain a suitable description of the entanglement of the excited states.

COMPLEXATION PROPERTIES OF MORIN TOWARDS METAL CATIONS

CHAPTER 1:

INTRODUCTION ON FLAVONOIDS, AIM AND METHODOLOGY

1.1 State of the art

In recent years, there has been an increasing ecological and global public health concern associated with environmental contamination by metals. Also, human exposure has risen dramatically as a result of an exponential increase of their use in several industrial, agricultural, domestic and technological applications. Reported sources of metals in the environment include geogenic, industrial, agricultural, pharmaceutical, domestic effluents, and atmospheric sources[1]. Although metals are naturally occurring elements that are found throughout the earth's crust, most environmental contamination and human exposure result from anthropogenic activities such as mining and smelting operations, industrial production and use, and domestic and agricultural use of metals and metal–containing compounds[2,3,4]. Metal accumulation in the different environmental compartments (soil, water and sediments) depends directly on different parameters such as pH, ionic strength, nature and concentration of inorganic and organic "ligands" plus the availability of adsorption surfaces such as clay minerals and organic matter[5]. Humic substances are ubiquitous, being found in all soils, sediments, and waters. These substances refer to organic material in the environment that results from the decomposition of plant and animal residues. These heterogeneous compounds exhibit, to varying degrees, four major properties:

1. Polyfunctionality, due to the existence of a variety of functional groups and a broad range of functional reactivity.
2. High electric charge density due to the presence of a large number of dissociated functional groups.

[1] He, Z. L., Yang, X. E., & Stoffella, P. J. (2005). Trace elements in agroecosystems and impacts on the environment. *Journal of Trace Elements in Medicine and Biology*, *19*(2–3), 125–140.
[2] John H. Duffus, « "Heavy metals" a meaningless term? (IUPAC Technical Report) », *Pure and Applied Chemistry* 74, nº 5 (1 janvier 2002): 793-807, https://doi.org/10.1351/pac200274050793.
[3] Casarett, L. J., Doull, J., & Klaassen, C. D. (2008). *Casarett and Doull's toxicology: The basic science of poisons*.
[4] Shallari, S., Schwartz, C., Hasko, A., & Morel, J. L. (1998). Heavy metals in soils and plants of serpentine and industrial sites of Albania. *Science of The Total Environment*, *209*(2–3), 133–142.
[5] Davies, C. A. L., Tomlinson, K., & Stephenson, T. (1991). Heavy metals in river tees estuary sediments. *Environmental Technology*, *12*(11), 961–972.

3. Structural lability, due to the ability to associate intermolecularly and to change molecular conformation in response to changes in pH, pE, ionic strength…
4. Size polydispersity.

All these properties are exhibited to varying degrees by all the biopolymers present in natural medium: proteins, polysaccharides, and humic substances. These humic substances mainly interact with metal ions by complexation mechanisms and depending upon the circumstances, this interaction may lead to immobilization of the metal. The nature of these substances is poorly defined and they are often described as coiled, long chain molecules of two or three dimensional cross linked macromolecules which may vary in molecular weight depending on type of humic materials and method of measurement. However, subfractions of humic substances have been isolated and given special names:

1. Humic acid is the fraction that is not soluble in water under acidic conditions (pH < 2.0) but is soluble at higher pH values,
2. Fulvic acid is the fraction of humic substances that is soluble in water under all pH conditions and
3. Humin is the fraction that is not soluble in water at any pH value.

Typically, 90% of the dissolved humic substances in natural waters consists of fulvic acid, and the remaining 10% consists of humic acid. This composition is in contrast to humic substances from soils, where the humic acid is in very large excess over the fulvic acid[6]. The ability of these substances to form stable complexes with metal ions can be accounted for by their high content of oxygen containing functional groups: carboxylic, phenolic and aliphatic –OH groups. Because of their high reactivity, humic substances control the bioavailability and the biogeochemical cycling of trace elements in the environment[7]. Metal–humic complexation occurs by metal binding to already ionised sites or sometimes by displacing a proton from its

[6] Malcolm, R. L., & MacCarthy, Patrick. (1986). Limitations in the use of commercial humic acids in water and soil research. *Environmental Science & Technology*, *20*(9), 904–911.
[7] Xia, K., Bleam, W., & Helmke, P. A. (1997). Studies of the nature of binding sites of first row transition elements bound to aquatic and soil humic substances using X-ray absorption spectroscopy. *Geochimica et Cosmochimica Acta*, *61*(11), 2223–2235.

position. Heterogeneous ligands like humic substances may exhibit characteristics that differ to that of a simple ligands: polyfunctionality which results in high electrical charge density, structural modification as a function of *e.g*. pH, ionic strength, metal binding, and variation in molecular weights[8,9]. With carboxylic acids, phenolic groups are considered as the most important groups for complexation with metal cations[10]. The characterization of metal ions complexes with macromolecular ligands (especially humic substances) has been an ongoing research interest to the scientific community, leading to the implementation of new models (e.g. charge neutralization or NICA–Donnan model[11]) to describe the complex stability with complexing agents of rather undefined structure and molecular size. The complexity and ill–defined nature of humic substances place a huge limitation on our ability to measure and interpret metal complexation equilibria with these compounds. Notably, it is very difficult to obtain information on the complexation process at the molecular level. To predict the specific behaviour for metal cation–organic matter interactions, we choose to investigate much simpler systems by studying the complexing properties of polyphenol molecules, which are commonly known as precursor of humic substances. This approach consists in the study of well–defined molecules, under controlled conditions, that exhibit the main characteristics and properties of humic substances, notably, the competition of several complexing sites within a simple ligand.

The multisite ligands chosen for this study are flavonoid compounds. Flavonoids are naturally available organic compounds that are widely present in fruits, vegetables, cereals and even coffee seeds[12]. These molecules are considered as secondary metabolites which present

[8] Buffle, J., Altmann, R. S., Filella, M., & Tessier, A. (1990). Complexation by natural heterogeneous compounds: Site occupation distribution functions, a normalized description of metal complexation. *Geochimica et Cosmochimica Acta*, *54*(6), 1535–1553.
[9] Filella, M. (2008). NOM site binding heterogeneity in natural waters: Discrete approaches. *Journal of Molecular Liquids*, *143*(1), 42–51.
[10] Chappaz, A., & Curtis, P. J. (2013). Integrating Empirically Dissolved Organic Matter Quality for WHAM VI using the DOM Optical Properties: A Case Study of Cu–Al–DOM Interactions. *Environmental Science & Technology*, *47*(4), 2001–2007.
[11] Fröhlich, D. R., & Panak, P. J. (2019). The complexation of Eu(III) and Cm(III) with polyacrylate as a model compound for complex polycarboxylates studied by laser fluorescence spectroscopy. *Journal of Luminescence*, *212*, 166–170.
[12] Panche, A. N., Diwan, A. D., & Chandra, S. R. (2016). Flavonoids: An overview. *Journal of Nutritional Science*, *5*.

interesting biological properties that are greatly exploited for medical ends. Flavonoids are good antioxidants[13,14,15], anti–inflammatories[16,17], and antifungals[18] and have excellent neuroprotective properties[19]. They have even more useful characteristics and it has been proven also that the consumption of an excess of flavonoids does not affect negatively living organisms[20]. As a matter of fact, several research work are ongoing to find ways to enhance the biological features that these molecules exhibit.

These secondary metabolites are mainly found in organic matter fixed in the soil or sediments and are also dissolved in natural water and due to that, they participate actively in the interaction with different organisms. The flavonoids present in plants help in the protection from ultraviolet sunlight by absorbing in the wavelength range in which most biological damages occur[21] (Figure 1).They also help in lipid peroxidation and against insect pests as they play a role in the growth and development of plants.

[13] Jovanovic, S. V., Steeden, S., Tosic, M., Marjanovic, B. & Simic, M.G. (1994). Flavonoids as Antioxidants. *Journal of the American Chemical Society*, 116. 4846-4851

[14] de Souza, R. F. V., & De Giovani, W. F. (2004). Antioxidant properties of complexes of flavonoids with metal ions. *Redox Report*, *9*(2), 97–104.

[15] Chen, G.-L., Fan, M.-X., Wu, J.-L., Li, N., & Guo, M.-Q. (2019). Antioxidant and anti-inflammatory properties of flavonoids from lotus plumule. *Food Chemistry*, *277*, 706–712.

[16] Fang, S.-H., Hou, Y.-C., Chang, W.-C., Hsiu, S.-L., Lee Chao, P.-D., & Chiang, B.-L. (2003). Morin sulfates/glucuronides exert anti-inflammatory activity on activated macrophages and decreased the incidence of septic shock. *Life Sciences*, *74*(6), 743–756.

[17] Rotelli, A. (2003). Comparative study of flavonoids in experimental models of inflammation. *Pharmacological Research*, *48*(6), 601–606.

[18] Cushnie, T. P. T., & Lamb, A. J. (2005). Antimicrobial activity of flavonoids. *International Journal of Antimicrobial Agents*, *26*(5), 343–356.

[19] Solanki, I., Parihar, P., Mansuri, M. L., & Parihar, M. S. (2015). Flavonoid-Based Therapies in the Early Management of Neurodegenerative Diseases. *Advances in Nutrition*, *6*(1), 64–72.

[20] Mierziak, J., Kostyn, K., & Kulma, A. (2014). Flavonoids as Important Molecules of Plant Interactions with the Environment. *Molecules*, *19*(10), 16240–16265.

[21] Caldwell, M.M., Robberecht, R., & Flint, S.D. (1983). Internal filters: Prospects for UV-acclimation in higher plants. *Physiologia Plantarum, 58*(3), 445-450

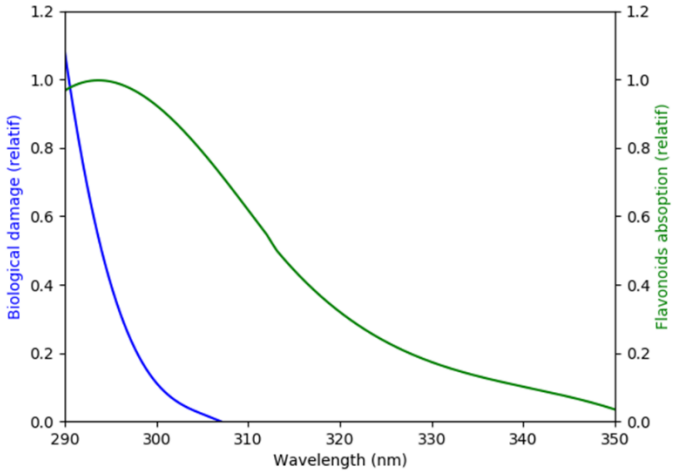

Figure 1 Evidence showing that flavonoids protect plants from biological damage

Moreover, by attracting animals with their colour, smell and flavour, they contribute in the pollination process. As it has been pointed out, the aforementioned compounds are a key in implementing a plant defence mechanism against insects but it was also established that they help plants fight pathogenic bacteria and fungi. One of the main problematics in living organisms is the presence of reactive oxygen and other free radicals species that are formed by enzymes or several reaction processes, which pushes them to, in turn, react actively with other parts of the plant to become more stable. This oxidative damage process is known as oxidative stress and it only results in a cascade of reactions that is very dangerous and leads to cell death. Flavonoids has the ability to sequester those free radicals because their structure is made up of many conjugated bonds. They have a low redox potential that helps to reduce strong free radicals[20,22].

Flavonoids are known to possess several functional groups which make them compounds that are prone to different types of reactions. Because of this ability and depending on the environment, flavonoids are able to undergo modifications by reacting with the species located in the vicinity. Their high reactivity eventually leads to an alteration in their physical properties, such as their solubility and stability as well as their biological characteristics.

[22] Torel, J., Cillard, J., & Cillard, P. (1986). Antioxidant activity of flavonoids and reactivity with peroxy radical. *Phytochemistry*, *25*(2), 383–385.

Speaking of solubility, one of the main problems of flavonoids is that they are not very soluble in aqueous solutions, resulting in poor absorption of the molecules in some environment[23,24].

From a structural point of view, flavonoids are polyphenols with two phenyl rings, denoted as ring A and ring B connected by a heterocyclic ring (γ–pyrone) named ring C as shown in Figure 2. It can be declined into different categories known as flavones, flavonols, isoflavones, flavanols and anthocyanins depending on their structural properties[12,19]. The first part of this thesis is mainly focused on three flavonoids; morin and quercetin belonging to the subfamily of flavonols (presenting a hydroxyl function in position 3) and luteolin which forms part of the subfamily of flavones. The current trends of the study related to flavonoids consist in the analysis of their biological properties to see the extent at which they can be exploited to combat cancer–related or neurodegenerative diseases amongst others.

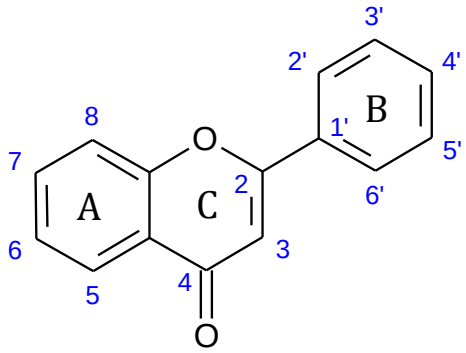

Figure 2 Skeleton of a flavonoid and atomic numbering (IUPAC notation)

What is interesting for us about the structure of flavonoids is the fact they have functional groups that can be found on organic matter, and hence, they can be used as model molecules in the study of complexation reactions. The behaviour of metal cations when there are closed to these precursor molecules of humic substances is used to mimic the behaviour of the same cations close to similar groups in the organic matter. Another reason for choosing flavonoids as multisite ligands is due to their various fixing sites that permit us to study and comprehend

[23] Chebil, L., Humeau, C., Anthoni, J., Dehez, F., Engasser, J.-M., & Ghoul, M. (2007). Solubility of Flavonoids in Organic Solvents. *Journal of Chemical & Engineering Data*, *52*(5), 1552–1556.
[24] Tommasini, S., Raneri, D., Ficarra, R., Calabrò, M. L., Stancanelli, R., & Ficarra, P. (2004). Improvement in solubility and dissolution rate of flavonoids by complexation with β-cyclodextrin. Journal of Pharmaceutical and Biomedical Analysis, 35(2), 379–387.

the regio–selectivity of the complexation reaction. Indeed, a metal cation will have a preferential fixing site compared to other parts of the molecule and it is essential to know the structure of the complex formed. It has been mentioned that flavonoids have very useful biological properties and this is mainly related to all the functional groups and the amount of conjugated bonds in their structure. Also, metal chelation is prone to alter these biological properties to a certain extent[25,26,27]. In most cases, when flavonoids interacts with metal salts, these properties are enhanced. This is essential as the complexed form of flavonoids can be used as therapeutics. In order to synthesise the complexes, it is important to have a better knowledge about the structure and the properties of these molecules and of their complexes. In our research team, some works have already been carried out to better understand complexation reactions with flavonoids[28,29].

In order to assess the complexing power of flavonoids and the structural modifications induced by the metal, some elements of the period 4 of the periodic table were considered. More specifically, the interaction of calcium, manganese and zinc with the flavonoids were studied. These elements have their specific characteristics which will be detailed later in their respective chapters. However, one of the main reasons for this choice is related to their electronic configuration. If we take a closer look at calcium and zinc, their electronic configurations are [Ar] $4s^2$ and [Ar] $3d^{10}$ $4s^2$ respectively. Both of them are of a similar nature since they have – fully occupied electronic shells. Manganese on the other hand has a semi–occupied d subshell ([Ar] $3d^5$ $4s^2$). Hence, it can be said that calcium, manganese and zinc have "comparable" electronic configurations with respect to all the other elements of the period 4

[25] Jabeen, E., Janjua, N. K., Ahmed, S., Murtaza, I., Ali, T., Masood, N., … Murtaza, G. (2017). DFT predictions, synthesis, stoichiometric structures and anti-diabetic activity of Cu (II) and Fe (III) complexes of quercetin, morin, and primuletin. *Journal of Molecular Structure*, *1150*, 459–468.
[26] Roy, A. S., Samanta, S. K., Ghosh, P., Tripathy, D. R., Ghosh, S. K., & Dasgupta, S. (2016). Cell cytotoxicity and serum albumin binding capacity of the morin–Cu(ii) complex and its effect on deoxyribonucleic acid. *Molecular BioSystems*, *12*(9), 2818–2833.
[27] Naso, L. G., Lezama, L., Rojo, T., Etcheverry, S. B., Valcarcel, M., Roura, M., Salado, C., Ferrer, E.G., Williams, P. A. M. (2013). Biological evaluation of morin and its new oxovanadium(IV) complex as antio-xidant and specific anti-cancer agents. *Chemico-Biological Interactions*, *206*(2), 289–301.
[28] Dangleterre, L., Cornard, J.-P., & Lapouge, C. (2008). Spectroscopic and theoretical investigation of the solvent effects on Al(III)–hydroxyflavone complexes. *Polyhedron*, *27*(6), 1581–1590.
[29] Moncomble, A., Falantin, C., & Cornard, J.-P. (2018). Electronic Spectroscopies Combined with Quantum Chemistry Calculations: Study of the Interactions of 3-Hydroxyflavone with Copper Ions. *The Journal of Physical Chemistry B*, *122*(38), 8943–8951.

of the periodic classification, supporting the choice of their study. The elements have been studied under their cationic state, that is, Ca^{II}, Mn^{II} and Zn^{II}, form in which they are present in the natural environment.

The aim of this work is to determine the preferential fixation site of a metal cation within flavonoids. To this end, it is important to choose an adequate multisite ligand bearing all the fixation sites that we wish to study in order to make them compete with each other. This will also allow the comprehension of the regio–selectivity of the complexation reactions.

1.2 Methodology

Depending on the features that are of interest and that are relevant for each complexation reactions, several techniques have been exploited to develop various methodologies in order to extract the desired information on the systems under study.

The most well–known technique that give excellent results on metal complexes is the X–Ray Diffraction method (XRD)[30,31,32], provided that the samples are crystalline. In other cases, the analytical techniques that are commonly used on flavonoids are electronic (UV–vis and fluorescence), Infrared, and Raman spectroscopy, ^{1}H–NMR, ^{13}C–NMR and mass spectrometry. The use of SEM (Scanning Electron Microscopy) can be interesting to know more about the morphology of the compound[32]. To assign tentative composition, it is convenient to use elemental analysis and thermal analysis (Thermogravimetric analysis (TGA) and Differential Scanning Calorimetry (DSC) amongst others). Some research groups also resort to other techniques like conductivity[33], cyclic voltammetry[34,35] and colorimetry[36,37].

[30] Mahapatra, B. B., Mishra, R. R., & Sarangi, A. K. (2016). Synthesis, characterisation, XRD, molecular modelling and potential antibacterial studies of Co(II), Ni(II), Cu(II), Zn(II), Cd(II) and Hg(II) complexes with bidentate azodye ligand. *Journal of Saudi Chemical Society*, *20*(6), 635-643.
[31] Naidja, A., Liu, C., & Huang, P. M. (2002). Formation of Protein–Birnessite Complex : XRD, FTIR, and AFM Analysis. *Journal of Colloid and Interface Science*, *251*(1), 46-56.
[32] Neelakantan, M. A., Marriappan, S. S., Dharmaraja, J., Jeyakumar, T., & Muthukumaran, K. (2008). Spectral, XRD, SEM and biological activities of transition metal complexes of polydentate ligands containing thiazole moiety. *Spectrochimica Acta Part A: Molecular and Biomolecular Spectroscopy*, *71*(2), 628-635.
[33] Coronado, E., Galán-Mascarós, J. R., Gómez-García, C. J., & Laukhin, V. (2000). Coexistence of ferromagnetism and metallic conductivity in a molecule-based layered compound. *Nature*, *408*(6811), 447-449.
[34] De Jong, H. G., Van Leeuwen, H. P., & Holub, K. (1987). Voltammetry of metal complex systems with different diffusion coefficients of the species involved. *Journal of Electroanalytical Chemistry and Interfacial Electrochemistry*, *234*(1-2), 1-16.
[35] De Jong, H. G., & Van Leeuwen, H. P. (1987). Voltammetry of metal complex systems with different diffusion coefficients of the species involved. *Journal of Electroanalytical Chemistry and Interfacial Electrochemistry*, *234*(1-2), 17-29.
[36] Ranyuk, E., Uglov, A., Meyer, M., Lemeune, A. B., Denat, F., Averin, A., Beletskaya, I., Guilard, R. (2011). Rational design of aminoanthraquinones for colorimetric detection of heavy metal ions in aqueous solution. *Dalton Transactions*, *40*(40), 10491.
[37] Zhou, L.-L., Sun, H., Li, H.-P., Wang, H., Zhang, X.-H., Wu, S.-K., & Lee, S.-T. (2004). A Novel Colorimetric and Fluorescent Anion Chemosensor Based on the Flavone Quasi-crown Ether−Metal Complex. *Organic Letters*, *6*(7), 1071-1074.

For our research work, we decided to combine the strength of electronic spectroscopy and DFT calculations in order to study the complex systems both from the experimental and theoretical point of view.

1.2.1 Electronic Spectroscopy

The complexation reactions under study are very specific since the work is done in solution at low concentrations (order of magnitude of 10^{-5} mol L^{-1}). With such diluted systems, it is very difficult, even impossible, to find only one analytical method that can be used to obtain accurate spectral and structural information. One technique that is very sensitive for low–concentrated solutions is electronic spectroscopy. However, electronic spectra do not give much information on the structure of the complex formed. This is why it is essential to conjugate this technique with another one, which will be discussed later on.

The Varian Cary 100 Bio and the Varian Cary 300 Bio double beam spectrometers were used to collect all the absorption spectra. The spectrometer works with a UV lamp and an iodine lamp for the visible domain. At the beginning of each experiment, the baseline is recorded and the correction is applied to the subsequent data. The set of spectra were taken in the range of 200 nm – 600 nm with a source changeover at 400 nm.

As for the fluorescence data, the spectrometer used was a Jobin Yvon Horiba Fluorolog spectrofluorometer that is able to save data in the range of 200 nm – 1100 nm. This spectrometer consists of a Xenon lamp (500 W) as source as well as a double excitation monochromator and a HR emission monochromator with, finally a photomultiplier as detector for photon counting. The Fluorolog is able to record emission spectra, excitation spectra, excitation emission fluorescence matrices and synchrone spectra. Before recording any data, the spectrometer needs to be calibrated. Firstly, the spectrum of the lamp is recorded in the excitation mode to ensure the correct wavelength of the most intense peak of the signal. Secondly, in the emission mode, the spectrum of water is recorded to note the wavelength and intensity of the peak (representing the Raman diffusion of the solvent) in order to

calibrate the instrument. Some parameters such as the integration time, the slit width and the grating can also be modified to optimise the signal.

A Hanna pHmeter was used for pH measurements and as for the titration measurements, a SI Analytics Piston burette TITRONIC® 300 basic device with a 50 mL dosing unit was used. In order to couple the reactor vessel (where the complexation reaction occurs) to the spectrometer, a circulation pump is used. Finally, to ensure the continuous motion of the solution right back to the reactor vessel, a specific circulation quartz cell (Hellma) with two ends is placed in the spectrometer.

Concerning the chemical products, morin hydrate, quercetin and luteolin were purchased from Sigma Aldrich. Zinc hydrate, manganese hydrate and calcium hydrate were also bought from Sigma Aldrich. The experimental work was performed in methanol (ultrapure, spectrophotometric grade, 99.8%) purchased from Alfa Aesar. 1 mol L^{-1}, 0.1 mol L^{-1} and 0.01 mol L^{-1} aqueous solutions of NaOH (white pellets, Fischer Scientific) and HCl (Fluka) were used to fix the pH during the titration. Water was obtained by a Millipore water purification system at 18 MΩ cm^{-1} for NaOH and HCl solutions. 0.1 mol L^{-1} of NaCl (Sigma Aldrich) was also prepared in order to fix the ionic strength of the solution.

Methodologically, a solution containing a flavonoid dissolved in methanol is prepared at a concentration of $5 \cdot 10^{-5}$ mol L^{-1}. Methanol is preferred to increase the solubility of flavonoids with respect to water, but keeping similar solute–solvent interactions. The concentration of the ligand solutions has to be low on one hand to stay within the limits of the Beer–Lambert law ($A = \varepsilon \cdot l \cdot c$), and, on the other hand, to be as close as possible to the conditions observed in the natural environment. The metal solutions are also prepared in methanol by preparing a fixed volume of solution. The concentration of the metal solution is adapted to the molar metal to ligand ratio expected at the end of the titration. Afterwards, the titration of morin and the metal cation is performed to observe the effect of the variation of the molar ratio. The titration setup (Figure 3) is coupled to a UV–visible or a fluorescence spectrometer using a circulation pump in order to record all the spectra. Each spectrum represents the system at its corresponding molar ratio, forming a set of spectra that follows the gradual

formation of the complex–es. Prior to the complexation reactions, the spectra of the metal cations were recorded to ensure that they do not absorb in the UV–vis range.

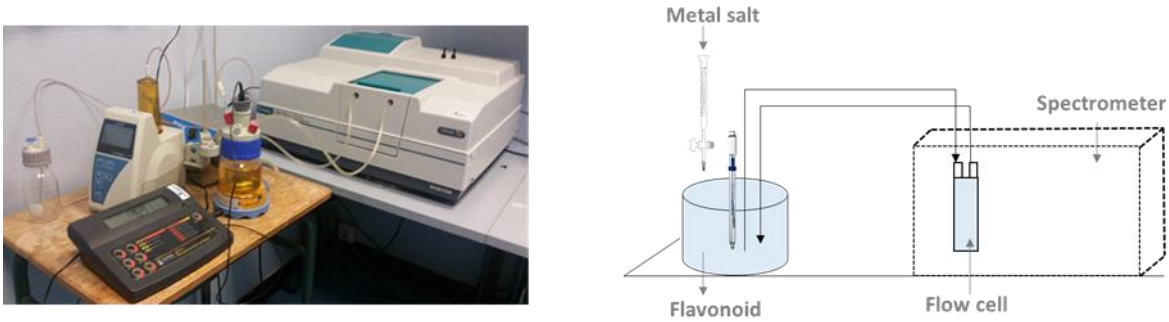

Figure 3 Experimental setup for the monitoring of the complexation reaction

This approach has been used numerous times on several systems in the team and has proven to be quite powerful.

During the titration, the pH value is kept constant (generally at 4.2 and 6.2 in this study). Indeed, the addition of metal causes a release of protons and therefore a decrease in pH; this is then adjusted by the addition of NaOH. The stoichiometry of the formed complexes was determined by the molar ratio method and the spectral variations with the pH were also studied at constant molar ratio.

1.2.2 Chemometric Analysis

Following the recording of the set of spectra, the data is retrieved for treatment. A chemometrics tool, known as ReactLab[38], that applies the principle of Evolving Factor Analysis[39,40] and that is used to fit the data is employed to obtain the stoichiometry of the complex–es, the spectra of the pure complex–es as well as a conditional complexation

[38] Reactlab Equilibria, version 1.00; Jplus Consulting PTY Ltd: Australia
[39] Gampp, H. (1986). Calculation of equilibrium constants from multiwavelength spectroscopic data—IV Model-free least-squares refinement by use of evolving factor analysis. *Talanta*, *33*(12), 943–951.
[40] Maeder, M., & Zuberbuehler, A. D. (1990). Nonlinear least-squares fitting of multivariate absorption data. *Analytical Chemistry*, *62*(20), 2220–2224.

constant, depending on the pH of the solution, which characterises the reaction. The principle of Evolving Factor Analysis consists in treating large sets of multivariate data (in this case, titration measurements) in order to isolate relevant information. More specifically, the large matrix of data obtained from the spectroscopic measurements consists of two matrices: the concentration profiles of the compounds present in the medium and the spectra. By an iteration process, the initial set of data is treated to determine the required concentration profiles. Moreover, some parameters are fed to the software, such as the initial concentration of the compounds, the initial volume in the reactor vessel and the stoichiometry of the complex that is believed to be formed. Using these additional details, a fit is done on the whole set of data to verify whether the given stoichiometry is feasible. Thus, through this trial and error method, the correct type of complex can be deduced along with its conditional complexation constant.

1.2.3 Density Functional Theory (DFT) and Time Dependent–Density Functional Theory (TD–DFT)

Computational chemistry calculations were employed in this study to do a comparison with the experimental data in order to back up non-predictable results. Throughout time, several calculation methods have been devised to obtain theoretical data on each system of interest as close as possible to real life occurrences. In our case, the Density Functional Theory (DFT) was applied as it is suitable for the type of molecules (that is small organic compounds and the associated complexes) that are modelled. As a matter of fact, DFT is considered as a good compromise between the accuracy of the results and the computation time. The quantum calculations were performed with Gaussian16 software[41].

[41] Gaussian 16, Revision C.01, Frisch, M. J.; Trucks, G. W.; Schlegel, H. B.; Scuseria, G. E.; Robb, M. A.; Cheeseman, J. R.; Scalmani, G.; Barone, V.; Petersson, G. A.; Nakatsuji, H.; Li, X.; Caricato, M.; Marenich, A. V.; Bloino, J.; Janesko, B. G.; Gomperts, R.; Mennucci, B.; Hratchian, H. P.; Ortiz, J. V.; Izmaylov, A. F.; Sonnenberg, J. L.; Williams-Young, D.; Ding, F.; Lipparini, F.; Egidi, F.; Goings, J.; Peng, B.; Petrone, A.; Henderson, T.; Ranasinghe, D.; Zakrzewski, V. G.; Gao, J.; Rega, N.; Zheng, G.; Liang, W.; Hada, M.; Ehara, M.; Toyota, K.; Fukuda, R.; Hasegawa, J.; Ishida, M.; Nakajima, T.; Honda, Y.; Kitao, O.; Nakai, H.; Vreven, T.; Throssell, K.; Montgomery, J. A., Jr.; Peralta, J. E.; Ogliaro, F.; Bearpark, M. J.; Heyd, J. J.; Brothers, E. N.; Kudin, K. N.; Staroverov, V. N.; Keith, T. A.; Kobayashi, R.; Normand, J.; Raghavachari, K.; Rendell, A. P.; Burant, J. C.; Iyengar, S. S.; Tomasi, J.; Cossi, M.; Millam, J. M.; Klene, M.; Adamo, C.; Cammi, R.; Ochterski, J. W.; Martin, R. L.; Morokuma, K.; Farkas, O.; Foresman, J. B.; Fox, D. J. Gaussian, Inc., Wallingford CT, 2016.

It is known, for a postulate of quantum mechanics, that the wavefunction of a system contains all of its information but unfortunately, it is not a quantity that can be directly measured. Contrary to wavefunction methods, the Density Functional Theory relies on the electronic density of the molecule, which can be expressed as the partial integral of the square of the wavefunction. This quantity, contrarily to the wavefunction, can be measured by X-ray diffraction.

Due to the partial integration, the number of spatial variables needed is reduced to 3 rather than 3*N* variables (*N* being the number of atoms). This considerably decreases the computation cost while keeping the most useful information on the studied system. Indeed, the first Hohenberg-Kohn theorem[42] unexpectedly states that all the information about the studied systems can be recovered from its electron density, especially its energy. DFT makes use of functionals dependent on the electronic density of systems to determine their properties, including the energy. A wide variety of functionals has been developed and they are classified in several categories depending on the nature of the variable that are explicitly involved in the analytical form of the functional. More precisely, if the sole local density appears, the functional is labelled as local functional; if the energy gradient is added (with some technical modifications), it is a GGA (Generalized Gradient Approximation) functional; and if the second spatial derivatives of energy appears (or the kinetic energy density), it is a meta-GGA functional.

Another modification should be made to recover a correct long-distance analytical form of the potential: hybrid functionals include a percentage of the exact exchange energy computed from Hartree-Fock theory on the basis of a virtual wavefunction (see below).

The second Hohenberg-Kohn justify the use of a variational method to compute simultaneously the electron density and the energy. Nevertheless, to vary an electron density is quite difficult and a much more efficient method has been developed in which the electron density is expressed as a function of a virtual underlying wavefunction in which the electrons

[42] Hohenberg, P., & Kohn, W. (1964). Inhomogeneous Electron Gas. *Physical Review*, *136*(3B), B864-B871.

do not interact with each other. This is the basis of the Kohn-Sham equation[43] which is mono-configurational, meaning that the body of *n* electrons is considered as *n* one-electron systems.

Hybrid functionals are known to give more accurate results compared to other functionals and are widely used for chemical applications. The functionals retained for this study are among this type.

DFT[44] is used to obtain the optimised geometry of the molecule at the ground state, as it is a variational method. The study of the excited states is more challenging due to this limitation. The Runge-Gross theorem[45] can be seen as a generalization of the Hohenberg-Kohn theorem. It deals with the case of time-depending Hamiltonians such as those representative of the presence of an electromagnetic wave on an electronic system. In these situations, the Runge-Gross theorem states that the time-dependant electron density is a functional of the initial density (before application of the time-dependant term) and of the applied external potential. Therefore, the range of application of this theorem includes the study of excited stated where an external electromagnetic field is applied to induce electronic transitions. The methods relying on this theorem are known as Time-Dependent DFT methods (TD–DFT).

TD–DFT[46,47,48] is used to optimise the geometry at the excited state and also to calculate the electronic transitions in the desired wavelengths range to compare it with the experimental data. Relevant information like the energy of the compounds, thermodynamic values as well as the theoretical excitation and emission wavelengths are gathered.

---

[43] Kohn, W., & Sham, L. J. (1965). Self-Consistent Equations Including Exchange and Correlation Effects. *Physical Review*, *140*(4A), A1133-A1138.
[44] Kohn, W., Becke, A. D., & Parr, R. G. (1996). Density Functional Theory of Electronic Structure. *The Journal of Physical Chemistry*, *100*(31), 12974–12980.
[45] Runge, E., & Gross, E. K. U. (1984). Density-Functional Theory for Time-Dependent Systems. *Physical Review Letters*, *52*(12), 997-1000.
[46] Adamo, C., & Jacquemin, D. (2013). The calculations of excited-state properties with Time-Dependent Density Functional Theory. *Chem. Soc. Rev.*, *42*(3), 845–856.
[47] Jacquemin, D., Mennucci, B., & Adamo, C. (2011). Excited-state calculations with TD-DFT: From benchmarks to simulations in complex environments. *Physical Chemistry Chemical Physics*, *13*(38), 16987-16998.
[48] Laurent, A. D., & Jacquemin, D. (2013). TD-DFT benchmarks: A review. *International Journal of Quantum Chemistry*, *113*(17), 2019–2039.

Concerning the first part of the thesis concerning the complexation reactions, the methodology applied is specific to our system. Both DFT and TD–DFT calculations are necessary to obtain the correct geometry at the ground and excited states. For all the computed systems, B3LYP (20% HF)[49,50,51,52] was used as functional with the 6–311+G** basis set[53,54,55,56]. This global hybrid functional is well–known for its ability to reproduce correctly geometries and excited states for small molecules[48]. Figure 4 confirms that B3LYP is appropriate for the systems under study since the experimental band of the ligand (quercetin in this case) is well described by the electronic calculations.

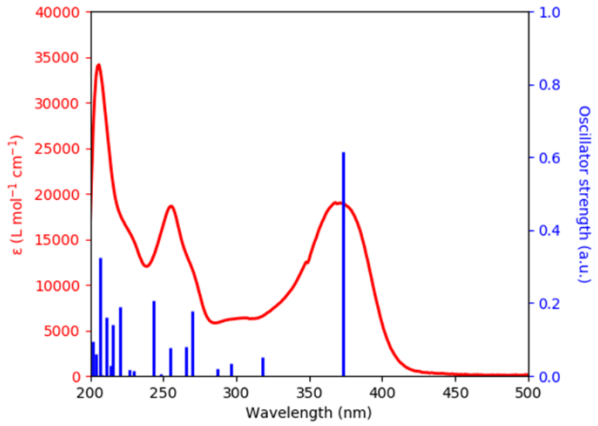

Figure 4 Overlap of the experimental spectrum of quercetin (in red) and the electronic transitions computed with the B3LYP/6-311+G** (blue vertical lines)

[49] Becke, A. D. (1993). Density-functional thermochemistry. III. The role of exact exchange. *The Journal of Chemical Physics*, *98*(7), 5648–5652.
[50] Lee, C., Yang, W., & Parr, R. G. (1988). Development of the Colle-Salvetti correlation-energy formula into a functional of the electron density. *Physical Review B*, *37*(2), 785–789.
[51] Becke, A. D. (1988). Density-functional exchange-energy approximation with correct asymptotic behavior. *Physical Review A*, *38*(6), 3098-3100.
[52] Vosko, S. H., Wilk, L., & Nusair, M. (1980). Accurate spin-dependent electron liquid correlation energies for local spin density calculations : A critical analysis. *Canadian Journal of Physics*, *58*(8), 1200-1211.
[53] Krishnan, R., Binkley, J. S., Seeger, R., & Pople, J. A. (1980). Self-consistent molecular orbital methods. XX. A basis set for correlated wave functions. *The Journal of Chemical Physics*, *72*(1), 650–654.
[54] McLean, A. D., & Chandler, G. S. (1980). Contracted Gaussian basis sets for molecular calculations. I. Second row atoms, *Z* =11–18. *The Journal of Chemical Physics*, *72*(10), 5639–5648.
[55] Hariharan, P. C., & Pople, J. A. (1973). The influence of polarization functions on molecular orbital hydrogenation energies. *Theoretica Chimica Acta*, *28*(3), 213–222.
[56] Clark, T., Chandrasekhar, J., Spitznagel, G. W., & Schleyer, P. V. R. (1983). Efficient diffuse function-augmented basis sets for anion calculations. III. The 3-21+G basis set for first-row elements, Li-F. *Journal of Computational Chemistry*, *4*(3), 294–301.

In order to carefully reproduce the experimental model for complexes, several parameters need to be taken into consideration. Since one of the aims is to know the fixation site of the metal cation, all the possibilities of complexed forms are computed. In addition to that, there are several hydroxyl groups present at each site, hence, all the plausible protonation states of the complex–es have been envisaged. It is important to note that the mono–dentate coordination mode was not taken into consideration as it is chemically unlikely that a metal cation would fix itself on an ether, carbonyl or hydroxyl group.

Moreover, whereas an implicit solvation model was suitable for computations involving a ligand only, a semi–implicit solvation model was needed for complexes[57]. In order to represent the coordination sphere around the metal cation, explicit solvent molecules were added. Since the structure of the coordination sphere and the metal coordination number are unknown, trials were performed with four, three and two molecules around the metal cation. The Polarisable Continuum Model (PCM) was then used to represent the environment[58,59]. Aside from the coordination sphere of the metal core, there is also the possibility of having several explicit solvent molecules around the ligand. However, it is very difficult to determine exactly how many molecules should be placed. Several tests were performed with the addition of some solvent molecules at the sites where they have a higher chance of forming bonds with the ligand. However, the calculated spectra varied a lot and were not at all coherent with the experimental one. This is why, for this study, the explicit solvent molecules were positioned only around the metal atom and PCM was applied to represent the environment of the complex. It should be noted that water molecules were used during the computations instead of methanol simply to reduce calculation time. The difference between the data obtained with the two solvents were negligible.

[57] Boumendil, S., Cornard, J.-P., Sekkal-Rahal, M., & Moncomble, A. (2015). Solvent effects to compute UV–vis spectra for ionic metal complexes. *Chemical Physics Letters*, *636*, 39–45.
[58] Cossi, M., Scalmani, G., Rega, N., & Barone, V. (2002). New developments in the polarizable continuum model for quantum mechanical and classical calculations on molecules in solution. *The Journal of Chemical Physics*, *117*(1), 43–54.
[59] Tomasi, J., Mennucci, B., & Cammi, R. (2005). Quantum Mechanical Continuum Solvation Models. *Chemical Reviews*, *105*(8), 2999–3094.

The solvent effect was also taken into consideration when the molecules were optimised at the excited state. In each case, a linear response formalism was used. The solvent was equilibrated in the ground state for optimization in the ground state and absorption computations, and in the excited state for optimization in the excited state and emission computations.

If we take the example of morin (flavonoid used in this study that will be elaborated later on), it bears four fixation sites; the α–hydroxyketo site, the β–hydroxyketo site, the hydroxyether site and the diol site. The first three sites possess one hydroxyl group each while two hydroxyl groups belong to the diol site. By taking into account the variation of the complexation site as well as the protonation state of the ligand, this totals up to ten hypothetical complexes. Adding to that the variation of the coordination sphere, we reach thirty hypothesis for possible complexes formed during a complexation reaction between a metal cation and morin to obtain a complex of 1:1 stoichiometry.

If the same procedure is applied to quercetin, having three fixation sites, we add up to twenty–four possibilities. As for luteolin possessing two fixation sites, eighteen hypothetical structures need to be calculated.

1.2.4 Quantum Theory – Atoms In Molecules (QT–AIM)

All the Quantum Theory of Atoms In Molecules (QT–AIM) calculations were performed by the AIMAll software[60]. These calculations were done on the molecules to have a better indication on the partial charges on each atom calculated by integration over Bader atoms and on the ionicity of some bonds. To harness the potential of this method, it is important to understand how it operates. As it is well–known, the electronic density is greatest over the nuclei and it decreases gradually along the bond, forming a structure similar to a well between two atoms of a molecule. It could be illustrated by the electron density along the axis of a linear molecule such as CO_2 as shown in Figure 5.

[60] T. A. Keith, AIMAll 17.01.25, TK Gristmill Software, Overland Park, 2017

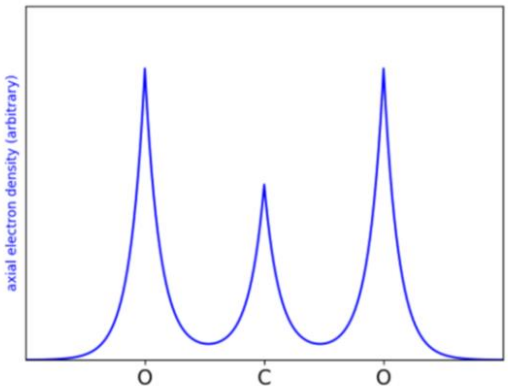

Figure 5 Sketch of the electron density profile along the principal axis of the CO_2 molecule

If we move on to a three dimension figure, for most bonds, a minimum of the electron density along one axis which is a maximum along the two other perpendicular axes is observed. This point is noted as the bond critical point (BCP). This BCP is a way to redefine the chemical bond properties: instead to the qualitative vision that is mostly encountered in chemistry, the properties of the chemical bond are linked to a unique point that is mathematically univocally defined.

QT–AIM[61] localises all the critical points and, thus, allows us to calculate the hessian eigenvalues of the electron density at each point. Based on the latter, we can determine the nature of the points. The most significant points are maxima (3 negative values in the Hessian matrix) that corresponds most often to the position of nuclei, and critical points of order 1 (2 negative values and 1 positive value in the Hessian matrix). If we go a bit further, for example for the case of benzene, the point in the middle of the ring is the ring critical point (RCP) where it is minimum with respect to plane containing the atoms and the BCPs but maximum when we move perpendicular to the surface of the ring. Finally, for the case of a caged molecule, there is the presence of a cage critical point (CCP) that is the minimum.

[61] Bader, R. F. W. (1994). *Atoms in molecules: A quantum theory*. Oxford [England]: New York: Clarendon Press; Oxford University Press.

Once these points localised, careful examination of the electron density properties computed at BCPs give insight in the nature of the chemical bond. For instance, the value of the Laplacian of the electron density computed at a BCP (that is, the sum of the eigenvalues) is often used as a tool to classify between closed–shell and open–shell interactions. If the positive eigenvalues contribution is the larger phenomenon, the point is considered as representative of a closed shell and the bond is considered to have an ionic character, quantified by the value of the Laplacian (the bigger the value, the higher the iconicity). The opposite is true, that is, a point where the positive eigenvalues contribution is the larger phenomenon is an open shell and the bond has a covalent nature.

This classification is, of course, very crude and the continuum between these two archetypes (covalent and ionic bond) should not be forgotten. More subtle indicators have been introduced and will be used later in this manuscript[62].

[62] Matta, C. F. (2006). Hydrogen–Hydrogen Bonding: The Non-Electrostatic Limit of Closed-Shell Interaction Between Two Hydro. In S. J. Grabowski (Ed.), *Hydrogen Bonding—New Insights* (pp. 337–375).

1.3 Study of morin

1.3.1 Structure of morin and presence of inter–ring hydrogen–bond

Morin (2',3,4',5,7–pentahydroxyflavone) is a flavonol bearing five hydroxyl groups, belonging to the subfamily of flavonoids. Largely present in the vegetal kingdom and in organic matter in general, this molecule has also been extensively studied in cases where it was subjected to complexation reactions[63,64,65,66,67,68,69,70].

Like its peers, morin has a low solubility in water and in order to enhance its bioavailability, morin was made to complex with several types of cyclodextrins[71]. The reaction was successful, forming a 1:1 complex and by absorption spectroscopy, it was shown that the solubility improved. The Rotating–frame Overhauser Effect SpectroscopY (ROESY), being a 2D–NMR technique was employed to study the inclusion complexes.

---

[63] Domínguez-Renedo, O., Marta Navarro-Cuñado, A., Ventas-Romay, E., & Asunción Alonso-Lomillo, M. (2019). Determination of aluminium using different techniques based on the Al(III)-morin complex. *Talanta*, *196*, 131–136.

[64] Kokulnathan, T., Sakthinathan, S., Chen, S.-M., Karthik, R., & Chiu, T.-W. (2018). Hexammine cobalt(iii) coordination complex grafted reduced graphene oxide composite for sensitive and selective electrochemical determination of morin in fruit samples. *Inorganic Chemistry Frontiers*, *5*(5), 1145–1155.

[65] Sentkowska, A., Kilian, K., Kopeć, M., Pyrzyńska, K., & Cheda, Ł. (2017). Ga(III) complex with morin for kidney cancer cell labelling. *Applied Organometallic Chemistry*, *31*(12), e3882.

[66] Woźnicka, E., Zapała, L., Pieniążek, E., Kosińska, M., Ciszkowicz, E., Lecka-Szlachta, K., Pusz, J., Maciołek, U., Dronka, J. (2017). Synthesis, characterization and antibacterial studies of Tm(III), Yb(III) and Lu(III) complexes of morin. *Journal of Coordination Chemistry*, *70*(8), 1451–1463.

[67] Pieniążek, E., Kalembkiewicz, J., Dranka, M., & Woźnicka, E. (2014). Syntheses, crystal structures and antioxidant study of Zn(II) complexes with morin-5'-sulfonic acid (MSA). *Journal of Inorganic Biochemistry*, *141*, 180–187.

[68] Liu, E., & Zhang, H. (2014). Interaction of the La(III)–Morin Complex with Human Serum Albumin. *Journal of Solution Chemistry*, *43*(8), 1402–1413.

[69] Panhwar, Q. K., & Memon, S. (2012). Synthesis and properties of zirconium(IV) and molybdate(II) morin complexes. *Journal of Coordination Chemistry*, *65*(7), 1130–1143.

[70] Bishop, E. (1950). The influence of anions on the morin test for aluminium, gallium, beryllium and zinc, and the identification of certain anions. *Analytica Chimica Acta*, *4*, 6–11.

[71] Jullian, C., Orosteguis, T., Pérez-Cruz, F., Sánchez, P., Mendizabal, F., & Olea-Azar, C. (2008). Complexation of morin with three kinds of cyclodextrin. *Spectrochimica Acta Part A: Molecular and Biomolecular Spectroscopy*, *71*(1), 269–275.

Studies on the characterisation of the reaction of copper cations with morin were carried. The importance of such work was to inspect the type of complex formed as well as its antioxidant activity using spectroscopic techniques like UV–vis, fluorescence, IR, NMR, and thermal, gravimetric and elemental analysis. The authors were able to show that the Cu^{II}–morin complex had antioxidant properties higher than morin[72]. The Cu^{II}–morin complex was also considered to quantify cysteine in porcine blood and human urine since the redox reaction involving the complex and cysteine revealed an enhanced fluorescence activity[73]. Another metal cation that easily forms a complex with morin is aluminium. A study was carried out to find out the aluminium content in drinking water. By reacting aluminium cations with morin, it was evidenced that the complex present a fluorescence emission[74]. DNA is, most of the time, the target molecule for anticancer drugs. Complexes involving morin are often able to bind with double–stranded DNA, which is useful since the morin–DNA complex can help to understand the interaction that DNA has with anticancer drugs. Indeed, europium and lanthanum cations have already been assessed in such complexed form with morin in the presence of DNA and both of them show an improvement in their fluorescence bands[75,76]. Chromium also adds itself to the several metal cations considered to investigate the features of the complexing power of morin[77]. Considering the good fluorescent abilities that morin complexes, the latter were even considered to be used as optical sensors for cations such as beryllium and aluminium[78,79].

[72] Panhwar, Q. K., Memon, S., & Bhanger, M. I. (2010). Synthesis, characterization, spectroscopic and antioxidation studies of Cu(II)–morin complex. *Journal of Molecular Structure*, *967*(1–3), 47–53.
[73] Liao, W.-S., Wu, F.-Y., Wu, Y.-M., & Wang, X.-J. (2008). Highly sensitive spectrofluorimetric determination of cysteine by Cu2+-morin complex. *Microchimica Acta*, *162*(1–2), 147–152.
[74] Al-Kindy, S. M. Z., Suliman, F. O., & Salama, S. B. (2003). A sequential injection method for the determination of aluminum in drinking water using fluorescence enhancement of the aluminum–morin complex in micellar media. *Microchemical Journal*, *74*(2), 173–179.
[75] Zhang, G., Guo, J., Pan, J., Chen, X., & Wang, J. (2009). Spectroscopic studies on the interaction of morin–Eu(III) complex with calf thymus DNA. *Journal of Molecular Structure*, *923*(1–3), 114–119.
[76] Liu, X., Li, Y., & Ci, Y. (1997). Interaction of the La3+-Morin Complex with DNA. *Analytical Sciences*, *13*(6), 939–944.
[77] Panhwar, Q. K., & Memon, S. (2014). Synthesis of Cr(III)-Morin Complex: Characterization and Antioxidant Study. *The Scientific World Journal*, *2014*, 1–8.
[78] Saari, L. A., & Seitz, W. R. (1984). *Optical Sensor for Beryllium Based on Immobilised Morin Fluorescence*. *109*, 655–657.
[79] Saari, L. A., & Seitz, W. Rudolf. (1983). Immobilized morin as fluorescence sensor for determination of aluminum(III). *Analytical Chemistry*, *55*(4), 667–670.

Morin has the ability to form chelates with metal cations onto four different complexation sites. The C2–C1' bond connecting the rings B and C can be freely rotated to give rise to several rotamers. Amongst them, there are two main conformers that stand out from the others. The first one, conformer 1, is represented on Figure 6 where we can see the first three sites denoted as α–hydroxyketo, β–hydroxyketo and hydroxyether. When the C2–C1' bond is rotated in such a way that the hydroxyl group in position 2' is in the vicinity of the position 3 hydroxyl group (Figure 6), denoted as conformer 2, the diol site becomes apparent and available as the fourth fixation site. The surprising fact is that, to date, this fixation site has never been mentioned in published works even though it can be seen that conformer 2 is a more stable compound at a first glance. It was introduced for the first time in one of our published works[80].

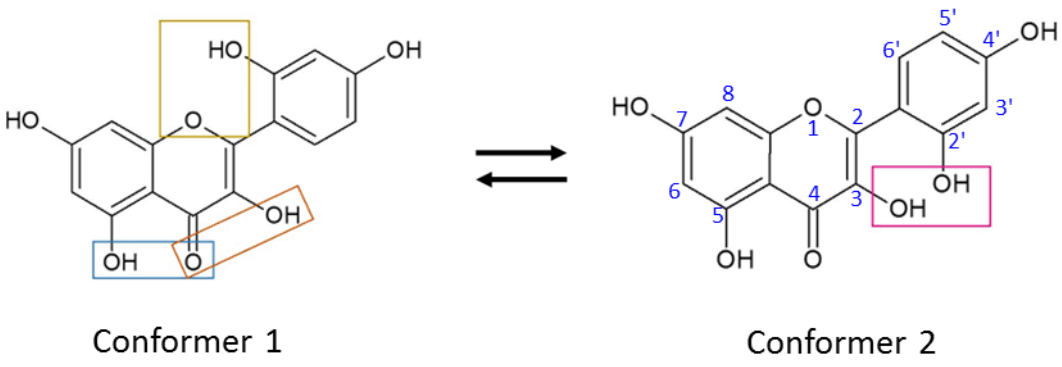

Figure 6 Structure of morin with the α–hydroxyketo (brown), β–hydroxyketo (blue) and hydroxyether (yellow) fixation sites on conformer 1 and the diol (pink) fixation site on conformer 2

The fact that the diol site is never mentioned in the articles concerning morin has led us to study in detail the structural and spectroscopic properties of this flavonoid. If we take a closer look at this rotamer, we can clearly see that there are three hydrogen bonds present; between O2'H2' and O3H3, between O3H3 and O4 and finally between O5H5 and O4. In this conformation, the molecule is considered to be most favourable due to the network of hydrogen bonds. The O2'H2' --- O3H3H-bond is named inter–ring hydrogen bond. In order to

[80] Moncomble, A., Jani Thaviligadu, D., Raoumbé Djendja, A., & Cornard, J.-P. (2018). The crucial role of the inter-ring hydrogen bond to explain the properties of morin. *New Journal of Chemistry*, *42*(10), 7691–7702.

assess the importance and stability of the inter–ring hydrogen bond, a thermodynamic study was performed on conformer 2 of morin, with and without the O2'H2' and O3H3 hydrogen bond.

The difference in the energy of both conformation isomers is quite low ($\Delta_r E$ = 3.4 kcal mol^{-1}) in favour of the isomer with the inter–ring hydrogen bond. If we add the vibrational contribution to this value to obtain the free Gibbs energy, we end up with a difference of $\Delta_r G$ = 2.6 kcal mol^{-1} still in the favour of the conformer with the inter–ring hydrogen bond. This difference is very weak and due to the accuracy of DFT, we cannot make a clear–cut conclusion based only on these values. We furthered this study by calculating the electronic transitions of each structure using TD–DFT to decipher which model corresponds best to the experimental spectrum. For comparison of experimental and theoretical spectra, the experimental spectrum was recorded at a pH of 4.2 to have the majority of fully protonated morin in the solution so as to do a precise comparison with the computed vertical transitions and avoid a distortion of the morin band located at 356 nm. Indeed, when working at a higher pH value, the deprotonated form of morin is clearly visible on the spectrum and this is a feature that needs to be avoided (Figure 7). The results obtained are reported on Figure 8.

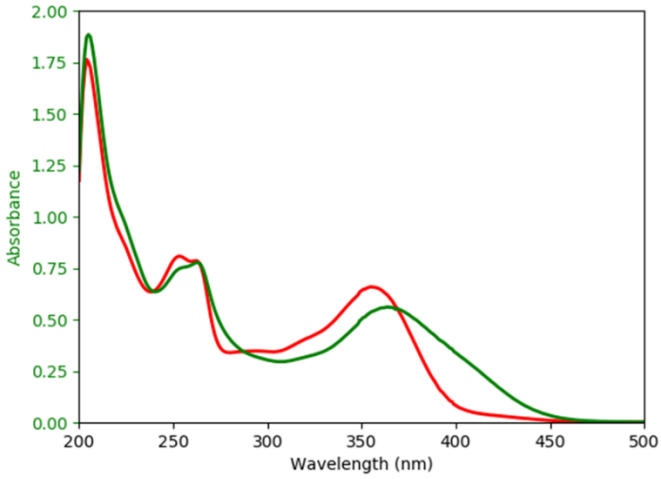

Figure 7 The overlap of two spectra of morin at pH 4.2 (red) and pH 6.2 (green)

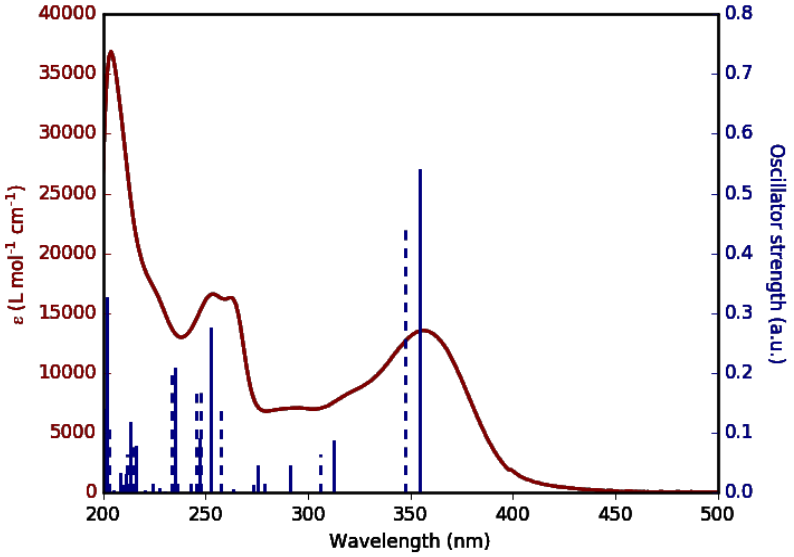

Figure 8 Overlap of the experimental absorption spectrum of morin (red curve) and the computed transitions for morin with (solid blue lines) and without (broken blue lines) the O3–H2' H–bond

Once again, the model bearing the inter–ring hydrogen bond is favoured since the lowest energy as well as the second lowest energy transitions are in excellent agreement with the experimental data and the shape of the band is well represented (Figure 8 and Table 1). Even if the corresponding electronic transitions are slightly blue–shifted, the model without the inter–ring hydrogen bond gives acceptable results as the experimental band is correctly reproduced. From a spectral point of view, both models are possible, hence, it does not matter which isomer is taken into consideration for spectra calculations in the following since both of them will give somewhat similar results. There is a high chance that the ETOH molecules form hydrogen bonds with the ligands. However, if we were to add explicit solvent molecules around the ligand, the electronic spectra calculated varies significantly depending on the number of EtOH molecules added and no more match the experimental spectrum.

The TD–DFT results also helped us to validate the computational method used for our systems as the electronic transitions corresponds well to the spectrum of morin. For sure, the various complexes computed will correctly describe the experimental data. The last two transitions at 354 nm and 313 nm corresponds to the HOMO → LUMO transition (the electron density shifts from ring B and the O3 atom to ring C and the π* molecular orbital on the C4O4 bond) and HOMO−1 → LUMO transition (the electron density shifts from ring A and ring B to ring C and

the π* molecular orbital on the C4O4 bond) respectively. The molecular orbitals of the mentioned transitions are illustrated in Figure 9.

Table 1 Experimental and computed wavelengths and energies for the low lying energy bands of morin

	Experimental data, λ, nm (E, eV)	Computed vertical transitions, λ, nm (ΔE, eV)	
		With inter–ring H–bond	Without inter–ring H–bond
Lowest energy band	356 (3.48)	354 (3.50)	348 (3.57)
Second lowest energy band	319 (3.89)	313 (3.96)	306 (4.05)

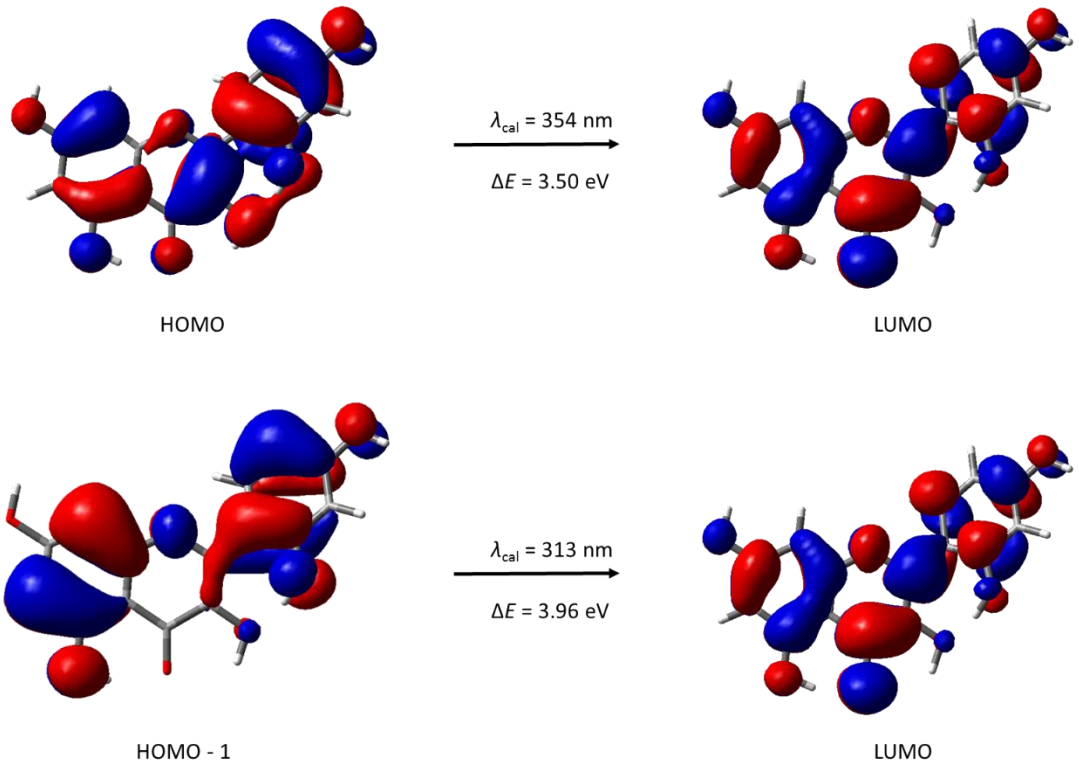

Figure 9 The HOMO–1 → LUMO and HOMO → LUMO transitions for the morin molecule with the inter–ring H–bond

1.3.2 pKa studies on morin

Compared with other flavonoids, the UV–visible spectra very quickly show a band corresponding to the deprotonated form of morin when the pH is increased. For these reasons, we undertook a study of the different states protonation of morin. Being a penta–hydroxyflavone, it is important to determine the first pK_a values of the molecule before going further in the experimental work. As a matter of fact, the study requires to know the protonation state of the different sites in competition. The determination of the different pK_as of morin was carried out both experimentally and theoretically. For the latter, great care will be given to the conformer of morin studied. In order to be consistent and precise, the model with the inter–ring hydrogen bond will be considered. In this conformation, the oxygens 5, 4, 3 and 2' are particular as they partly share the three hydrogen atoms that they carry. The diol fixation site contains two hydroxyl groups and this configuration can facilitate the removal of one proton.

The experimental part of this study concerns a titration procedure of morin by sodium hydroxide starting from an acidic pH in methanol solution. In order to obtain spectroscopic results from this experiment, a spectrum is taken at the different pH values. The obtained spectral data set presented in Figure 10 shows two consecutive deprotonation occurrences. A first shift in the absorption bands showing the formation of the first deprotonated species at 389 nm and the apparition of a doubly–deprotonated species is evidenced by a band seen at around 400 nm. The classical method to obtain the pK_a of morin is to do a plot of the number of moles of sodium hydroxide added to the morin solution with respect to the corresponding pH values.

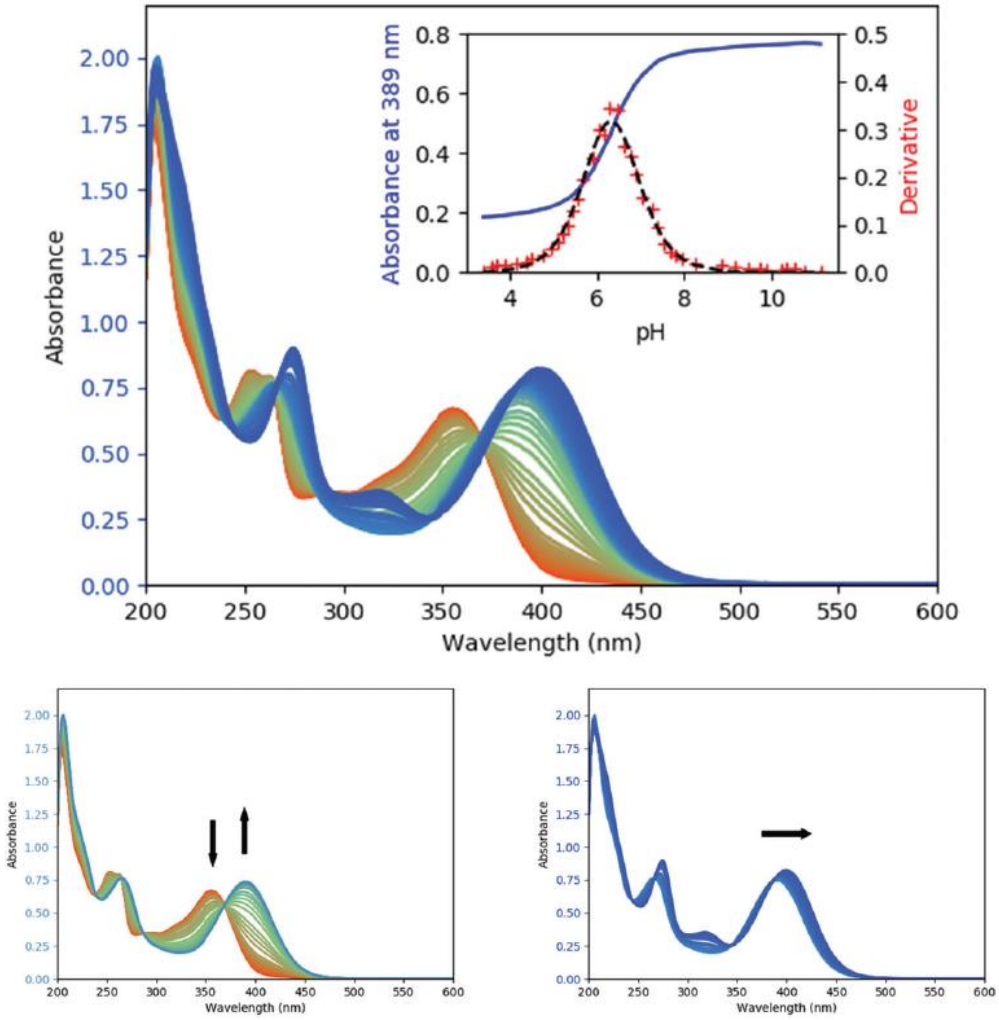

Figure 10 Set of UV–vis spectra measured during the titration of morin against sodium hydroxide: whole set (top), and restriction to the values of pH below (bottom left) and above (bottom right) 8.2. Inset: Absorbance at 389 nm (plain blue curve), and its derivative function (red +) and interpolation (broken black curve) with respect to the pH

Nonetheless, by doing so, it is not possible to get the sudden pH rise needed to calculate the pK_a value as depicted in Figure 11.

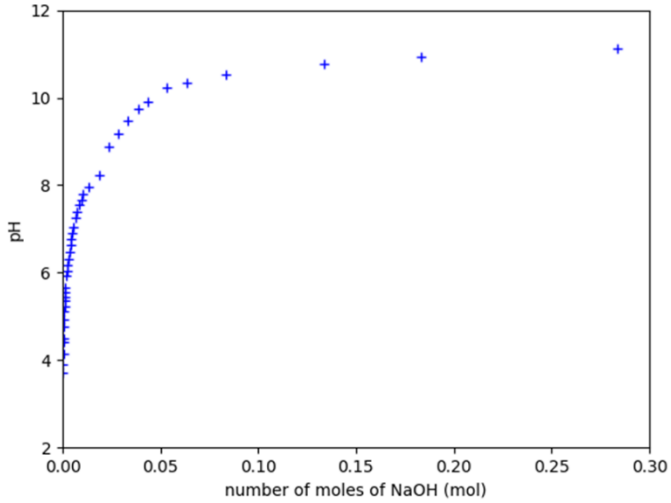

Figure 11 Titration of morin with sodium hydroxide with the evolution of the pH versus the number of moles of NaOH, n (mol)

Another method to obtain the pK_a values is to plot the absorbance at a specific wavelength (in this case at 389 nm corresponding to the first deprotonated species) with respect to the pH. It is useful to do a graphical representation of the derivative of the absorbance against the pH value to quantify the pK_a (Inset of Figure 10). The obtained values of the derivative were fitted by the analytical relation expected for an equilibrium between an acid and its conjugated base: (Equation 1)

$$\frac{\partial A}{\partial \mathrm{pH}} = \frac{\alpha\, 10^{\mathrm{pH}-\mathrm{p}K_a}}{(1+10^{\mathrm{pH}-\mathrm{p}K_a})^2} \qquad \textit{Equation 1}$$

where α is a constant depending on the absorption molar coefficient of both species, the total concentration in morin and the optical path length. The least–square fitting computes a value of 6.3 for the first pK_a of morin. This value is consistent with the one measured in water since pK_a values in methanol are usually higher than those in water[81]. However, this is quite surprising to obtain such a low value because generally, the first pK_a values of most flavonoids are located higher, ranging from 7.0 to 9.0. The same step was done with the second deprotonated species at 400 nm. Unfortunately, no conclusive results were obtained as its

[81] Rived, F., Canals, I., Bosch, E., & Rosés, M. (2001). Acidity in methanol–water. *Analytica Chimica Acta*, *439*(2), 315–333.

value is too close to that of the first deprotonated species. Other methods such as capillary electrophoresis can be suitable if there is a need to determine the second pK_a[82].

In order to find the structure of the deprotonated morin molecule theoretically, assumptions should be made on the molecule by doing DFT computations on each possible deprotonated species. The deprotonation of the morin molecule can be downsized to Equation 2.

$$\mathrm{Morin} \rightarrow \mathrm{Morin}^- + \mathrm{H}^+ \qquad \textit{Equation 2}$$

According to this equation, there is a need to consider the Gibbs free energy of a proton and it is well–known that there are some difficulties related to the calculations of pK_a values[83,84,85]. Therefore, we decided to use an alternate approach by using the concept of acid–base pairs associated to Equation 3. Instead of considering only the deprotonation of morin, the latter can be made to equilibrate with another compound, named the 3–hydroxyflavone (3HF). As the name suggests, the 3–hydroxyflavone is a flavonoid which has only one hydroxyl group at position 3. Thus, it is easier to determine its free Gibbs energy as well as that of its deprotonated form. By interacting both molecules, the problem caused by the proton is solved as only the free Gibbs energy of the two flavonoids and their deprotonated forms are needed for the calculations of the pK_a values. The procedure applied was such that the difference of the pK_a values of the deprotonated morin species with respect to the 3–hydroxyflavone (p*K*a of 9.12[86]).

---

[82] Cabot, J. M., Fuguet, E., & Rosés, M. (2014). Determination of acidity constants of sparingly soluble drugs in aqueous solution by the internal standard capillary electrophoresis method: CE and CEC. *ELECTROPHORESIS*, *35*(24), 3564–3569.

[83] Thapa, B., & Schlegel, H. B. (2016). Density Functional Theory Calculation of p K_a 's of Thiols in Aqueous Solution Using Explicit Water Molecules and the Polarizable Continuum Model. *The Journal of Physical Chemistry A*, *120*(28), 5726–5735.

[84] Bochevarov, A. D., Watson, M. A., Greenwood, J. R., & Philipp, D. M. (2016). Multiconformation, Density Functional Theory-Based p K_a Prediction in Application to Large, Flexible Organic Molecules with Diverse Functional Groups. *Journal of Chemical Theory and Computation*, *12*(12), 6001–6019.

[85] Galano, A., Pérez-González, A., Castañeda-Arriaga, R., Muñoz-Rugeles, L., Mendoza-Sarmiento, G., Romero-Silva, A., … Alvarez-Idaboy, J. R. (2016). Empirically Fitted Parameters for Calculating p K_a Values with Small Deviations from Experiments Using a Simple Computational Strategy. *Journal of Chemical Information and Modeling*, *56*(9), 1714–1724.

[86] Wolfbeis, O. S., Leiner, M., Hochmuth, P., & Geiger, H. (1984). Absorption and Fluorescence Spectra, pKa Values, and Fluorescence Lifetimes of Monohydroxyflavones and Monomethoxyflavones. *Berichte Der Bunsengesellschaft Für Physikalische Chemie*, *88*(8), 759–767.

$$\text{Morin} + 3\text{HF}^- \rightarrow \text{Morin}^- + 3\text{HF} \qquad \textit{Equation 3}$$

Contrarily to 3–hydroxyflavone, different deprotonated species need to be considered for the deprotonated form of morin. The values obtained are summarised in Table 2. At this point, the role of the inter–ring hydrogen bond gains importance. With the removal of the H2' atom, two configurations of the deprotonated molecule are possible: either by maintaining the hydrogen bond between O3H3 and O4 or by forming a new hydrogen bond between O3H3 and O2'. Interestingly enough, the base with the O3H3 and O2' hydrogen bond has a theoretical pK_a eight units less than the former structure. This characteristic emphases on the fact that morin is more acidic compared to other flavonoids and this is because of the combined effort of O2'H2' and O3H3 hydroxyl. If we were to remove one of them, its pK_a increases considerably. The difference of the values computed reaches 8.22 (H2') or 11.44 (H3). In the case where either the H2' or the H3 is missing, the most labile proton becomes H7 or H4' depending on the other modifications on the substitution pattern of the molecule. From these results, we can deduce that, generally, in the absence of both H2' and H3, the most acidic proton is H7 or H4' and the protons H2' and H3 have pK_a values much higher. However, when both H2' and H3 are present on a molecule, the influence of the inter–ring hydrogen bond system is great and it causes the first pK_a of the molecule to drop considerably[87]. The most acidic proton then becomes either 2' or 3. This uncertainty is not due to a lack of knowledge, but simply to the fact that in both cases, the formed species is the same. The mechanism that yields the deprotonated species differs, but the final form is the same, that is the only important aspect for thermodynamic computations such as those involved in pK_a computations.

In addition to that, it has been observed that there is no change in the base structure when the H3 proton is removed. This leads us to say that the most important aspect is the structure of the deprotonated molecule and not the proton that departs. Based on all these observations, the theoretical value of the first pK_a of morin was found to be between 3.5 and

[87] Álvarez-Diduk, R., Ramírez-Silva, M. T., Galano, A., & Merkoçi, A. (2013). Deprotonation Mechanism and Acidity Constants in Aqueous Solution of Flavonols: A Combined Experimental and Theoretical Study. *The Journal of Physical Chemistry B*, *117*(41), 12347–12359.

5.5, which is coherent with the measured value in water (5.0) as well as the experimental value obtained in methanol in this study (6.3). Because of the low pK_a values, the experimental work carried out when working with morin will be performed at a low pH value of 4.2 to ensure that the majority of the ligand molecules are fully protonated.

Table 2 Acid–base features for the conceivable deprotonation of morin: ΔpK_a are computed with the lowest value as a reference. The H–bond network is depicted only where an ambiguity occurs

Removed hydrogen	H–bond network	ΔpK_a
H3	O4 O3 O2’ – – H	11.44
H3	O4 O3 – – H – – O2’	0.00
H5		9.44
H7		3.51
H2’	O4 – – H – – O3 O2’	8.22
H2’	O4 O3 – – H – – O2’	0.00
H4’		5.68

1.4 Molecules associated to morin

1.4.1 Quercetin

One of the flavonoids investigated for this study is the 3,3',4',5,7–pentahydroxyflavone or simply known as quercetin ($C_{15}H_{10}O_7$). It is the most well–known flavonoid available and it is even commercially available as nutritional supplements because of its biological properties. It forms part of the sub–category of flavonols. Quercetin has been a subject of thorough study for a long time. Largely present naturally in the plant kingdom especially under the form of the *O*–glycoside, it has the possibility to interact with several other species. Quercetin which is good for the metabolism, is consumed in various meals such as onions, broccoli, berries, tea, wine and food supplements.

Free radicals are a source of problem in plants and the human system. They can easily bind themselves with the different species found in the organisms, like DNA for example, causing oxidative stress and eventually cell death. Quercetin has the ability to stabilise free radicals both in plants and the human body because it has many conjugated bonds in its structure[88]. Largely present in plants, it also protects the latter from strong ultraviolet radiations. Besides, Mierziak figured out that plants that are more exposed to UV radiations have a higher concentration of quercetin in their organs[20]. In addition to that, quercetin is a source of numerous studies related to its ability to chelate transition metals that will be discussed later on in this chapter.

Alongside all these properties, quercetin is also a multisite ligand and has the ability to form chelates with several metal cations. Incidentally, it possesses three fixation sites: α–hydroxyketo, β–hydroxyketo and catechol site and they are designated in Figure 12. These functional groups are usually present in organic matter and most of the time, they are partially responsible for the interactions that can occur with cations and other species present in the

[88] Aliaga, C., & Lissi, E. A. (2004). *Comparison of the free radical scavenger activities of quercetin and rutin—An experimental and theoretical study*. *82*, 1668–1673.

environment. From some calculations, it was concluded that the protons located at positions 4', 7, 3', 3 and 5 can be ranked as such going from the most acidic to the most basic[89].

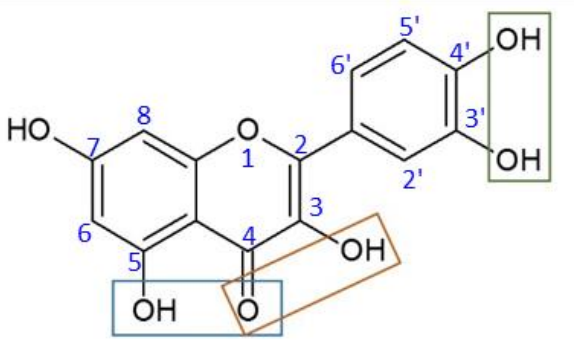

Figure 12 Structure of quercetin with the α–hydroxyketo (brown), β–hydroxyketo (blue) and catechol (green) fixation sites

Although not officially acknowledged as a treatment for cancer–related or neurodegenerative–type diseases since the degree of quercetin's absorption *in vivo* is not well defined, all the environmental and biological features pertaining to quercetin are a source of interest to many researchers worldwide. That led to many studies exploring their interactions with different metal cations using different operating modes. In most papers, different methods are used to find a way to exploit and enhance the antioxidant properties of quercetin.

Research groups worldwide have investigated the complexation reactions of metal cations with quercetin. Pękal et al. were interested in the mechanism of the reaction of Cu^{II} with quercetin as well as the interaction with free radicals[90]. They used UV–vis, IR and ESI–MS techniques to go a follow–up of the complexation reaction. They were able to evidence a 1:1 complex and deduced that the complex was a much better free radical stabiliser than quercetin alone. Another complex that was published was the Sn^{II}–quercetin complex[91]. The objective of this work matched that of the Cu^{II}–quercetin complex, that is, the formation of

[89] Amorati, R., Baschieri, A., Cowden, A., & Valgimigli, L. (2017). The Antioxidant Activity of Quercetin in Water Solution. *Biomimetics*, *2*(4), 9.
[90] Pękal, A., Biesaga, M., & Pyrzynska, K. (2011). Interaction of quercetin with copper ions: Complexation, oxidation and reactivity towards radicals. *BioMetals*, *24*(1), 41–49.
[91] Dehghan, G., & Khoshkam, Z. (2012). Tin(II)–quercetin complex: Synthesis, spectral characterisation and antioxidant activity. *Food Chemistry*, *131*(2), 422–426.

the complex using spectroscopic methods and investigating the radical scavenging activity. Liu et al. devised an experimental method using soft ionisation mass spectroscopy at high sensitivity to elucidate the structure of quercetin complexes formed from the metal cations Fe^{II}, Co^{II}, Ni^{II}, Cu^{II} and Zn^{II} [92]. This can be considered to be an accurate technique of analysis,

Our team started working on the complexation reactions related to quercetin a few years ago by investigating its reaction with aluminium[93], lead[94] and magnesium cations[95]. It has been shown that the 3–hydoxyketo group is the most favourable fixation site of Al^{III}, whereas Pb^{II} preferentially form a complex with the catechol function. Magnesium was a source of interest since it is one of the most important in the human body and it participates in intracellular reactions. Moreover, since the complexation reactions of Mg^{II} was already studied with 3–hydroxyflavone and 5–hydroxyflavone, it was thought that it could be interesting to investigate a reaction where the sites compete against each other to determine which one is chosen preferentially and it was how quercetin was a good candidate for this study. In this paper, Mg^{II} was made to react with the three monosite flavonoids and quercetin according to our methodology involving both electronic spectroscopies and quantum chemical calculations. Also, based on the conditional complexation constants of the monosite flavonoids, it was deduced that the sites could be classified as α–hydroxyketo ($\log \beta = 2.43 \pm 0.01$) > β–hydroxyketo ($\log \beta = 2.08 \pm 0.01$) ≫ catechol ($\log \beta = -0.30 \pm 0.02$). The electronic transitions computed for each site were compared with the corresponding experimental spectrum of the complex. After a thorough study, it was shown that there was an equilibrium of two 1:1 complexes in the medium involving the α–hydroxyketo or the β–hydroxyketo site, evidenced by their similar complexing power and good comparison with the theoretical results.

[92] Liu, Y., & Guo, M. (2015). Studies on Transition Metal-Quercetin Complexes Using Electrospray Ionization Tandem Mass Spectrometry. *Molecules*, *20*(5), 8583–8594.
[93] Cornard, J. P., & Merlin, J. C. (2002). Spectroscopic and structural study of complexes of quercetin with Al(III). *Journal of Inorganic Biochemistry*, *92*(1), 19–27.
[94] Cornard, J. P., Dangleterre, L., & Lapouge, C. (2005). Computational and Spectroscopic Characterization of the Molecular and Electronic Structure of the Pb(II)−Quercetin Complex. *The Journal of Physical Chemistry A*, *109*(44), 10044–10051.
[95] Moncomble, A., & Cornard, J.-P. (2014). Elucidation of complexation multi-equilibrium with Mg^{II} and a multisite ligand. A combined electronic spectroscopies and DFT investigation. *RSC Advances*, *4*(55), 29050–29061.

1.4.2 Luteolin

The second flavonoid chosen for this study is the 3',4',5,7–tetrahydroxyflavone, more commonly known as luteolin. This molecule is similar to quercetin with a major exception. The hydroxyl group in position 3 does not exist and hence, luteolin instead forms part of the flavone sub–family. We recall that in the family of flavonoids, flavonols (morin and quercetin) are compounds with the hydroxyl group in position 3. If the latter is removed, we obtain flavones (including luteolin). It can be found in natural products like honey and pollen. This flavonoid holds the same biological properties as the other molecules[96]. However, the magnitude of these properties is not as marked as quercetin and it will be demonstrated further ahead in this work. Despite that, some studies have shown that luteolin reacts well with metal cations. One such study involved the complexation reaction of Pb^{II} with luteolin with the use of not only various spectroscopic techniques like electronic spectroscopy, IR and ^{1}H–NMR but also of DFT calculations for the optimisation of the geometries of the molecules and their spectral characteristics[97]. The authors were able to determine the fixation site and also prove that the yield of the reaction is appreciable. Luteolin is also known to be one of the compounds that is present in early art dyestuff called weld. Upon complexation with Al^{III}, an organic pigment that was very popular in the past for manuscripts and paintings was produced[98]. To know more about the conservation of those dyes, many spectroscopic techniques were used. DFT and TD–DFT methods were also put forward to learn more about the molecular systems of the Al^{III}–luteolin complexes and to compare the theoretical values to the experimental ones. The authors showed that the thermodynamic data was not enough to determine the type of complex formed but only the general trends that the 4–5 site was favoured. It was much better to do a comparison of the experimental and computed absorption spectra. This way they were able to deduce the stoichiometry of the complex and that the β–hydroxyketo site is preferentially chosen by Al^{III} with respect to the catechol

[96] Atohoun, Y. G. S., & Doco, R. C. (2016). *Theoretical Study of antioxidant properties of three isomers flavonoids: Kaempferol, luteolin and fisetin*. *7*(6), 145–152.
[97] Wang, Q., Zhao, L., Zhao, H., Liu, X., Gao, L., Cheng, N., & Cao, W. (2019). Complexation of luteolin with lead (II): Spectroscopy characterization and theoretical researches. *Journal of Inorganic Biochemistry*, *193*, 25–30.
[98] Amat, A., Clementi, C., Miliani, C., Romani, A., Sgamellotti, A., & Fantacci, S. (2010). Complexation of apigenin and luteolin in weld lake: A DFT/TDDFT investigation. *Physical Chemistry Chemical Physics*, *12*(25), 6672.

fixation site. In another work, luteolin was used as a complexing agent to determine the presence of the aluminium cation in river water and pharmaceutical products using a spectrofluorimetric method[99]. Like all flavonoids, luteolin is not very soluble in water and ways have been devised to improve its solubility such as complexing the ligand with cyclodextrins[100]. These different examples show that luteolin easily forms complexes with different types of metal cations when they are found in the same environment.

With the absence of the hydroxyl group in position 3, luteolin is left with only two fixation sites, the β–hydroxyketo site and the catechol site that are highlighted in Figure 13. This molecule was chosen not only because it is a multisite ligand and it has a good complexation power, but also because of the two fixation sites it possesses, which are both present on quercetin, whereas the site that is often the most complexing in quercetin is removed. Since luteolin has one site less, it was deemed interesting to investigate how it would interact when it is in contact with the same metal cations Zn^{II}, Mn^{II} and Ca^{II} as quercetin. By comparing the complexation reactions of metal cations with quercetin and luteolin, we could determine whether the site readily chosen by the metal cations is present in both compounds (β–hydroxyketo and catechol) or not (α–hydroxyketo).

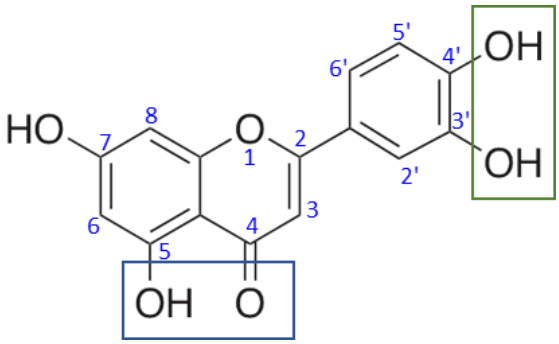

Figure 13 Structure of luteolin and the β–hydroxyketo (blue) and catechol (green) fixation sites

[99] Struchkov, P., Beloborodov, V., Kolkhir, V., Voskoboynikova, I., & Savvateev, A. (2018). Comparison of spectrophotometric methods of total flavonoid assay based on complex formation with aluminum chloride as applied to multicomponent herbal drug angionorm. *Journal of Pharmaceutical Negative Results*, *9*(1), 1–7.

[100] Kim, H.-M., Kim, H.-W., & Jung, S. (2008). Aqueous Solubility Enhancement of Some Flavones by Complexation with Cyclodextrins. *Bulletin of the Korean Chemical Society*, *29*(3), 590–594.

1.4.3 Nomenclature of chelating sites

The next three chapters will deal with the complexation reactions of morin with the zinc, manganese and calcium cations. A comparison work with also be done by using quercetin and luteolin. It is important to note that the studies carried out with the different metal cations were not performed exactly to same way for all of them. For the better comprehension of the several molecules mentioned, a specific nomenclature and colour code of the complexes were used (Figure 6, Figure 12 and Figure 13).

- The complex at position 3–4 α–hydroxyketo complex brown
- The complex at position 4–5 β–hydroxyketo complex blue
- The complex at position 1–2’ hydroxyether complex yellow
- The complex at position 3–2’ diol complex pink
- The complex at position 3’–4’ catechol complex green

CHAPTER 2:

ZINC

2.1 Properties and importance of zinc

Zinc is an element that is essential in the human body. It acts as a co–factor in enzymatic reactions and is involved in nervous and reproductive systems. It is known to have properties similar to flavonoids since it is a good oxidant[101] and anti–inflammatory[102].

The Zn^{II} cation interaction with flavones has already been studied[103,104] and, more specifically, several research groups worked on the determination of the structure of the Zn^{II}–morin complex[105,106,107,108,109,110], the results of their studies are reported in the Table 3 that enlightens also the diversity of the methods used for these investigations. No consensus can therefore be obtained and no bias seems explained by the use of one method only. Moreover, no study associates both computations and experiments that is, as stated before, a good way

[101] Prasad, A. S., Beck, F. W., Bao, B., Fitzgerald, J. T., Snell, D. C., Steinberg, J. D., & Cardozo, L. J. (2007). Zinc supplementation decreases incidence of infections in the elderly: Effect of zinc on generation of cytokines and oxidative stress. *The American Journal of Clinical Nutrition*, *85*(3), 837–844.

[102] Wong, C. P., Rinaldi, N. A., & Ho, E. (2015). Zinc deficiency enhanced inflammatory response by increasing immune cell activation and inducing IL6 promoter demethylation. *Molecular Nutrition & Food Research*, *59*(5), 991–999.

[103] Uivarosi, V., Badea, M., Olar, R., Drăghici, C., & Bărbuceanu, Ş. (2013). Synthesis and Characterization of Some New Complexes of Magnesium (II) and Zinc (II) with the Natural Flavonoid Primuletin. *Molecules*, *18*(7), 7631–7645.

[104] Primikyri, A., Mazzone, G., Lekka, C., Tzakos, A. G., Russo, N., & Gerothanassis, I. P. (2015). Understanding Zinc(II) Chelation with Quercetin and Luteolin: A Combined NMR and Theoretical Study. *The Journal of Physical Chemistry B*, *119*(1), 83–95.

[105] Qi, Z., Liufang, W., Xiang, L., Shuben, L., & Fengying, H. (1996). Synthesis, characterization and antitumour properties of metal(II) solid complexes with Morin. *Transition Metal Chemistry*, *21*(1), 23–27.

[106] Payán-Gómez, S. A., Flores-Holguín, N., Pérez-Hernández, A., Piñón-Miramontes, M., & Glossman-Mitnik, D. (2011). Computational molecular characterization of the flavonoid Morin and its Pt(II), Pd(II) and Zn(II) complexes. *Journal of Molecular Modeling*, *17*(5), 979–985.

[107] Zhang, H., & Mei, P. (2011). Synthesis of Morin–Zinc(II) Complex and its Interaction with Serum Albumin. *Biological Trace Element Research*, *143*(2), 677–687.

[108] Wei, Y., & Guo, M. (2014). Zinc-Binding Sites on Selected Flavonoids. *Biological Trace Element Research*, *161*(2), 223–230.

[109] Sendrayaperumal, V., Iyyam Pillai, S., & Subramanian, S. (2014). Design, synthesis and characterization of zinc–morin, a metal flavonol complex and evaluation of its antidiabetic potential in HFD–STZ induced type 2 diabetes in rats. *Chemico-Biological Interactions*, *219*, 9–17.

[110] Yasarawan, N., Thipyapong, K., & Ruangpornvisuti, V. (2016). Chelation behavior of various flavonols and transfer of flavonol-chelated zinc(II) to alanylaspartic dipeptide: A PCM/DFT investigation. *Journal of Molecular Structure*, *1107*, 278–290.

to compensate for the limitations of each aspect. Notably, the environment is also not fully considered in these publications, especially the computational ones: the protonation state of morin is either assumed without justification[110] or chosen on the basis of the lability of proton in free morin[106], and possible solvent molecules in the coordination sphere of the cation are often neglected. Therefore, we chose to re–investigate this system using the methodology developed in our group. The experimental measurements are carried out in standardised conditions used earlier so the results will compare fairly with those obtained for other flavonoids. At the same time, the computational model has been shown to be quite robust and does not need any assumption on the behaviour of the complex. The model is applied to the study of the complexation of morin with the Zn^{II} cation. Once the structure of the Zn^{II}–morin complex determined, further studies give more insight in some of its physico–chemical properties and shed light on the nature of the interactions in it.

Table 3 Propositions found in the literature for the binding site of the Zn^{II} cation on morin

Proposed site	Stoichiometry	Method
1,2' [105,108]	1:2	NMR, IR, UV–vis
	1:2 and 1:1	NMR
3,2' [106,107]	1:2	DFT computations
	1:2	NMR
3,4 [110]	1:2 and 1:1	DFT computations
3,4 and 4,5 [109]	1:2	Literature comparison

2.2 Zn^{II}–Morin system

2.2.1 Absorption and DFT results

In order to determine the structure of the complex formed when Zn^{II} interacts with morin, we proceeded with a stepwise approach. Experimentally, the complexation reaction of Zn^{II} with morin was carried out as described previously in the methodology section. The morin solution is pale yellow in colour. Initially, the titration was performed at a fixed pH of 6.5. In contrast, the spectra acquired under more acidic conditions (pH = 4.2) confirm the very low presence of the mono–deprotonated form when the pH is fixed 2 units under the pK_a value of morin in methanol. This feature is illustrated by the difference in the shape of the first spectra between sub–figures (a) and (b) of Figure 9: in the case of more alkaline conditions (a), another absorption band is observed at around 390–400 nm, corresponding to the values measured for the conjugated base. With each addition of the zinc solution, the yellow colour intensifies and the pH decreases. Due to the latter, it is safe to say that there is a deprotonation process taking place at the fixation site during the complexation reaction. The two set of spectra at pH 6.5 and 4.2 respectively, show that the ligand band in the long wavelength range gradually decreases and at the same time, the band of the complex grows.

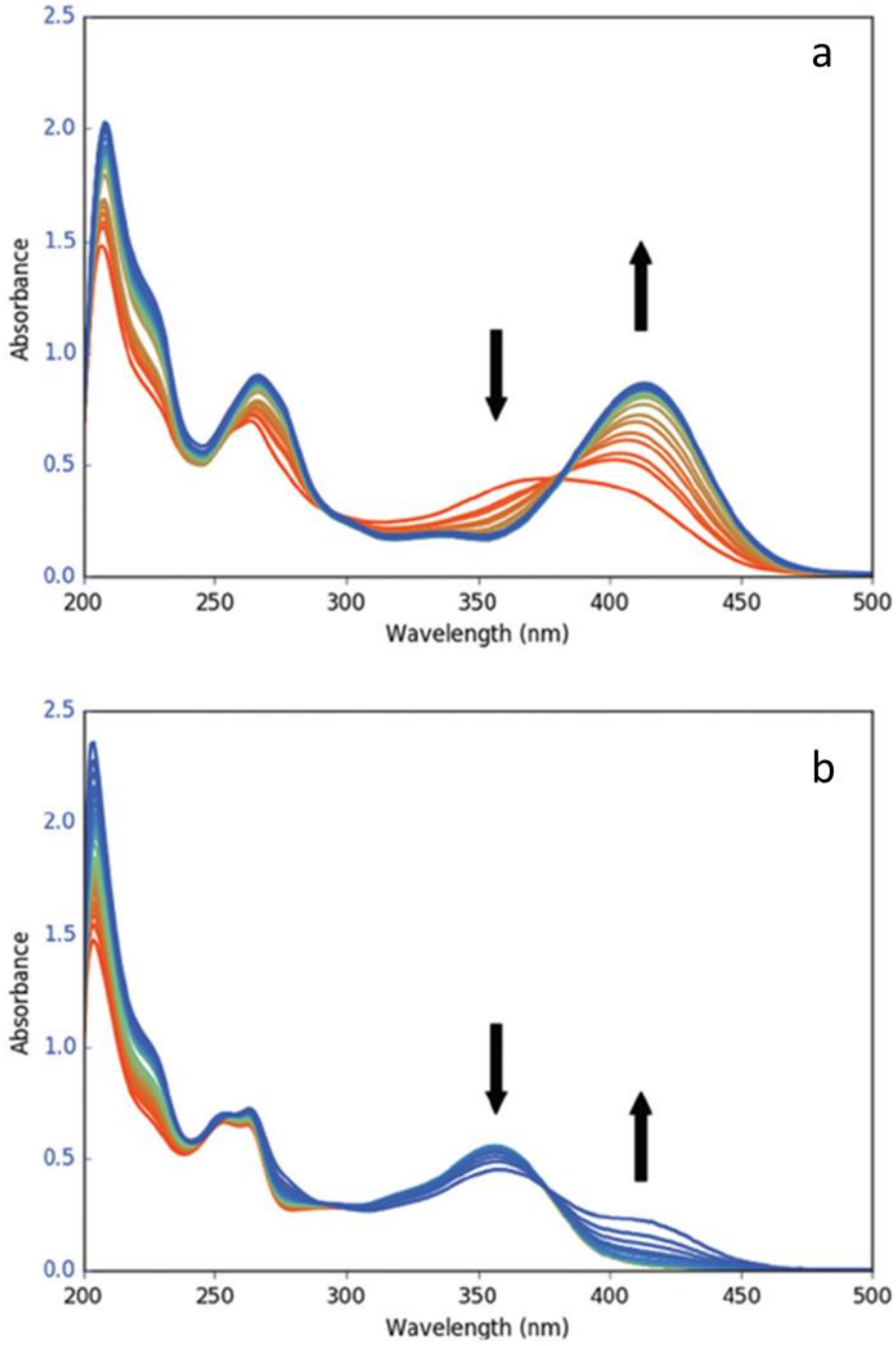

Figure 14 Set of UV–vis spectra measured during the titration of morin against zinc chloride solution with the pH fixed at (a) 6.5 (molar ratio ranging from 0 to 15) and at (b) 4.2 (molar ratio ranging from 0 to 150)

The large set of spectral data obtained was treated first of all by correcting the dilution, then was fed to the chemometrics software that will apply the principle of Evolving Factor Analysis. After trying different possible ratio of metal to ligand combinations, the determination of a complex with a stoichiometry of 1:1 was evidenced. The spectra of the 1:1 complex extracted

from these two experiments are very similar and their comparison confirms the formation of the same 1:1 complex in both cases. The conditional stability constant (log β) calculated at pH 4.2 is 1.50 ± 0.02.

$$\mathrm{Morin} + \mathrm{Zn^{II}} \rightleftharpoons \mathrm{Zn-Morin} \qquad \log \beta = 1.50 \pm 0.02$$

With $\beta = \frac{[\mathrm{Zn-Morin}]}{[\mathrm{Morin}][\mathrm{Zn^{II}}]}$

The last result obtained from the chemometrics analysis is the spectrum of the complex formed without any contribution of the ligand or other species. This data is the key to the next step of this work as it will enable us to elucidate the structure of the entity formed during this complexation reaction.

Before proceeding to the comparison of both techniques, we can already eliminate some assumptions for the structure of the complex according to the observations made during the experiments and calculations respectively. During the complexation reaction, the value of the pH decreased when the zinc chloride solution was introduced in the reactor, evidencing a deprotonation process. Hence, all the complexes that are fully protonated at the level of their fixation sites can be eliminated. In parallel, the optimisation of the hypothetical structures was carried out. Amongst the initial thirty possibilities, only twenty four hypothetical complexes could be optimised with acceptable structures. The complex involving the hydroxyether site, irrespective of the protonation state of the site as well as the coordination sphere of the zinc cation, does not give satisfactory results, meaning that, the geometrical constraints were too strong to allow the cation to bind onto the two oxygen atoms. Another structure that could not be optimised is the diol complex with the zinc cation having a coordination number higher than three. Due to the loss of the fourth solvent molecule, the remaining explicit solvent molecules rearranges themselves around the zinc atom. This results in a change of stereochemistry around the cation as it was no longer considered to be an octahedral. The departure of the solvent molecule was not just an artefact from the implicit model mimicking the explicit molecule.

We are left with the deprotonated α–hydroxyketo complex (deprotonated in 3), the β–hydroxyketo complex (deprotonated in 5) and the diol complexes (mono–deprotonated in 3, mono–deprotonated in 2' and fully deprotonated). The electronic transitions calculated for each hypothetical structure were overlapped with the pure electronic spectrum of the complex retrieved. The purpose is to do a spectral comparison and to single out the model that corresponds best to the experimental data obtained. The first step for structural clarification is to do a spectral comparison between the four different fixation sites.

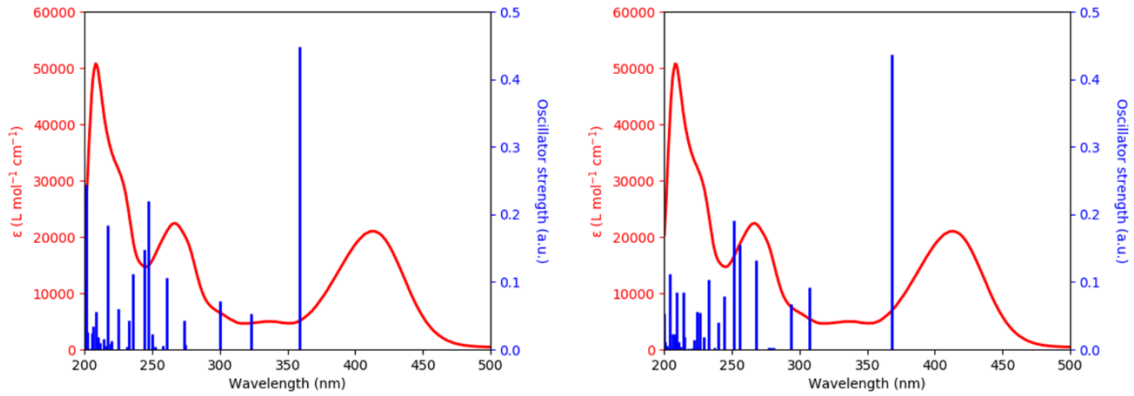

Figure 15 The overlap of the recorded spectrum of the Zn^{II}-morin complex with the calculated electronic transitions of the hypothetical diol complexes (left) deprotonated in 2' (right) deprotonated in 3

Figure 15 illustrated the overlap of the recorded absorption spectrum and the electronic transitions of the mono-deprotonated diol complexes in positions 2' and 3 respectively. Clearly, from the general shape, these two complexes do not fit the model.

Figure 16 shows the overlap of the experimental spectrum with the electronic transitions corresponding to three hypothetical structures: these three were chosen as representatives of each fixation site. The overlap of the experimental spectrum with the theoretical electronic transitions of the β–hydroxyketo complex deprotonated in position 5 does not match at all either. Interestingly, the relative intensities of the two lowest transitions are of the same magnitude. The computed transition at 328 nm (3.78 eV) has an oscillator strength of 0.280. This value is very high in comparison to what is observed on the experimental spectrum. As a matter of fact, the latter located at 337 nm (3.68 eV) is approximately ten times smaller than

the lowest energy band at 413 nm (3.00 eV). This 1:10 ratio of the second lowest energy transition is a behaviour that is identified for the α–hydroxyketo (323 nm, 3.84 eV) and diol complex (337 nm, 3.68 eV) having their oscillator strengths of 0.056 and 0.013. This argument is enough to eliminate the hypothesis that the β–hydroxyketo complex is the compound formed following the reaction. The fully α–hydroxyketo complex and diol complex have very small differences when we look at the calculated spectra. However, when their lowest energy bands are opposed (experimental value of 413 nm, 3.00 eV), the α–hydroxyketo complex whose band is positioned at 403 nm (3.07 eV) shows a better agreement with respect to the diol complex band found at 385 nm (3.22 eV), which is too blue-shifted. Hence, based in these observations, the zinc cation positions itself at the α–hydroxyketo site.

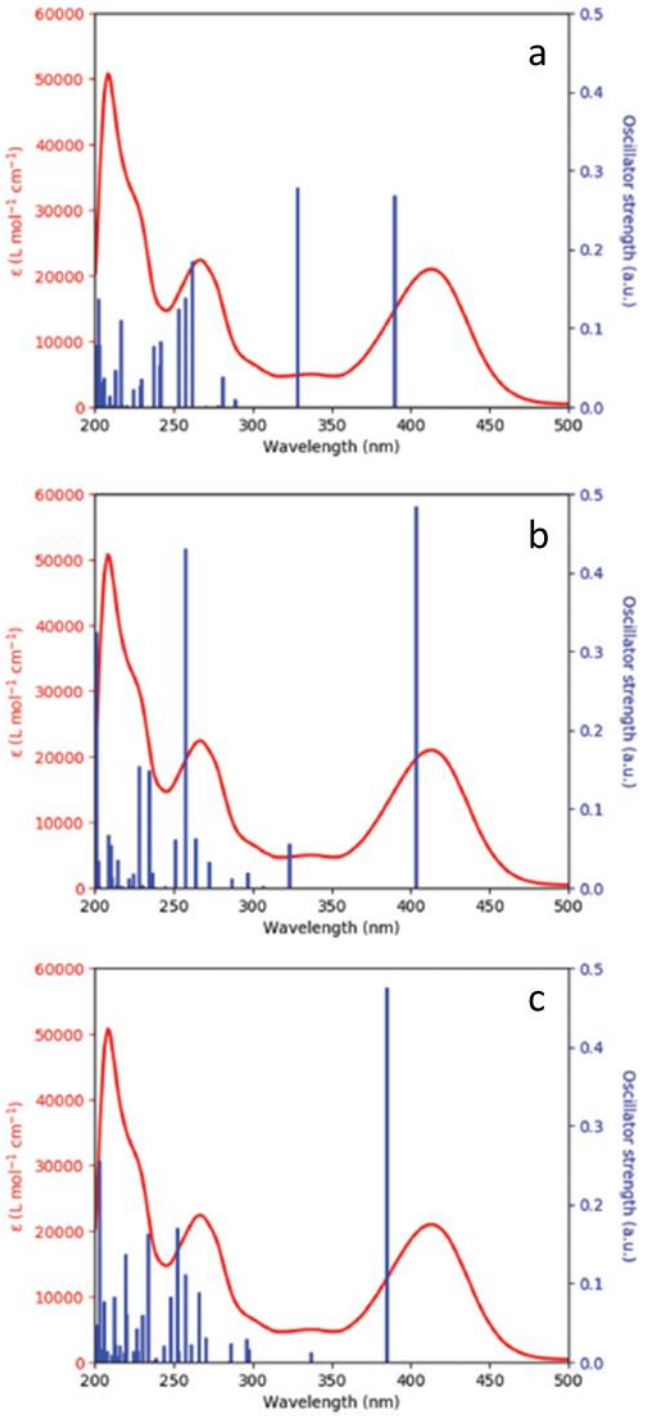

Figure 16 Overlap of the experimental absorption spectrum of the 1:1 complex between morin and the Zn^{II} cation (red curve) and the computed transitions (blue lines) for the fully deprotonated (a) β–hydroxyketo, (b) α–hydroxyketo and (c) diol complex. For the calculated transitions, two explicit solvent molecules have been added in the coordination sphere of the Zn cation.

Now that the fixation site has been located, the next step is to study the influence of the number of solvent molecules in the coordination sphere of the zinc cation. Figure 17 illustrates

the electronic configurations of the complex with two, three and four explicit solvent molecules overlapped with the experimental spectrum.

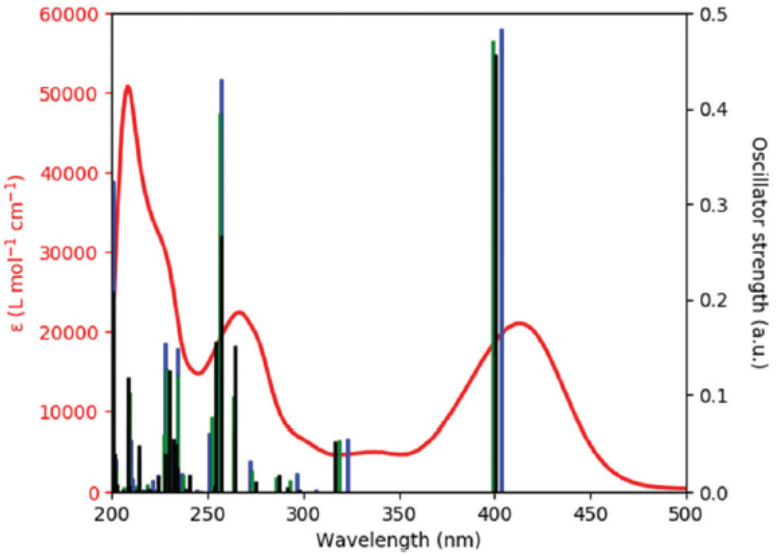

Figure 17 Overlap of the experimental UV–vis spectrum of the 1:1 complex between morin and the Zn^{II} cation (red curve) and the computational results for the α–hydroxyketo site with two (blue lines), three (green lines) and four (black lines) explicit water molecules around the zinc atom

Initially, when looking at the stacking of data, the complex with only 2 solvent molecules in the coordination sphere seems to give the best results. Even so, in order to compare the three hypotheses in depth, the difference in energy between the best and the worst of the three possibilities was calculated for the two lowest transitions. There is a difference of 0.03 eV (4 nm) for the lowest energy transition and a gap of 0.08 eV (6 nm) for the second lowest one. These disparities are below the accuracy of TD–DFT and cannot be used as argument to distinguish among the three coordination number of the metal atom. Due to the lability of the water molecules in the solvation sphere of the Zn^{II} cation, the number of solvent molecules in the first coordination sphere may have only little sense and molecular dynamics could be a better tool to precise it, but this would be beyond the scope of this work and in addition to that, recent works associated with neutron scattering and molecular dynamics have shown that current force fields are not well–fitted for the reproduction of the coordination sphere of the Zn^{II} cation[111].

[111] Duboué-Dijon, E., Mason, P. E., Fischer, H. E., & Jungwirth, P. (2018). Hydration and Ion Pairing in Aqueous Mg^{2+} and Zn^{2+} Solutions: Force-Field Description Aided by Neutron Scattering Experiments

In the following, the structure of the complex will be assumed to possess two explicit molecules of solvent, but it has to be kept in mind that the sphere of the Zn^{II} cation is certainly more complex due to the aforementioned effects. Figure 18 shows the structure of the complex formed at the α–hydroxyketo fixation site when morin reacts with Zn^{II}.

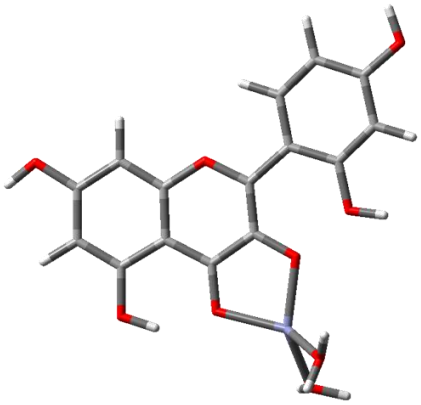

Figure 18 The 3D structure of the Zn^{II}–morin complex with the α–hydroxyketo as fixation site

2.2.2 Fluorescence studies

In order to confirm the interpretations made with the analysis of the absorption spectrum and the hypothetical computed spectra, fluorescence studies were carried out. The experimental setup is the same as before only with a spectrofluorometer coupled to the titration reactor. As the formation of the deprotonated form is low in these conditions, the fluorescence of this deprotonated fluorescent form will not be significantly observed, which is fluorescent unlike morin. Despite the acidic condition, we will notice the weak emission band of the deprotonated form of morin (Figure 19). During the titration, the intensity of the emission band of the complex, located at 509 nm increases. The first excited state of the α–hydroxyketo complex was optimised to compute the theoretical emission wavelength which was found to be 491 nm (2.52 eV), close to the experimental value of 509 nm (2.44 eV). The computed emission wavelength for the deprotonated diol complex is 485 nm (2.56 eV). Even if the

and Ab Initio Molecular Dynamics Simulations. *The Journal of Physical Chemistry B*, *122*(13), 3296–3306.

closeness of these values prevents a definitive attribution of the structure on the sole basis of this fluorescence study, it is satisfactory to obtain the closest computed value from the experimental one for our structural proposition.

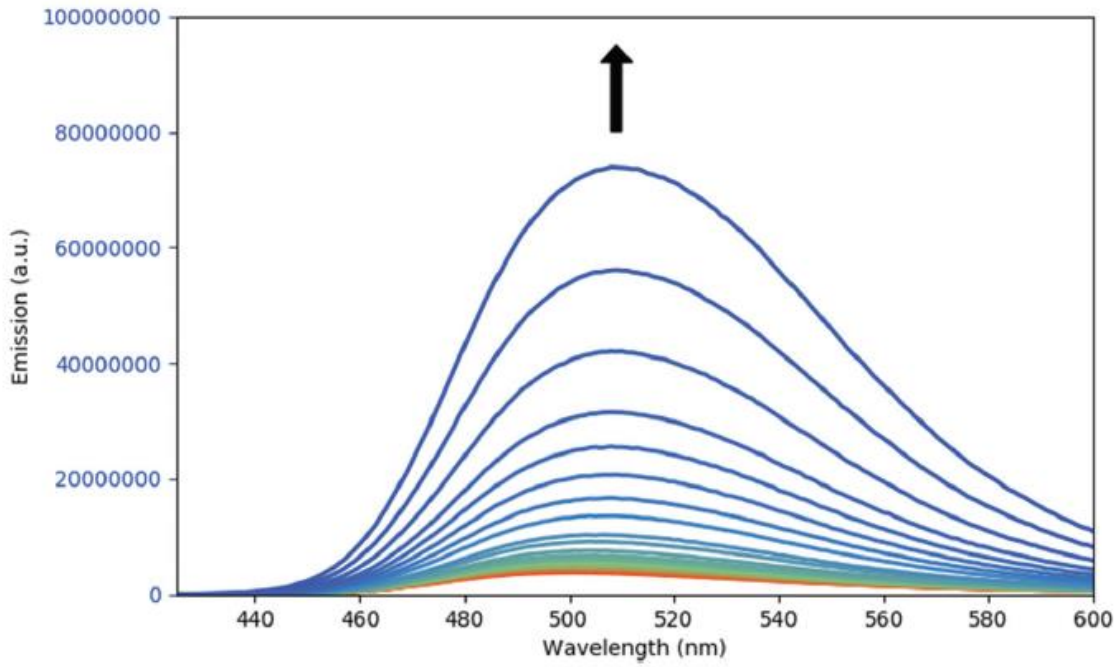

Figure 19 Set of fluorescence spectra (excitation wavelength: 410 nm) obtained during the titration of morin against the Zn^{II} salt with pH adjusted to 4.2 (molar ratio ranging from 0 to 150)

2.2.3 Molecular orbitals study

The nature of the electronic transitions involved in the formation of the complex was investigated by doing a close inspection of the molecular orbitals for each case. The latter concerns the fully deprotonated α–hydroxyketo complex, β–hydroxyketo complex and diol complex. The molecular orbitals of the complexes were also generated without the Zn^{II} cation together with its coordination sphere in order to study a system without the influence of the cation and to compare it with the Zn^{II}–morin complex. The computed wavelengths, the energies and the oscillator strengths of the two lowest electronic transitions are detailed in Table 4 and the molecular orbitals are illustrated in Figure 20 and Figure 21.

Table 4 Computed wavelengths (nm), energies (eV), oscillators strengths and decomposition in excitations (H stands for HOMO and L for LUMO) for the lowest energy transitions of the three deprotonation schemes of morin corresponding to H34, H45 and H32', and for the complexes themselves

Deprotonated hydroxyl group(s)	Without the Zn^{II} cation	With the Zn^{II} cation
None*	354 (3.50); f=0.541; H → L 313 (3.96); f=0.088; H–1 → L	—
O3H3	418 (2.97); f=0.346; H → L 341 (3.63); f=0.002; H–1 → L	404 (3.07); f=0.484; H → L 323 (3.84); f=0.056; H–1 → L
O5H5	403 (3.08); f=0.186; H → L 337 (3.68); f=0.002; H–2 → L 304 (4.08); f=0.426; H–1 → L	389 (3.19); f=0.268; H → L 328 (3.78); f=0.280; H–1 → L
O3H3 and O2'H2'	456 (2.72); f=0.393; H → L 369 (3.36); f=0.011; H–1 → L	385 (3.22); f=0.475; H → L 337 (3.68); f=0.013; H–1 → L

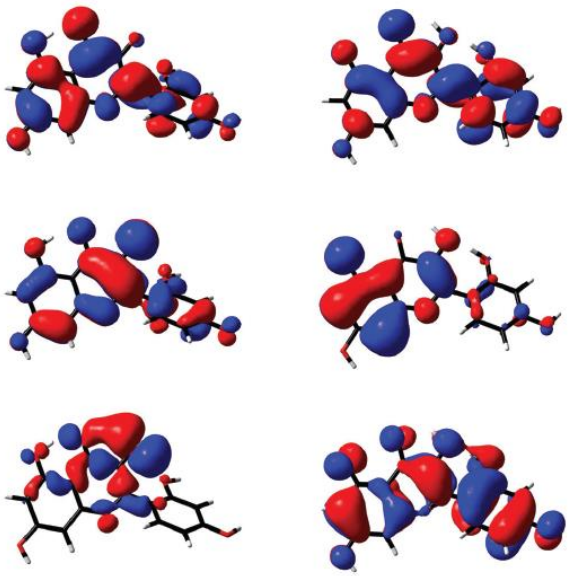

Figure 20 LUMO (top), HOMO (middle) and HOMO–1 (bottom) for the morin deprotonated in position 3 (left) and 5 (right)

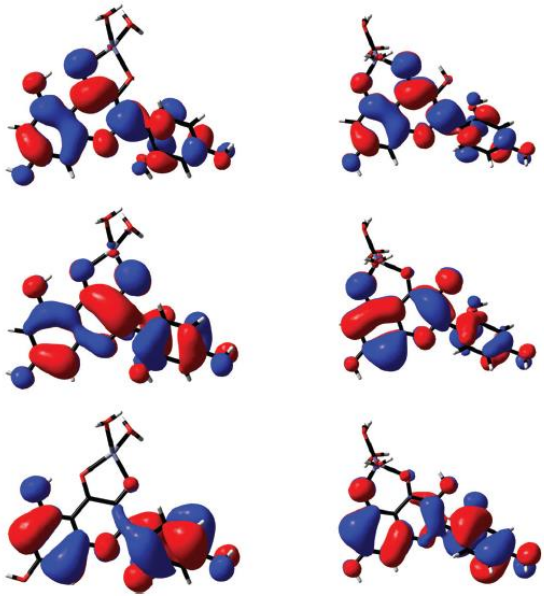

Figure 21 LUMO (top), HOMO (middle) and HOMO–1 (bottom) for the α–hydroxyketo complex (left) and β–hydroxyketo complex (right)

The most striking result is the similarity between the relative oscillator strength values for the transitions computed with and without the Zn^{II} cation. Especially, a strong contribution of the HOMO–1 → LUMO transition is computed for the species where the hydroxyl group in position 5 is deprotonated. This oscillator strength is very small in the other cases (0.002 for the α–hydroxyketo complex and 0.011 for the diol complex compared to 0.426 for the β–hydroxyketo complex). Some molecular orbitals are depicted for the deprotonated morin in position 3 or 5 (Figure 20) and for the α–hydroxyketo and β–hydroxyketo complex (Figure 21). The molecular orbitals for the diol complex hypothesis and the corresponding deprotonated morin were not depicted as they are very similar to those for the α–hydroxyketo one.

The results obtained for the deprotonated morin are quite easy to understand. In the case of the O3H3 deprotonated form, the HOMO–1 → LUMO transition has a pronounced nπ* character, that explains a low intensity band due to the selection rules, while in the O5H5 deprotonated form, this transition is a ππ* one. The same explanation cannot be given for the case of the complexes. Indeed, even if the influence of the cation on the shape of the orbitals is low, it has an influence on the energies, which is coherent when we consider the ionic character of the bond that will be investigated in the next sub–section. Especially, the

molecular orbital corresponding to the HOMO–1 of the O3H3 deprotonated form is stabilized in its complex with the Zn^{II} cation: it is recovered at the HOMO–5 position (1.68 eV below the HOMO–1).

Then, to explain the different behaviour of α–hydroxyketo and and β–hydroxyketo complexes, several parameters such as the D_{CT} value[112] or the transferred charge have been computed for each transition but without significant difference. Moreover, the difference between the charges of the species could lead to some misinterpretations. Nevertheless, the computation of the ratio η between an approximated version of the Λ diagnostic tool[113] (using only the most involved orbital pair for each transition) for the second and the first transition was processed:

$$\eta = \frac{<|\psi_{LUMO}|||\psi_{HOMO-1}|>}{<|\psi_{LUMO}|||\psi_{HOMO}|>}$$

The physical significance of each term of this ratio is the unsigned spatial overlap between involved orbitals for the considered transition. Therefore, their ratio η estimates the ratio between the spatial shifts of the electronic density for the two transitions. This value has been computed to 0.75 for α–hydroxyketo, 0.88 for β–hydroxyketo, and 0.72 for diol complexes. An explanation for the difference of behaviour for the second low–energy band of the complexes of morin with the Zn^{II} cation could root in this observation: the second transition of β–hydroxyketo complex appears to be different in nature from those of the other complexes. Nevertheless, this explanation is to be confirmed by a further examination on a wider range of compounds.

[112] Le Bahers, T., Adamo, C., & Ciofini, I. (2011). A Qualitative Index of Spatial Extent in Charge-Transfer Excitations. *Journal of Chemical Theory and Computation*, *7*(8), 2498–2506.
[113] Peach, M. J. G., Benfield, P., Helgaker, T., & Tozer, D. J. (2008). Excitation energies in density functional theory: An evaluation and a diagnostic test. *The Journal of Chemical Physics*, *128*(4), 044118.

2.2.4 QT–AIM study

The nature of bonding was investigated in the complexes to better understand the characteristics of the absorption spectra. In particular, the similarities between the complexes and the associated deprotonated forms suggest an ionic bonding that needs to be checked. In this part, the investigation was done on the three completely deprotonated complexes: α–hydroxyketo, diol and β–hydroxyketo complex as well as their associated deprotonated morin molecule for comparison. Figure 22 depicts the QT–AIM structures after analysing the structures and Table 5 shows the data retrieved post–analysis where the following parameters are used as local indicators to understand the nature of the metal-oxygen bond:

1. The QT–AIM charges, *q* (a.u) for O2', O3, O4, O5 for the complexes and their affiliated deprotonated morin molecule,
2. The Zn–O bond lengths, *l* (pm) at each site,
3. The electronic density, ρ_b (a.u) at each bond critical point (BCP),
4. The Laplacian of the electronic density, $\nabla^2\rho_b$ (a.u) at the BCP, and
5. The opposite to the ratio of the kinetic energy density to the potential energy density, $-G_b/V_b$ at the BCP.

The electronic density at the BCP will enable us to know if the metal-oxygen bond formed after the complexation reaction is involved in the electronic delocalisation over the whole molecule. The $-G_b/V_b$ value at the BCP is usually calculated to evaluate the electron charge density at the BCP. It was stated that the G_b (kinetic energy density) shows the tendency of the system to dilute electrons at the BCP while the V_b represents the capacity of the system to concentrate electrons at the BCP.

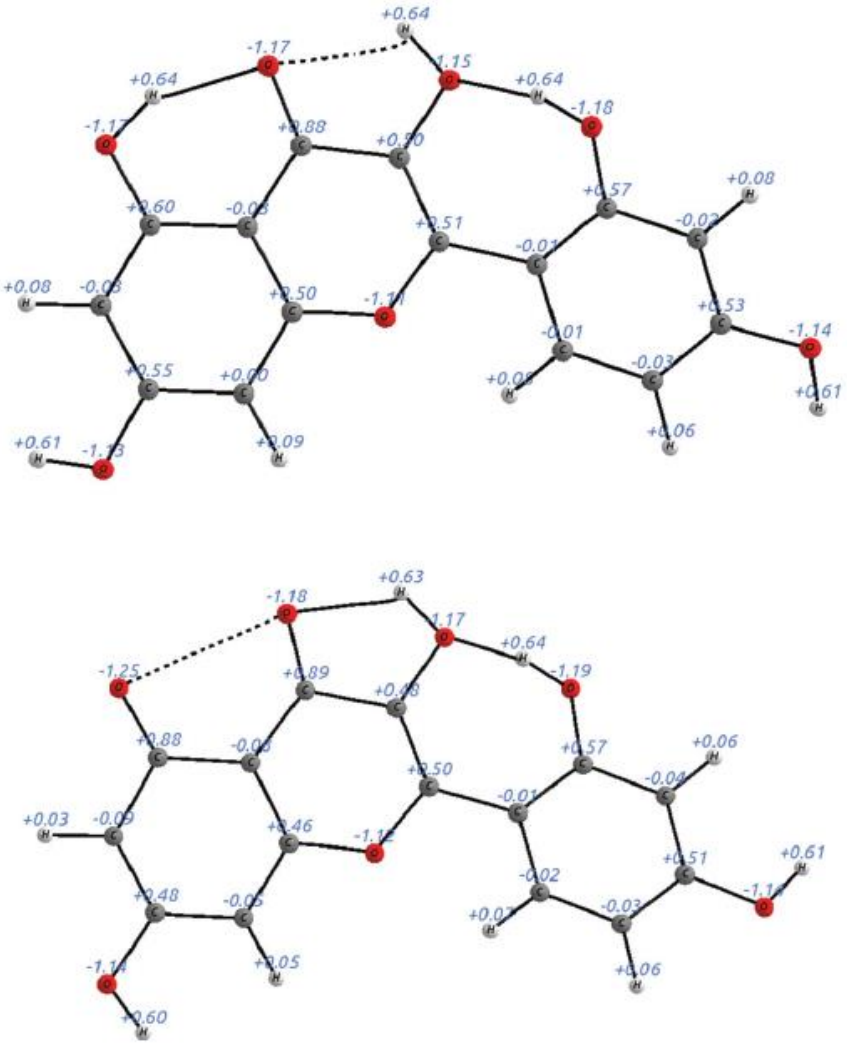

Figure 22 QT–AIM results showing the partial charges for the morin molecule (top) and the α–hydroxyketo Zn^{II}–morin complex (bottom)

Table 5 Selected QTAIM charges (q, au) for the α–hydroxyketo, β–hydroxyketo and diol complexes and the associated deprotonated morin (in brackets), bond lengths (l, pm), electronic densities at the BCP (ρ_b, au), Laplacian of the electronic density at the BCP ($\nabla^2\rho_b$, au) and opposite to the ratio of the kinetic energy density to the potential energy density at the BCP ($-G_b/V_b$) for the α–hydroxyketo, β–hydroxyketo and diol complexes. For each hypothesis, bolded values indicates the oxygen atoms involved in the complexation (or deprotonation)

	α–hydroxyketo complex	β–hydroxyketo complex	diol complex
$q(Zn^{II})$	1.45	1.45	1.45
q(O3)	**–1.19 (–1.26)**	–1.15 (–1.17)	**–1.16 (–1.28)**
q(O4)	–1.18 (–1.19)	–1.19 (–1.18)	–1.17 (–1.20)
q(O5)	–1.17 (–1.20)	**–1.22 (–1.25)**	–1.17 (–1.20)
q(O2')	–1.13 (–1.13)	–1.18 (–1.19)	**–1.23 (–1.29)**
Zn–O3			
l	191.6		219.8
ρ_b	0.0874		0.0471
$\nabla^2\rho_b$	0.4484		0.1941
$-G_b/V_b$	0.9167		0.8941
Zn–O4			
l	203.3	199.2	
ρ_b	0.0716	0.0768	
$\nabla^2\rho_b$	0.3402	0.4022	
$-G_b/V_b$	0.9118	0.9292	
Zn–O5			
l		193.4	
ρ_b		0.0888	
$\nabla^2\rho_b$		0.4895	
$-G_b/V_b$		0.9285	
Zn–O2'			
l			190.5
ρ_b			0.0938
$\nabla^2\rho_b$			0.5204
$-G_b/V_b$			0.9260

The nature of the bonding was investigated in the complexes to better understand the characteristics of the absorption spectra. Especially, the similarities between the complexes and the associated deprotonated forms evoke an ionic bonding that need to be checked. The main structural and electronic parameters are gathered in Table 5. A first interesting result is

the small differences between the charges of deprotonated and protonated oxygen atoms in the morin derivatives. For instance, when the deprotonation occurs on the hydroxyl group at position 5 (example chosen because it is the one where the H–bond network is least perturbed, see Figure 22), the O5 atom bears a –1.25 charge while the other oxygen atoms bear charges ranging from –1.17 to –1.19. This low variation is due to a large delocalization over the entire molecule. Indeed, the removal of the H5 atom in morin modifies mainly the C5 charge (increase of 0.28 upon deprotonation) but the other charge changes are below 0.1 units. This can be understood by the great charge (+0.64) carried by the H5 atom in morin: only –0.36 had to be redistributed on the whole molecule after the deprotonation.

Considering these small differences between the complexes and the deprotonated forms leads us to propose, in line with our previous studies on this kind of systems, that the ionicity of the bonds between the oxygen atom of morin and the Zn^{II} cation is quite important. To test this hypothesis, a study of the local QT-AIM properties at the two Bond Critical Points (BCPs) binding morin to the Zn^{II} cation was processed, and the results are reported in Table 5. The small values of the electronic density and the positive value of the Laplacian of the electron density at the BCPs confirms our hypothesis of an ionic bonding as proposed by usual criterions[62]. The values of $-G_b/V_b$ computed around 1 confirms this even if it appears to be a slight dative bonding (the values being always less than 1). The comparison of the bond parameters with previously published values assesses the nature of this bond as comparable to those between the catechol of esculetin and the Cu^{II} cation[114].

[114] Le Person, A., Moncomble, A., & Cornard, J.-P. (2014). The Complexation of Al^{III}, Pb^{II}, and Cu^{II} Metal Ions by Esculetin: A Spectroscopic and Theoretical Approach. *The Journal of Physical Chemistry A*, *118*(14), 2646–2655.

2.3 Comparison with Zinc–Quercetin and Zinc–Luteolin complexes

2.3.1 Zn^{II}–Quercetin system

The zinc–quercetin complex was a study that was already published where the complexation reaction was analysed by NMR spectroscopy and DFT calculations[104]. The experimental conditions are not similar to ours because the concentration of the quercetin solution is in the order of 10^{-3} mol L^{-1}. The theoretical work, on the contrary, resembles a lot what we perform on our systems. Several functionals, notably, B3LYP, M05–2X and ωB97X–D have been tried. Some problems were encountered while optimising the geometry at the catechol site. Computations with B3LYP failed but were successful with the other two functionals. However, regardless of the functional used, the catechol binding site was excluded. The final complex structure determined was that of the zinc cation getting fixed at the α–hydroxyketo site. The experimental complexation study of quercetin with zinc has been carried out in our team and the formation of the complex is evidenced in Figure 23. The data treatment by chemometrics predicted a 1:1 complex with a conditional complexation constant, log β of 4.41 ± 0.02 at a pH of 4.2. Since the regio–selectivity of the zinc cation with respect to quercetin had already been solved, no additional work was done on this complex.

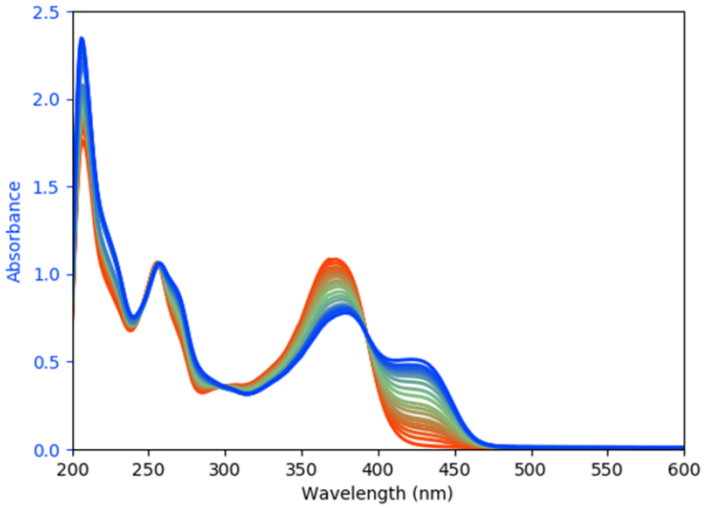

Figure 23 The set of spectra showing the formation of the Zn^{II}-quercetin complex

2.3.2 Zn^{II}–Luteolin system

The previously described article in relation with the zinc–quercetin complex also dealt with the study of the zinc–luteolin complex[104]. Luteolin can accommodate the zinc cation in only two positions. The favoured α–hydroxyketo fixation site till now is no longer present on the molecule. After data analysis, the binding site located was the β–hydroxyketo site, however, the zinc cation was found to be more tightly bound to quercetin than luteolin.

CHAPTER 3:
MANGANESE

3.1 Properties and importance of manganese

Manganese is a period 4 transition metal and is the fifth most abundant metal produced worldwide. It is an oligo–element and an over–exposure in plants or over–consumption in the human body can lead to serious health problems like Parkinson or manganism[115]. The formation of resulted complex between Mn^{II} and morin, quercetin and luteolin is beneficial as it enables the decrease of the concentration of an eventual excess of manganese in the organism and at the same time, the biological properties of the complex formed are enhanced in comparison to that of the free ligand[116].

Anthropogenic emission of manganese is responsible for a huge portion of soil and hydro resource contamination, including that in subterranean and superficial water. Manganese ions are present in several industrial wastewaters, such as those of textile industries, presenting concentrations of 100–200 mg L^{-1}, and those of hydrometallurgical processes with concentrations of 2–5 g L^{-1}. In mine–draining processes, the concentration of manganese ions in the basin is near 200 mg L^{-1} [117,118,119].

In this chapter, we expose the reaction of manganese under its cationic form with morin, quercetin and luteolin respectively to determine the characteristics of the product formed, more specifically, the type of complex formed as well as its environment and the nature of bonding within, by the means of the study of the topology of its electronic density.

---

[115] Gawlik, M., Gawlik, M. B., Smaga, I., & Filip, M. (2017). Manganese neurotoxicity and protective effects of resveratrol and quercetin in preclinical research. *Pharmacological Reports*, *69*(2), 322–330.
[116] Memon, S., Panhwar, Q. K., Bukhari, S. B., Bhanger, M. I., & Samejo, M. Q. (2016). Synthesis, Characterization and Biological Activity of Mn(II)-Morin Complex. *Pakistan Journal of Analytical & Environmental Chemistry*, *17*(2), 155–164.
[117] Yang, X., Jie, F., Wang, B., & Bai, Z. (2019). High-efficient synergistic extraction of Co(II) and Mn(II) from wastewater via novel microemulsion and annular centrifugal extractor. *Separation and Purification Technology*, *209*, 997–1006.
[118] Zhang, W., Cheng, C. Y., & Pranolo, Y. (2010). Investigation of methods for removal and recovery of manganese in hydrometallurgical processes. *Hydrometallurgy*, *101*(1–2), 58–63.
[119] Neculita, C. M., & Rosa, E. (2019). A review of the implications and challenges of manganese removal from mine drainage. *Chemosphere*, *214*, 491–510.

Several studies have already been carried out on the Mn^{II}–quercetin complex and are summarised in Table 6 below. Different techniques have been used to finally determine that the main complexation site is the α–hydroxyketo one. However, the stoichiometry of the complex seems to depend on the solvent.

Table 6 Indexation of the Mn(II)–Quercetin complexes

Type of complex	Complexation site	Solvent	pH	Technique
1:2 [120]	α–hydroxyketo	Ethanol	7–8	Elemental analysis
1:2 [121]	α–hydroxyketo	Ethanol	–	Titration with EDTA
1:1 [122]	α–hydroxyketo	Water	9.6	Molecular docking
1:2 [123]	α–hydroxyketo	Ethanol	–	Titration with EDTA

Concerning the Mn^{II}–morin complex, only one study has been done previously where a 1:1 complex was formed in methanol at a pH value of 5.6 and the complexation site was found to be the α–hydroxyketo[116]. However, this paper illustrating the formation and properties of the Mn^{II}–morin brings forward some points that do not seem to be very clear. First of all, they claim that the band at 357 nm corresponds to the B ring absorption and the one at 262 nm is characteristic of the A ring absorption. This theory that was considered long ago is no longer believed to be completely true. Moreover, like several publications involving morin, the diol complexation site is never taken into account while this site is quite important as it influences the complexation ability of morin. Furthermore, it was mentioned that the most acidic proton is the one connected to the hydroxyl group in position 3, argument that was misused to justify the regio-selectivity of the complexation. Even though both molecules are flavonols and have

[120] Jun, T., Bochu, W., & Liancai, Z. (2007). Hydrolytic cleavage of DNA by quercetin manganese(II) complexes. *Colloids and Surfaces B: Biointerfaces*, *55*(2), 149–152.
[121] Zhou, J., Wang, L., Wang, J., & Tang, N. (2000). Antioxidative and anti-tumour activities of solid quercetin metal(II) complexes. *Transition Metal Chemistry*, *26*, 57–63.
[122] da Silva, E. R., Maquiaveli, C. do C., & Magalhães, P. P. (2012). The leishmanicidal flavonols quercetin and quercitrin target Leishmania (Leishmania) amazonensis arginase. *Experimental Parasitology*, *130*(3), 183–188.
[123] Tan, J., Zhu, L., & Wang, B. (2011). GC (Guanine-Cytosine)-Selective DNA-Binding and Antitumor Activity of a Quercetin-Manganese(II) Complex. *Chemistry & Biodiversity*, *8*(8), 1550–1559.

some of their hydroxyl groups at the same position on the skeleton of the molecule, the pK_a of their respective protons cannot be considered to bear the same values. Additionally, the interpretation of the NMR data provided is not sufficient to confirm the assignment of the peaks of the proton in position 3 and 2' for example. Lastly, the coordination sphere of the complex was determined by thermal study. Three molecules of water were lost in the first decomposition, followed by the loss of two other molecules of water at a higher temperature. It was interpreted as such: two water molecules were present in the first coordination sphere and the other three in the second coordination sphere. While that explanation is plausible, it is also possible that water molecules present in the first coordination sphere were removed during the first decomposition.

Whether it is morin, quercetin or luteolin, the pH of the reaction is an important parameter to be respected depending on the first pK_a of each molecule. It is preferable to work with a ligand present in solution in a single state of protonation, thus avoiding the addition of spectra of free ligands in different forms which has the consequence of greatly complicating the treatment of the data sets. The first experimental pK_a values being around 8.45[89] and 6.50[80] for quercetin and morin respectively, naturally, we cannot take into consideration the data detailed above as the pH at which the experiments were done is too high. For these three molecules, the interaction of Mn^{II} with the ligand is studied in details using the same methodology as applied for the Zn^{II}–morin system.

3.2 Mn^{II}–Morin system

3.2.1 Absorption and DFT studies

The approach used with the Zn^{II}–morin system was successfully carried out and the aims of the investigation were met. The same methodology was applied to the Mn^{II}–morin complexation study to achieve the same objectives.

The experimental setup remains the same as before, that is, an automatic burette with the manganese chloride solution is linked to the reactor containing the morin solution fixed at pH 4.2. The latter is, in turn, connected to the UV–vis and the fluorescence spectrometers in order to record a spectrum after each addition of the manganese chloride solution. The experiment ends when all the morin has been complexed. All the spectra taken are overlapped as illustrated in Figure 24 to have an overview of stepwise formation of the complex. It clearly shows that the band located at 359 nm, which accounts for the presence of morin in the medium slowly decreases and simultaneously, a new band at 417 nm is formed. From the molar ratio 0 to 2, several isobestic points are observed and give an indication that only two absorbing species are present in the solution, one being the ligand and the second one being a complex. At some point, if two spectra are similar, it means that the concentration of ligand in the solution is practically zero and that the reaction is over. The molar ratio was varied from 0 to 30 and was enough for the free morin to be consumed and the reaction to be complete.

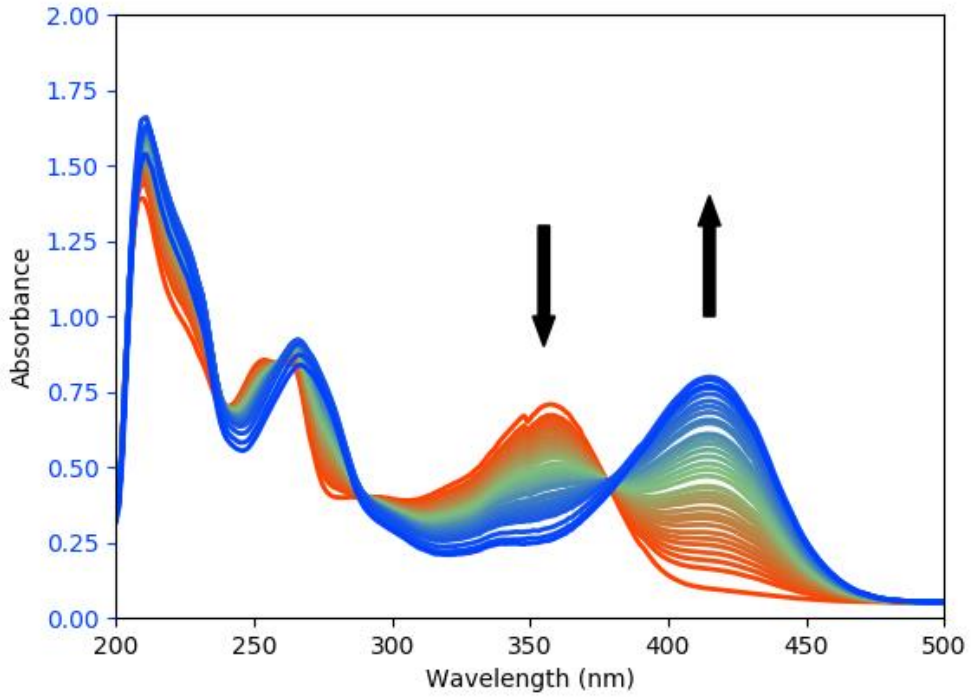

Figure 24 Set of UV–vis spectra recorded during the titration of morin against the Mn^{II} salt at a fixed pH of 4.2 (molar ratio ranging from 0 to 30)

When the manganese chloride is added to the morin, the yellow colour of the solution intensifies and a bathochromic shift is observed. This confirms that the manganese is complexing the ligand. A decrease in pH is also observed and reveals a deprotonation process happening at the fixation site. The pH is brought back to its set value that is 4.2, after each fluctuation. Following this step, all the data collected were treated using the Evolving Factor Analysis. As mentioned before, several cases are assumed and the chemometrics tool is run to determine which combination fits best the model. To this end, the cases considered in this work are the 1:1 complex, the 2:1 complex, the 1:2 complex, a mixture of 1:1 and 1:2 complexes and a mixture of 1:1 and 2:1 complexes. According to the trend of the data retrieved, solely a complex of ratio 1:1 was evidenced and its pure spectrum was extracted from the data. The conditional complexation constant arose to 4.825 ± 0.002.

$$\mathrm{Morin} + \mathrm{Mn^{II}} \rightleftharpoons \mathrm{Mn-Morin} \qquad \log \beta = 4.825 \pm 0.002$$

With $\beta = \frac{[\mathrm{Mn-Morin}]}{[\mathrm{Morin}][\mathrm{Mn^{II}}]}$

In order to continue the data analysis, the pure spectrum of the complex is overlapped with the electronic transitions calculated for each plausible 1:1 complex species to identify the structure of the product formed following the reaction of manganese cations with morin. Since manganese is a transition element, with five electrons in the 3d orbital, the multiplicity of the compound is a parameter that is essential. Based on whether the molecule is subject to a low or high ligand field, the multiplicity can have the value of 6 or 2 respectively. Tests with both values were tried and it turned out that the calculations with a multiplicity of 6 gave satisfactory results, meaning that the calculations done with a multiplicity of 2 failed. This is consistent with the use of oxygen–based ligands that are generally low–field ligands. Interestingly, when four solvent molecules were incorporated in the manganese coordination sphere, no correspondence were spotted between the vertical electronic spectra and the experimental curve except for the α–hydroxyketo and diol complex both protonated at the H3 of the relating hydroxyl group. Each fixation site will be discussed successively.

The hydroxyether site (1–2' site):

Six species can be formed if the manganese cation fixation occurs with the hydroxyether site. Howbeit, no matter the protonation state of the 2' hydroxyl group or the variation of the number of water molecules around the manganese cation, no structure at this fixation site could successfully be optimised. The same situation was observed for the Zn^{II}–morin compound. This can be explained by the fact that the structure is too rigid as depicted in Figure 25. Hence, it can be concluded that the hydroxyether complex cannot be formed.

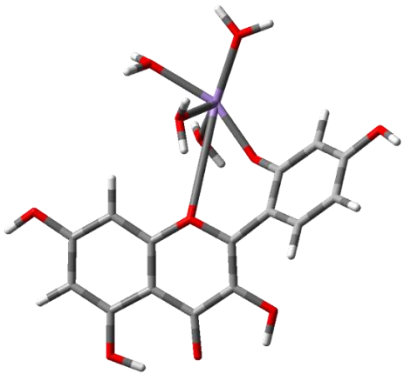

Figure 25 Non-optimised structure of the hypothetical structure of the hydroxyether complex

The β–hydroxyketo complex (4–5 site):

Both the protonated and deprotonated β–hydroxyketo complex were successfully optimised but while comparing the experimental and theoretical spectra as depicted on Figure 26, we can already conclude that they are not the complexes formed. The calculated deprotonated complex bears two electronic transitions, the HOMO → LUMO and HOMO–1 → LUMO, of equivalent oscillator strength, a feature that was encountered too with the β–hydroxyketo Zn^{II}–morin complex. This trait seems to be very characteristic when a metal cation positions itself at the deprotonated 4–5 position on the ligand. Concerning the protonated version of this complex, the HOMO → LUMO transition is blue–shifted with respect to the experimental band, whatever the number of molecules in the coordination sphere, eliminating this assumption.

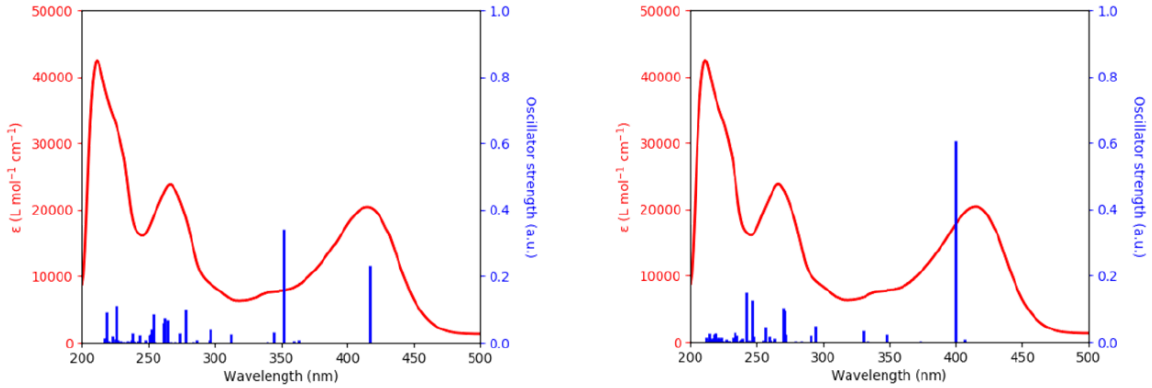

Figure 26 Overlap of the experimental UV–vis spectrum of the 1:1 complex between morin and the Mn^{II} cation (red curve) and the computed transitions (blue lines) for the deprotonated (left) and protonated (right) β–hydroxyketo complex with 3 water molecules in the coordination sphere

The α–hydroxyketo complex (3–4 site):

The protonated α–hydroxyketo complex can be cast out as the calculated HOMO → LUMO transition is too blue–shifted compared to the actual value (a calculated value of 389 nm (3.19 eV versus a measured value of 417 nm (2.97 eV)). On the other hand, the deprotonated α–hydroxyketo theoretical spectrum gives a very good agreement with the experimental one. The computed value was located at 420 nm (2.95 eV), which is only 3 nm away from the experimental value, a difference which is considered to be insignificant (Figure 27).

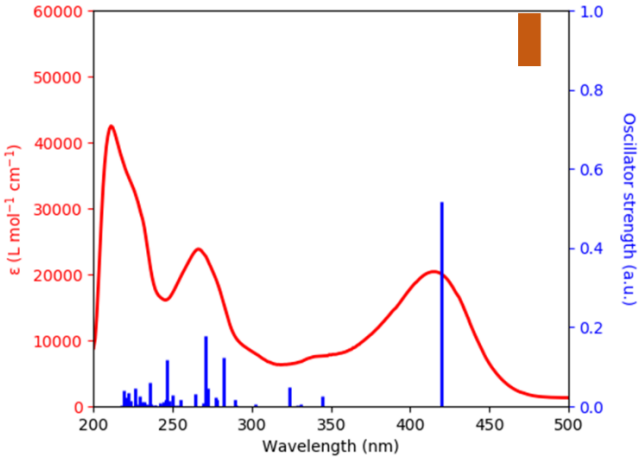

Figure 27 Overlap of the experimental UV–vis spectrum of the 1:1 complex between morin and the Mn^{II} cation (red curve) and the computed transitions (blue lines) for the deprotonated α–hydroxyketo complex

The diol complex (3–2' site):

This fixation site offers four possible types of complexes. Amongst them, the fully protonated form can be eliminated based on the experimental–theoretical comparison (electronic transition computed at 389 nm (3.19 eV) vs measured absorption value at 417 nm (2.97 eV)) as well as the observed decrease in pH of the solution right after adding the metal suggesting a deprotonation. Moving on to the two mono–deprotonated structures, they do not give any satisfactory match either. The HOMO → LUMO transition of the one being deprotonated in position 3 is too blue–shifted (calculated value of 388 nm (3.20 eV)). As for the structure that lost its H2' proton, the HOMO → LUMO band is situated at 406 nm (3.05 eV, f = 0.23), which is a bit too low in energy and if we focus on the HOMO–1 → LUMO contribution, it has an

oscillator strength of 0.18. This value is almost equivalent to the intensity of the HOMO → LUMO band. Since experimentally the second lowest energy band is lower in intensity that the lowest energy band, this structure cannot be the complex formed. Finally, the last possible structure is the fully deprotonated diol complex. The electronic vertical transitions of this complex are different from the other optimised mono–deprotonated structures. First of all, there are several transitions with low oscillator strengths located between 330 nm and 360 nm that can justify the presence of the small band at 341 nm. Secondly, while all of the other structures had only one transition (generally the HOMO → LUMO transition) that accounted for the experimental band at 417 nm, this structure bears two contributions at 422 and 411 nm, respectively as shown on Figure 28.

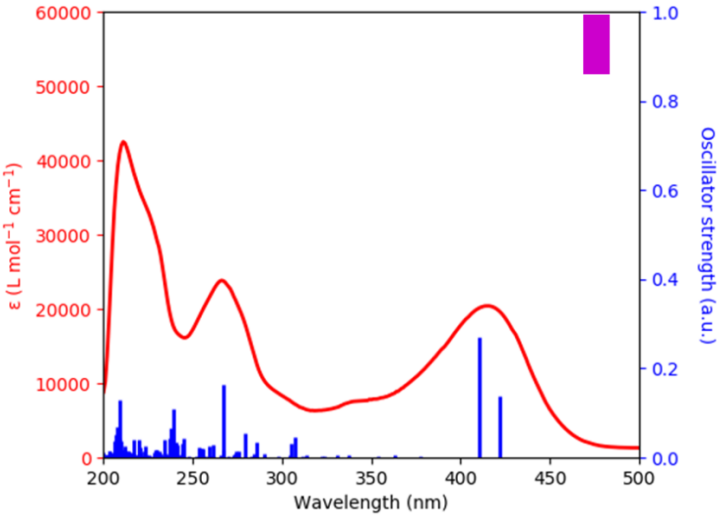

Figure 28 Overlap of the experimental UV–vis spectrum of the 1:1 complex between morin and the Mn^{II} cation (red curve) and the computed transitions (blue lines) for the fully deprotonated diol complex

Table 7 reports the different electronic transitions of all the hypothetical complexes that were taken into account as well as their nature and the number of water molecules surrounding the manganese atom. These theoretical values were compared to the experimental results, where the lowest–lying energy band is observed at 417 nm (2.97 eV) and the second lowest energy band, which is also twice less intense at 340 nm (3.65 eV).

Table 7 Computed wavelengths (nm), energies (eV), oscillators strengths for the transitions corresponding to H → L and H–1 → L (H stands for HOMO and L for LUMO) for all the possible Mn^{II}–morin complexes envisaged (with the maximum number of water molecules that can be included in the coordination sphere)

Fixation location	Band position, λ, nm (E, eV)	Oscillator strength, f	Nature of transition	Number of water molecules
3–4 site protonated in 3	389 (3.19) 351 (3.54)	0.3798 0.0690	H → L H−1 → L	4 4
3–4 site deprotonated in 3	420 (2.95) 345 (3.60)	0.5173 0.0262	H → L H−1 → L	3 3
4–5 site protonated in 5	400 (3.10) 348 (3.56)	0.6062 0.0235	H → L H−1 → L	3 3
4–5 site deprotonated in 5	417 (2.97) 352 (3.53)	0.2322 0.3428	H → L H−1 → L	3 3
3–2' site fully protonated	363 (3.42) 330 (3.76)	0.1756 0.2763	H → L H−1 → L	3 3
3–2' site deprotonated in 3	388 (3.20) 320 (3.87)	0.3812 0.0713	H → L H−1 → L	3 3
3–2' site deprotonated in 2'	406 (3.05) 351 (3.54)	0.2255 0.1848	H → L H−1 → L	4 4
3–2' site fully deprotonated	422 (2.94) 411 (3.02)	0.1383 0.2715	H → L H−1 → L	3 3

Since it is not possible to conclude based only on the discussed results, we wanted to know if there was a possibility that there was a co–existence of several species in the medium similar to the phenomenon evoked in the Mg^{II}–quercetin study[95]. To test the legibility of this occurrence, we wanted to check the number of contributions that are required to form the band of the complex at 417 nm by decomposing it into several Gaussian functions. Indeed, if we take a closer look at the former, we notice that it is not very symmetrical that would have us believe that the presence of two transitions is possible. Figure 29 demonstrates the result obtained when two Gaussian bands are generated to fit under the experimental band. It

should be noted that the x–axis drawn on Figure 29 is given in terms of the wavelength in nm, however, the model was fit according to the value of the energy in eV and the values were converted back to nanometres so as to simplify the overlap between the Gaussian bands and the experimental band. The two Gaussian functions modelled are noted as Gaussian 2 (G2) and Gaussian 3 (G3):

$$G2(E) = \frac{1}{0.24\sqrt{2\pi}} e^{-\frac{1}{2}\left(\frac{(E-3.10)}{0.24}\right)^2}$$

$$G3(E) = \frac{1}{0.17\sqrt{2\pi}} e^{-\frac{1}{2}\left(\frac{(E-2.93)}{0.17}\right)^2}$$

G1 is used to partially describe the shoulder observed in the short wavelengths of the lower energy band. Some tests were carried out to check the possibility to add more Gaussian functions. The results were not satisfactory: either the intensity of the added functions were very small, or the new function was very close to a previous one. The use of two Gaussian functions to describe the lowest–energy band was thus considered as adequate.

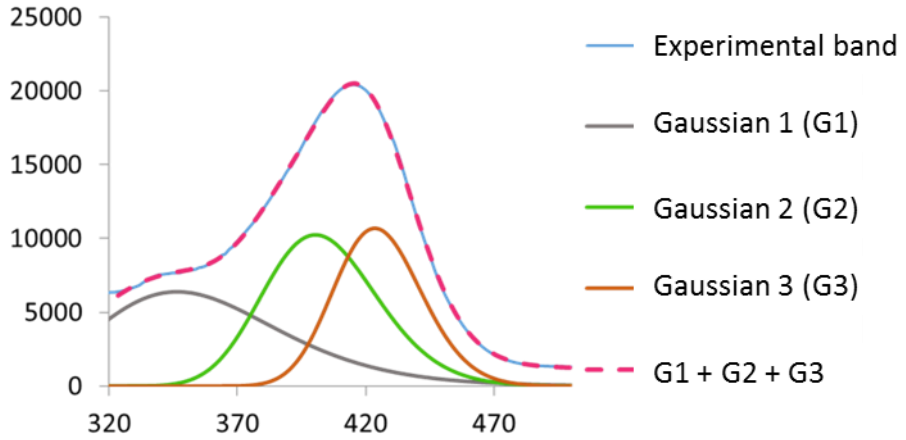

Figure 29 Deconvolution of the experimental band of the 1:1 complex (ranging from 320 nm to 470 nm) to fit three Gaussian bands

Based on this deconvolution of spectra, the two bands G2 and G3 were found to be located at 400 nm and 424 nm respectively. The calculated value for the diol complex associated to G2

is 411 nm and G3 is 422 nm, which can be considered to be a very good agreement. Therefore, this hypothesis is definitely possible.

Another hypothesis that was considered for this particular case was the presence of an M2L2–type compound. Indeed a 2:2 metal to ligand compound can also be assimilated to a 1:1 complex. In several situations, the presence of binuclear manganese centres was evidenced, most of the time in proteins and sometimes they are substituted intentionally in proteins to explore active sites or to investigate structural properties. Usually, spectroscopic techniques like EPR (Electron Paramagnetic Resonance) and EXAFS (Extended X–Ray Absorption Fine Structure) are used on such systems[124,125,126]. In this present work, since manganese ions are prone to form binuclear complexes, there is a possibility that the complex formed is in the ratio of 2:2. Indeed, when Evolving Factor Analysis is applied, the type of structure that can fit the model is given in its irreducible form. Hence, it can be deduced that the resulting solution can potentially be constituted of a 2:2 complex as it can be reduced to 1:1. With the previous analysis, it was clearly proven that the α–hydroxyketo and the diol fixation sites are likely to accept the manganese cation. Based on this observation, the molecules were constructed in such a way that $manganese_1$ would be fixed to $morin_1$ at the α–hydroxyketo site and to $morin_2$ at the diol site. Hence, $manganese_2$ would occupy the α–hydroxyketo site with $morin_2$ and the diol site with $morin_1$ and used as starting structures for the optimisations. In order to represent the M2L2 structures, there are two possible conformations: *cis* and *trans*. DFT calculations were performed on these two molecules using the same methodology as the other structures. Unfortunately, the 2:2 compounds did not deliver any results as the geometry could not be optimised. Some changes were brought to the computation method. One of them was to change the B3LYP functional to CAM–B3LYP to be able to take into account the long range interactions but once again, the molecules could

[124] Golombek, A. P., & Hendrich, M. P. (2003). Quantitative analysis of dinuclear manganese(II) EPR spectra. *Journal of Magnetic Resonance*, *165*(1), 33–48.
[125] Baffert, C., Collomb, M.-N., Deronzier, A., Kjærgaard-Knudsen, S., Latour, J.-M., Lund, K. H., McKenzie, C.J., Mortensen, M., Nielsen, L.P., & Thorup, N. (2003). Biologically relevant mono- and di-nuclear manganese ii/iii/iv complexes of mononegative pentadentate ligands. *Dalton Transactions*, (9), 1765–1772.
[126] Howard, T., Telser, J., & DeRose, V. J. (2000). An Electron Paramagnetic Resonance Study of $Mn_2(H_2O)(OAc)_4(tmeda)_2$ (tmeda = *N* , *N* , *N* ‘, *N* ‘-Tetramethylethylenediamine): A Model for Dinuclear Manganese Enzyme Active Sites. *Inorganic Chemistry*, *39*(15), 3379–3385.

not be optimised. The computations were switched to molecular mechanics by using the Universal Force Field (UFF) in order to get the stable conformation of the hypothetical complex.

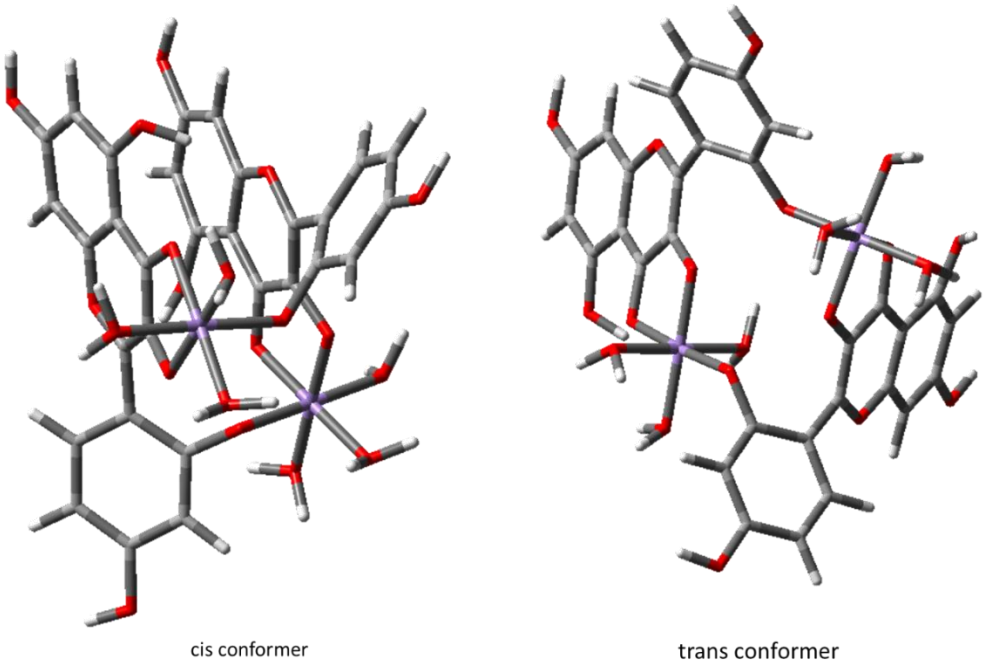

Figure 30 *Cis* and *trans* conformers of an M2L2–type complex for a Mn^{II}–morin system optimised by molecular mechanics

Figure 30 illustrated the two conformers of a 2:2 Mn^{II}–morin complex. From the structures, it can be seen, for both cases, that the two manganese atoms are fixed at the α–hydroxyketo site of one morin molecule and forms a bridge with the second morin molecule by forming a bond with the O2' atom. However, even though these two conformers were optimised by molecular mechanics, it does not change the fact that they present much steric hindrance and could not be optimised by quantum mechanics. Therefore, this possible presence of a 2:2 complex in solution seems unlikely.

Depending on all the results obtained on the complexation reaction of the manganese cations with morin, and in particular the fact that the band observed at long wavelengths has several components suggests that the complex formed involves the completely deprotonated diol function. However, the simultaneous presence in solution of another complex with Mn^{II}

bound to the deprotonated α–hydroxyketo function cannot be ruled out. The structures of these two complexes are depicted in Figure 31 below.

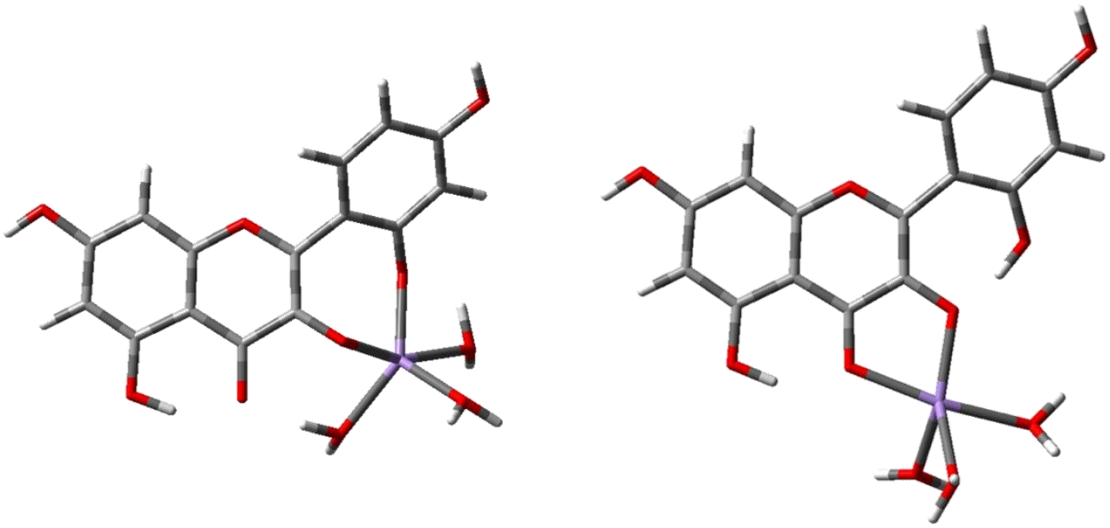

Figure 31 The structures of the diol complex with three water molecules (left) and the α-hydroxyketo complex with three water molecules (right)

3.2.2 Molecular orbitals study

So far, we narrowed down the possibilities of the complex to two structures: the fully deprotonated diol and α–hydroxyketo complexes. The molecular orbitals of these two complexes were analysed to investigate the distribution of the electronic density around the molecules and to see how the charge transfer operates for each transition. The main focus was put on the electronic transitions that are responsible for the complex band at 417 nm.

Starting with the α–hydroxyketo complex, from Figure 32, we observe an intra–ligand charge transfer. The movement of electrons are mainly localised on the ligand for the HOMO → LUMO electronic transition. The manganese cation does not play an important role in the formation on this type of transition.

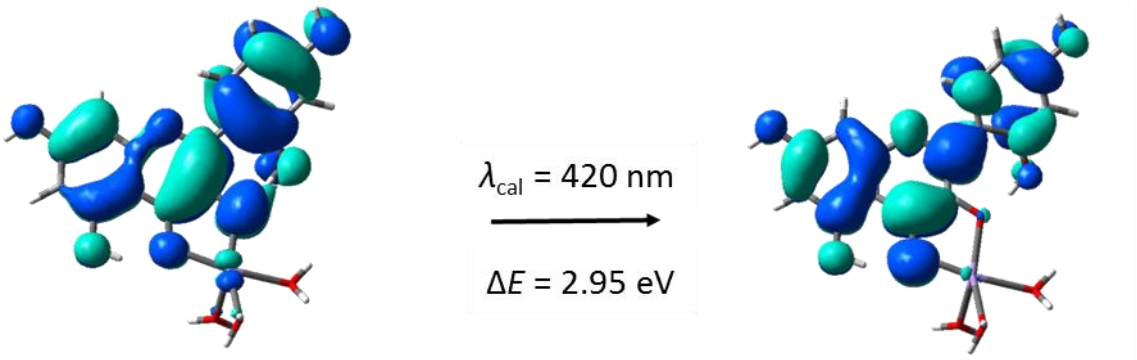

Figure 32 The HOMO (left) and LUMO (right) orbitals for the α–hydroxyketo complex

As for the diol complex, it was determined previously that there were two contributions accounting for the experimental band at 417 nm. The HOMO → LUMO transition situated at 422 nm (2.94 eV) showed an intra–ligand charge transfer, similar to the one for the α–hydroxyketo complex. On the other hand, the second transition at 411 nm (3.02 eV) corresponds to a metal to ligand charge transfer. From the look of the orbitals on Figure 33, the HOMO−1 orbital involves the participation of a d orbital on the manganese cation (Figure 33).

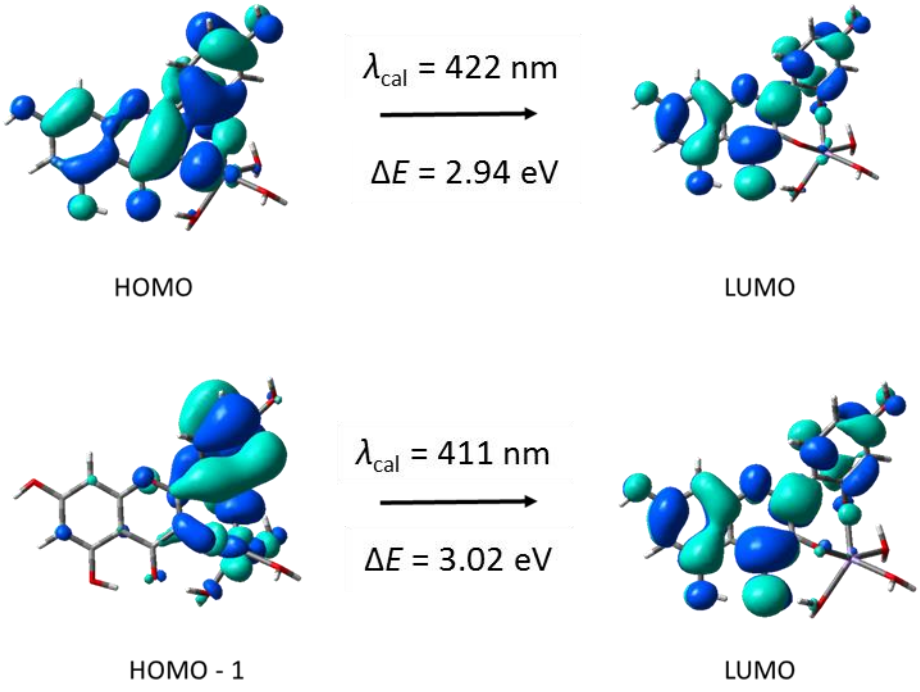

Figure 33 The HOMO–1, HOMO and LUMO orbitals for the fully deprotonated diol complex

This is quite interesting since the nature of the electronic transitions for the two complexes are different one from the other. However, the α–hydroxyketo complex cannot be excluded based only on this interpretation since a very good theoretical–experimental comparison was obtained. From the deconvolution of the band on the experimental spectrum, two bands were successfully extracted but it is also possible that there is a third hidden contribution since the transitions calculated are very close to each other.

3.2.3 QT–AIM study

All the data concerning the electronic density of the α–hydroxyketo and diol complexes are compiled in Figure 34 and Table 8. The positive values of the Laplacian of the electronic density at the bond critical points give an indication of the ionic nature of the Mn–O bond formed. This statement is reinforced by the $-G_b/V_b$ values which evolve around 1.

For both complexes, the Mn^{II} atom bears almost the same charges. The associated oxygen atoms to each complex also do not have a big variation in their charges either. The charges for the oxygen atoms of the Zn^{II}–morin complex are very similar to the one calculated for the Mn^{II}–morin complexes. The Mn^{II} charge however, is slightly higher than the one related to Zn^{II}in the complex with morin. This can be explained by a smaller electronic delocalisation over the complex than in the case of Zn^{II}. Based on the bond lengths of Mn−O3 and Mn−O4 for the α–hydroxyketo complex and the Mn−O3 and Mn−O2' on the diol complex, it can be seen that the manganese atom is closer to the diol site than the α–hydroxyketo site. The values of the electronic densities computed for each Mn−O bond are very small, giving an indication that the electronic population is quite scarce along the metal oxygen bond. Finally, the $-G_b/V_b$ parameter is always found to be around 1. According to the QT–AIM parameters, the Mn−O bond is most likely to possess an ionic character[127].

[127] Lepetit, C., Fau, P., Fajerwerg, K., Kahn, M. L., & Silvi, B. (2017). Topological analysis of the metal-metal bond: A tutorial review. *Coordination Chemistry Reviews*, *345*, 150–181.

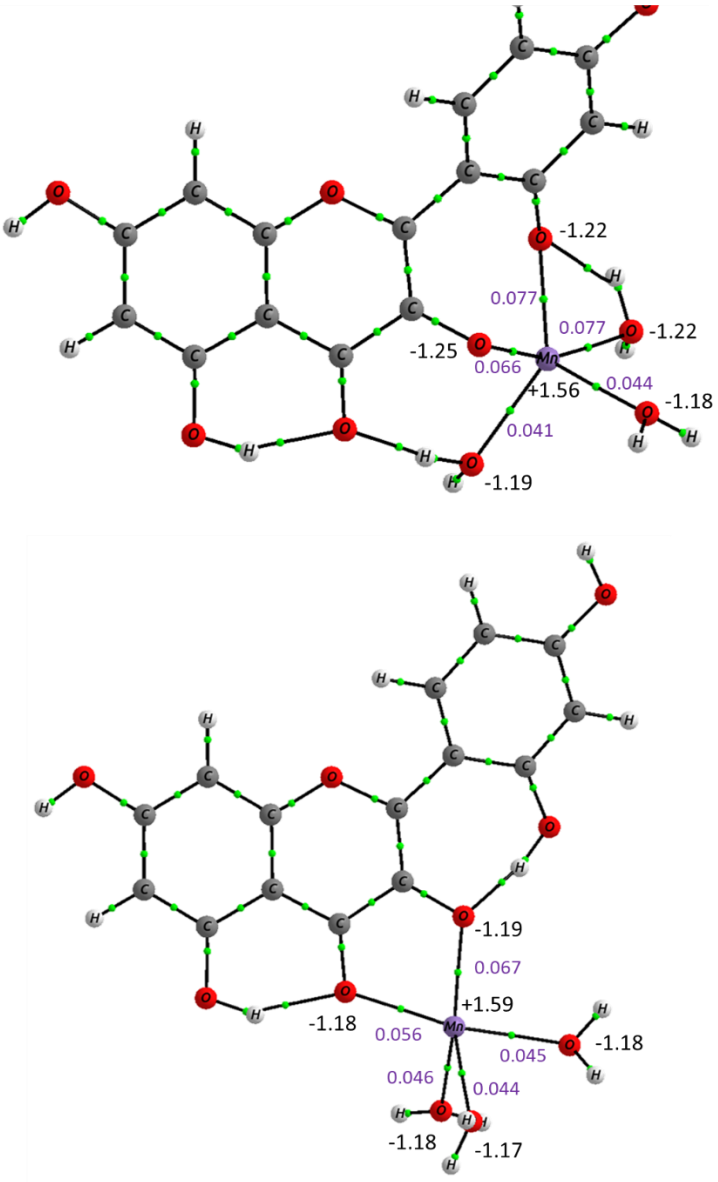

Figure 34 QT–AIM data of the two Mn^{II}–morin complexes: the diol complex on top and the α–hydroxyketo on the bottom showing the partial charges of the calcium atoms and the connected oxygens atoms as well as the electronic density value at the BCP

Table 8 Selected QTAIM charges (q, au) for the α–hydroxyketo and diol complexes, bond lengths (l, pm), electronic densities at the BCP (ρ_b, au), Laplacian of the electronic density at the BCP ($\nabla^2\rho_b$, au) and opposite to the ratio of the kinetic energy density to the potential energy density at the BCP ($-G_b/V_b$)

	α–hydroxyketo complex	diol complex
$q(Mn^{II})$	+1.59	+1.56
q(O3)	−1.19	−1.25
q(O4)	−1.18	–
q(O2')	–	−1.22
Mn–O3		
l	208.8	203.2
ρ_b	0.067	0.066
$\nabla^2\rho_b$	0.349	0.400
$-G_b/V_b$	0.981	0.959
Mn–O4		
l	216.4	
ρ_b	0.056	
$\nabla^2\rho_b$	0.277	
$-G_b/V_b$	1.000	
Mn–O2'		
l		208.4
ρ_b		0.077
$\nabla^2\rho_b$		0.348
$-G_b/V_b$		0.990

3.3 Comparison with Mn^{II}–Quercetin and Mn^{II}–Luteolin complexes

3.3.1 Mn^{II}–Quercetin system

The methodology applied for all the complexation systems is used for the reaction of Mn^{II} with quercetin. This experiment is performed not only to determine the structure of the complex but also to compare it with that of the morin complex. Undoubtedly, both of their structures are practically the same with the exception of the 2' hydroxyl of morin located at position 3' for quercetin. The inter–ring hydrogen bond with H3 and H2' is inexistent for quercetin, which has a large effect on the acid–base properties. This is interesting because due to the absence of the proton in 2', the competition is resumed between the α–hydroxyketo and β–hydroxyketo fixation sites.

Unlike morin, the first pK_a of quercetin is 8.54[89]. Therefore, it is possible to work at a pH value that is representative of the conditions in the natural environment. That is why the experimental work was performed at a pH of 6.2, where most of the fully protonated ligand is present. Note that, this pH value is situated two units above the one used for the Mn^{II}–morin reaction.

Upon titration, the yellow colour of the solution sharpens similar to the reaction with morin previously, showing a complex formation. After each addition of the manganese solution, the pH decreases and this one was brought back to 6.2 to maintain the same physico–chemical conditions during the titration. Figure 35 contains the set of spectra that shows the gradual formation of the complex at 430 nm in solution with the disappearance of the quercetin band at 377 nm in the long wavelength range. Several isobestic points are also visible, indicating the presence of two species in the medium (Figure 35).

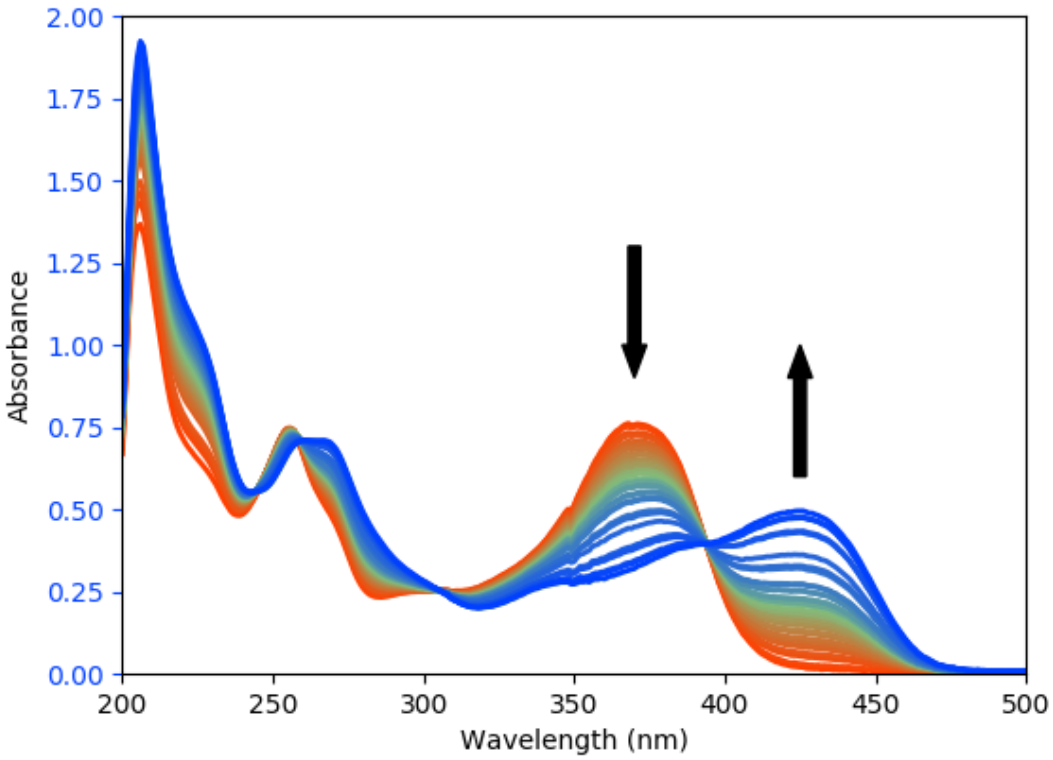

Figure 35 Set of UV–vis spectra recorded showing the formation of the Mn^{II}–quercetin complex at pH 6.2 (molar ratio ranging from 0 to 30)

The chemometric analysis gave a conditional complexation constant value (log β) of 5.713 ± 0.035 and the stoichiometry of the complex was found to be 1:1 based on the data fit.

$$\text{Quercetin} + \text{Mn}^{\text{II}} \rightleftharpoons \text{Mn} - \text{Quercetin} \qquad \log \beta = 5.713 \pm 0.035$$

With $\beta = \frac{[\text{Mn}-\text{Quercetin}]}{[\text{Quercetin}][\text{Mn}^{\text{II}}]}$

Alongside, the DFT and TD–DFT computations were run on the twenty–four hypothetical structures. Similar to the calculations run with the Mn^{II}–morin hypotheses, special care needs to be given to the multiplicity of the compound since manganese possesses five unpaired electrons in its 3d orbitals. All computations were carried out with a multiplicity of 6.

Unlike for morin, no main difficulties were met since all hypothetical molecules were successfully optimised except for the fully protonated catechol complex. Indeed, the most challenging sites in morin involves the OH2', that is not present in quercetin.

The overlap of the experimental spectrum is depicted on Figure 36 for the three fully deprotonated possible sites with four water molecules in the coordination sphere of the manganese cation.

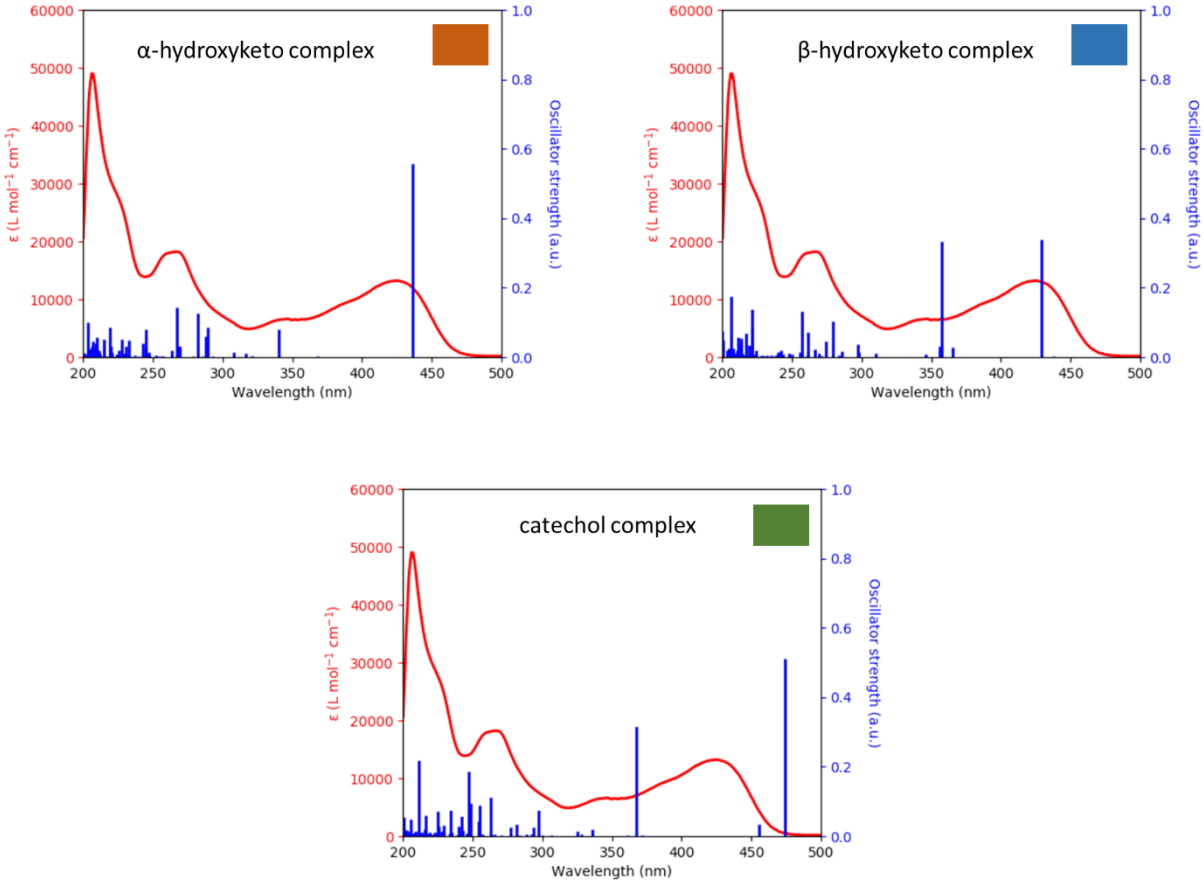

Figure 36 Overlap of the experimental UV–vis spectrum of the 1:1 complex between quercetin and Mn^{II} (red curve) and the computed transitions (blue lines) for the (a) α–hydroxyketo (b) β–hydroxyketo and (c) catechol complexes

Two equally intense electronic transitions are computed for the HOMO → LUMO and HOMO–1 → LUMO for the β–hydroxyketo complex. However, this is not a feature that it visible on the UV–vis spectrum, thereby, eliminating this possibility. Concerning the catechol complex, the theoretical model does not correspond at all to the experimental spectrum.

Indeed, if we look at the electronic transition at 474 nm (2.61 eV), it is red–shifted with respect to the band at 430 nm representing the complex. In addition to that, the electronic transition at 368 nm (3.37 eV) is quite intense and does not seem to coincide with any band. All the data related to the theoretical calculations about electronic transitions of all the plausible complexes have been compiled in Table 9.

Table 9 Computed wavelengths (nm), energies (eV), oscillators strengths for the transitions corresponding to H → L and H−1 → L (H stands for HOMO and L for LUMO) for all the possible Mn^{II}–quercetin complexes envisaged

Fixation location	Band position, λ, nm (E, eV)	Oscillator strength, f	Nature of transition
3–4 site protonated in 3	395 (3.14) 357 (3.47) 317 (3.91)	0.46 0.06 0.09	H → L H−1 → L H−2 → L
3–4 site deprotonated in 3	437 (2.84) 340 (3.64)	0.56 0.08	H → L H−1 → L
4–5 site protonated in 5	411 (3.02) 325 (3.82)	0.71 0.06	H → L H−2 → L
4–5 site deprotonated in 5	429 (2.89) 358 (3.47)	0.34 0.33	H → L H−1 → L
3'–4' site fully protonated	–	–	–
3'–4' site deprotonated in 3' 3'–4' site deprotonated in 3'	411 (3.02) 361 (3.44)	0.35 0.21	H → L H−1 → L
3'–4' site deprotonated in 4' 3'–4' site deprotonated in 4'	411 (3.02) 405 (3.06)	0.80 0.05	H → L H−1 → L
3'–4' site fully deprotonated 3'–4' site fully deprotonated	474 (2.61) 368 (3.37)	0.51 0.32	H → L H−1 → L

By careful observation, based on the experimental data and the theoretical computations, it can be deduced that, the product formed is the α–hydroxyketo complex. Its 3D structure is depicted on Figure 37.

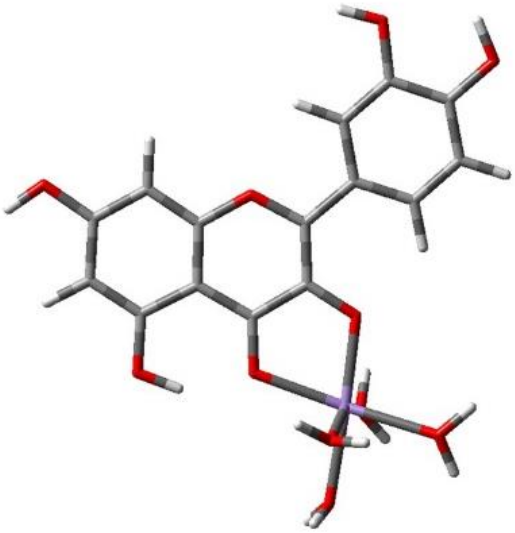

Figure 37 Structure of the α–hydroxyketo complex

The molecular orbitals of the α–hydroxyketo complex were analysed to examine their behaviour and to determine whether the metal cation plays a role in the complexation process. As we have seen for the Mn^{II}–morin complex, there is a double contribution accounting for the complex band, one of them revealing a metal to ligand charge transfer. It could be interesting to see if the same phenomenon (type of charge transfer) is observed for the Mn^{II}–quercetin complex. In this particular case, there is only one electronic transition that is responsible for the low–energy lying band of the complex spectrum for the α–hydroxyketo complex. If we take a closer look at the HOMO and LUMO orbitals, mainly the ligand is involved in the charge transfer (Figure 38). There seems to be a very small contribution coming from the manganese cation, however, it is too weak to consider that it is taking part in the charge transfer. In conclusion, we can observe an intra–ligand charge transfer. The involvement of Mn^{II} in the low–lying transitions appears to be a characteristic of the morin complex.

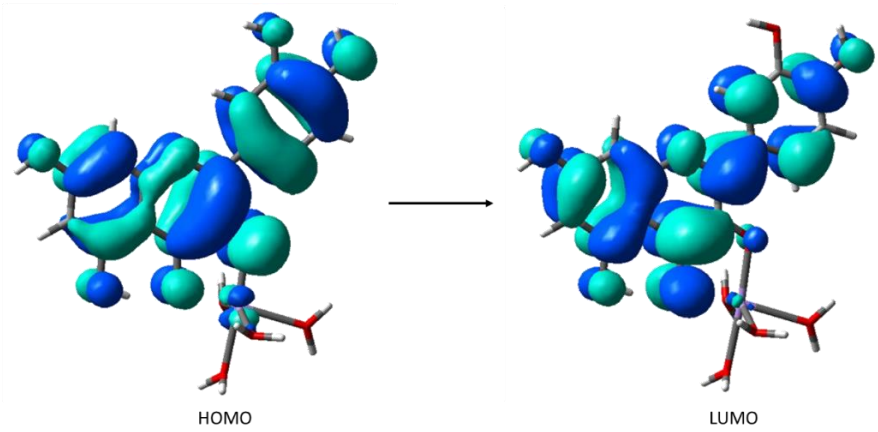

Figure 38 The HOMO and LUMO orbitals for the α–hydroxyketo Mn^{II}–quercetin complex

QT–AIM calculations on the Mn^{II}–quercetin system gave a few features on the geometrical changes posterior to the formation of the complex as depicted on Figure 39 and Table 10. It is striking how the QT–AIM data for the Mn^{II}–quercetin complex is similar to that of the α–hydroxyketo Mn^{II}–morin complex. The charges of the manganese and oxygen atoms can be considered to be identical with a slight variation due to the delocalisation of the electrons over the whole molecule. The same observations are made for the local indicators at the BCP, that is, the electronic densities and Laplacian value of the electronic density as well as $-G_b/V_b$ value. They all suggest that the Mn–O bond retains an ionic nature.

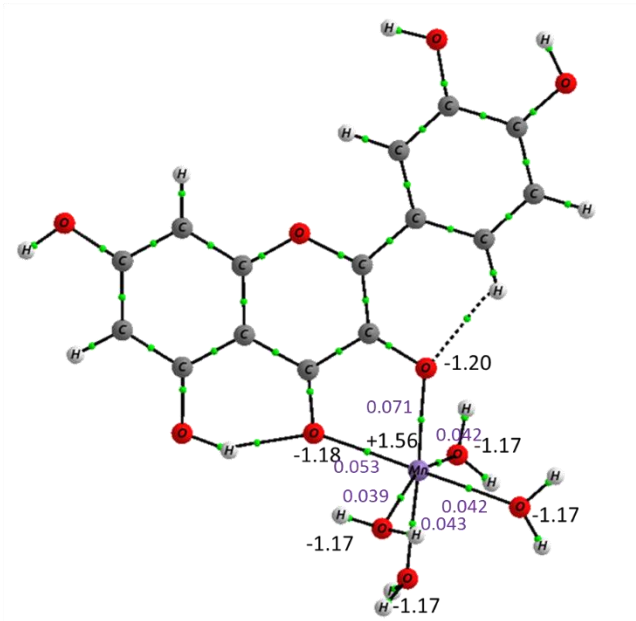

Figure 39 QT–AIM data of the Mn^{II}–quercetin complex showing the partial charges of the calcium atoms and the connected oxygens atoms as well as the electronic density value at the BCP

Table 10 Selected QTAIM charges (q, au) for the α–hydroxyketo complex, bond lengths (l, pm), electronic densities at the BCP (ρ_b, au), Laplacian of the electronic density at the BCP ($\nabla^2\rho_b$, au) and opposite to the ratio of the kinetic energy density to the potential energy density at the BCP ($-G_b/V_b$)

	α–hydroxyketo complex
$q(Mn^{II})$	+1.56
q(O3)	−1.20
q(O4)	−1.18
Mn–O3	
l	207.1
ρ_b	0.071
$\nabla^2\rho_b$	0.364
$-G_b/V_b$	0.967
Mn–O4	
l	219.4
ρ_b	0.053
$\nabla^2\rho_b$	0.253
$-G_b/V_b$	1.000

3.3.2 Mn^{II}–Luteolin system

The flow cell was set up to carry out the same experiment as previously but this time with luteolin as flavonoid. However, after several small addition of the $MnCl_2$ solution like it was done for morin and quercetin, the ligand spectrum does not seem to be affected. No bathochromic effects, which usually accounts for the formation of a complex, are observed. A larger amount of metal solution is added to have a set of spectra with the molar ratio varying from 0 to 200. The reaction seems to be happening but at a very slow rate. The ligand band at 342 nm is decreasing and at around 412 nm, the absorption is increasing gradually but we do not really see the appearance of a new band. Unfortunately, with the look of the set of spectra on Figure 40, not much information can be extracted from it. Since the reaction is not over, the chemometrics analysis was useless. The conclusion that can be derived from this experiment is that manganese cations have much difficulty fixing themselves onto the β–

hydroxyketo and catechol site. This enabled us to understand better the importance of the position 3 hydroxyl group on the flavonoid molecule. It has a direct participation in the inter–ring hydrogen bond on morin and is present on the quercetin molecule, justifying the high reactivity of both flavonoids when they interact with metal cations. This result can also be seen as an *a posteriori* confirmation of our assignment of structures with manganese complexes that were involving the 3OH position. Indeed, the non–formation of complexes without this group is not a proof in itself, but it supports our reasoning.

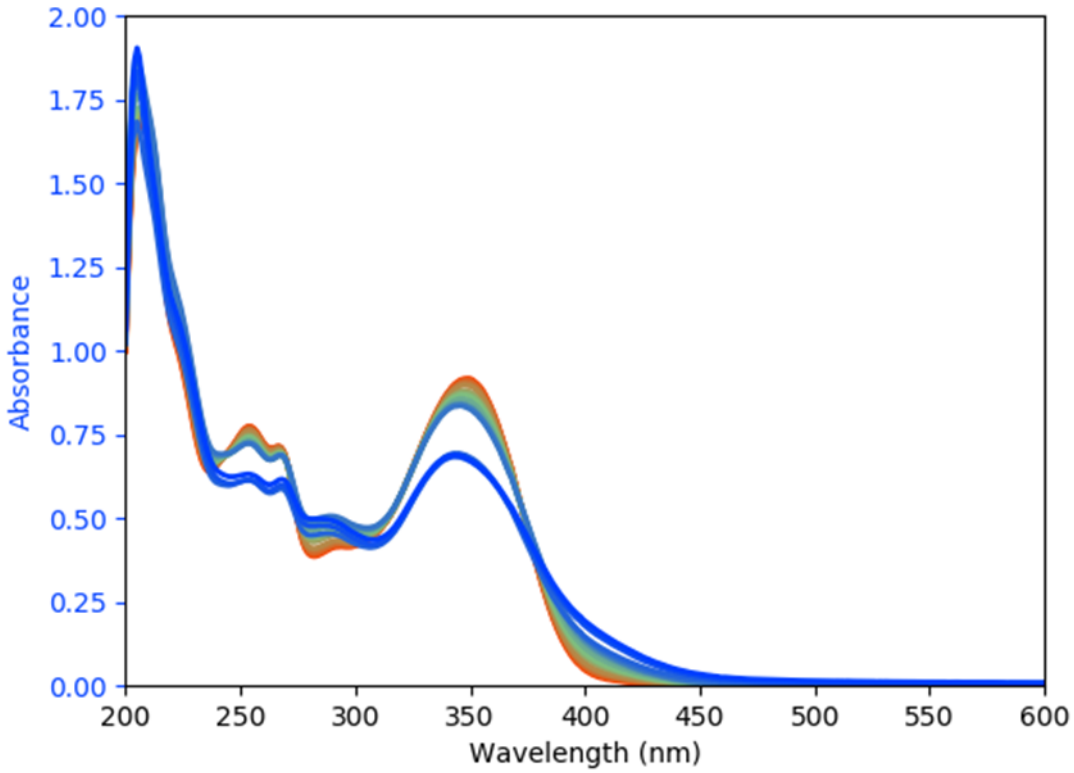

Figure 40 Set of UV–vis spectra measured during the titration of luteolin against the Mn^{II} salt with the pH adjusted to 6.2 (molar ratio ranging from 0 to 200)

CHAPTER 4:

CALCIUM

4.1 Properties and importance of calcium

In general, block d metals are the elements of interest for complexation reactions. They possess d orbitals that facilitate the formation of coordination complexes. However, in this part of the thesis, interest was put on the calcium cation, which is not very commonly used despite the fact that it is widely present in soil and is essential in the human body.

Being one of the most abundant elements present in the Earth crust, it is available in many areas worldwide mostly in the form of salts. These ions are useful for the environment as they represent one of the required constituent for the growth of plants[128]. The calcium ions present in the soil is taken up by the xylem[129]. The amount of the mineral taken depends on the cation exchange capacity of the root cell walls and this movement is regulated to prevent an excess of Ca^{II} in the shoots that can easily hinder the growth of plants. On another note, a deficiency in the cationic mineral generally occurs in tomatoes, green leaves like lettuces, celery and especially in plants that are fed by the phloem instead of the xylem. Ca^{II} plays an essential role in maintaining the integrity of cell walls and cell membranes. As a positively–charged ion, not only does it act as a counter cation with respect to the anions in the vacuoles of the cells but it also combines with proteins to allow the transduction of the cytosolic Ca^{II} concentration signal[130].

Calcium is also known to be the most abundant metal in an individual, constituting 2% of the body weight. Calcium is one of the key factors not only in the regeneration of bones in our body but also in nerves and muscles function. Like other chemicals, a deficiency or an excess of calcium cations can cause serious problems in the organism[131,132]. Ca^{II} is essential for the

[128] Karley, A. J., & White, P. J. (2009). Moving cationic minerals to edible tissues: Potassium, magnesium, calcium. *Current Opinion in Plant Biology*, *12*(3), 291–298.
[129] White, P. J., & Broadley, M. R. (2003). Calcium in Plants. *Annals of Botany*, *92*(4), 487–511.
[130] White, P. J., Broadley, M. R., El-Serehy, H. A., George, T. S., & Neugebauer, K. (2018). Linear relationships between shoot magnesium and calcium concentrations among angiosperm species are associated with cell wall chemistry. *Annals of Botany*, *122*(2), 221–226.
[131] Calì, T., Ottolini, D., & Brini, M. (2012). Mitochondrial Ca2+ and neurodegeneration. *Cell Calcium*, *52*(1), 73–85.
[132] Calì, T., Ottolini, D., & Brini, M. (2016). CHAPTER 27 Mitochondrial Calcium Homeostasis and Implications for Human Health. In *Calcium: Chemistry, Analysis, Function and Effects*, 448–467.

human cell activities, acting as a secondary messenger to transmit biological information from one cell to the other[133,134]. As a matter of fact, the biochemical mechanism of the whole nervous system assimilates the concentration Ca^{II} in its complex pathways. The cellular Ca^{II} signaling occurs in the mitochondria. The intracellular concentration of Ca^{II} is controlled by the mitochondria and also by specific Ca^{II} binding proteins[135]. This concentration is highly dependent on the proton electrochemical gradient, where the equilibrium is never attained due to the exchange occurring between H^+/Ca^{2+} and Na^+/Ca^{2+}. An improper regulation of the concentration can lead to mitochondrial dysfunction, defective production of ATP and even a rapid decrease in the lifespan of cells. Researches performed on animals showed that there is a direct relationship between the changes in Ca^{II} concentration and mitochondrial misbalance, leading eventually to the Parkinson disease. In fact, one of the early features of the Parkinson disease could be due to the alteration of the Ca^{II} homeostasis rather than neuronal malfunction.

The main objective of this chapter is to study experimentally and theoretically the interaction of calcium cations with morin, quercetin and luteolin in order to investigate if a complex can be formed with the reactants chosen and the type of complex formed. More specifically, the goal is to determine the morin site preferentially involved in calcium fixation and to study the influence of pH on the structure of the complex–es formed. The experimental part of the work is done by electronic spectroscopy (both absorption and fluorescence emission spectroscopies) and has been supported by quantum chemistry calculations.

[133] Brini, M., Calì, T., Ottolini, D., & Carafoli, E. (2013). Intracellular Calcium Homeostasis and Signaling. In L. Banci (Ed.), *Metallomics and the Cell*, 119–168.
[134] Calì, T., Ottolini, D., & Brini, M. (2014). Calcium signaling in Parkinson's disease. *Cell and Tissue Research*, *357*(2), 439–454.
[135] Brini, M., Calì, T., Ottolini, D., & Carafoli, E. (2014). Neuronal calcium signaling: Function and dysfunction. *Cellular and Molecular Life Sciences*, *71*(15), 2787–2814.

4.2 Ca^{II}–Morin system

4.2.1 Absorption and fluorescence studies

The same experimental procedure were applied to determine the formation of Ca^{II}–morin complex. However, compared to the other systems, it was more difficult to determine the fixation site, hence, additional studies had to be carried out. The absorption and fluorescence set of data were registered. The pH effect on the complexation reaction was also investigated to do a follow–up of the deprotonation process and through this method, extra information can be obtained to locate the fixation site. Hence, the first two methodologies required fixing the pH and varying the molar ratio whereas the third methodology consisted in fixing the molar ratio at a value where the largest amount of complex is present and varying the pH to deprotonate the complex.

Figure 41 shows the set of spectra recorded post titration of $CaCl_2$ with morin. Before the addition of the metal solution, two characteristic bands were observed at 357 nm and 253 nm, values in accordance with those published in the literature. As expected, a bathochromic shift is observed progressively with the addition of the $CaCl_2$ solution. After varying the molar ratio of metal to ligand from 0 to 30, with the pH constantly fixed at 4.2, and after proper data treatment, the spectrum of the complex is acquired. The two bands previously spotted occupied new positions at 410 nm and 264 nm respectively. Along with that, another band having a weak intensity with respect to the others is seen at 330 nm. Moreover, the appearance of some isosbestic points are detected, indicating that the ligand and one complex are in equilibrium throughout the experiment. The Evolving Factor Analysis confirmed that the complex formed corresponded to a 1:1 complex. The same experiment was repeated at a pH of 6.2 to study the behaviour of Ca^{II} and morin at a pH value that can be compared to environmental conditions. The two spectra of pure morin do not correspond since the band at 357 nm is broader at pH 6.2. This is simply because this band is the contribution of the fully protonated ligand and its mono–deprotonated form. Unlike the ligand, the two spectra of the complex showed no difference. The conditional stability constant for this complex at both pH values were estimated to be $\log \beta = 4.40 \pm 0.02$ at pH 4.2 and 6.87 ± 0.05 at pH 6.2.

$$\text{Morin} + \text{Ca}^{\text{II}} \rightleftharpoons \text{Ca} - \text{Morin}$$

log β = 4.40 ± 0.02 at pH 4.2

log β = 6.87 ± 0.05 at pH 6.2

With $\beta = \frac{[\text{Ca–Morin}]}{[\text{Morin}][\text{Ca}^{\text{II}}]}$

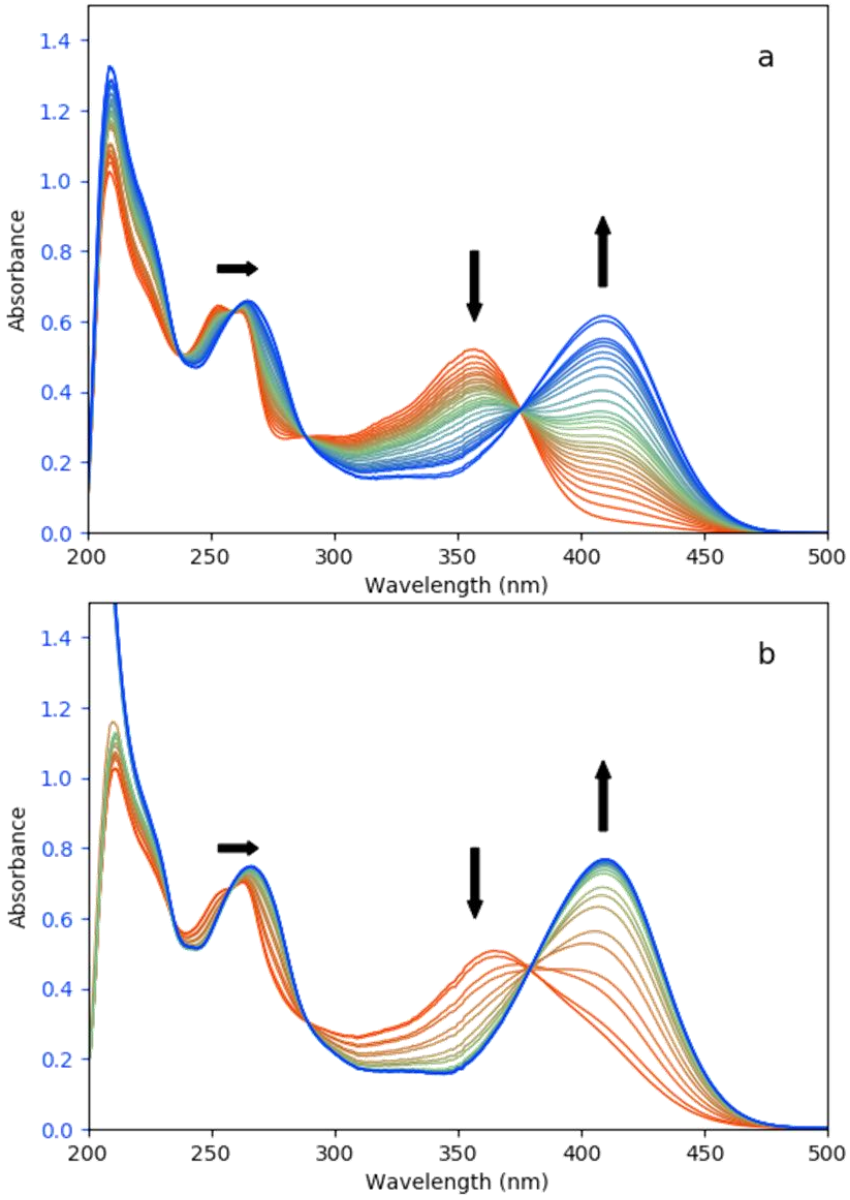

Figure 41 Set of the UV–vis spectra of morin upon the addition of Ca^{II} (a) at pH 4.2 for molar ratio ranging from 0 to 20 (b) at a pH of 6.2 for molar ratio ranging from 0 to 4

Right after acquiring the absorption data, we proceeded the same way to obtain the set of fluorescence spectra. To obtain the latter, the solution was excited at 410 nm which corresponds to the maximum of the Ca^{II}–morin band. In addition to that, the fluorescence excitation emission matrix (EEM) was also recorded at pH 4.2 when the solution contained the complex with a molar ratio of metal to ligand of 2. Figure 42 illustrates the two figures detailed above: on Figure 42(b), the first spectrum with a band at 501 nm in red has a very low emission intensity and it corresponds to the mono–deprotonated form of morin.

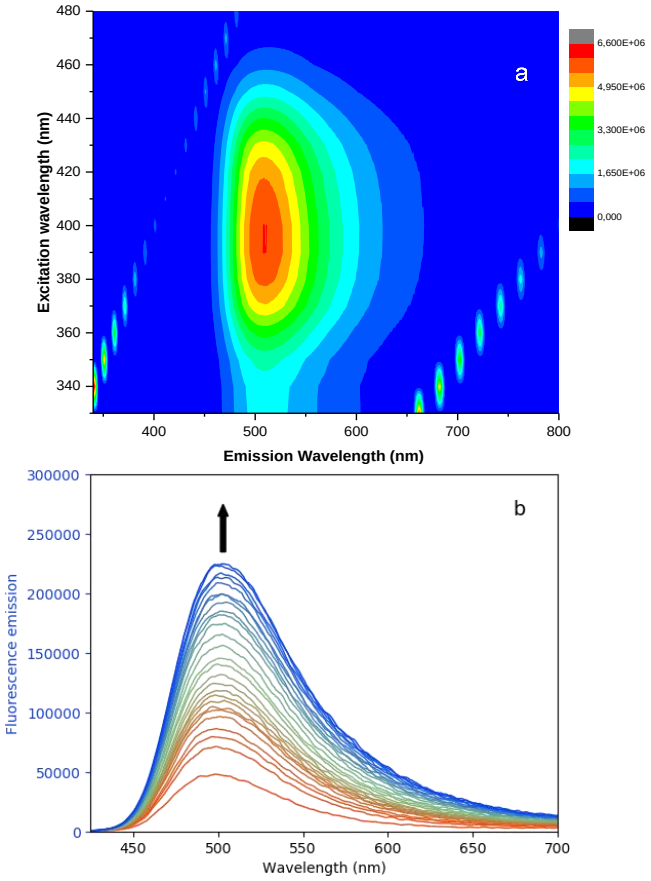

Figure 42 (a) Excitation Emission Matrix of fluorescence of Ca^{II}–morin system at pH 4.2 (molar ratio of 2) and (b) Set of fluorescence spectra of the complex (molar ratio from 0 to 20) at pH 4.2 excited at a wavelength of 410 nm

It is observed even at a pH 4.2 because a small amount of the mono–deprotonated form is found in the solution. Fluorescence spectroscopy is a technique that it more sensitive than absorption spectroscopy, thus, the mono–deprotonated morin is more conspicuous when the fluorescence study is performed. It should be noted that morin is not a fluorescent molecule.

The intensity of the band increases progressively as the manganese chloride solution is added. The complex formed at 504 nm after the reaction is fluorescent and this observation is also confirmed with the EEM on Figure 42(a), where a red spot is formed which confirms the presence of only one species, that is, the complex. Since there is no dual fluorescence on the set of spectra or matrix, it is an indication that there is no excited state intramolecular proton transfer (ESIPT), a phenomenon that is observed in the 3–hydroxyflavone or quercetin. At this point, it is quite difficult to give a reason for the absence of proton transfer. It can be due to a modification in the structure of the complex formed that prohibits the formation of the tautomeric form or simply a deprotonation during the complexation reaction. The chemometrics analysis is also performed on the set of emission spectra and the complexation constant, log β of the 1:1 complex arose to 4.41 ± 0.2.

$$\mathrm{Morin} + \mathrm{Ca^{II}} \rightleftharpoons \mathrm{Ca-Morin} \qquad \log \beta = 4.41 \pm 0.2$$

With $\beta = \frac{[\mathrm{Ca-Morin}]}{[\mathrm{Morin}][\mathrm{Ca^{II}}]}$

The third part of the experimental work consisted in assessing how the variation of the pH of the solution can affect the complex. At a molar ratio equal to 2, it was considered that the solution contained a high percentage of 1:1 complex. The objective was to keep the molar ratio fixed at 2 and to vary the pH from an acidic to basic solution. Figure 43(a) depicts the evolution of the absorption spectra of the Ca^{II}–morin complex when the pH is made to vary from 1.84 to 11.29. At a first glance, bathochromic effects are apparent. In order to easily interpret the data collected, the set of spectra was decomposed so that the formation of each deprotonated species could be noticeable. The decomposition was carried out in such a way that the spectra which shared an isobestic point would be regrouped together. By proceeding like this, Figure 43(a) was successfully broken down into Figure 43(b), (c) and (d).

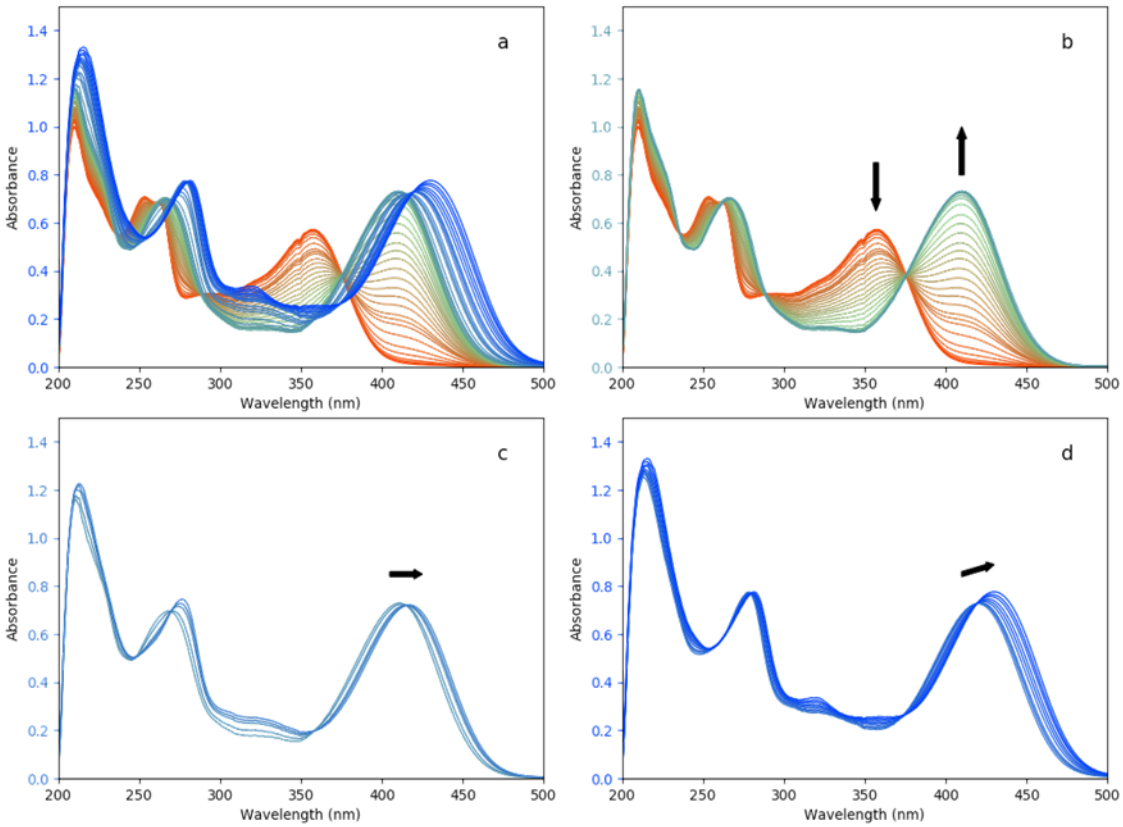

Figure 43 Evolution of the UV–visible spectrum of Ca^{II}–morin system (R = 2) with the pH varying from: (a) 1.84 to 11.29, (b) 1.84 to 7.6, (c) 7.96 to 9.16 and (d) 9.75 to 11.29

At pH 1.84, only the ligand band is seen as the complex does not absorb in acidic conditions. From this value till pH 7.6, the 1:1 complex gradually shows itself at 410 nm. We can also confirm the co–habitation of two types of molecules in the medium as four isobestic points are situated at 238 nm, 259 nm, 289 nm and 375 nm. Till now, we saw the evolution of the ligand to the 1:1 complex which we already certified beforehand. After pH 7.6, we no longer see the band of the ligand, showing that all the ligand molecules have been complexed. From pH 7.96 to 9.16 and there is also a change in the isobestic point, moving to new positions at 250 nm, 270 nm, 361 nm and 417 nm. The band at 410 nm experienced a bathochromic shift to 417 nm. We can interpret this transition as the first deprotonation of the Ca^{II}–morin complex and the presence of the isobestic points shows the equilibrium of the complex formed as well as its mono–deprotonated form. Finally, the last decomposition concerned the spectra recorded from the pH values of 9.75 to 11.29. The new isobestic points occupied new positions at 259 nm, 281 nm, 378 nm and 420 nm and the mono–deprotonated complex band

formerly at 417 nm moved to 427 nm. The new species formed can be related to the bi–deprotonated form of the Ca^{II}–morin complex.

If the spectral data clearly shows, on one hand, the formation of the complex and, on the other hand, the successive deprotonation of the latter, it is also possible to obtain, from these data, some thermodynamic quantities such as the formation constant of the complex as well as its first two pK_a values. The change in absorbance plotted at 410 nm with respect to the variation of the pH from 1.84 to 7.60 has the characteristic shape of a sigmoid curve (Figure 44(a)). In the investigated pH range, the absorbance measured at 410 nm can be expressed as:

$$A = \varepsilon_{\mathrm{LH}} l\,[\mathrm{LH}] + \varepsilon_{\mathrm{LCa^+}} l\,[\mathrm{LCa^+}] \qquad (1)$$

To write equation (1), the only equilibrium considered is:

$$\mathrm{LH} + \mathrm{Ca^{2+}} = \mathrm{LCa^+} + \mathrm{H^+} \quad K \text{ (formation constant)}$$

Notably, the presence of the deprotonated morin is not taken into account that is justified by the results obtained below. It can be easily shown (using matter conservation and laws of mass action) that the relations:

$$K\,[\mathrm{LH}]^2 + [\mathrm{LH}]\big([\mathrm{H^+}] + c\,K(R-1)\big) - c\,[\mathrm{H^+}] = 0 \qquad (2)$$

and

$$[\mathrm{LCa^+}] = \frac{R\,c\,10^{-\mathrm{p}K_a}\,[\mathrm{LH}]}{10^{-\mathrm{pH}}c^\circ + 10^{-\mathrm{p}K_a}\,[\mathrm{LH}]} \qquad (3)$$

hold, with K the complexation constant, c the initial concentration of morin, and c° the standard concentration (1 mol L^{-1}). Thus, the expressions of [LH], from (2), and [LCa^+], from [LH] and (3), lead to an analytical expression of A, that has been computed for each pH value. The parameters, especially K, were optimized using a least–square fitting. A good agreement

was obtained depicted on Figure 44(a). Due to the lack of characteristic features, the derivatives were numerically computed both from the fitted model and from the experimental data. Once again, a good agreement was obtained, ensuring that the model reproduce correctly the data.

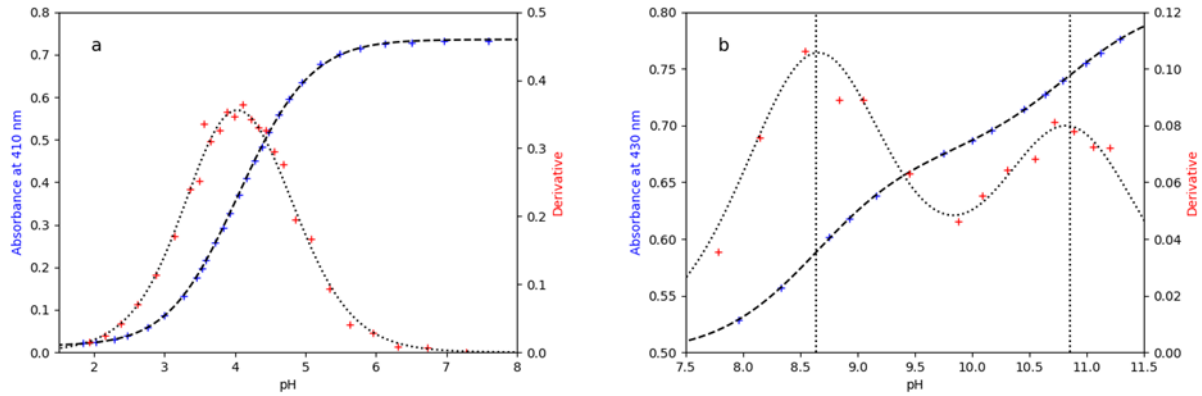

Figure 44 (a) Plot of absorbance at 410 nm with respect to pH (blue +), its derivative function (red +) and fitted model and its derivative and (b) Plot of absorbance at 430 nm with respect to pH (blue +), its derivative function (red +) and fitted model and its derivative. The vertical dotted lines are located at the pH corresponding to extracted pKa values

The calculation gives a value of log *K* of –0.13. As $K = \beta \cdot [H^+]$ and consequently that log β = log *K* + pH, the values of log β calculated for pH = 4.2 and 6.2 are 4.07 and 6.07 respectively, which are consistent with those obtained from the complexation titration at fixed pH.

$$\text{Morin} + \text{Ca}^{\text{II}} \rightleftharpoons \text{Ca} - \text{Morin} \qquad \text{with } \beta = \frac{[\text{Ca–Morin}]}{[\text{Morin}][\text{Ca}^{\text{II}}]}$$

In the same way, the variation of the absorbance at 430 nm plotted as a function of the pH between 7.96 and 11.29 shows two inflection points (Figure 44(b)), indicating the presence of several equilibria. The obtained curve was treated similarly to the one above.

Nevertheless, the involved equilibria are quite different: two successive deprotonations were hypothesized. In the investigated pH range, the absorbance measured at 430 nm can be expressed as:

$$A = \varepsilon_{\mathrm{LCa^+}} l\,[\mathrm{LCa^+}] + \varepsilon_{\mathrm{LCa^+(-H^+)}} l\,[\mathrm{LCa^+(-H^+)}] + \varepsilon_{\mathrm{LCa^+(-2H^+)}} l\,[\mathrm{LCa^+(-2H^+)}] \qquad (4)$$

To write equation (4), the two equilibria considered are:

$$\mathrm{LCa^+} = \mathrm{LCa^+(-H^+)} + \mathrm{H^+} \qquad K_{a1}$$

$$\mathrm{LCa^+(-H^+)} = \mathrm{LCa^+(-2H^+)} + \mathrm{H^+} \quad K_{a2}$$

Once again, the presence of the deprotonated morin is not taken into account, which is justified by the results obtained below. Notably, no hypothesis is made either about the number of mono–deprotonated species ($\mathrm{LCa^+(-H^+)}$ could stand for several complexes), or about the site of deprotonation. The same holds for the doubly–deprotonated species.

The analytical expressions are more easily writable than in the previous case: it is quite straightforward to derive from matter conservation and laws of mass action:

$$A = c\,l\,\frac{\varepsilon_{\mathrm{LCa^+}} 10^{\mathrm{p}K_{a1}-\mathrm{pH}} + \varepsilon_{\mathrm{LCa^+(-H^+)}} + \varepsilon_{\mathrm{LCa^+(-2H^+)}} 10^{\mathrm{pH}-\mathrm{p}K_{a2}}}{10^{\mathrm{p}K_{a1}-\mathrm{pH}} + 1 + 10^{\mathrm{pH}-\mathrm{p}K_{a2}}} \qquad (5)$$

with K_{a1} and K_{a2} the acid–base constants defined by the equilibrium above, c the initial concentration in morin, and l the optical path length. Thus, A has been computed for each pH value. The parameters, especially K_{a1} and K_{a2}, were optimized using a least–square fitting. A good agreement was obtained depicted on Figure 44(b). Like in the case of Figure 44(a), the derivatives were numerically computed both from the fitted model and from the experimental data and a good agreement was obtained, ensuring that the model reproduce correctly the data. Remarkably, the pK_a values do not correspond exactly to the inflection points of A and to the maxima of its derivative, due to a small coexistence of both equilibria.

The values of the first two pK_a of the complex 1:1 are 8.6 and 10.9, respectively. However, it is useful to note that these values do not corresponding to the first deprotonation of the morin molecule, which has already undergone deprotonation–s upon complexation. Thus, these obtained values cannot be easily compared to those of the free ligand.

The same experiment was carried out using fluorescence spectroscopy as shown on Figure 45. At pH 1.84, since morin is not fluorescent, practically no emission is seen. The intensity of the band progressively increases at 504 nm as the pH increases. The first mono–deprotonated form appears with the band maximum at 525 nm, followed by the bi–deprotonated species of the complex centred at 560 nm. The bathochromic effects in fluorescence spectroscopy are more marked than those in absorption spectroscopy. The Stokes shifts values are 94 nm, 108 nm and 133 nm for the three species in the order of formation.

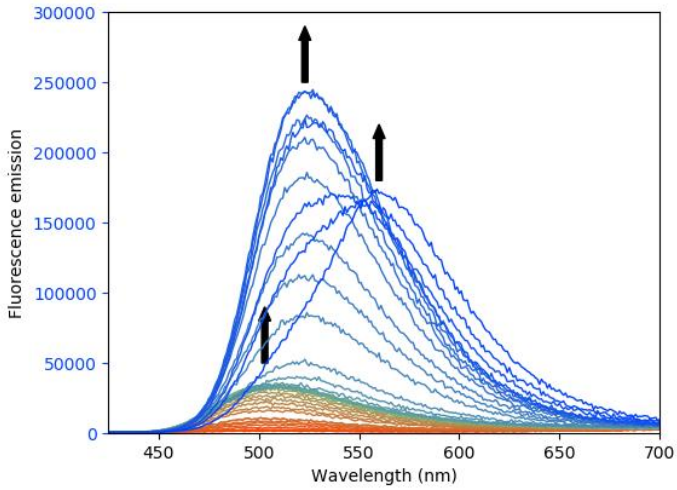

Figure 45 Evolution of the fluorescence spectrum of the Ca^{II}–morin system (R = 2) with pH varying from 1.84 to 11.29 (excitation wavelength: 410 nm)

To summarise the experimental work related to the comprehension of the effect of the variation of the pH on the complex solution fixed at a molar ratio of 2, we notice that in acidic conditions, only the ligand absorbs and as the pH gradually increases, we can see the band of the complex appearing. As the solution becomes more basic, the complex undergoes a first deprotonation then a second one as displayed on the absorption spectra.

4.2.2 DFT calculations and comparison with experimental data

Moving on to the theoretical part of this work, more calculations had to be done in order to identify the species that matches the experimental data. First of all, the thirty hypothetical structures were optimised and their electronic transitions were calculated. Moreover, since the fluorescence spectrum of the complex was also recorded, the theoretical emission wavelengths of all the hypotheses were computed. Furthermore, it will be seen afterwards that the computations on the different structures does not allow to conclude on the complex formed. Hence, there was a need to account theoretically for all the possibilities of deprotonated species. Thus, certain hypothetical deprotonated structures were optimised at their ground and first excited state and their absorption electronic transitions were computed to gather their theoretical excitation and emission wavelengths with DFT and TD–DFT. In line with our methodology, the experimental and theoretical data of the complex was compared to narrow down the possibilities. Afterwards, the remaining structures which had a good comparison were subjected to different deprotonation schemes.

The electronic transitions computed were firstly compared with the data acquired during the first and second part of the experimental work, that is, the set of absorption and fluorescence spectra when the molar ratio was varied and the pH was fixed. The two main transitions that enabled the sorting out among all the possibilities were the band at 410 nm and the one at 330 nm.

The hydroxyether site (1–2' site):

As with other cations, this fixation site can already be dismissed without even doing any comparison work simply because the structures could not be optimised. Indeed, at this site, six different complex molecules were considered and they were determined by changing the number of solvent molecules in the coordination sphere of the calcium cation or by modifying the protonation state. Unfortunately, not a single one gave a satisfying optimised structure. We observe the same phenomenon as we previously had with the complexes involving the zinc and manganese cations. The reasons for this behaviour given previously may be applied to this case also. The fact that the distance between O1 and O2’ being too important and the

structure not being flexible enough at this position may explain why the metal cation does not get fixed to this position.

The β–hydroxyketo complex (4–5 site):

First of all, the fully protonated β–hydroxyketo complex can be ruled out because a decrease in pH was noticed right after the calcium chloride solution was added. This occurrence gave an indication that the fixation site is being deprotonated, hence, the complex formed cannot be completely protonated at its fixation site. Concerning the fully deprotonated β–hydroxyketo complex, the HOMO → LUMO band calculated at 412 nm corresponded perfectly with the experimental value at 410 nm. The problem arose when the focus was placed on the HOMO–1 → LUMO band whose oscillator strength was 0.38, which is even higher than the transition at 412 nm. This occurrence did not represent at all the experimental curve where the HOMO–1 → LUMO transition has an absorption value about 50 times less intense than the HOMO → LUMO one (Figure 46). Therefore, this fixation site can definitely be excluded from the preferential fixation site of the calcium cation without even comparing the fluorescence data.

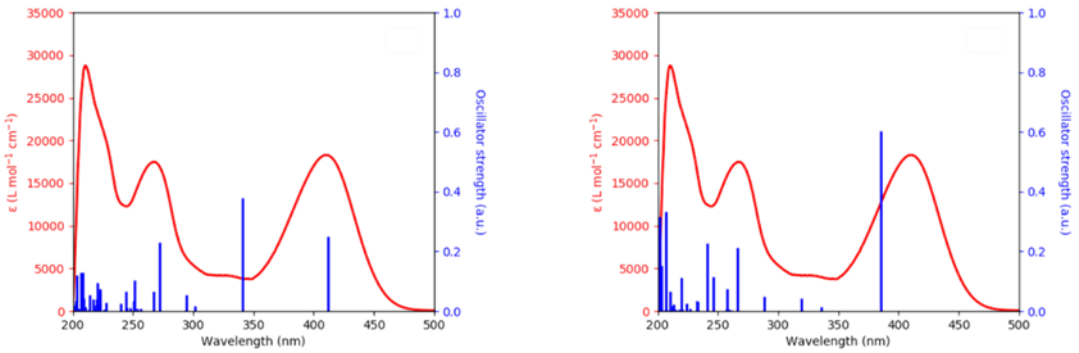

Figure 46 Overlap of the experimental UV–vis spectrum of the 1:1 complex between morin and the Ca^{II} cation (red curve) and the computed transitions (blue lines) for the protonated (left) and deprotonated (right) β–hydroxyketo complex

The α–hydroxyketo complex (3–4 site):

Regarding the fully protonated α–hydroxyketo complex, the HOMO → LUMO transition describes well the experimental band, however, it is not the case for the HOMO–1 → LUMO transition which is computed with an oscillator strength higher than the HOMO → LUMO one.

Therefore, the protonated α–hydroxyketo complex cannot be the complex formed. As illustrated on Figure 47, the computed spectrum for the fully deprotonated α–hydroxyketo complex reproduced well the experimental absorption spectrum. At 415 nm, the HOMO → LUMO transition with an oscillator strength of 0.52 justified the experimental band at 410 nm. As for the experimental band at 330 nm, it is described by two transitions: the HOMO–1 → LUMO transition at 338 nm (f = 0.03) and the HOMO–2 → LUMO at 315 nm (f = 0.05). The fluorescence values were also checked to see if the values match as in absorption spectroscopy. As a matter of fact, the theoretical emission wavelength is found be at 526 nm, which is near the experimental emission wavelength at 504 nm. From this interpretation, the deprotonated α–hydroxyketo complex is a good candidate to be the complex formed during the reaction between Ca^{II} and morin.

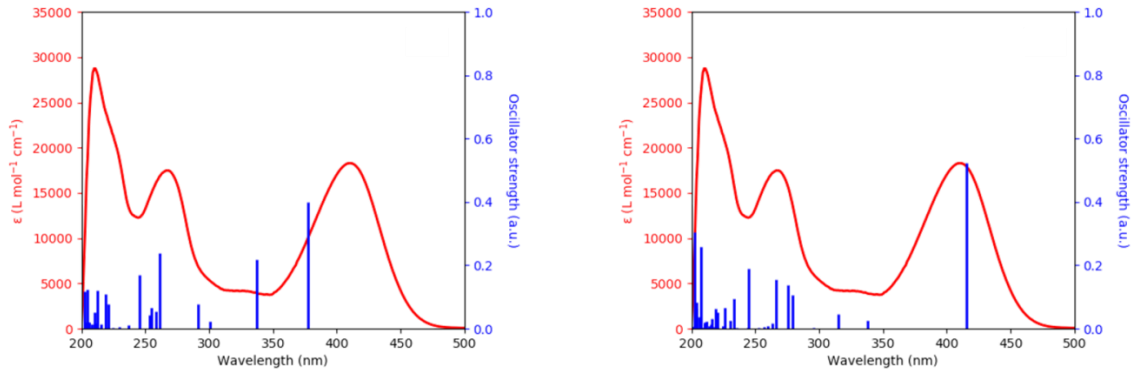

Figure 47 Overlap of the experimental UV–vis spectrum of the 1:1 complex between morin and the Ca^{II} cation (red curve) and the computed transitions (blue lines) for the protonated (left) and deprotonated (right) α–hydroxyketo complex

The diol complex (3–2' site):

The last fixation site to be considered is the diol fixation site. If we recall, based on its two hydroxyl groups, the number of potential complexes that can be formed here is 12. We can already omit all the hypotheses related to the fully protonated diol complex due to aforementioned reasoning. We start by considering the fully deprotonated diol complex. The HOMO → LUMO transition situated at 422 nm, with a difference of 0.08 eV from the observed band. Two transitions were also responsible for the experimental band at 330 nm and they were located at 357 nm and 311 nm. The theoretical emission wavelength was found to be at 522 nm compared to the experimental value of 504 nm. We have a fair agreement regarding

the absorption and fluorescence results. We are left with the two mono–deprotonated species. The one that was easily eliminated was the diol complex deprotonated in position 2'. Despite the fact that the HOMO → LUMO transition was well calculated at 416 nm (f = 0.30), the presence of a transition at 350 nm, with an oscillator strength of 0.20 disrupted the harmony of the overlap between the experimental and the theoretical curves. In addition to that, the theoretical fluorescence emission was situated at 569 nm, far from the measured value of 504 nm. This leaves us with the last species at this site, that is, the diol complex mono–deprotonated in 3. The HOMO → LUMO and HOMO–1 → LUMO transitions located at 401 nm (f = 0.40) and 314 nm (f = 0.05) respectively reproduced well the experimental data. Even the fluorescence emission wavelength was well calculated at 499 nm.

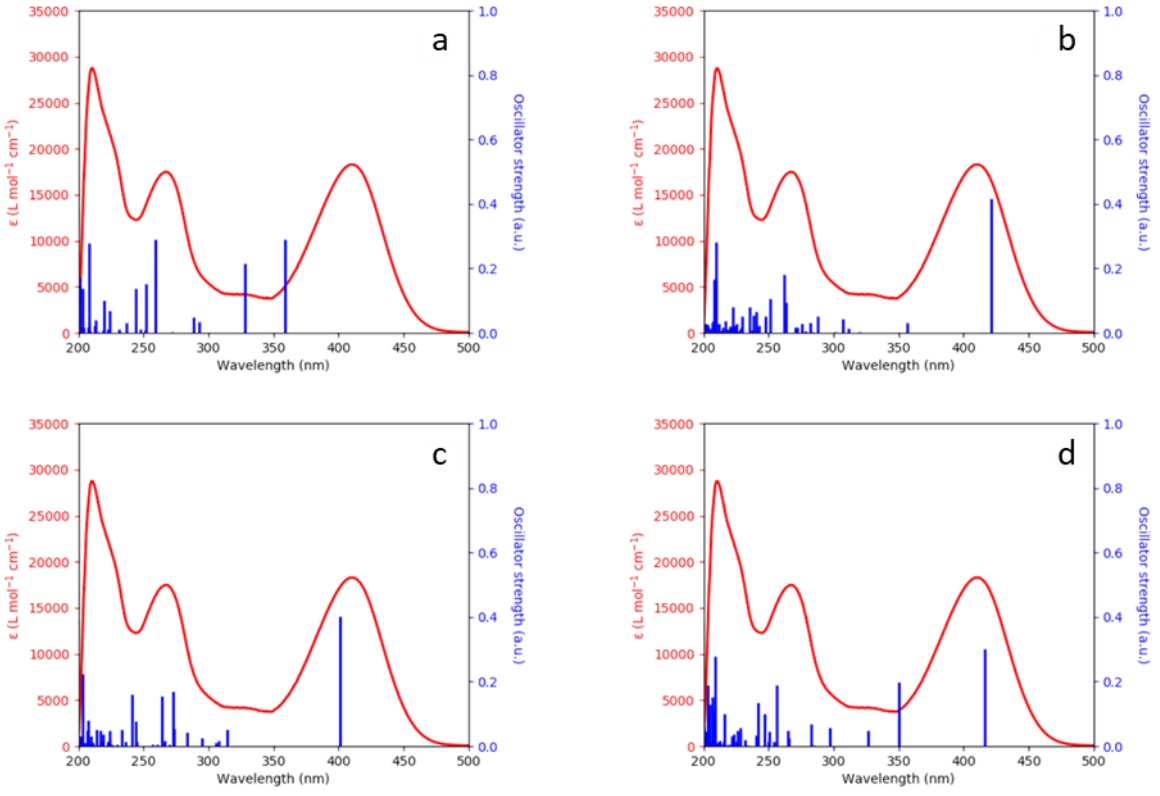

Figure 48 Overlap of the experimental UV–vis spectrum of the 1:1 complex between morin and the Ca^{II} cation (red curve) and the computed transitions (blue lines) for the (a) fully protonated diol complex, (b) fully deprotonated diol complex, (c) diol complex deprotonated in 3, and (d) diol complex deprotonated in 2'

From the initial proposed structures, we were able to narrow down the possibilities to three specimens (the coordination sphere of calcium will be discussed later on). At this point, from

a spectral point of view, it is not possible to distinguish between the fully deprotonated α–hydroxyketo, fully deprotonated diol and mono–deprotonated diol (in position 3) complexes. However, from an energetic aspect, the α–hydroxyketo and the mono–deprotonated diol can easily be compared since they have the same number of atoms and they undergo the deprotonation process only once. Thermodynamic calculations were performed on the two structures to determine the different in the Gibbs free energy. Three functionals of different nature, B3LYP, M06–2X and ωB97X–D were chosen for this part of the work in order to compare the values obtained and to test the homogeneity of the results. The M06-2X functional was chosen since it is made up of a higher percentage Hartree-Fock exchange contribution (54% versus 20% for B3LYP) while the ωB97X-D functional was tested on the molecules to take into consideration possible long range interactions and dispersion effects. The latter are detailed in Table 11.

Table 11 Difference in the Gibbs free energy between the diol complex and the α–hydroxyketo complex according to three different functionals

Functional	Gibbs free energy ($\Delta_r G$, kcal mol^{-1})
B3LYP	14.3
M06–2X	12.1
ωB97XD	10.7

The $\Delta_r G$ for the three cases are in the same order of magnitude and they are all in favour of the α–hydroxyketo complex (lower energy value). The energy difference is significant enough to observe to eliminate the mono–deprotonated diol complex. It is quite tricky to proceed similarly with the fully deprotonated diol complex as it possesses one proton less than the α–hydroxyketo complex. There is a possibility to simply add the Gibbs free energy of the proton to the one of the diol complex. However, the calculated $\Delta_r G$ of a proton is accompanied by large errors due to the solvation of the proton despite the latest data published where the value is more and more accurate. In order to reduce the uncertainty present in the value, successive deprotonations were considered.

Therefore, the spectral study of successive deprotonations could help to determine which site is favoured. Before moving on to the next step where the influence of the pH is observed on the complex, we tried to understand what happens to the calculated spectra when the number of solvent molecules are varied.

While comparing the theoretical and experimental values at each site, the number of solvent molecules in the coordination sphere of the calcium atom was evoked. For some structures like the α–hydroxyketo, the variation of the number of solvent molecules is independent of the look of the theoretical spectra (Figure 49(a)). The difference between the electronic transitions is negligible. In contrast, the change in the number of components in the coordination sphere of the calcium atom for the diol complex is more visible (Figure 49(b)). This can be explained by the steric hindrance that may be caused at this position. We considered four solvent molecules for the two potential complexes for the next step.

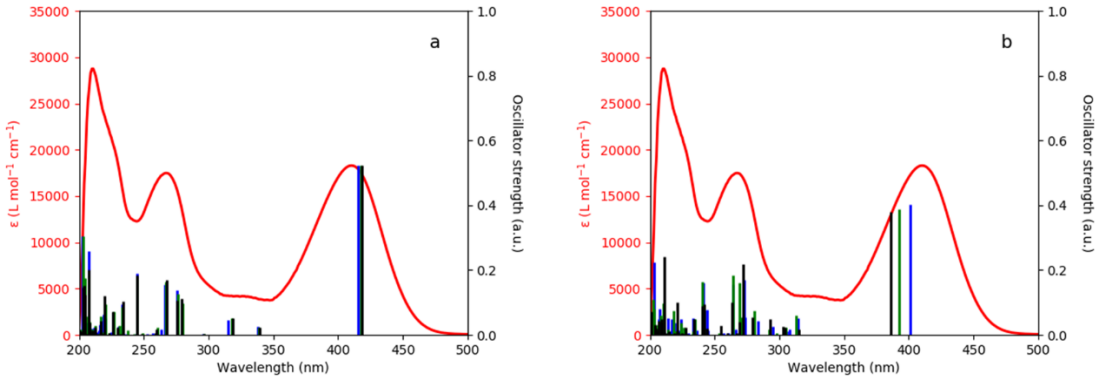

Figure 49 Overlap of the experimental spectrum of the (a) α-hydroxyketo and (b) diol Ca^{II}-morin complex with two, three and four molecules of water

As seen before, what differentiates the α–hydroxyketo complex and the diol complex is that the latter has one proton less. The main idea is to investigate the various possible deprotonated species of the two complexes by removing the most labile protons. Since we witnessed a double deprotonation experimentally (Figure 43), this phenomenon will be investigated theoretically. Therefore, if we consider the α–hydroxyketo complex, the most labile protons are those found in positions 4', 7, 2' and one from a water molecule in the coordination sphere of the calcium. As for the diol complex, the labile protons removed were

located in positions 4', 7 and one from a water molecule in the coordination sphere of the calcium. Once again, we applied our methodology on the deprotonated structures. The experimental absorption and fluorescence data for the three species studied are tabulated in Table 12 below.

Table 12 The experimental UV–vis and fluorescence wavelengths λ (nm) for the formed Ca^{II}–morin complex and its two deprotonated species

1:1 complex	1st deprotonation	2nd deprotonation
410 nm; 504 nm	417 nm; 525 nm	430 nm; 560 nm

The diol complex and its deprotonated species (Figure 50):
Of the three possibilities of the deprotonated species of the diol complex, only the removal of the 4' proton did not seem to give a good agreement. Interestingly enough, when a water molecule is deprotonated in the first step, the 7 proton was lost on the second step and vice versa. The comparison of the absorption and fluorescence wavelength matched very well with a mean difference of 0.07 eV. At this stage, it did not matter which route the complex took for the deprotonation.

The α–hydroxyketo complex and its deprotonated species (Figure 50):
The data analysis was different for the α–hydroxyketo complex. When the molecule was deprotonated for a first time, the only possibility that was feasible was when a water molecule in the coordination sphere of the calcium atom was removed. For the second step, it seemed that the 7 proton departed from the molecule.

A flowchart was set up in Figure 50 to summarise the step–by–step procedure to determine the structure of the complex and its deprotonated species. Even though, some light was shed upon the behaviour of the complex in different media, we still cannot distinguish between the α–hydroxyketo and diol complex if we rely only on the spectral data: three deprotonation schemes are consistent with the experimental data. This is why we decided to complete this study by comparing also the thermodynamic values. These values should be carefully handled

because of the important entropic factors and of the uncertainty on the value of the solvation free energy of the proton. Therefore, instead of doing the calculations on only one pair of molecules, the thermodynamic study will be carried out on all the molecules present on the chain of deprotonation (Figure 51).

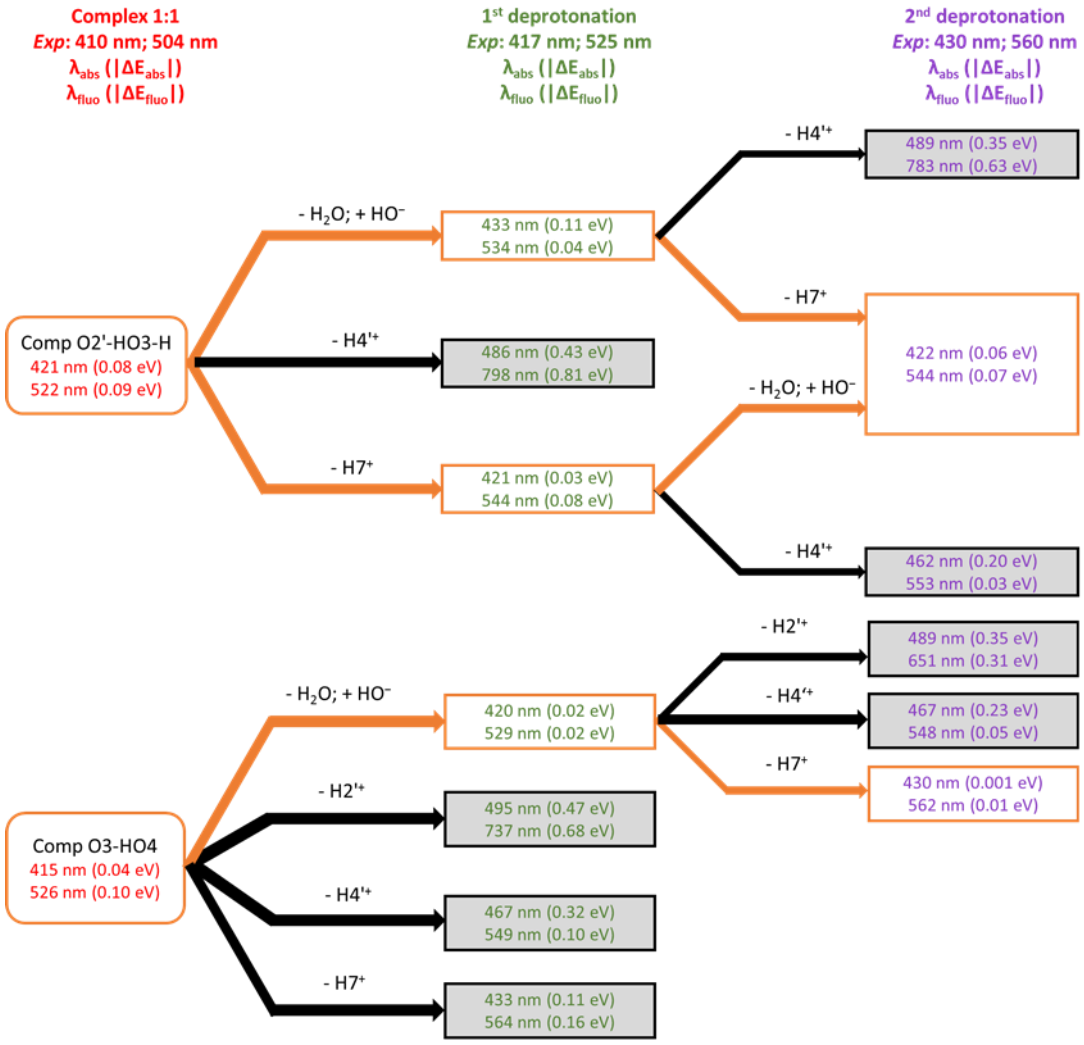

Figure 50 Experimental absorption and emission wavelengths of the complex 1:1 and its two deprotonated forms and calculated absorption (HOMO → LUMO transition) and fluorescence wavelengths for the different hypothesis of complex deprotonation. The values in brackets are the difference between the calculated and experimental energy transitions (in absolute values)

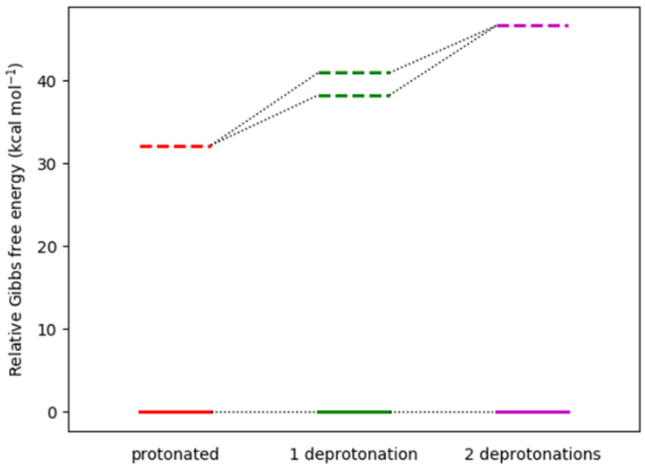

Figure 51 Relative Gibbs free energy (kcal mol^{-1}) for the α–hydroxyketo complex and its two deprotonates species (solid line) with respect to the diol complex and its associated deprotonated species (broken line)

By progressing as such, it was evidenced that, throughout the chain of deprotonation, all the species related to the formation of the α–hydroxyketo had a lower Gibbs free energy than those connected to the diol complex. The reasoning relies on a key assumption that is that the fixation site does not change upon deprotonation. The large (and increasing) difference between Gibbs free energies along the deprotonation process is sufficient to exclude a potential shift of the cation. Thus, we can establish that the complex formed was the deprotonated α–hydroxyketo complex, which later underwent a first deprotonation when a water molecule lost one proton in the coordination sphere of the calcium atom and finally a second deprotonation of the hydroxyl group at position 7. Figure 52 shows the evolution of the formation of the complexes and their geometrical parameters are given in Table 13.

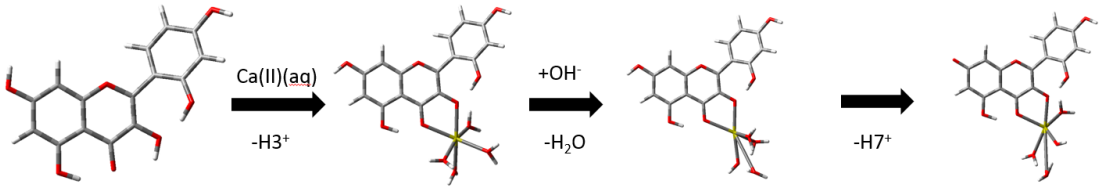

Figure 52 Reaction scheme illustrating the regio–selectivity of Ca^{II} binding by morin and the two successive deprotonations of the formed complex

The main structural modifications of the ligand which occur with the complexation or the successive deprotonations of the obtained complex are listed in Table 13. As expected, the different C3O3 and C4O4 bond lengths in morin tend to get much closer with the chelate formation even though the C3O3 bond remains longer than C4O4 in the calcium–containing ring. The inter–ring bond increases in the complexes with respect to the free ligand, which would indicate a decrease in the electronic delocalization over the entire molecule. However, the inter–ring dihedral angle decreases for the complexed forms, this could be due to the increase of the strength of the intra–molecular hydrogen bond H2'O3. The deprotonation of a solvent molecule in the coordination sphere of calcium hardly changes the structure of the ligand. This observation depicts the strong ionic nature of the metal–ligand bonds. Finally, the deprotonation of the hydroxyl function in position 7 has a much greater impact on the geometry of the ligand even at the metal binding site.

Table 13 Main geometrical parameters for morin and its complexes with Ca^{II}, at different protonation states. The bond lengths are given in Å and the inter–ring dihedral angle is in °

	Morin	1:1 complex	1st deprotonated species	2nd deprotonated species
C2C1'	1.459	1.465	1.465	1.469
C3O3	1.359	1.327	1.323	1.335
C4O4	1.254	1.279	1.279	1.289
O3Ca		2.356	2.355	2.405
O4Ca		2.389	2.398	2.371
H2'O3	1.701	1.508	1.490	1.505
C3C2C1'C2'	−35.9	−29.7	−29.1	−31.1

It is important to understand that for such systems, we cannot rely solely on thermodynamic results. The methodology that we established is very robust and accurate to solve such type of issue.

4.2.3 QT–AIM study

Figure 53 and Table 14 report the data obtained following the QT–AIM calculations on the Ca^{II}–morin complex. The calcium atom possesses a charge of +1.73, which is higher than the charges calculated for manganese (+1.56) and zinc (+1.45). The charges of the oxygens atoms,

on the other side, still have the same values as the previously studied complexes. This shows that due to the strong electron delocalisation over the whole molecule, the charges of the oxygens atoms are distributed evenly in all the complexes and do not vary much. The calcium atom does not intervene much in the electronic motion. This observation is also backed up with the fact the electronic density at the BCP of the Ca–O bond is quite small. The nature of the Ca–O was investigated by retrieving the Laplacian value at the BCP. Once again, its positive value suggests that an ionic character is present in the bond. However, unlike the previous cases exposed, the $-G_b/V_b$ values at the bond critical point are above the value of 1. This means that the kinetic energy density at the BCP of Mn–O is the leading contribution compared to the potential energy density. Since G_b is thought to have a tendency to dilute electrons at the BCP, the iconicity of the Mn–O bond is further insinuated.

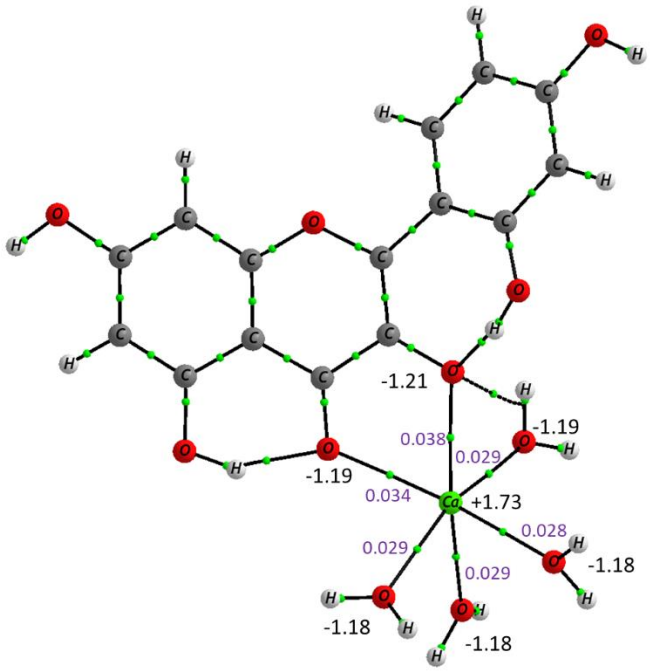

Figure 53 QT–AIM data of the Ca^{II}–morin complex showing the partial charges of the calcium atoms and the connected oxygens atoms as well as the electronic density value at the BCP

Table 14 Selected QTAIM charges (q, au) for the α–hydroxyketo complex, bond lengths (l, pm), electronic densities at the BCP (ρ_b, au), Laplacian of the electronic density at the BCP ($\nabla^2\rho_b$, au) and opposite to the ratio of the kinetic energy density to the potential energy density at the BCP ($-G_b/V_b$)

	α–hydroxyketo complex
$q(Ca^{II})$	+1.73
q(O3)	−1.21
q(O4)	−1.19
Ca–O3	
l	235.6
ρ_b	0.038
$\nabla^2\rho_b$	0.194
$-G_b/V_b$	1.131
Ca–O4	
l	239.0
ρ_b	0.034
$\nabla^2\rho_b$	0.176
$-G_b/V_b$	1.148

4.3 Comparison with the Ca^{II}–Quercetin and Ca^{II}–Luteolin complexes

4.3.1 Ca^{II}–Quercetin system

The formation of the Ca^{II}–quercetin complex turned out to be more challenging than expected. As usual, when dealing with quercetin, the complexation reaction was carried out at a pH of 6.2. However, major difficulties were encountered during the experiment as Ca^{II} does not readily complex quercetin. It was seen previously that a solution having a molar ratio of 30 was more than enough to complex all the morin but it is not the case with quercetin. Figure 54 illustrates the evolution of the absorption spectra of the stepwise formation of Ca^{II}–quercetin complex. In order to record the latter, there was a need to go up to a molar ratio of 6000 and even despite this large amount of metal solution, the ligand band at 373 nm is still visible. The gradual formation of the complex is observed at 420 nm. Nevertheless, the set of data was treated by chemometrics to get an idea on the rate and feasibility of the reaction. The EFA showed the formation of a 1:1 complex. This fact is confirmed by the presence of several isobestic points on Figure 54 at 259 nm, 300 nm and 393 nm.

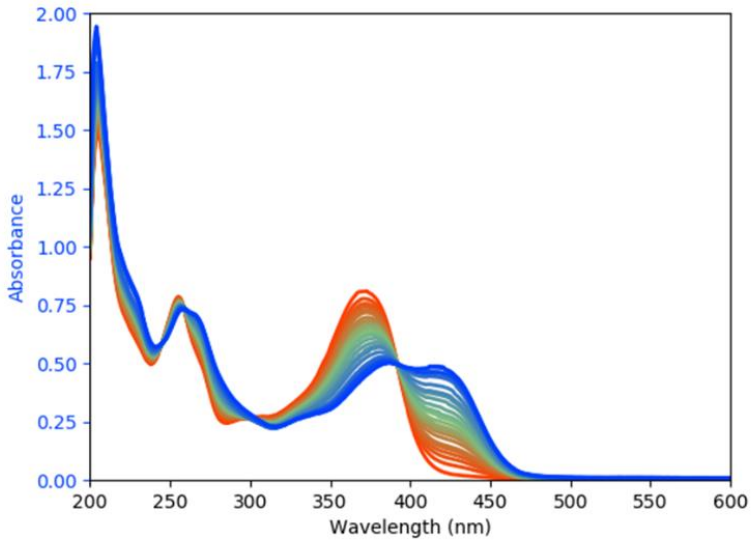

Figure 54 Set of the UV–vis spectra of quercetin upon the addition of Ca^{II} at a pH of 6.2 for molar ratio ranging from 0 to 6000

A conditional complexation constant, log β was calculated and the value arose only to 1.05 ± 0.05

$$\text{Quercetin} + \text{Ca}^{\text{II}} \rightleftharpoons \text{Ca} - \text{Quercetin} \qquad \log \beta = 1.05 \pm 0.05$$

With $\beta = \frac{[\text{Ca}-\text{Quercetin}]}{[\text{Quercetin}][\text{Ca}^{\text{II}}]}$

Through this reaction, we recognise the importance of the inter–ring hydrogen bond present on morin. The presence of the hydroxyl group in position 2' enhances the acidity of the position 3 that favours the thermodynamics of the complexation reaction and enables the Ca^{II} to fix itself to the α–hydroxyketo site. It is possible to make this statement because the α–hydroxyketo fixation site is also present in quercetin but there is a big difference between how the calcium cations react with each ligand.

Figure 55 shows the evolution of the set of fluorescence spectra from a molar ratio of 0 to 3000 when the solution is excited at the maximum of the absorption band of the complex, that is, at 420 nm.

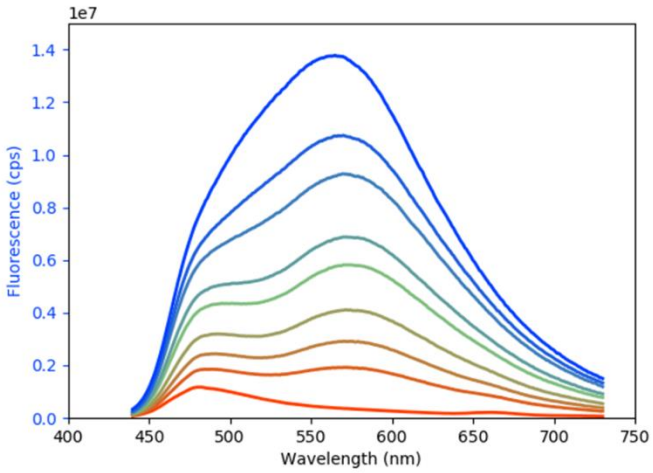

Figure 55 Set of fluorescence spectra of the complex (molar ratio from 0 to 3000) at pH 6.2 excited at a wavelength of 420 nm

Initially, before the addition of the calcium chloride solution, the fluorescence of quercetin only is present at 485 nm (2.56 eV). With the increase of the molar ratio, a new band is formed on the fluorescence spectrum corresponding to the emission of the complex at 580 nm (2.14 eV).

The absorbance spectrum of the 1:1 complex was retrieved from the absorbance data to compare it with the computed transitions. The theoretical emission wavelengths were also calculated at each fixation site to find a match with the experimental value of 580 nm. Four of the hypotheses stood out from the rest of the twenty–four initially considered and they are illustrated in Figure 56 below.

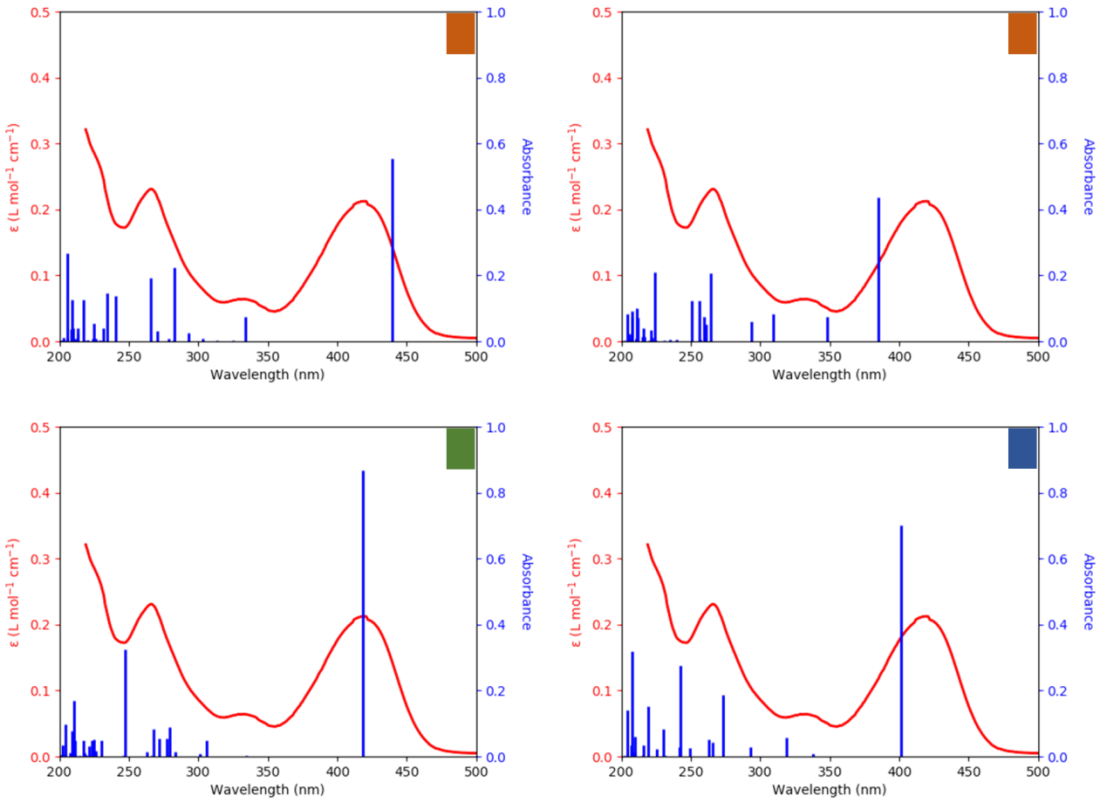

Figure 56 Overlap of the experimental UV–vis spectrum of the 1:1 complex between quercetin and the Ca^{II} cation (red curve) and the computed transitions (blue lines) for the (a) deprotonated α–hydroxyketo complex, (b) protonated α–hydroxyketo complex, (c) catechol complex deprotonated in 4', and (d) protonated β–hydroxyketo complex

Both the protonated and deprotonated α–hydroxyketo gave a good agreement with the experimental spectrum of the complex as well as the protonated β–hydroxyketo complex and

the catechol complex deprotonated in 4'. The two protonated α–hydroxyketo and β–hydroxyketo complex are not realistically plausible since a fluctuation in the pH is observed when the calcium chloride solution is added to the quercetin solution. Irrespective of this fact, the emission wavelengths were calculated for these two complexes. Table 15 reports the theoretical wavelengths for the four complexes to be compared with the wavelength of 580 nm.

Table 15 Theoretical emission wavelengths, λ(nm) for the listed complexes and the difference between the theoretical and experimental emission wavelength, ($|\Delta\lambda|$, nm)

Complex	Theoretical emission wavelength (λ, nm)	Difference between the calculated and the experimental emission wavelength ($|\Delta\lambda|$, nm)
Deprotonated α–hydroxyketo	526	54
Protonated α–hydroxyketo	471	109
Protonated β–hydroxyketo	465	115
Diol deprotonated in 4'	482	98

Based on the additional information obtained from fluorescence spectroscopy, it was evidenced that the only complex that had a good agreement both for the absorbance and emission spectra is the deprotonated α–hydroxyketo site.

The QT–AIM results of Ca^{II}–quercetin complex are represented in Figure 57 and Table 16 to learn more about the topology of the electronic density of this system. The comparison of this data with that of the Ca^{II}–morin complex clearly shows that the charges and nature of the Ca–O bond do not change much (only negligible variations) when another ligand in used. Once again the Ca–O bond is thought to be ionic based on the positive value of the Laplacian of the electronic density at the BCP. The small value of the electronic density suggests that the electronic delocalisation is very minimal at the BCP. The value of $-G_b/V_b$ (greater than 1) shows that the kinetic energy contribution is higher than that of the potential energy density. This means that the kinetic energy density at the BCP of Mn–O is the leading contribution

compared to the potential energy density. Since G_b is thought to have a tendency to dilute electrons at the BCP, the iconicity of the Mn–O bond is further insinuated.

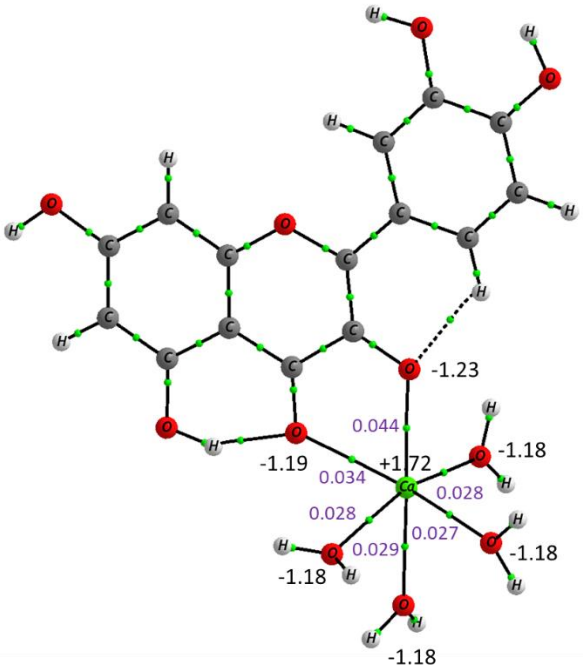

Figure 57 QT–AIM data of the Ca^{II}–quercetin complex showing the partial charges of the calcium atoms and the connected oxygens atoms as well as the electronic density value at the BCP

Table 16 Selected QTAIM charges (q, au) for the α–hydroxyketo complex, bond lengths (l, pm), electronic densities at the BCP (ρ_b, au), Laplacian of the electronic density at the BCP ($\nabla^2\rho_b$, au) and opposite to the ratio of the kinetic energy density to the potential energy density at the BCP ($-G_b/V_b$)

	α–hydroxyketo complex
$q(Ca^{II})$	+1.72
q(O3)	−1.23
q(O4)	–1.19
Ca–O3	
l	229.1
ρ_b	0.044
$\nabla^2\rho_b$	0.230
$-G_b/V_b$	1.105
Ca–O4	
l	239.4
ρ_b	0.034
$\nabla^2\rho_b$	0.174
$-G_b/V_b$	1.148

4.3.2 Ca^{II}–Luteolin system

The study of the formation of the Ca^{II}–luteolin complex is pretty much similar to that of the Mn^{II}–luteolin one. A considerable amount of the $CaCl_2$ solution was added, however, no visible change was observed on the absorption spectra. Finally, a lump of solid $CaCl_2$ was put directly in the reactor vessel. The resulting solution was stirred for a long time for all the solid to dissolve. Even after that, the Ca^{II} does not seem to fix itself to any of the two fixation sites on luteolin. It can be easily deduced that the methodology applied in this work to instigate the formation of the Ca^{II}–luteolin molecule is not adapted and that the reaction is not feasible. Once again, the importance of the hydroxyl group in position 3 to trigger the formation of the flavonoid complex is evidenced. If the complexation process was hard with quercetin, it seems logical that it would be even harder for luteolin.

CONCLUSION

The focus of this study was put on the reactivity of the multisite ligand, morin with zinc, manganese and calcium cations for the purpose of determining the preferential fixation site of the metal ions. Throughout this work, it was evidenced that morin was a good complexing agent due to the fact that the complexes were formed with greater ease compared to the two associated molecules, quercetin and luteolin. The complexing power of this flavonol was mainly attributed to the presence of a hydroxyl group in position 2', which forms an inter–ring hydrogen bond with the 3–OH group. This causes the formation of a new fixation site (diol) that has never been evoked in the literature beforehand.

The three elements belonging to the period 4 of the periodic table used in this study to complex with morin, quercetin and luteolin were chosen based on their electronic configuration. While calcium and zinc have their electronic shells fully filled ([Ar] $4s^2$ and [Ar] $3d^{10}$ $4s^2$ respectively), manganese possess a half–filled electronic shell ([Ar] $3d^5$ $4s^2$).

Table 17 contains the conditional complexation constant for all the reactions carried out. It was demonstrated that the three flavonoids under study has different complexation power with respect to each other.

Table 17 Summary of the conditional complexation constant (log β) and involved sites for each studied system

	Zinc	Manganese	Calcium
Morin (pH = 4.2)	1.50 α-hydroxyketo	4.83 diol/α-hydroxyketo	4.40 α-hydroxyketo
Quercetin (pH = 6.2)	4.41 α-hydroxyketo	5.71 α-hydroxyketo	1.05 α-hydroxyketo
Luteolin	–	–	–

Whatever the studied metal cation, luteolin has a very low or even non-existent complexing power. This fact evidences the importance of the presence of the hydroxyl group in position 3, present in quercetin and morin. It was observed that for all complexes of quercetin, the metal always binds to the α-hydroxyketo site. The 3-hydroxyl group is also involved in morin

in the fixation of the metal cation, either with the keto function or the hydroxyl group in position 2' depending on the nature of the metal. From the data obtained for morin and quercetin, it can be observed that the order of the complexing power differs:

Morin: $Mn^{II} > Ca^{II} >> Zn^{II}$

Quercetin: $Mn^{II} > Zn^{II} >> Ca^{II}$

These tendencies show that Mn^{II} always has the highest affinity for both ligands. However, even though Ca^{II} and Zn^{II} have the same chelating site (α-hydroxyketo) with morin and quercetin, it was surprising to see that the affinities of the two metal cations are inversed. Morin has a much higher complexing power towards Ca^{II} than quercetin. Indeed, considering that the experiments were not performed at the same pH, it can be noticed that a factor of 10^5 separates the computed stability constants. These unexpected results show the difficulty to investigate these chemical systems which present an uncontrolled behaviour. This is why it is important to carry out a complete study of each metal-flavonoid pair in order to determine their affinity as well as the structure of the complex (chelating site). The QT-AIM studies performed on all systems allow us to highlight the ionic character of the metal-oxygen bond formed upon complexation. Further investigations in this direction could be a way to get a unified and predictive vision on the studied systems.

While the fixation site involved in the complexation reaction with morin and quercetin was found to be the α–hydroxyketo for the zinc and calcium cations, a distinctive behaviour was observed with the manganese cations: the fixation site of the metal ion was the diol and maybe mixed with the α–hydroxyketo. It was also interesting to note the minor effect of the metal cation on the absorption spectrum of the complex except for the Mn^{II}–morin system. Indeed, the long wavelength absorption band of the latter is described by two calculated transitions for the diol complex.

These results led to enquire about the reactivity of another ligand possessing only the diol and the α–hydroxyketo site to verify whether a similar behaviour to morin is observed. This is the upcoming work of a new thesis that will deal with 2',3–dihydroxyflavone.

PHOTOPHYSICS OF POLYCYCLIC AROMATIC HYDROCARBONS

CHAPTER 1:
CONTEXT

1.1 Environmental aspect

Polycyclic aromatic hydrocarbons, popularly known as PAHs are world-class pollutants[136]. Their presence can be detected in the interstellar medium[137] as well as in the Earth atmosphere. They can be formed by natural sources posterior to phenomena such as forest wildfires, volcanic eruptions, vegetative decay and seepage of petroleum. Their main source in the Earth atmosphere is due to anthropogenic means. The latter encompasses emission from catalytic chimneys, aluminium, coke and asphalt production, residential heating systems amongst many other human actions. In general, polycyclic aromatic hydrocarbons are produced following the incomplete combustion of organic matter (most of the time coal, oil and petroleum) and they form a large group of compounds that have carcinogenic, mutagenic and toxic properties. They are ubiquitous compounds, present in the air, soil and water[138,139]. PAHs having up to six aromatic rings are designated to be small PAHs and those possessing seven rings or more are large PAHs[140].

1.1.1 Location of PAHs

Within the framework of the LabeX CaPPA, a great importance is given to the study of aerosols, soot and other related compounds in the atmosphere to review and devise ways to improve the quality of air. Aerosols form part of the European list of atmospheric polluting

[136] Lee, M. (2014). *Analytical Chemistry of Polycyclic Aromatic Compounds.* Retrieved from http://qut.eblib.com.au/patron/FullRecord.aspx?p=1155754

[137] Chen, T. (2018). Formation of Covalently Bonded Polycyclic Aromatic Hydrocarbons in the Interstellar Medium. *The Astrophysical Journal*, *866*(2), 113.

[138] Baklanov, A., Hänninen, O., Slørdal, L. H., Kukkonen, J., Bjergene, N., Fay, B., … Ødegaard, V. (2007). Integrated systems for forecasting urban meteorology, air pollution and population exposure. *Atmospheric Chemistry and Physics*, *7*(3), 855–874.

[139] Menzie, C. A., Potocki, B. B., & Santodonato, J. (1992). Exposure to carcinogenic PAHs in the environment. *Environmental Science & Technology*, *26*(7), 1278–1284.

[140] Abdel-Shafy, H. I., & Mansour, M. S. M. (2016). A review on polycyclic aromatic hydrocarbons: Source, environmental impact, effect on human health and remediation. *Egyptian Journal of Petroleum*, *25*(1), 107–123.

agents[141]. It is known for a fact, excluding the interstellar environment, that the atmosphere is the medium where PAHs are mostly detected. These molecules have the ability to remain in the gas state in the air or be adsorbed onto particles of aerosols and other particulate of matter present in air[142,143,144]. The concentration of PAHs depends on their size. It has been demonstrated that the higher the molecular weight of the compounds, the lower is their vapour pressure and hence, the easier they cling to the particulate matter in air. Therefore, it is highly probable to find big-sized polycyclic aromatic hydrocarbons on aerosols whereas the small ones remain in the gas state in the atmosphere.

Though in smaller quantities compared to their presence in the atmosphere, PAHs are deposited and accumulated in soil[145,146]. As they are bound to the soil particles, small-sized PAHs are most likely to be mobile. They can fit inside the pores of the particles and spread throughout the medium with greater ease[147]. The problem arises when there is an accumulation of polycyclic aromatic hydrocarbons in the soil because they will eventually be absorbed in plants through the roots and be distributed to all the organs. Their toxicity is further accentuated in the presence of ultraviolet light since the latter breaks down the molecules into radically-active species[148]. The formed radicals easily bind to other useful compounds in the plant cells, which decreases their availability and eventually leads to cell death. Polycyclic aromatic hydrocarbons can be adsorbed on fine-grained organic rich

[141] Borrás, E., & Tortajada-Genaro, L. A. (2007). Characterisation of polycyclic aromatic hydrocarbons in atmospheric aerosols by gas chromatography–mass spectrometry. *Analytica Chimica Acta*, *583*(2), 266–276.
[142] Zhang, Y., & Tao, S. (2009). Global atmospheric emission inventory of polycyclic aromatic hydrocarbons (PAHs) for 2004. *Atmospheric Environment*, *43*(4), 812–819.
[143] Ravindra, K., Sokhi, R., & Vangrieken, R. (2008). Atmospheric polycyclic aromatic hydrocarbons: Source attribution, emission factors and regulation. *Atmospheric Environment*, *42*(13), 2895–2921.
[144] Wang, Z., Ren, P., Sun, Y., Ma, X., Liu, X., Na, G., & Yao, Z. (2013). Gas/particle partitioning of polycyclic aromatic hydrocarbons in coastal atmosphere of the north Yellow Sea, China. *Environmental Science and Pollution Research*, *20*(8), 5753–5763.
[145] Masih, A., & Taneja, A. (2006). Polycyclic aromatic hydrocarbons (PAHs) concentrations and related carcinogenic potencies in soil at a semi-arid region of India. *Chemosphere*, *65*(3), 449–456.
[146] Cachada, A., Pato, P., Rocha-Santos, T., da Silva, E. F., & Duarte, A. C. (2012). Levels, sources and potential human health risks of organic pollutants in urban soils. *Science of The Total Environment*, *430*, 184–192.
[147] Riccardi, C., Di Filippo, P., Pomata, D., Di Basilio, M., Spicaglia, S., & Buiarelli, F. (2013). Identification of hydrocarbon sources in contaminated soils of three industrial areas. *Science of The Total Environment*, *450–451*, 13–21.
[148] Yu, H. (2002). Environmental carcinogenic polycyclic aromatic hydrocarbons: photochemistry and phototoxicity. *Journal of Environmental Science and Health, Part C*, *20*(2), 149–183.

molecules that are deposited on water surfaces such as lakes, rivers and oceans[149,150]. They are fanned out with the water current or are gathered in sediments[151]. Their toxic character deeply affects the aquatic life as studies revealed that the concentration of PAHs in fish and shellfish was higher than from the environment it was taken[140]. With time, microorganisms present in the soil and sediments reduce the PAHs into smaller compounds and this microbial degradation process can last for weeks to months.

1.1.2 Impact of PAHs

The negative impact of PAHs affects not only plants but the human health also. Since they are present in all the media that surrounds us, they can easily be deposited on our body from the air or when our skin is in contact with surfaces containing those compounds. The latter can also be inhaled and the source of inhalation can vary from a small smoke from tobacco to large fumes from industries and fire sources. Another way through which humans are contaminated by polycyclic aromatic hydrocarbons is when the pollutants are ingested through plants and animals that were previously contaminated. Smoked foods have PAHs molecules amassed on them when they are grilled[152]. Unless a person is constantly exposed to a PAH-rich environment, a small dose of PAH is not deadly for a human being. Most of the time, the compounds are excreted by urine or faeces[153]. However, since polycyclic aromatic hydrocarbons are fat-soluble, they are prone to be stocked in body fat. The organs that are more inclined to store PAHs are those that are rich in adipose tissue like the kidneys and the liver. Since the liver and kidneys have a tendency to store the PAH molecules, the increased

[149] Wolska, L., Mechlińska, A., Rogowska, J., & Namieśnik, J. (2012). Sources and Fate of PAHs and PCBs in the Marine Environment. *Critical Reviews in Environmental Science and Technology*, *42*(11), 1172–1189.
[150] Guitart, C., García-Flor, N., Bayona, J. M., & Albaigés, J. (2007). Occurrence and fate of polycyclic aromatic hydrocarbons in the coastal surface microlayer. *Marine Pollution Bulletin*, *54*(2), 186–194.
[151] Marini, M., & Frapiccini, E. (2014). Do lagoon area sediments act as traps for polycyclic aromatic hydrocarbons? *Chemosphere*, *111*, 80–88.
[152] Lee, J.-G., Kim, S.-Y., Moon, J.-S., Kim, S.-H., Kang, D.-H., & Yoon, H.-J. (2016). Effects of grilling procedures on levels of polycyclic aromatic hydrocarbons in grilled meats. *Food Chemistry*, *199*, 632–638.
[153] Campo, L., Rossella, F., Pavanello, S., Mielzynska, D., Siwinska, E., Kapka, L., … Fustinoni, S. (2010). Urinary profiles to assess polycyclic aromatic hydrocarbons exposure in coke-oven workers. *Toxicology Letters*, *192*(1), 72–78.

concentration of the latter is more likely to result in liver and kidney failure[154]. The symptoms of a prolonged exposure to PAHs can vary from simply an eye irritation, nausea, vomiting and diarrhoea to the increased risk of contracting cancerous diseases attacking the lungs, skin and bladder[155,156]. The immune system becomes defective and the person is inclined to develop severe breathing problems.

1.1.3 Uses of PAHs

The PAH can be used as organic tracers to help identify the origin of combustion sources[157]. Li et al. showed that the chemical signature of a series of known PAHs can be used to differentiate between residential wood combustion, gasoline spark ignition emissions and diesel engine emissions. This technique is useful as long as the signature of each PAH is available[158]. Several scientific works used certain PAHs and their ratios as markers for determining their various sources[159,160]. For example, benzo[*a*]pyrene, pyrene and chrysene are compounds that are detected in diesel engine emissions while benzo[*g,h,i*]perylene and indene[*1,2,3-c,d*]pyrene are characteristics of gasoline engine emissions[161]. They are sometimes used as intermediates in pharmaceutical and agricultural synthesis, lubricants and

[154] Karami, S., Boffetta, P., Brennan, P., Stewart, P. A., Zaridze, D., Matveev, V., … Moore, L. E. (2011). Renal Cancer Risk and Occupational Exposure to Polycyclic Aromatic Hydrocarbons and Plastics: *Journal of Occupational and Environmental Medicine*, *53*(2), 218–223.
[155] Unwin, J., Cocker, J., Scobbie, E., & Chambers, H. (2006). An Assessment of Occupational Exposure to Polycyclic Aromatic Hydrocarbons in the UK. *The Annals of Occupational Hygiene*, *50*(4), 395–403.
[156] Caricchia, A. M., Chiavarini, S., & Pezza, M. (1999). Polycyclic aromatic hydrocarbons in the urban atmospheric particulate matter in the city of Naples (Italy). *Atmospheric Environment*, *33*(23), 3731–3738.
[157] Stout, S. A., & Wang, Z. (2016). Chemical fingerprinting methods and factors affecting petroleum fingerprints in the environment. In *Standard Handbook Oil Spill Environmental Forensics* (pp. 61–129).
[158] Li, C. K., & Kamens, R. M. (1993). The use of polycyclic aromatic hydrocarbons as source signatures in receptor modeling. *Atmospheric Environment. Part A. General Topics*, *27*(4), 523–532.
[159] Kulkarni, P., & Venkataraman, C. (2000). Atmospheric polycyclic aromatic hydrocarbons in Mumbai, India. *Atmospheric Environment*, *34*(17), 2785–2790.
[160] Liu, J., Li, J., Lin, T., Liu, D., Xu, Y., Chaemfa, C., … Zhang, G. (2013). Diurnal and nocturnal variations of PAHs in the Lhasa atmosphere, Tibetan Plateau: Implication for local sources and the impact of atmospheric degradation processing. *Atmospheric Research*, *124*, 34–43.
[161] Norramit, P., Cheevaporn, V., Itoh, N., & Tanaka, K. (2005). Characterization and Carcinogenic Risk Assessment of Polycyclic Aromatic Hydrocarbons in the Respirable Fraction of Airborne Particles in the Bangkok Metropolitan Area. *JOURNAL OF HEALTH SCIENCE*, *51*(4), 437–446.

thermosetting plastics[162]. Naphthalene is thought-out to be of the most famous PAH as it is sold worldwide as moth repellent. Anthracene acts as reactant in dyes, explosives, plastics and lubricants. PAHs are also found at low concentrations in some special-purpose skin products and shampoos that contain coal tars[163]. Nevertheless, their uses are insignificant compared to the countless damages they cause. Most of the time polycyclic aromatic hydrocarbons are the principal subject of several research works due to the threat that they pose to the environment.

1.1.4 Removal of PAHs

Nowadays, the impact of pollution is becoming more and more conspicuous and the need for methods to get rid of PAHs is crucial. Some primary steps have already been established, for example, the decrease of the PAH concentration in extender oils that are often used in car tyres[164]. Several pro-environmental laws against polycyclic aromatic hydrocarbons were voted[165,166,167]. There are two main paths envisaged nowadays to eliminate these pollutants. The molecules can either be degraded or be removed from the atmosphere. Polycyclic aromatic hydrocarbons can be subjected to three types of degradation: biodegradation[168],

[162] Casarett, L. J., Doull, J., & Klaassen, C. D. (2008). *Casarett and Doull's toxicology: The basic science of poisons*.

[163] Lim, L., Okouchi, Y., & Takeuchi, T. (2007). On-line preconcentration of trace carcinogenic polycyclic aromatic hydrocarbons (PAHs) in microcolumn liquid chromatography via large volume injection. *Talanta*, *72*(5), 1600–1608.

[164] Lü, Y., Pan, H., & Yin, J. (2012). Removal of the Polycyclic Aromatic to Produce Eco-friendly Aromatic-rich Rubber Extender Oils. *Petroleum Science and Technology*, *30*(13), 1335–1342.

[165] Commission Regulation (EU) No 835/2011 of 19 August 2011 amending Regulation (EC) No 1881/2006 as regards maximum levels for polycyclic aromatic hydrocarbons in foodstuffs. *Official Journal of the European Union, L 215*/4, https://eur-lex.europa.eu/legal-content/EN/TXT/PDF/?uri=CELEX:32011R0835&from=EN

[166] COMMISSION REGULATION (EU) No 1272/2013 of 6 December 2013 amending Annex XVII to Regulation (EC) No 1907/2006 of the European Parliament and of the Council on the Registration, Evaluation, Authorisation and Restriction of Chemicals (REACH) as regards polycyclic aromatic hydrocarbons. *Official Journal of the European Union, L 328/69,* https://eur-lex.europa.eu/legal-content/EN/TXT/PDF/?uri=CELEX:32013R1272&from=fr

[167] COMMISSION RECOMMENDATION of 4 February 2005 (EC) No 2005/108 on the further investigation into the levels of polycyclic aromatic hydrocarbons in certain foods. *Official Journal of the European Union, L34/43, https://www.fsai.ie/uploadedFiles/Commission_Recommendation_2005_108_EC.pdf*

[168] NATO Advanced Research Workshop on the Utilization of Bioremediation to Reduce Soil Contamination: Problems and Solutions, Šašek, V., Glaser, J. A., & Baveye, P. (2003). *The utilization of*

chemical degradation or photolysis. However, the three methods are successful only when some conditions are respected. If we take the biodegradation technique for example, it is important that the PAHs should be bioavailable for the bacteria to attack the molecules and this is the case only when the PAH is in gas state or when it is dissolved[169,170,171,172]. The molecules that are adsorbed onto the particulate matter are not bioavailable as the enzymes that break them down cannot access them[173,174]. In addition to that, enzymatic reactions are not reliable in this case because if there are other chemicals present in the medium that may act as inhibitors. The bioavailability does not depend solely on the environment of the PAHs but also on their solubility and, hence the size of the PAHs. Chemical degradation is less popular than biodegradation as this technique requires the use of chemicals to break down the PAH molecules. Most of the time, strong oxidising agents are used; these compounds or their degradation products can be harmful for the environment. Chemical degradation includes homogenous gas-phase particle reactions and heterogeneous reactions on particles[175]. Finally, the third degradation technique tried was that of photolysis by exciting

bioremediation to reduce soil contamination: Problems and solutions : proceedings of the NATO Advanced Workshop on the Utilization of Bioremediation to Reduce Soil Contamination--Problems and Solutions, held in Prague, Czech Republic, from 14 to 19 June 2000. Retrieved from http://site.ebrary.com/id/10655065

[169] Cerniglia, C. E. (2003). Recent Advances in the Biodegradation of Polycyclic Aromatic Hydrocarbons by Mycobacterium Species. In V. Šašek, J. A. Glaser, & P. Baveye (Eds.), *The Utilization of Bioremediation to Reduce Soil Contamination: Problems and Solutions* (pp. 51–73).

[170] Dandie, C. E., Thomas, S. M., Bentham, R. H., & McClure, N. C. (2004). Physiological characterization of Mycobacterium sp. Strain 1B isolated from a bacterial culture able to degrade high-molecular-weight polycyclic aromatic hydrocarbons. *Journal of Applied Microbiology*, *97*(2), 246–255.

[171] Fredslund, L., Sniegowski, K., Wick, L. Y., Jacobsen, C. S., De Mot, R., & Springael, D. (2008). Surface motility of polycyclic aromatic hydrocarbon (PAH)-degrading mycobacteria. *Research in Microbiology*, *159*(4), 255–262.

[172] Uyttebroek, M., Vermeir, S., Wattiau, P., Ryngaert, A., & Springael, D. (2007). Characterization of Cultures Enriched from Acidic Polycyclic Aromatic Hydrocarbon-Contaminated Soil for Growth on Pyrene at Low pH. *Applied and Environmental Microbiology*, *73*(10), 3159–3164.

[173] Hatzinger, P. B., & Alexander, Martin. (1995). Effect of Aging of Chemicals in Soil on Their Biodegradability and Extractability. *Environmental Science & Technology*, *29*(2), 537–545.

[174] Kim, S.-J., Kweon, O., Jones, R. C., Freeman, J. P., Edmondson, R. D., & Cerniglia, C. E. (2007). Complete and Integrated Pyrene Degradation Pathway in Mycobacterium vanbaalenii PYR-1 Based on Systems Biology. *Journal of Bacteriology*, *189*(2), 464–472.

[175] Schauer, C., Niessner, R., & Pöschl, U. (2003). Polycyclic Aromatic Hydrocarbons in Urban Air Particulate Matter: Decadal and Seasonal Trends, Chemical Degradation, and Sampling Artifacts. *Environmental Science & Technology*, *37*(13), 2861–2868.

the PAHs with a light source[176]. Low molecular weight molecules and those which are less stable with respect to the others are more prone to degrade due to their bioavailability.

Instead of decomposing the polycyclic aromatic hydrocarbons, they could simply be removed from the environment by dry or wet deposition. With respect to the atmospheric conditions, dry deposition is possible when the PAHs stick onto the particulate matter. Obviously, PAHs with a higher molecular weight will land more quickly[177]. Wet deposition, contrarily to dry deposition, consists in precipitating the PAHs whether they are in the atmospheric particles or in the gas state[178].

1.1.5 Identification of PAHs

Once the molecules of polycyclic aromatic hydrocarbons are removed from their respective environment, we should be able to fall back on some analytical techniques in order to identify individually the PAHs collected. As of today, there is a lack of pure PAH standards which makes it difficult to retrieve individual PAH signatures from samples[158]. The most popular PAH extraction technique is the Soxhlet method which consists in separating the desired compounds from a solid mixture. However, it requires a large amount of solvent and the experiment can last for a very long time (hours or days) during which the samples may degrade. Borras et al. investigated several filters, extraction and analytical techniques to identify and quantify polycyclic aromatic hydrocarbons in aerosols. They optimised their experimental methodology by using quartz filters to collect the PAH molecules and then, the latter were isolated by the ultrasonic extraction. Finally, GC-MS was considered to be the most appropriate analytical technique since the concentration of PAH in aerosols is quite low[141]. In another paper, they also tested the GC-MS/MS technique for the determination of eighteen

[176] Sabaté, J., Bayona, J. M., & Solanas, A. M. (2001). Photolysis of PAHs in aqueous phase by UV irradiation. *Chemosphere*, *44*(2), 119–124.
[177] Chang, K.-F., Fang, G.-C., Lu, C., & Bai, H. (2003). Imating PAH Dry Deposition by Measuring Gas and Particle Phase Concentrations in Ambient Air. *Aerosol and Air Quality Research*, *3*(1), 41–51.
[178] Lim, L., Wurl, O., Karuppiah, S., & Obbard, J. P. (2007). Atmospheric wet deposition of PAHs to the sea-surface microlayer. *Marine Pollution Bulletin*, *54*(8), 1212–1219.

polycyclic aromatic hydrocarbons in soil[179]. Hawthorne et al. worked on the comparison of different extraction methods to determine the most suitable pathway to extract and detect specific PAH compounds from the contaminated soil of a former gas plant site. They concluded by proving that supercritical fluid extraction and subcritical water extraction were selective methods which were more suitable compared to the techniques requiring organic solvents (Soxhlet and pressurised liquid extraction), as proven by the analysis conducted by GC-MS (gas chromatography-mass spectrometry) and GC-FID (gas chromatography-flame ionisation detection)[180]. Another spectroscopic technique that is often employed is electronic spectroscopy. Some PAHs can be identified from their unique UV-vis spectrum based on their size. It is common for PAHs to form charge-transfer complexes with themselves or with amines, for example and are detected by fluorescence spectroscopy[181]. Indeed, PAHs have very interesting fluorescent features, which will be discussed in the next part.

[179] Shang, D., Kim, M., & Haberl, M. (2014). Rapid and sensitive method for the determination of polycyclic aromatic hydrocarbons in soils using pseudo multiple reaction monitoring gas chromatography/tandem mass spectrometry. *Journal of Chromatography A*, *1334*, 118–125.
[180] Hawthorne, S. B., Grabanski, C. B., Martin, E., & Miller, D. J. (2000). Comparisons of Soxhlet extraction, pressurized liquid extraction, supercritical fluid extraction and subcritical water extraction for environmental solids: Recovery, selectivity and effects on sample matrix. *Journal of Chromatography A*, *892*(1–2), 421–433.
[181] Goodpaster, J. V., Harrison, J. F., & McGuffin, V. L. (2002). Ab Initio Study of Selective Fluorescence Quenching of Polycyclic Aromatic Hydrocarbons. *The Journal of Physical Chemistry A*, *106*(44), 10645–10654.

1.2 Dual fluorescence

From the family of organic compounds, polycyclic aromatic hydrocarbons are formed when two or more aromatic rings are bonded in linear, angular or cluster patterns[182], with a network of delocalised electrons over the whole molecule. Clustered polycyclic aromatic hydrocarbons are formed when the aromatic rings are fused in a circular way like benzo[*g,h,i*]perylene. Linear PAHs are compounds where the benzene rings are aligned side by side as we can observe for anthracene for example. Angular PAHs, such as dibenz[*a,h*]anthracene are those whose structure consist of a mixture of linear and clustered aromatic rings. The different types of PAHs are illustrated in Figure 58.

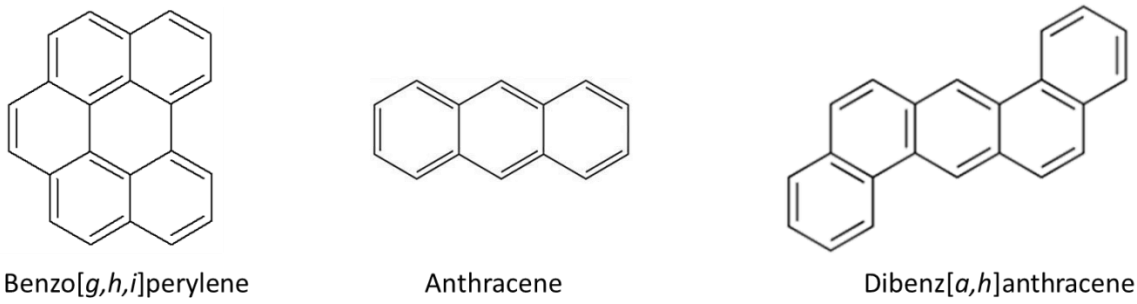

Figure 58 Examples of clustered PAHs (benzo[*g,h,i*]perylene), linear PAHs (anthracene) and angular PAHs (dibenz[*a,h*]anthracene)

In this study, the main focus will be on clustered PAHs. As their name suggests, PAHs are constituted solely of carbon and hydrogen atoms. Concerning their nomenclature, it has evolved throughout time as big molecules tend to have burdensome names[183]. A NIST report has been revised in 2011 to index most the the PAHs known[184].

In general, PAHs are colourless, white or pale yellow solids. They have a low aqueous solubility and this solubility decreases even more with additional benzene rings on the molecules. On

[182] Arey, J., & Atkinson, R. (2003). Photochemical Reactions of PAHs in the Atmosphere. In P. E. T. Douben (Ed.), *Ecological and Environmental Toxicology Series* (pp. 47–63).
[183] Ehrenhauser, F. S. (2015). PAH and IUPAC Nomenclature. *Polycyclic Aromatic Compounds*, *35*(2–4), 161–176.
[184] Allison, T. (2013). *NIST Polycyclic Aromatic Hydrocarbon Structure Index, NIST Standard Reference Database 204*.

the other side, they are very lipophilic. Due to their planar structure, some inter-molecular interactions (such as π stacking) emerge that explain their high melting and boiling points. They are stable compounds and are resistant to heat and corrosion in addition to have good conductivity properties. Bigger PAHs are more resistant to oxidation and reduction[185].

1.2.1 Optical properties of PAHs

One of the various processes that a molecule undergoes is luminescence, which concerns the emission of light from any molecule from its excited states. Of all the types of luminescence that are possible, the emphasis will be put on photoluminescence. A molecule subjected to electromagnetic radiation is capable of partially absorbing photons which causes its passage into an excited state. Succeeding to this step, the molecules are relaxed back to their initial position. Depending on the nature of the excited state, there are several possible emission phenomena that can be observed. When the excited states involved in the S_1-S_0 transition, the emission is characterised as fluorescence. However, it is also possible to have emission that originate from the triplet excited states despite the fact that it is spin-forbidden and then the emission is qualified as phosphorescence. Figure 59 below is the Jablonski diagram which summarises the main transitions that are of interest in this study[186].

[185] Achten, C., & Andersson, J. T. (2015). Overview of Polycyclic Aromatic Compounds (PAC). *Polycyclic Aromatic Compounds*, *35*(2–4), 177–186.
[186] Frackowiak, D. (1988). The Jablonski diagram. *Journal of Photochemistry and Photobiology B: Biology*, *2*(3), 399.

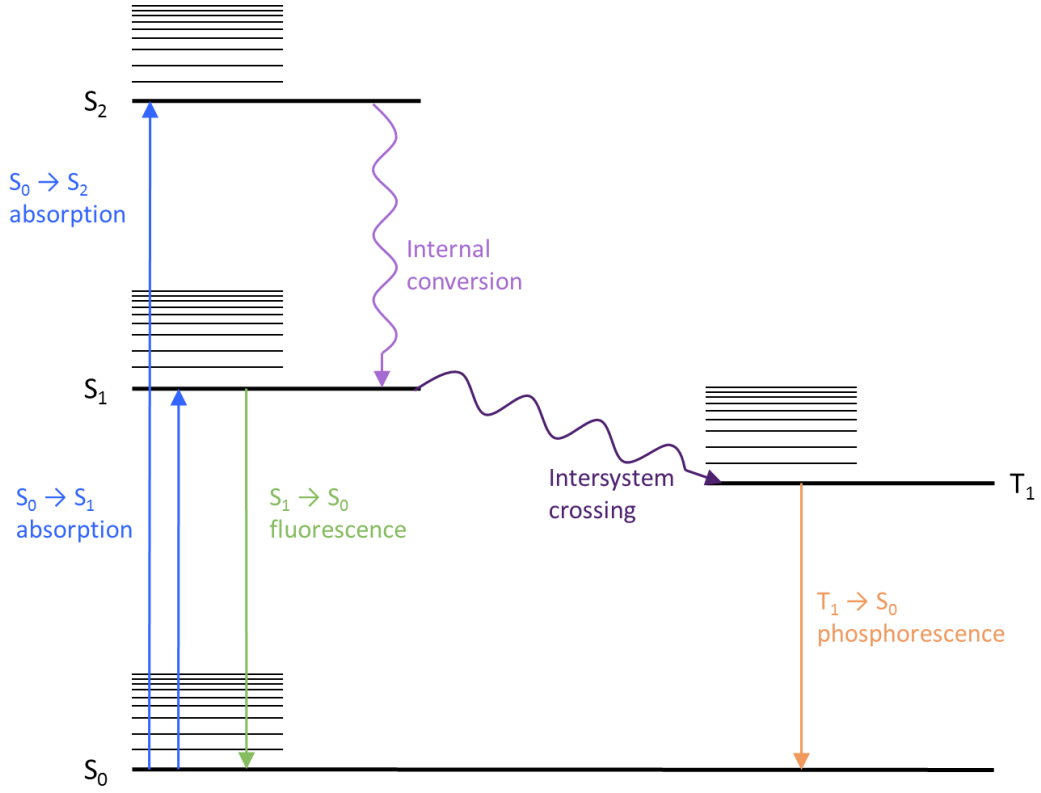

Figure 59 The Jablonski diagram

Kasha rule is a principle in the photochemistry of electronically excited molecules. The rule states that photon emission (fluorescence or phosphorescence) occurs in appreciable yield only from the lowest excited state of a given multiplicity. Usually, an excited molecule relaxes back to its ground state with emission at a specific wavelength. Dual fluorescence is a rare occurrence where two emission bands can be observed on an emission spectrum, phenomenon considered as an anomalous behaviour.

1.2.2 Possible dual fluorescence mechanisms

There are three main mechanisms that can account for the dual fluorescence of a compound. One of them is known as the Excited State Intramolecular Proton Transfer (ESIPT) and this usually happens when a Brönsted donor and acceptor are in close proximity in the molecule, facilitating the proton transfer. When this mechanism occurs, there is a high probability that two species are formed at the excited state by the rearrangement of the excited molecule as shown in Figure 60. The quercetin molecule has been studied in the first part of this thesis.

This compound is well-known to present an ESIPT and a dual fluorescence with two emission bands relative to the normal form (N) and tautomer form (T), respectively. Several scientific works have been published related to ESIPT mechanisms and are commented below.

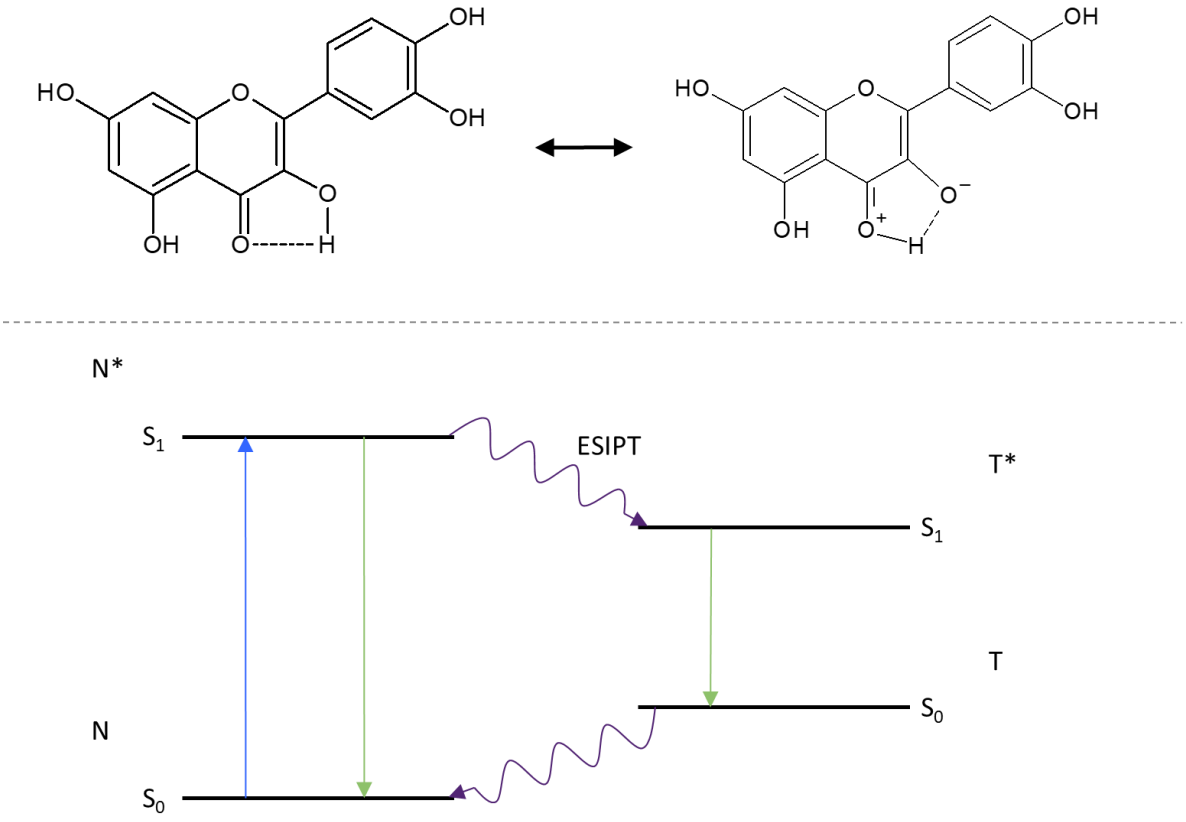

Figure 60 Intramolecular proton transfer on a molecule of quercetin (on the top) and the ESIPT mechanism (on the bottom)

The ESIPT mechanism, therefore, corresponds to the fluorescence band of the $S_1 \rightarrow S_0$ transition for each species at the excited state, which is compliant with the Kasha rule. ESIPT molecules have proved to be useful in many applications, notably, novel materials for optoelectronics[187], molecular probing of materials and liquid solvents[188], chemical sensing[189],

[187] Kwon, J. E., & Park, S. Y. (2011). Advanced Organic Optoelectronic Materials: Harnessing Excited-State Intramolecular Proton Transfer (ESIPT) Process. *Advanced Materials*, *23*(32), 3615–3642.
[188] Kimura, Y., Fukuda, M., Suda, K., & Terazima, M. (2010). Excited State Intramolecular Proton Transfer Reaction of 4'- *N* , *N* -Diethylamino-3-hydroxyflavone and Solvation Dynamics in Room Temperature Ionic Liquids Studied by Optical Kerr Gate Fluorescence Measurement. *The Journal of Physical Chemistry B*, *114*(36), 11847–11858.
[189] Wu, Y., Peng, X., Fan, J., Gao, S., Tian, M., Zhao, J., & Sun, S. (2007). Fluorescence Sensing of Anions Based on Inhibition of Excited-State Intramolecular Proton Transfer. *The Journal of Organic Chemistry*, *72*(1), 62–70.

bio sensing[190], cell imaging[191] and light emitting diode materials[192]. An example of a molecule exhibiting the ESIPT mechanism is that of doxorubicin hydrochloride (anticancer drug) and the interesting fact is that the dual fluorescence observed is dependent on the excitation wavelength. On its absorbance spectrum, two bands at 480 nm and 346 nm are observed. When the molecule is excited at 480 nm, a single fluorescence band is recorded on the emission spectrum. However, when 346 nm is chosen as the excitation wavelength, a dual fluorescence is seen. The latter is believed to originate from an intramolecular double proton transfer in the ground and excited states from the keto-enol tautomeric forms. Time-resolved emission spectroscopy and DFT results confirmed the presence of more than one species at the excited state[193]. Germino et al. studied the salicylidene-5-chloroaminepyridine molecule because of its dual emission due to ESIPT (proximity of the hydrogen and iminic group). The molecule emitted a dual emission depending on the solvent used that was characterised using FTIR, cyclic voltammetry, mass spectrometry, single-crystal X-Ray Diffraction, DFT and TD-DFT. As a matter of fact, in DMSO an equilibrium is seen between the keto and enol forms. However, only the enol species is identified in methanol because of the formation of hydrogen bonds between the molecule and methanol, stabilizing the enol tautomer[194]. The paper of Tasaki et al. concerned the chemical modification of a molecule for it to exhibit dual fluorescence according to the ESIPT mechanism. Substituents were added to the analysed molecule in order to have a hydroxyl and carbonyl group close to each other. Depending on the position of the substitution of the π-extension, the energy of the excited state of the

[190] Enander, K., Choulier, L., Olsson, A. L., Yushchenko, D. A., Kanmert, D., Klymchenko, A. S., … Altschuh, D. (2008). A Peptide-Based, Ratiometric Biosensor Construct for Direct Fluorescence Detection of a Protein Analyte. *Bioconjugate Chemistry*, *19*(9), 1864–1870.

[191] Oncul, S., Klymchenko, A. S., Kucherak, O. A., Demchenko, A. P., Martin, S., Dontenwill, M., … Mély, Y. (2010). Liquid ordered phase in cell membranes evidenced by a hydration-sensitive probe: Effects of cholesterol depletion and apoptosis. *Biochimica et Biophysica Acta (BBA) - Biomembranes*, *1798*(7), 1436–1443.

[192] Tarkka, R. M., Zhang, X., & Jenekhe, S. A. (1996). Electrically Generated Intramolecular Proton Transfer: Electroluminescence and Stimulated Emission from Polymers. *Journal of the American Chemical Society*, *118*(39), 9438–9439.

[193] Rana, D. K., Dhar, S., Sarkar, A., & Bhattacharya, S. C. (2011). Dual Intramolecular Hydrogen Bond as a Switch for Inducing Ground and Excited State Intramolecular Double Proton Transfer in Doxorubicin: An Excitation Wavelength Dependence Study. *The Journal of Physical Chemistry A*, *115*(33), 9169–9179.

[194] Germino, J. C., Barboza, C. A., Quites, F. J., Vazquez, P. A. M., & Atvars, T. D. Z. (2015). Dual Emissions of Salicylidene-5-chloroaminepyridine Due to Excited State Intramolecular Proton Transfer: Dynamic Photophysical and Theoretical Studies. *The Journal of Physical Chemistry C*, *119*(49), 27666–27675.

normal form was decreased while that of the tautomer remained unchanged, achieving an energetically balanced excited state with dual fluorescence emission and hence, favouring the double emission[195].

When the principle of dual fluorescence is evoked, two other mechanisms are also possible, which corresponds to emission coming from both the S_1 and the S_2 states. This phenomenon is not very common because it does not respect the Kasha rule. Nevertheless, it can still be visible on fluorescence spectra. One of them (Anti Kasha mechanism 1 on the left of Figure 61) shows the first two electronic excited states close to one another, with a forbidden transition originating from S_1. The vibrational states of the S_1 and S_2 states are sure to overlap due to the small energy gap for vibronic coupling and a thermal equilibrium is established. There is a high probability that the population is distributed in such a way that there is a major emission coming from the S_2 excited state and a minor one from the S_1 state. Unlike the ESIPT mechanism, there is only one species present in the environment at the excited states. On the right of Figure 61, we are confronted to the third case scenario where the first two excited states are well-separated, in such a way that vibronic coupling is not an event that can be considered (Anti Kasha mechanism 2). When this phenomenon takes effect, there cannot be a redistribution of the population of the two excited states. That being said, the only possible way to have a dual fluorescence is when both the S_1 and S_2 states are populated individually. Some examples illustrating these two processes are given below.

[195] Tasaki, S., Momotake, A., Kanna, Y., Sato, T., Nishimura, Y., & Arai, T. (2015). Producing a dual-fluorescent molecule by tuning the energetics of excited-state intramolecular proton transfer. *Photochemical & Photobiological Sciences*, *14*(10), 1864–1871.

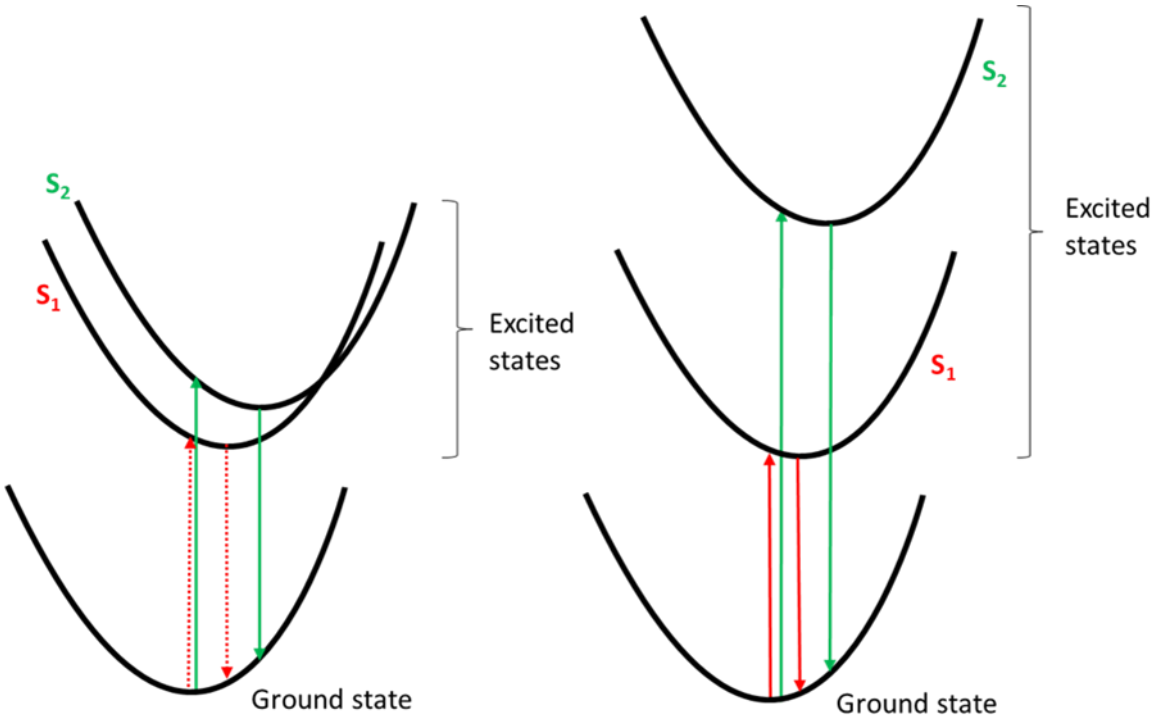

Figure 61 Two mechanisms that explains the presence of dual fluorescence when there is emission from the first and second excited states

Brancato et al. (Figure 62) observed an anti-Kasha dual fluorescence on a derivative of the coumarin molecule.

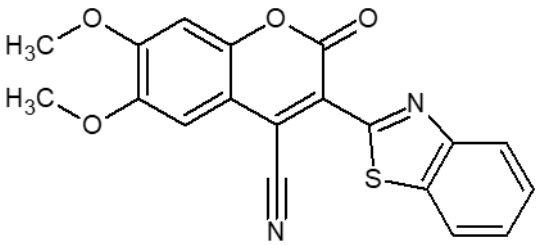

Figure 62 Structure of the derivative of coumarin studied by Brancato et al.

They were able to confirm their hypothesis since the structure of the molecule upon excitation and emission did not change a lot. In addition, there is a small energy difference between the S_1 and S_2 and a fast internal conversion of 200 fs was recorded between these two states,

leading to simultaneous decay from the two excited states[196]. The proximity of the two excited states could allow a thermic equilibrium that leads to a dual fluorescence (AK 1).

Another molecule known to emit a dual fluorescence is graphene oxide[197], frequently used for optoelectronic applications. Indeed, it was shown that the dual fluorescence of graphene oxide was dependent on its concentration, the excitation wavelength and the pH value of the solution. The blue emission recorded at 400 nm corresponded to a n → π* transition and the band is quite sharp. Its formation is favoured by a low concentration of graphene oxide, a short excitation wavelength and high pH value. One of the emitting components of the blue emission is pH sensitive which is useful for application in sensing H^+ as well as fluorescence lifetime imaging. The second emission band located at 700 nm is broader and is attributed to a π → π* transition[198]. As the emission wavelengths depend on the excitation ones, the AK 2 mechanism is presumed. In some studies though, only a single emission was detected[199,200]. The reasons for this observation were because the emission selected was at wavelengths longer than that of the blue emission and also due to the fact that the absorption at the emission wavelength was too high, resulting in more than 90% of the blue emission to be reabsorbed.

[196] Brancato, G., Signore, G., Neyroz, P., Polli, D., Cerullo, G., Abbandonato, G., … Bizzarri, R. (2015). Dual Fluorescence through Kasha's Rule Breaking: An Unconventional Photomechanism for Intracellular Probe Design. *The Journal of Physical Chemistry B*, *119*(20), 6144–6154.
[197] Eda, G., Lin, Y.-Y., Mattevi, C., Yamaguchi, H., Chen, H.-A., Chen, I.-S., … Chhowalla, M. (2010). Blue Photoluminescence from Chemically Derived Graphene Oxide. *Advanced Materials*, *22*(4), 505–509.
[198] Zhang, X.-F., Shao, X., & Liu, S. (2012). Dual Fluorescence of Graphene Oxide: A Time-Resolved Study. *The Journal of Physical Chemistry A*, *116*(27), 7308–7313.
[199] Cuong, T. V., Pham, V. H., Tran, Q. T., Hahn, S. H., Chung, J. S., Shin, E. W., & Kim, E. J. (2010). Photoluminescence and Raman studies of graphene thin films prepared by reduction of graphene oxide. *Materials Letters*, *64*(3), 399–401.
[200] Chen, J.-L., & Yan, X.-P. (2011). Ionic strength and pH reversible response of visible and near-infrared fluorescence of graphene oxide nanosheets for monitoring the extracellular pH. *Chemical Communications*, *47*(11), 3135.

Biphenylene (Figure 63) is a polycyclic aromatic hydrocarbon that has also been the centre of many scientific publications due to its dual emission properties[201,202,203].

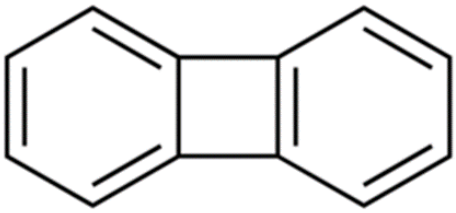

Figure 63 Structure of biphenylene

The formation of delayed $S_1 \rightarrow S_0$, $S_2 \rightarrow S_0$ and the excimer fluorescence as well as phosphorescence on the biphenylene molecule was highlighted. It was pointed out that the emissions were delayed as a result of the triplet-triplet annihilation phenomenon[204] while some people believed that the dual fluorescence was due to an impurity[205]. Emission from the S2 state appeared to be wavelength dependent[206], so AK 2 mechanism could be evoked.

Dual fluorescence has also been observed coming from some clustered polycyclic aromatic hydrocarbons. In 1971, Kropp & Stanley showed the evolution of the fluorescence spectra of ovalene with respect to temperature to illustrate the principle of dual fluorescence. By increasing the temperature, it was evidenced that there was a rise in the thermal population of the S_2 state[207]. Following these studies, Johnson claimed that the energy gap between the first two excited states was small enough to populate both the S_1 and S_2 excited states. This

[201] Lin, H.-B., & Topp, M. (1979). Spectroscopic measurements of biphenylene singlet states. *Chemical Physics Letters*, *64*(3), 452–456.
[202] Peradejordi, F., Tetreau, C., & Lavalette, D. (1972). Triplet states of biphenylene. *The Journal of Physical Chemistry*, *76*(2), 225–231.
[203] Elsaesser, T., Lärmer, F., Kaiser, W., Dick, B., Niemeyer, M., & Lüttke, W. (1988). Picosecond spectroscopy of electronically excited singlet states in biphenylene. *Chemical Physics*, *126*(2–3), 405–416.
[204] Hertzberg, J., & Nickel, B. (1989). Delayed S1→S0 AND S2→S0 fluorescence, delayed excimer fluorescence, and phosphorescence from biphenylene. *Chemical Physics*, *132*(1–2), 235–242.
[205] Hochstrasser, R. M., & McAlpine, R. D. (1966). On the Nonconfirmation of the Dual Emission Properties of Biphenylene. *The Journal of Chemical Physics*, *44*(9), 3325–3328.
[206] Shizuka, H., Ogiwara, T., Cho, S., & Morita, T. (1976). Weak fluorescence from the S2(1Lb) state of biphenylene. *Chemical Physics Letters*, *42*(2), 311–314.
[207] Kropp, J. L., & Stanley, C. C. (1971). The temperature dependence of ovalene fluorescence. *Chemical Physics Letters*, *9*(6), 534–538.

resulted in a double emission of the ovalene molecule. This paper also conveyed the change in pressure to modify the energy gap of the excited states[208]. Amirav also worked on the dual fluorescence of isolated ultra-cold ovalene[209]. As seen from some of the examples mentioned above, when the first two excited states are in close proximity, the temperature becomes a non-negligible factor since it determines the population of each state. The dual fluorescence phenomenon was detected in benzo[*g,h,i*]perylene and benzo[*a*]pyrene[210,211,212,213,214]. The assignments of the bands corresponded to a hot $S_1 \rightarrow S_0$ and $S_2 \rightarrow S_0$ emissions for benzo[*a*]pyrene. Although most of the examples discussed concerned dual fluorescence in polycyclic aromatic hydrocarbons, this behaviour is not observed in all of them. One such example is perylene.

1.2.3 *Referenced theoretical works on PAHs*

If we focus only on the advances of the theoretical works performed on PAHs, several papers related to the molecular mechanics and molecular orbital calculations to determine their optimised geometries and enthalpies of formation were published[215,216]. The computation of some properties of PAHs, including the estimation of their reactivity using semi-empirical

[208] Johnson, P. C., & Offen, H. W. (1972). Two-Level Fluorescence of Ovalene. *The Journal of Chemical Physics*, *57*(1), 336–338.
[209] Amirav, A., Even, U., & Jortner, J. (1980). Intermediate level structure in the s2 state of the isolated ultracold ovalene molecule. *Chemical Physics Letters*, *69*(1), 14–17.
[210] Kajiwara, T., Shirotani, I., Inokuchi, H., & Iwashima, S. (1969). Absorption and fluorescence spectra of benzo-[g, h, i,]-perylene, C22H12. *Journal of Molecular Spectroscopy*, *29*(1–3), 454–460.
[211] Birks, J. B., Easterly, C. E., & Christophorou, L. G. (1977). Stokes and anti-Stokes fluorescence of 1,12-benzoperylene in solution. *The Journal of Chemical Physics*, *66*(9), 4231–4236.
[212] Hoytink, G. J. (1973). *The 'Anomalous' fluorescence of 1,12-benzperylene in n-heptane*. *22*(1), 3.
[213] Easterly, C. E., Christophorou, L. G., & Carter, J. G. (1972). *Fluorescence from the second excited π singlet state of aromatic hydrocarbons in solution*. 471–483.
[214] Van Den Bogaardt, P. A. M., Rettschnick, R. P. H., & Van Voorst, J. D. W. (1973). *Anomalous vibrational relaxation of a hot S1* state of 3,4-benzpyrene in 2-methyl pentane*. *18*(3), 351–354.
[215] Schulman, J. M., Peck, R. C., & Disch, R. L. (1989). Ab initio heats of formation of medium-sized hydrocarbons. 11. The benzenoid aromatics. *Journal of the American Chemical Society*, *111*(15), 5675–5680.
[216] Peck, R. C., Schulman, J. M., & Disch, R. L. (1990). Ab initio heats of formation of medium-sized hydrocarbons. 12. 6-31G* studies of the benzenoid aromatics. *The Journal of Physical Chemistry*, *94*(17), 6637–6641.

methods[217,218] have been performed. The theoretical infrared spectra of PAHs were also estimated[219,220]. Adding to these data, the excited states of polycyclic aromatic hydrocarbons were also investigated using the Pariser-Parr-Pople approximation[221,222,223] as well as CI methods[224,225,226] to find the energies of the transitions and their corresponding intensities. Moreover, the study of the observed photo-induced toxicity was linked to the energy gap of the frontier orbitals[227]. Goodpaster et al. performed an ab initio study of the clustered PAHs, pyrene and benzo[*a*]pyrene at their ground and excited states to contribute to what is already known about PAHs in their electronic states[228]. They also studied the quenching of alternant PAHs (hydrocarbons with benzene rings) with nitromethane, which is interesting to provide sensitivity and selectivity for the analysis of the hydrocarbons[181].

---

[217] Hites, R. A., & Simonsick, W. J. (1987). *Calculated molecular properties of polycyclic aromatic hydrocarbons*. Amsterdam ; New York : New York: Elsevier ; Distributors for the U.S. and Canada, Elsevier Science Pub. Co.

[218] Rabinowitz, J. R., & Little, S. B. (1994). Comparison of quantum mechanical methods to compute the biologically relevant reactivities of cyclopenta-polycyclic aromatic hydrocarbons. *International Journal of Quantum Chemistry*, *52*(3), 681–691.

[219] Vala, M., Szczepanski, J., Pauzat, F., Parisel, O., Talbi, D., & Ellinger, Y. (1994). Electronic and Vibrational Spectra Of Matrix-Isolated Pyrene Radical Cations: Theoretical and Experimental Aspects. *The Journal of Physical Chemistry*, *98*(37), 9187–9196.

[220] Langhoff, S. R. (1996). Theoretical Infrared Spectra for Polycyclic Aromatic Hydrocarbon Neutrals, Cations, and Anions. *The Journal of Physical Chemistry*, *100*(8), 2819–2841.

[221] Nishimoto, K., & Forster, L. S. (1965). SCF calculations of aromatic hydrocarbons the variable β Approximation. *Theoretica Chimica Acta*, *3*(5), 407–417.

[222] Nishimoto, K. (1967). Electron interaction in molecules: II. π-Electronic structure of some aromatic hydrocarbons and their derivatives. *Theoretica Chimica Acta*, *7*(3), 207–219.

[223] Pucci, R., Baldo, M., Martin-Rodero, A., Piccitto, G., & Tomasello, P. (1984). Dimensional and geometrical effects on the electronic structure of polycyclic hydrocarbons. *International Journal of Quantum Chemistry*, *26*(5), 783–791.

[224] Das Gupta, A., Chatterjee, S., & Das Gupta, N. K. (1979). Theoretical Studies of Some Nonbenzenoid Hydrocarbons. V. Benzazulenes and Benzofluoranthenes. *Bulletin of the Chemical Society of Japan*, *52*(10), 3070–3075.

[225] Das Gupta, N. K., & Birss, F. W. (1978). Semi-Empirical Configuration Interaction Studies on the π-Electron Spectra of Nonbenzenoid Molecules. *Bulletin of the Chemical Society of Japan*, *51*(4), 1211–1219.

[226] Sühnel, J., Kempka, U., & Gustav, K. (1980). Molecular geometry and excited electronic states. III. Theoretical Study on Excited State Geometry and Fluorescence Properties of Fluoranthene. *Journal Für Praktische Chemie*, *322*(4), 649–654.

[227] Mekenyan, O. G., Ankley, G. T., Veith, G. D., & Call, D. J. (1994). QSAR Estimates of Excited States and Photoinduced Acute Toxicity of Polycyclic Aromatic Hydrocarbons. *SAR and QSAR in Environmental Research*, *2*(4), 237–247.

[228] Goodpaster, J. V., Harrison, J. F., & McGuffin, V. L. (1998). Ab Initio Study of Polycyclic Aromatic Hydrocarbons in Their Ground and Excited States. *The Journal of Physical Chemistry A*, *102*(19), 3372–3381.

Nevertheless, the excited states of PAHs have never been the subject of a detailed theoretical study that could include the estimation of emission properties, especially the potential emission from the first two excited states. Even the structures of both these excited states have never been accurately compared, that is a good starting point for this part of the study.

1.3 Aim of the work

Dual fluorescence is the main reason that motivated this research work on clustered polycyclic aromatic hydrocarbons. It was noticed that only some of them exhibit this anti-Kasha behaviour and it could be interesting to establish a pattern between several molecules or to decipher whether there is a specific feature that triggers this dual emission.

Perylene is a small PAH that possesses five aromatic rings in its structure. It seems that it has only one emission band on its fluorescence spectrum. Coronene, on the other hand, presents a dual fluorescence from the S_1 and S_2 states. It has seven aromatic rings in its structure. Following this observation, we came up with the idea of selecting a few intermediate molecules between perylene and coronene to investigate their behaviour at the excited state and thus, deduce a plausible relationship between the molecules. Four intermediate molecules were chosen based on the number of benzene rings, that is, the size of the clustered PAH as well as their commercial availability. Hence, when the polycyclic aromatic hydrocarbons are placed one beside each other, it creates a continuum connecting pyrene to coronene. The molecules picked were pyrene, perylene, benzo[*a*]pyrene, benzo[*e*]pyrene, benzo[*g,h,i*]perylene and coronene and their structures are shown in Figure 64.

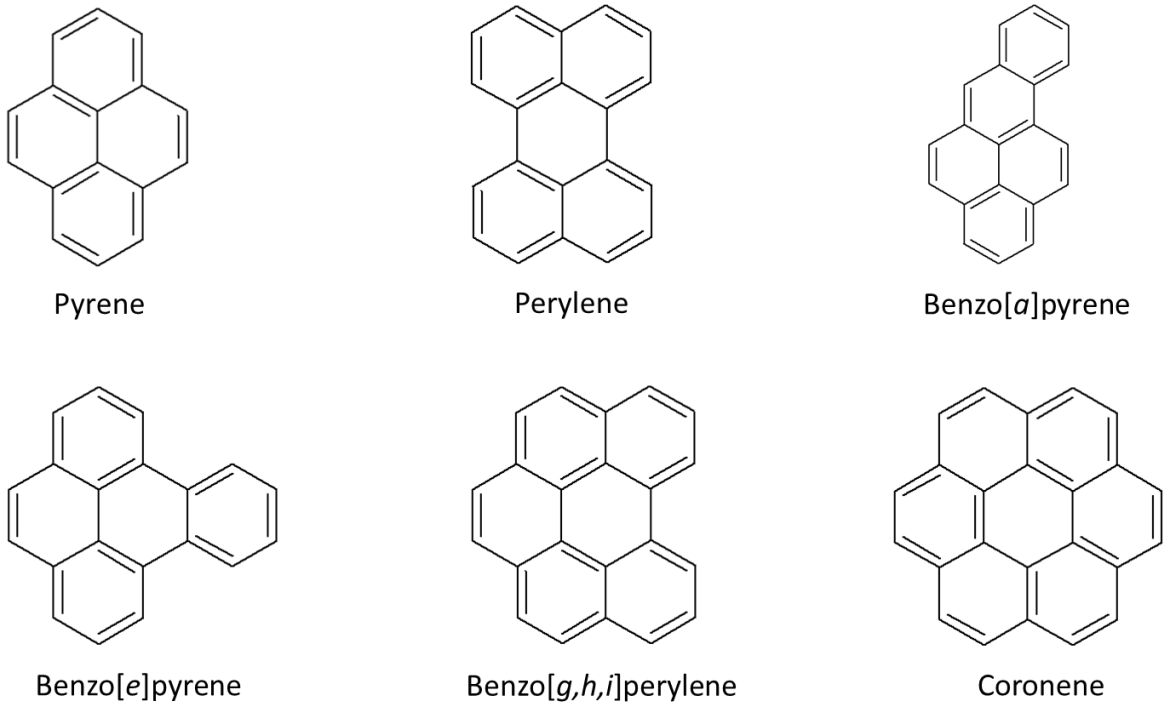

Figure 64 The selected polycyclic aromatic hydrocarbons for this study

Based on all the various aspects that have been exposed previously, PAHs have been extensively studied for a long time using various techniques, notably mass spectrometry, absorption, steady-state and time-resolved fluorescence. This enabled the creation of a large database on the chemical, physical and photo-physical properties of those compounds. However, if the focus is put on the theoretical aspect of the study, very few information related to their excited states is available.

While justifying the choice of the molecules in this study, the stress was put on the fact that some of them have a double emission originating from their excited states. This prompted us to speculate the reason for such a behaviour. In order to shed light upon this matter, a theoretical investigation was led on the chosen molecules to understand the mechanism when they are excited and how they *surf* on their potential energy surfaces. To this end, a theoretical approach was adopted using the DFT and TD-DFT.

1.4 Methodology

1.4.1 Electronic Spectroscopy

Absorption and fluorescence spectroscopy were used only for verification purposes. The Varian Cary 100 Bio double beam spectrometer was used to record the absorption spectrum and the emission spectrum was obtained using the Jobin Yvon Fluorolog (Horiba). The spectrometers were calibrated as detailed in the first part of this manuscript. The solvent used to dissolve all the samples was toluene. The latter was chosen because it was one of the only solvents readily available that could dissolve all our samples.

1.4.2 Density Functional Theory and Time Dependent – Density Functional Theory

Concerning this part, DFT[229] and TD-DFT were computational methods used throughout the work using the Gaussian16 software[230]. A previous work concerning acenes showed that DFT methods are still appropriate for molecules bearing up to seven aromatic rings in their structure[231]. A benchmark to determine the correct functional and basis set was carried out in order to have the best fit between theoretical and experimental data. Geometry optimisation at the ground state as well as the first two excited states for all the molecules (geometry optimisation for the first four excited states for coronene) have been carried out

[229] Kohn, W., Becke, A. D., & Parr, R. G. (1996). Density Functional Theory of Electronic Structure. *The Journal of Physical Chemistry*, *100*(31), 12974–12980.

[230] Gaussian 16, Revision C.01, Frisch, M. J.; Trucks, G. W.; Schlegel, H. B.; Scuseria, G. E.; Robb, M. A.; Cheeseman, J. R.; Scalmani, G.; Barone, V.; Petersson, G. A.; Nakatsuji, H.; Li, X.; Caricato, M.; Marenich, A. V.; Bloino, J.; Janesko, B. G.; Gomperts, R.; Mennucci, B.; Hratchian, H. P.; Ortiz, J. V.; Izmaylov, A. F.; Sonnenberg, J. L.; Williams-Young, D.; Ding, F.; Lipparini, F.; Egidi, F.; Goings, J.; Peng, B.; Petrone, A.; Henderson, T.; Ranasinghe, D.; Zakrzewski, V. G.; Gao, J.; Rega, N.; Zheng, G.; Liang, W.; Hada, M.; Ehara, M.; Toyota, K.; Fukuda, R.; Hasegawa, J.; Ishida, M.; Nakajima, T.; Honda, Y.; Kitao, O.; Nakai, H.; Vreven, T.; Throssell, K.; Montgomery, J. A., Jr.; Peralta, J. E.; Ogliaro, F.; Bearpark, M. J.; Heyd, J. J.; Brothers, E. N.; Kudin, K. N.; Staroverov, V. N.; Keith, T. A.; Kobayashi, R.; Normand, J.; Raghavachari, K.; Rendell, A. P.; Burant, J. C.; Iyengar, S. S.; Tomasi, J.; Cossi, M.; Millam, J. M.; Klene, M.; Adamo, C.; Cammi, R.; Ochterski, J. W.; Martin, R. L.; Morokuma, K.; Farkas, O.; Foresman, J. B.; Fox, D. J. Gaussian, Inc., Wallingford CT, 2016.

[231] Trinquier, G., & Malrieu, J.-P. (2018). Predicting the Open-Shell Character of Polycyclic Hydrocarbons in Terms of Clar Sextets. *The Journal of Physical Chemistry A*, *122*(4), 1088–1103.

and electronic transitions have been calculated in the range varying from 200 nm to 800 nm. The PCM model was applied to take into consideration toluene as solvent. In addition to that, a sampling of the PES was carried out for the first two excited states. NMR calculations were performed on the molecules to evaluate the aromaticity on each molecule using the GIAO (Gauge Independent Atomic Orbitals) method[232]. Furthermore, the cube files were created for the ground and excited states of each molecule to be able to calculate the charge transfer index between each states.

1.4.3 Python Scripts

Several Python scripts were written to simplify the data treatment of the large sets of data and to compute parameters introduced in the following.

[232] Wolinski, K., Hinton, J. F., & Pulay, P. (1990). Efficient implementation of the gauge-independent atomic orbital method for NMR chemical shift calculations. *Journal of the American Chemical Society*, *112*(23), 8251-8260.

CHAPTER 2:

ESTABLISHING THE OPTICAL PROPERTIES OF SELECTED PAHS

2.1 Optical properties of polycyclic aromatic hydrocarbons

TD-DFT has been recognised over time as one of the best methods for the reproduction of low-lying vertical excitation energies of organic molecules[233,234]. However, in some cases, with the increasing number of atoms, DFT and its corresponding TD method no longer become adequate as the systems cannot be well described with a single configurational approach. Trinquier at al. evoked the problem of how polycyclic aromatic hydrocarbons can undergo spin-symmetry breaking at the singlet ground state, which makes them develop an open-shell character whilst they are usually seen as closed-shell singlets[235]. They also published their works on the polyradical character of long acenes. They exposed once again the problem of the breaking of the spin-symmetry as the length of the acene increases[236]. Indeed, a spin instability was detected for heptacene and it was accounted for a HOMO – LUMO mixing[237]. The conclusion that can be drawn is that, for PAHs having more than seven aromatic rings in their structure, they lose their close-shell feature because they act as polyradicals. In this case, DFT cannot be considered reliable enough for the computations. The polycyclic aromatic hydrocarbons chosen for this study possess less than seven benzene rings, so DFT and TD-DFT can be safely applied on the molecules. Moreover, the cyclic nature of the species chosen decreases the size of a molecule for a given number of rings, that reduces the issues encountered with long-range interactions.

[233] Jacquemin, D., Mennucci, B., & Adamo, C. (2011). Excited-state calculations with TD-DFT : From benchmarks to simulations in complex environments. *Physical Chemistry Chemical Physics*, *13*(38), 16987.
[234] Champagne, B., Guillaume, M., & Zutterman, F. (2006). TDDFT investigation of the optical properties of cyanine dyes. *Chemical Physics Letters*, *425*(1–3), 105–109.
[235] Trinquier, G., & Malrieu, J.-P. (2018). Predicting the Open-Shell Character of Polycyclic Hydrocarbons in Terms of Clar Sextets. *The Journal of Physical Chemistry A*, *122*(4), 1088–1103.
[236] Trinquier, G., David, G., & Malrieu, J.-P. (2018). Qualitative Views on the Polyradical Character of Long Acenes. *The Journal of Physical Chemistry A*, *122*(34), 6926–6933.
[237] Bendikov, M., Duong, H. M., Starkey, K., Houk, K. N., Carter, E. A., & Wudl, F. (2004). Oligoacenes: Theoretical Prediction of Open-Shell Singlet Diradical Ground States. *Journal of the American Chemical Society*, *126*(24), 7416–7417.

2.1.1 Absorption and emission spectra

The experimental spectra of the molecules dissolved in toluene were recorded in absorption and fluorescence spectroscopy and are depicted in Figure 65 and Figure 66. The absorption of the solvent was observed on the spectra in the range of 200 – 300 nm which justifies why this region is not present in the absorbance spectra. In general, it can be seen that each molecule has its own signature on the UV-vis and emission spectra. The vibronic bands of the PAHs molecules are visible on the absorption as well as on the emission spectra. Due to this effect, it is quite hard to differentiate the dual fluorescence bands from the vibronic ones. For this purpose, only the lowest lying energy band was considered useful as it will be used to determine the most adequate functional and basis set for the upcoming computations. It should be noted that these spectra were taken in order to compare the data with the computations. The absorption are reported in Table 18 below. Because of the intricate fluorescence spectra, it is quite difficult to pick a single value to characterise the band.

Table 18 The experimental absorption wavelengths and transition energies of selected PAHs

	Absorption wavelength, λ, nm (E, eV)
Pyrene	337 (3.68)
Perylene	438 (2.83)
Benzo[*a*]pyrene	388 (3.20)
Benzo[*e*]pyrene	333 (3.72)
Benzo[*g,h,i*]perylene	387 (3.20)
Coronene	431 (2.88)

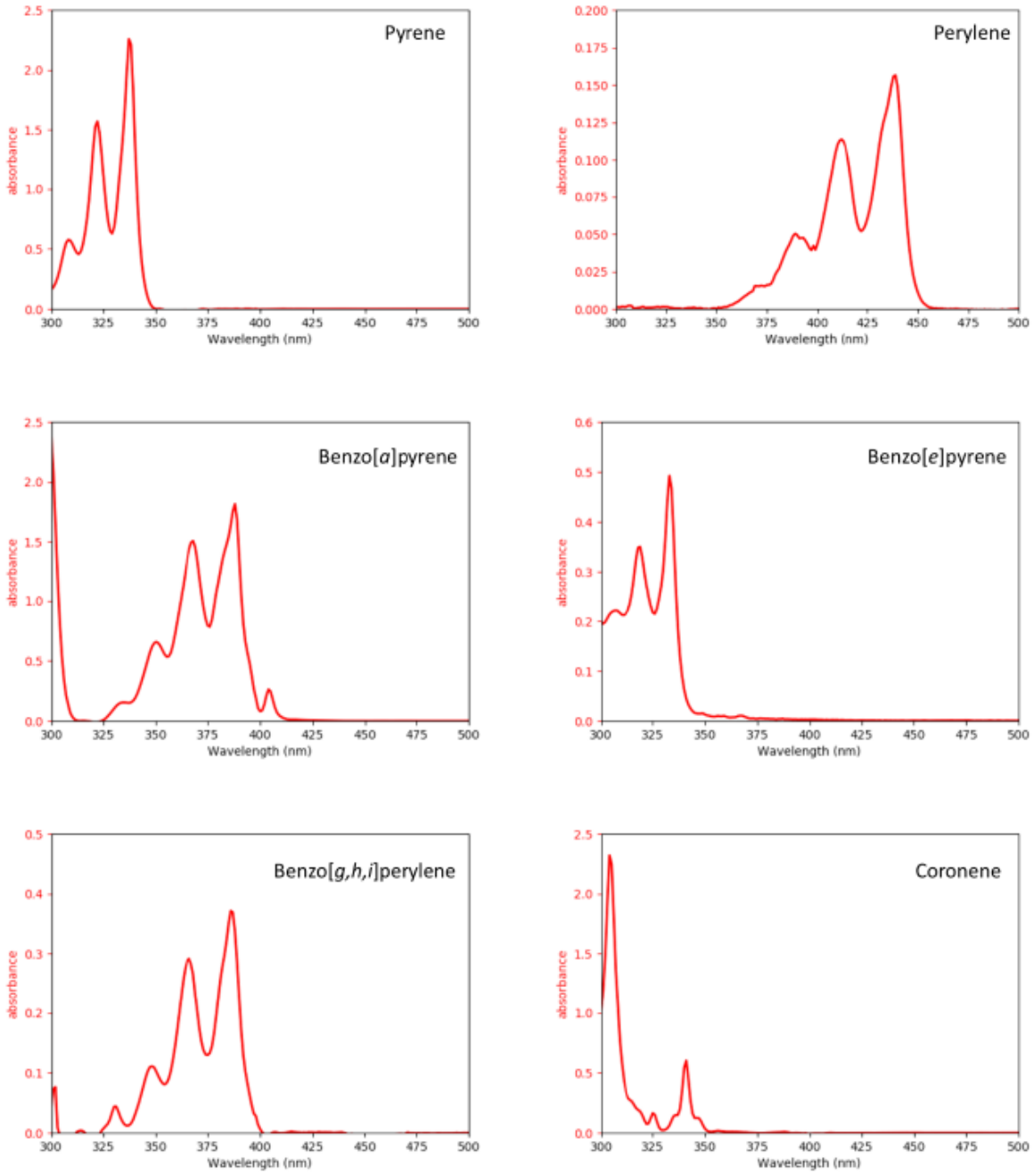

Figure 65 Absorption spectra of the selected molecules

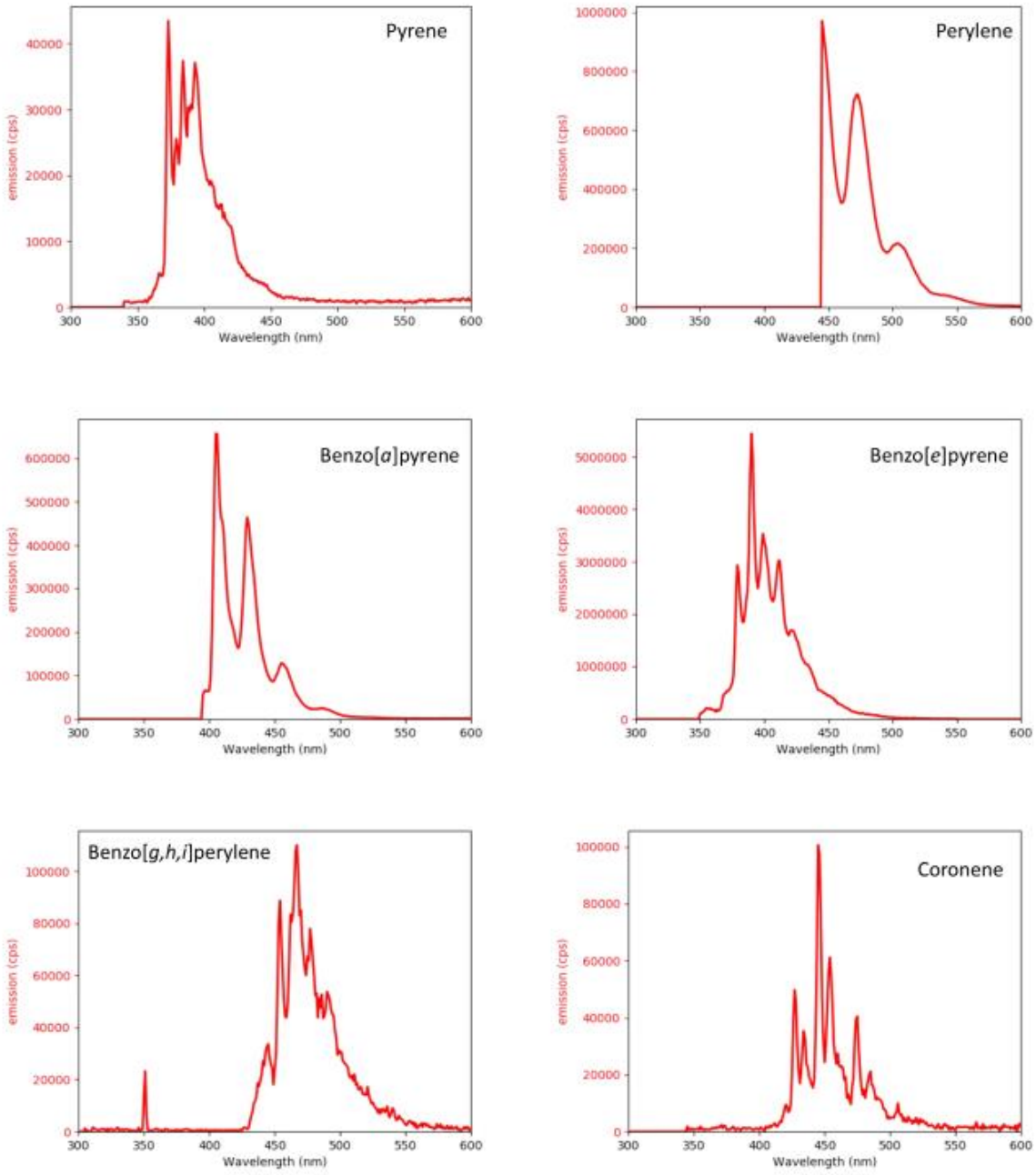

Figure 66 Fluorescence spectra of the selected molecules

2.1.2 Benchmark

A benchmark was carried out on the six polycyclic aromatic hydrocarbons to determine the most appropriate computational parameters to depict the experimental optical properties of the compounds. Several hybrid functionals varying from the classic PBE0[238,239] (25% HF exchange contribution) and B3LYP[240,241,242,243] (20% HF exchange contribution) to the hybrid meta GGA functional M06-2X[244] (54% HF exchange contribution) and ωB97X-D[245], which takes into consideration empirical dispersion and long-range corrections (22% to 100% HF exchange contribution) were tested. The influence of empirical dispersion was also checked with PBE0. The resulting data are reported in Table 19. In this Table, the pyrene molecule was fully re-optimised for each model and the electronic transitions were computed on this optimized structure.

[238] Perdew, J. P., Ernzerhof, M., & Burke, K. (1996). Rationale for mixing exact exchange with density functional approximations. *The Journal of Chemical Physics*, *105*(22), 9982–9985.
[239] Adamo, C., & Barone, V. (1999). Toward reliable density functional methods without adjustable parameters : The PBE0 model. *The Journal of Chemical Physics*, *110*(13), 6158-6170.
[240] Becke, A. D. (1993). Density-functional thermochemistry. III. The role of exact exchange. *The Journal of Chemical Physics*, *98*(7), 5648–5652.
[241] Lee, C., Yang, W., & Parr, R. G. (1988). Development of the Colle-Salvetti correlation-energy formula into a functional of the electron density. *Physical Review B*, *37*(2), 785–789.
[242] Vosko, S. H., Wilk, L., & Nusair, M. (1980). Accurate spin-dependent electron liquid correlation energies for local spin density calculations : A critical analysis. Canadian Journal of Physics, 58(8), 1200-1211.
[243] Becke, A. D. (1988). Density-functional exchange-energy approximation with correct asymptotic behavior. *Physical Review A*, *38*(6), 3098-3100.
[244] Zhao, Y., & Truhlar, D. G. (2008). The M06 suite of density functionals for main group thermochemistry, thermochemical kinetics, noncovalent interactions, excited states, and transition elements: Two new functionals and systematic testing of four M06 functionals and 12 other functionals. *Theoretical Chemistry Accounts*, *119*(5–6), 525–525.
[245] Chai, J.-D., & Head-Gordon, M. (2008). Long-range corrected hybrid density functionals with damped atom–atom dispersion corrections. *Physical Chemistry Chemical Physics*, *10*(44), 6615.

Table 19 Benchmark for the pyrene molecule summarising the absorption wavelengths, energies and their difference with respect to the experimental value (λ = 337 nm, E = 3.68 eV)

Functional	Additional parameters	Basis set	Absorption wavelength, λ (nm)	Absorption energy, E (eV)	Difference, $\Delta\lambda$, nm (ΔE, eV)
PBE0		6-31G	325	3.81	12 (0.13)
		6-31G**	331	3.74	6 (0.06)
		6-31+G	331	3.75	6 (0.07)
		6-31+G**	337	3.68	0 (0.00)
		6-311G	326	3.80	11 (0.12)
		6-311G**	334	3.72	3 (0.04)
		6-311+G	329	3.77	8 (0.09)
		6-311+G**	337	3.68	0 (0.00)
		cc-pvdz	335	3.70	2 (0.02)
		cc-pvtz	335	3.70	2 (0.02)
		aug-cc-pvdz	340	3.65	3 (0.03)
		aug-cc-pvtz	337	3.68	0 (0.00)
	GD3	6-311G	326	3.80	11 (0.12)
		6-311G**	334	3.72	3 (0.04)
		6-311+G	329	3.77	8 (0.09)
		6-311+G**	337	3.68	0 (0.00)
	GD3BJ	6-311G	326	3.80	11 (0.12)
		6-311G**	334	3.72	3 (0.04)
		6-311+G	329	3.77	8 (0.09)
		6-311+G**	337	3.68	0 (0.00)
B3LYP		cc-pvtz	344	3.60	7 (0.08)
		aug-cc-pvtz	346	3.58	9 (0.10)
M06-2X		cc-pvtz	309	4.01	28 (0.33)
		aug-cc-pvtz	312	3.98	25 (0.30)
ωB97X-D		cc-pvtz	311	3.98	26 (0.30)
		aug-cc-pvtz	313	3.96	24 (0.28)

From the data collected, it can be seen that all the computed energies are quite close and are in line with what is observed experimentally. This further backs up the choice of using DFT as computational method. The global hybrid functionals, PBE0 and B3LYP gives somewhat similar results, which is coherent with the work published by Laurent et al.[246]. On the other hand, the electronic transitions calculated with M06-2X were always blue-shifted with respect to the

[246] Laurent, A. D., & Jacquemin, D. (2013). TD-DFT benchmarks: A review. *International Journal of Quantum Chemistry*, *113*(17), 2019–2039.

experimental band. In order to take into account long range interactions and dispersion effects, ωB97X-D was also tested. The results were similar to what was observed with M06-2X. Indeed, classic functionals like PBE0 and B3LYP are more likely to calculate the vertical excitation energies with a very good precision in comparison with the other two[246]. With the advent of the latest version of the Gaussian software (2016), the frequency calculations at the excited state are quicker, so the process to optimise and check the minima obtained for the largest molecules we chose is tractable in a reasonable duration. Several basis sets, of different nature (Pople and Dunning basis sets) and size were also tested. It was seen that the time required for the calculations performed by the Pople basis set was faster than those with the Dunning basis set. It was also highlighted that the same electronic transition energies are obtained whether a double zeta or a triple zeta is applied on the model (the energy difference is the same), so the convergence of the transition energies is obtained. The Pople triple zeta basis set gives accurate data within a reasonable computational delay, so it was preferentially chosen. In addition to that, several tests were performed with polarised functions, diffused functions and both of them. The computations with the polarised functions improved the accuracy of the absorption values. This effect is more modest than we expected but is observable, that lead us to add these functions in further computations. On the opposite, the use of diffuse functions on heavy atoms seems not so useful, but the small amount of time added to the computations by these functions lead us to keep them in the computations. The effect of dispersion was quantified using to different models (GD3 and GD3BJ) with PBE0 calculations, and the unchanged absorption wavelengths revealed that this effect seems negligible. Therefore, from all the arguments exposed, the PBE0/6-311+G**, being a good compromise between accuracy and computation time, was chosen for all the forthcoming studies of the excited states of polycyclic aromatic hydrocarbons.

This model was also checked for the larger molecules to test its scalability. Table 20 reports some computed data for perylene, benzo[a]pyrene, benzo[e]pyrene and benzo[*g,h,i*]perylene to investigate their behaviour with respect to the corresponding functional and basis set. First of all, it can be seen that for perylene and benzo[*g,h,i*]perylene, no data was obtained when the molecules were optimised with M06-2X/aug-cc-pvtz. The lowest frequencies calculated were imaginary and despite several trials, the molecules could not be optimised. The same

issue was observed for perylene, benzo[*a*]pyrene, benzo[*e*]pyrene and benzo[*g,h,i*]perylene with ωB97X-D/aug-cc-pvtz.

Table 20 Benchmark for perylene, benzo[*a*]pyrene, benzo[*e*]pyrene and benzo[*g,h,i*]perylene summarising the absorption wavelengths, energies and the difference with respect to the experiments

Molecule (Experiments)	Functional	Basis set	Absoprtion wavelength, λ (nm)	Absoprtion energy, E (eV)	Difference
Perylene (438 nm, 2.83 eV)	PBE0	cc-pvdz	439	2.83	1 (0.00)
		cc-pvtz	442	2.80	4 (0.03)
		aug-cc-pvdz	453	2.74	15 (0.09)
		aug-cc-pvtz	449	2.76	11 (0.07)
		6-31+G**	447	2.77	9 (0.06)
		6-311+G**	448	2.77	10 (0.06)
	B3LYP	cc-pvtz	455	2.72	17 (0.11)
		aug-cc-pvtz	463	2.68	25 (0.15)
	M06-2X	cc-pvtz	398	3.11	40 (0.28)
	ωB97X-D	cc-pvtz	395	3.14	43 (0.31)
Benzo[*a*]pyrene (388 nm, 3.20 eV)	PBE0	cc-pvdz	392	3.17	4 (0.03)
		cc-pvtz	391	3.17	3 (0.03)
		aug-cc-pvdz	397	3.12	9 (0.08)
		aug-cc-pvtz	393	3.15	5 (0.05)
		6-31+G**	393	3.16	5 (0.04)
		6-311+G**	393	3.16	5 (0.04)
	B3LYP	cc-pvtz	403	3.08	15 (0.12)
		aug-cc-pvtz	405	3.06	17 (0.14)
	M06-2X	cc-pvtz	355	3.49	33 (0.29)
		aug-cc-pvtz	357	3.47	31 (0.27)
	ωB97X-D	cc-pvtz	354	3.50	34 (0.30)
Benzo[*e*]pyrene (333 nm, 3.72 eV)	PBE0	cc-pvdz	331	3.74	2 (0.02)
		cc-pvtz	330	3.76	3 (0.04)
		aug-cc-pvdz	336	3.70	3 (0.02)
		aug-cc-pvtz	332	3.73	1 (0.01)
		6-31+G**	333	3.72	0 (0.00)
		6-311+G**	332	3.73	0 (0.00)
	B3LYP	cc-pvtz	341	3.64	8 (0.08)
		aug-cc-pvtz	343	3.61	10 (0.11)
	M06-2X	cc-pvtz	307	4.04	26 (0.32)
		aug-cc-pvtz	309	4.02	24 (0.30)
	ωB97X-D	cc-pvtz	307	4.04	26 (0.32)

Benzo[*g,h,i*]perylene (387 nm, 3.20 eV)	PBE0	cc-pvdz	379	3.27	8 (0.07)
		cc-pvtz	381	3.26	6 (0.06)
		aug-cc-pvdz	388	3.20	1 (0.00)
		aug-cc-pvtz	384	3.23	3 (0.03)
		6-31+G**	383	3.24	4 (0.04)
		6-311+G**	384	3.23	3 (0.03)
	B3LYP	cc-pvtz	393	3.16	6 (0.04)
		aug-cc-pvtz	397	3.12	10 (0.08)
	M06-2X	cc-pvtz	345	3.60	42 (0.40)
	ωB97X-D	cc-pvtz	342	3.63	45 (0.43)

With the exception of the benzo[*g,h,i*]perylene, it was noticed that, for the other molecules, all the calculations done with the aug-cc-pvdz and aug-cc-pvtz irrespective of the functional gave a worse comparison than their corresponding basis set without the diffuse functions added to them. Beyond this aspect, it can be seen that the trends got in the case of pyrene are recovered for this set of molecules. Especially, as with the pyrene molecule, the double zeta and triple zeta values are very close, meaning that convergence is easily reached by using the double zeta basis sets, and the PBE0/6-311+G** model appears to be accurate enough to study these compounds.

2.2 Difficulties during calculations

The computational study on the polycyclic aromatic hydrocarbons was relatively smooth, except for some difficulties encountered, illustrated below.

2.2.1 Vibronic band calculations

The presence of vibronic structures on the electronic spectra led to an attempt to compute the theoretical vibronic transitions. Two methods are available with the Gaussian software. The first one is a module implemented in the software that calculates the vibronic spectrum

with the keyword freq=FC and with the checkpoint file of the optimised excited state[247]. The second method is to use FCCLASSES[248]. It is a software that use Gaussian output files and gives detailed results on the vibronic transitions. However, we were unable to match the experimental data and computed vertical transitions to the vibronic bands calculated by both methods, and even the computed data with these two approaches were not matching. Since the determination of the vibronic structure was not crucial for this study and due to the lack of time, this part was not further explored.

2.2.2 Excited states of benzo[e]pyrene

One particular phenomenon was observed during the TD-DFT calculations of the benzo[*e*]pyrene molecule. An inversion of the first two theoretical emission wavelengths was observed along the optimisation pathway, due to the closeness of these two excited states. When this behaviour occurs, special attention needs to be given at each optimisation step to ensure that the correct state is being followed, for the software happens to mix the states and to follow the wrong one. Generally speaking, once the crossing has been passed, the optimisation became easier.

2.2.3 Excited states of coronene

The oscillator strength of the first two excited states of coronene was found to be equal to zero while the third and the fourth had relatively comparable non-zero values. This behaviour can be assimilated to the dark bands and light bands. Due to this behaviour, the first four excited states of the coronene molecule had to be optimised instead of only the first two. However, due to lack of time and long calculation time for coronene, the in-depth study for this molecule could not be done.

[247] Barone, V., Bloino, J., & Biczysko, M. (2009). *Vibrationally-resolved electronic spectra in GAUSSIAN 09*. 1–20.
[248] Santoro F., "*FCclasses*, a Fortran 77 code": visit http://village.ipcf.cnr.it

CHAPTER 3:
EXCITED STATED OF PAHS

3.1 Structural changes upon excitation

The benchmark allowed us to determine the functional and basis set that had to be used in Gaussian16 for the DFT calculations. From there onwards, PBE0/6-311+G** was used for all the computations. The electronic transitions obtained for each molecules from the TD-DFT calculations were carefully studied. It was noticed that, especially when looking at the first two excited states, only one of them is emissive (that could be consistent with an AK 1 mechanism). The emission wavelengths were tabulated for all the molecules and are given in the Appendix (SI.2). There was a need to understand how these two states are positioned with respect to each other and to investigate how they draw closer and eventually cross so that a plausible explanation for dual fluorescence can be found. A strategy was set up to be able to comprehend the behaviour of each chosen polycyclic aromatic hydrocarbons when they are excited. This strategy involved the inquiry on the geometry modification of the molecules at the two lowest excited states with respect to the ground state and following that, the stepwise motion of each molecule was closely investigated to get an idea of the aspect of each potential energy surfaces. This is important since it can potentially give an indication on how each excited state is being populated and hence, enable to decipher if a dual fluorescence is possible.

One aspect that has shown to be very useful in many scientific works is to find a reaction coordinate that can allow us to keep track of the evolution from one optimised structure to the other[249,250]. A simple example to illustrate this concept is the case of a diatomic molecule where it is possible to vary the inter-nuclear distance, *r* (considered as a reaction coordinate) and to calculate the potential energy at each point to visualise the potential energy surface. Polycyclic aromatic hydrocarbons are more intricate compounds. It is quite difficult to employ a single reaction coordinate that will be adequate for all molecules without proper research work beforehand.

[249] Frontiera, R. R., Fang, C., Dasgupta, J., & Mathies, R. A. (2012). Probing structural evolution along multidimensional reaction coordinates with femtosecond stimulated Raman spectroscopy. *Phys. Chem. Chem. Phys.*, *14*(2), 405–414.
[250] Bolhuis, P. G., Dellago, C., & Chandler, D. (2000). Reaction coordinates of biomolecular isomerization. *Proceedings of the National Academy of Sciences*, *97*(11), 5877–5882.

The first step was to examine the geometry of the optimised molecules at their ground state and their first two excited states and to observe the apparent changes when moving from one state to the other. Prima facie, the molecules do not seem to undergo a big change since they do not seem to be distorted and, more specifically, their planarity is retained. In order to visualise the difference in the structures, the bond lengths were gathered and thoroughly compared at each electronic state.

Table 21, Table 22, Table 23, Table 24 and Table 25 report the information extracted from pyrene, perylene, benzo[*a*]pyrene, benzo[*e*]pyrene and benzo[*g,h,i*]perylene respectively. The first two columns indicate the numbering of the two carbons that forms the bond. The three following columns contain the bond lengths at the ground state (S_0), lowest excited state (S_1) and second lowest excited state (S_2). Finally, the last two columns include the calculated difference in bond lengths between the lowest excited state, S_1 and the ground state, S_0 as well as the second lowest excited state, S_2 and the ground state, S_0. To determine the most important variations experienced by the PAHs during excitation, the bond length values were sorted out. The first condition applied was to suppose that if the difference of bond length was greater or smaller by 0.020 Å, it meant that that the variation was significant. They are represented with a dark blue background and white numbers. The second condition was to identify a change in the bond length varying between 0.015 Å and 0.020 Å. This variation is considered to be weaker than the previous one but not negligible. They are represented by the light blue background with a dark blue font. The limits of the boundaries were established by the team.

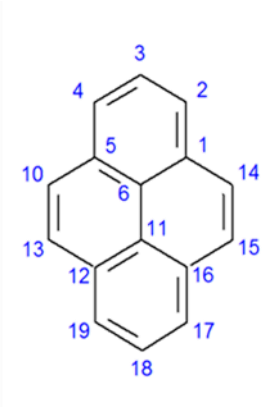

Figure 67 Pyrene with the numbered carbon atoms

Table 21 Bond lengths of all the bonds on the **pyrene** molecule at the ground state, first excited state and second excited state as well as the difference in bond length from the ground state to the respective excited states

Carbon atom numbering		Bond lengths (*l*,Å)			Difference in bond lengths (*l*,Å)	
C1	C2	S_0	S_1	S_2	($S_1 - S_0$)	($S_2 - S_0$)
1	14	1.435	1.407	1.424	**−0.028**	−0.011
13	12	1.435	1.407	1.424	**−0.028**	−0.011
15	16	1.435	1.407	1.424	**−0.028**	−0.011
5	10	1.435	1.407	1.424	**−0.028**	−0.011
11	6	1.424	1.417	1.391	−0.006	**−0.032**
3	4	1.392	1.390	1.405	−0.001	0.013
18	17	1.392	1.390	1.405	−0.001	0.013
19	18	1.392	1.390	1.405	−0.001	0.013
2	3	1.392	1.390	1.405	−0.001	0.013
12	11	1.424	1.430	1.448	0.006	**0.024**
5	6	1.424	1.430	1.448	0.006	**0.024**
16	11	1.424	1.430	1.448	0.006	**0.024**
6	1	1.424	1.430	1.448	0.006	**0.024**
12	19	1.402	1.432	1.406	**0.030**	0.004
1	2	1.402	1.432	1.406	**0.030**	0.004
17	16	1.402	1.432	1.406	**0.030**	0.004
4	5	1.402	1.432	1.406	**0.030**	0.004
10	13	1.360	1.397	1.378	**0.037**	**0.018**
14	15	1.360	1.397	1.378	**0.037**	**0.018**

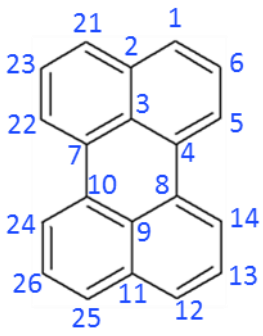

Figure 68 Perylene with the numbered carbon atoms

Table 22 Bond lengths of all the bonds on the **perylene** molecule at the ground state, first excited state and second excited state as well as the difference in bond length from the ground state to the respective excited states

Carbon atom numbering		Bond lengths (*l*,Å)			Difference in bond lengths (*l*,Å)	
C1	C2	S_0	S_1	S_2	($S_1 - S_0$)	($S_2 - S_0$)
1	2	1.416	1.413	1.408	−0.003	−0.008
1	6	1.374	1.392	1.388	**0.018**	0.014
2	3	1.431	1.433	1.453	0.003	**0.022**
2	21	1.416	1.413	1.408	−0.003	−0.008
3	4	1.429	1.426	1.427	−0.003	−0.002
3	7	1.429	1.426	1.427	−0.003	−0.002
4	5	1.389	1.423	1.403	**0.035**	0.015
4	8	1.473	1.437	1.448	**−0.035**	**−0.025**
5	6	1.405	1.386	1.407	**−0.019**	0.003
7	10	1.473	1.437	1.448	**−0.035**	**−0.025**
7	22	1.388	1.423	1.403	**0.035**	0.015
8	9	1.429	1.426	1.427	−0.003	−0.002
8	14	1.388	1.423	1.403	**0.035**	0.015
9	10	1.429	1.426	1.427	−0.003	−0.002
9	11	1.431	1.433	1.453	0.003	**0.022**
10	24	1.388	1.423	1.403	**0.035**	0.015
11	12	1.416	1.413	1.408	−0.003	−0.008
11	25	1.416	1.413	1.408	−0.003	−0.008
12	13	1.374	1.392	1.388	**0.018**	0.014
13	14	1.405	1.386	1.407	**−0.019**	0.003
21	23	1.374	1.392	1.388	**0.019**	0.014
22	23	1.405	1.386	1.407	**−0.019**	0.002
24	26	1.405	1.386	1.407	**−0.019**	0.002
25	26	1.374	1.392	1.388	**0.019**	0.014

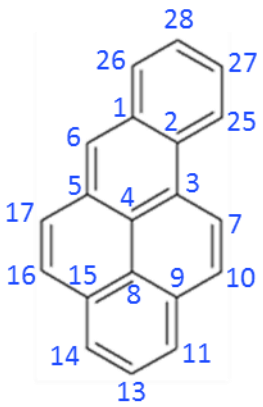

Figure 69 Benzo[*a*]pyrene with the numbered carbon atoms

Table 23 Bond lengths of all the bonds on the **benzo[*a*]pyrene** molecule at the ground state, first excited state and second excited state as well as the difference in bond length from the ground state to the respective excited states

Carbon atom numbering		Bond lengths (*l*,Å)			Difference in bond lengths (*l*,Å)	
C1	C2	S_0	S_1	S_2	($S_1 - S_0$)	($S_2 - S_0$)
1	2	1.430	1.435	1.455	0.006	**0.025**
1	6	1.412	1.406	1.407	−0.006	−0.005
1	26	1.420	1.419	1.408	−0.002	−0.012
2	3	1.439	1.462	1.425	**0.023**	−0.013
2	25	1.418	1.395	1.423	**−0.022**	0.005
3	4	1.415	1.434	1.444	**0.019**	**0.029**
3	7	1.429	1.407	1.429	**−0.021**	0.000
4	5	1.438	1.430	1.443	−0.008	0.005
4	8	1.427	1.417	1.401	−0.011	**−0.026**
5	6	1.381	1.414	1.401	**0.032**	**0.020**
5	17	1.439	1.413	1.420	**−0.027**	**−0.020**
7	10	1.364	1.381	1.378	**0.017**	0.014
8	9	1.422	1.427	1.444	0.004	**0.022**
8	15	1.426	1.436	1.439	0.010	0.012
9	10	1.426	1.421	1.415	−0.005	−0.011
9	11	1.407	1.407	1.412	−0.001	0.004
11	13	1.386	1.406	1.391	**0.020**	0.005
13	14	1.397	1.378	1.407	**−0.018**	0.011
14	15	1.397	1.429	1.404	**0.032**	0.007
15	16	1.439	1.406	1.424	**−0.033**	**−0.015**
16	17	1.355	1.390	1.374	**0.034**	**0.018**
25	27	1.377	1.406	1.383	**0.030**	0.006
26	28	1.373	1.391	1.390	**0.018**	**0.017**
27	28	1.412	1.393	1.412	**−0.019**	0.000

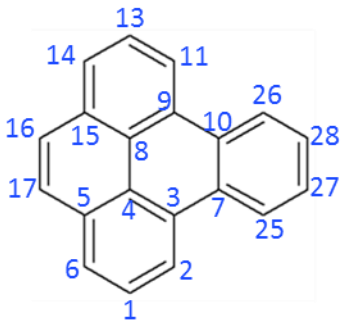

Figure 70 Benzo[*e*]pyrene with the numbered carbon atoms

Table 24 Bond lengths of all the bonds on the **benzo[*e*]pyrene** molecule at the ground state, first excited state and second excited state as well as the difference in bond length from the ground state to the respective excited states

Carbon atom numbering		Bond lengths (*l*,Å)			Difference in bond lengths (*l*,Å)	
C1	C2	S_0	S_1	S_2	($S_1 - S_0$)	($S_2 - S_0$)
1	2	1.394	1.392	1.393	−0.002	−0.001
1	6	1.385	1.400	1.384	**0.015**	−0.001
2	3	1.399	1.415	1.429	**0.016**	**0.030**
3	4	1.422	1.445	1.424	**0.024**	0.003
3	7	1.464	1.441	1.435	**−0.023**	**−0.029**
4	5	1.426	1.443	1.435	**0.018**	0.009
4	8	1.433	1.401	1.426	**−0.032**	−0.007
5	6	1.402	1.405	1.430	0.003	**0.028**
5	17	1.433	1.417	1.404	**−0.016**	**−0.029**
7	10	1.417	1.441	1.447	**0.024**	**0.030**
7	25	1.410	1.413	1.417	0.003	0.007
8	9	1.422	1.445	1.424	**0.024**	0.003
8	15	1.425	1.443	1.435	**0.018**	0.009
9	10	1.464	1.441	1.435	**−0.023**	**−0.029**
9	11	1.399	1.415	1.429	**0.016**	**0.030**
10	26	1.410	1.413	1.417	0.003	0.007
11	13	1.394	1.392	1.393	−0.002	−0.001
13	14	1.385	1.400	1.384	**0.015**	−0.001
14	15	1.402	1.405	1.430	0.003	**0.028**
15	16	1.433	1.417	1.404	**−0.016**	**−0.029**
16	17	1.357	1.377	1.396	**0.020**	**0.039**
25	27	1.382	1.391	1.376	0.010	−0.006
26	28	1.382	1.391	1.376	0.010	−0.006
27	28	1.399	1.397	1.413	−0.003	0.013

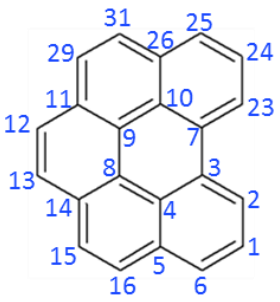

Figure 71 Benzo[*g,h,i*]perylene with the numbered carbon atoms

Table 25 Bond lengths of all the bonds on the **benzo[*g,h,i*]perylene** molecule at the ground state, first excited state and second excited state as well as the difference in bond length from the ground state to the respective excited states

Carbon atom numbering		Bond lengths (*l*,Å)			Difference in bond lengths (*l*,Å)	
C1	C2	S_0	S_1	S_2	($S_1 - S_0$)	($S_2 - S_0$)
1	2	1.396	1.386	1.401	−0.010	0.005
1	6	1.384	1.392	1.388	0.008	0.004
2	3	1.397	1.430	1.407	**0.033**	0.010
3	4	1.425	1.419	1.433	−0.006	0.009
3	7	1.465	1.435	1.450	**−0.030**	**−0.015**
4	5	1.425	1.430	1.442	0.005	**0.016**
4	8	1.429	1.428	1.408	−0.001	**−0.021**
5	6	1.405	1.416	1.410	0.011	0.005
5	16	1.431	1.413	1.420	**−0.018**	−0.011
7	10	1.425	1.419	1.433	−0.006	0.009
7	23	1.397	1.430	1.407	**0.033**	0.010
8	9	1.424	1.410	1.434	−0.014	0.010
8	14	1.416	1.438	1.442	**0.023**	**0.026**
9	10	1.429	1.428	1.408	−0.001	**−0.021**
9	11	1.416	1.438	1.442	**0.023**	**0.026**
10	26	1.425	1.430	1.442	0.005	**0.016**
11	12	1.415	1.434	1.407	**0.019**	−0.008
11	29	1.429	1.399	1.419	**−0.030**	−0.010
12	13	1.373	1.361	1.399	−0.012	**0.026**
13	14	1.415	1.434	1.407	**0.019**	−0.008
14	15	1.429	1.399	1.419	**−0.030**	−0.010
15	16	1.361	1.392	1.377	**0.031**	**0.016**
23	24	1.396	1.386	1.401	−0.010	0.005
24	25	1.384	1.392	1.388	0.008	0.004
25	26	1.405	1.416	1.410	0.012	0.005
26	31	1.431	1.413	1.420	**−0.018**	−0.011
29	31	1.361	1.392	1.377	**0.031**	**0.016**

After analysing each structure meticulously, we were able to spot the bonds that were subject to modifications when the molecules are excited. The main changes are displayed in Figure 72.

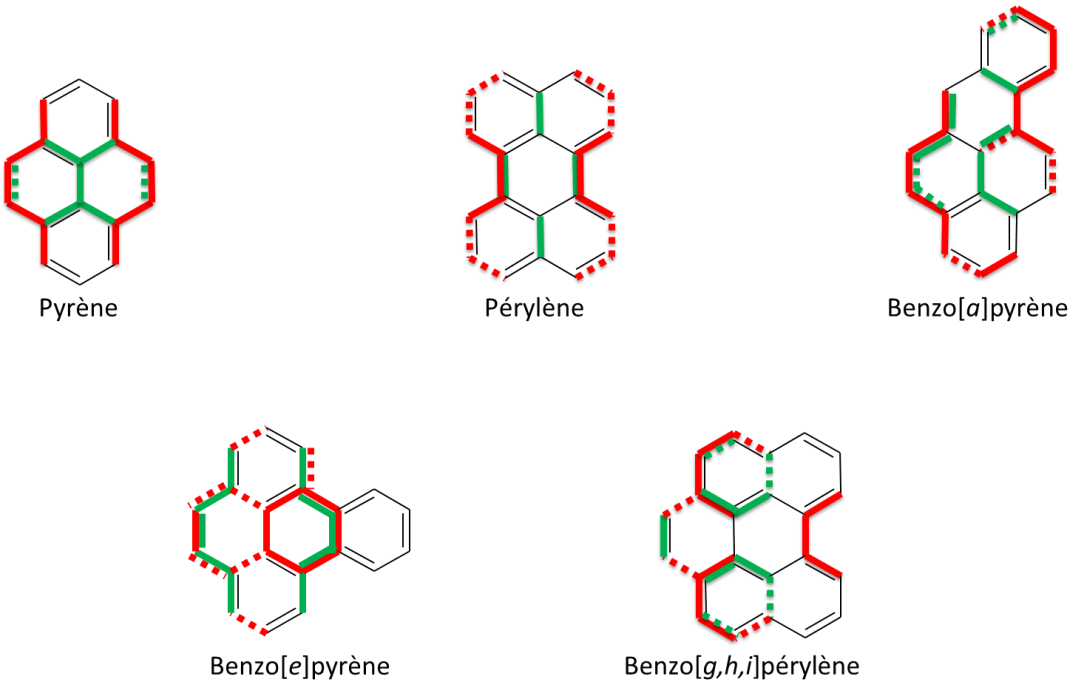

Figure 72 The structures of pyrene, perylene, benzo[*a*]pyrene, benzo[*e*]pyrene and benzo[*g,h,i*]perylene where all the highlighted bonds are those that vary a lot

The bonds in red are those that are impacted when the molecule is excited to the lowest excited state and the ones in green are those altered when moving to the second lowest excited state, whatever the sign of the variation. When the coloured bonds are represented in full line, it means that the changes respected the first condition (variation above 0.020 Å) and when they are represented by broken lines, the changes obeyed the second condition (variation between 0.015 and 0.020 Å). The bonds highlighted in red are located mainly inside the molecules. This gives the impression that the PAH is being flattened as it moves to the lowest excited state, S_1. Conversely, the green bonds are found on the perimeter of the molecule. When the molecules are excited to the second lowest excited state, S_2, it can be presumed that they are being stretched. These observations are striking for the symmetrical molecules like pyrene and perylene. It is less obvious for the non-symmetric PAHs but the pattern is still present. These modifications are illustrated in Figure 73.

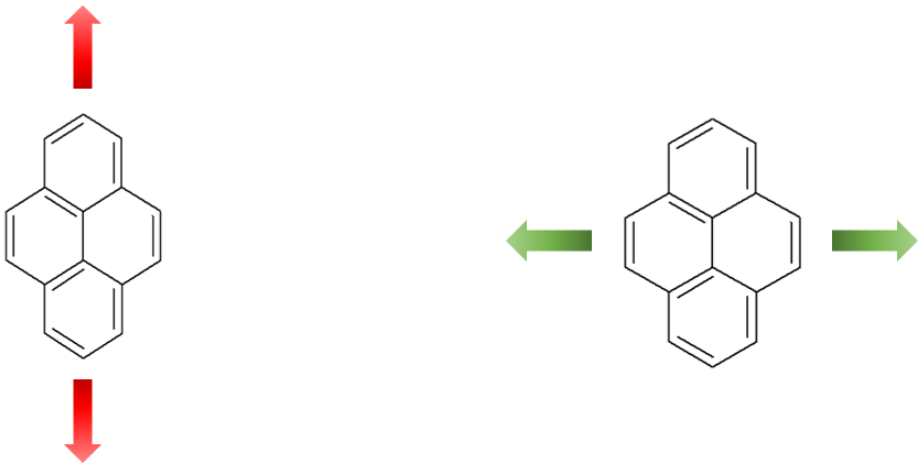

Figure 73 Modification of the geometry when the molecule moves to the first excited state (on the left) and to the second excited state (on the right)

The deformation of the molecules when they are excited let us envisage a form factor as potential reaction coordinate. So, three form factors were considered:

- RC1 (related to the perimeter and the surface area of the compound),
- RC2 (corresponding to the Singular Value Decomposition concept applied to the structure) and,
- RC3 (optimisation of an ellipse around the molecule).

These three factors are representative of a similar phenomenon that is the “flattening” or the “stretching” of the structure evoked above. Their mathematical definition will be detailed below, but a first glance on their physical meaning can be given. The first one will measure the deviation of the global shape of the studied PAH from a circle by a ratio between perimeter and surface. The second one will use a description of the position of the atoms in a plane, by the means of the favoured directions of spreading in two dimensions. Last, RC3 describe the shape similarity between a PAH and an ellipse that is characterised by its axes.

Two additional factors were also taken into consideration. They are not directly related to the structure of the molecule but are plausible candidates as reaction coordinates for polycyclic aromatic hydrocarbons:

- RC4 (related to the aromaticity of rings in each structure) and,

- RC5 (charge transfer index between states).

Indeed, RC4 is a global measurement of several variations of bond lengths: the aromaticity of a ring can be considered as a summary of several bonds evolving in opposite directions (typically a modification of bond alternations). RC5 is more difficult to connect to the trends observed, but recent studies suggest that its evolution is linked to the transition between states[251] and was therefore included in this study.

[251] Adamo, C., Le Bahers, T., Savarese, M., Wilbraham, L., García, G., Fukuda, R., Ehara, M., Rega, N., & Ciofini, I. (2015). Exploring excited states using Time Dependent Density Functional Theory and density-based indexes. *Coordination Chemistry Reviews*, *304-305*, 166-178.

3.2 Sampling of the PES

The main goal, after the selection of the reaction coordinate, is to compute and describe the potential energy surface (PES) that connects the optimised structures of each PAH at their ground state, first excited state and second excited state. It can be seen as a triangle that connects the three optimised structures to better visualise the dependence of each state with respect to each other. To compare easily the results obtained for each PAH, a normalised PES was defined without any reference to a specific PAH. We sampled these PES as follows.

Initially, a *triangle* was constructed in such a way that two of the sides were divided into nine intervals delimited by ten points, interpolated from the optimised geometries computed before. Each corner of the *triangle* represented the ground state, first excited state and second excited state. Moreover, a sampling inside the triangle was also carried out to get a convenient picture of the PES in between the three optimised structure. The energy was calculated at all the defined points. At this point, to fill the *triangle*, we have a total of fifty-five points as depicted on Figure 74.

Nevertheless, the description of the PES obtained this way is not sufficient. Indeed, we cannot presume that the expected surface crossing will occur in between the optimised structures as it is clearly seen on the bottom graphical representation of Figure 74. Thus, it is necessary to describe as well the surroundings of each of these three structures outside of the previously described triangle. We planned to expand the triangle to have a sufficient description around each corner of the basis triangle. If we consider the distance between GS and ES1 to be equivalent to two parts, therefore, we choose to add one part before GS and two parts after ES1 in order to maintain the shape of the model. The same principle was applied to the distance between GS and ES2. Hence, the size of the triangle was modified from nine intervals to twenty-five to keep a similar sampling as in the previous case. A slight modification has been done (the small triangle is now described by ten intervals instead of nine) for parity reasons. The new corners of the *triangle* were labelled P0, P1 and P2 as shown in Figure 75.

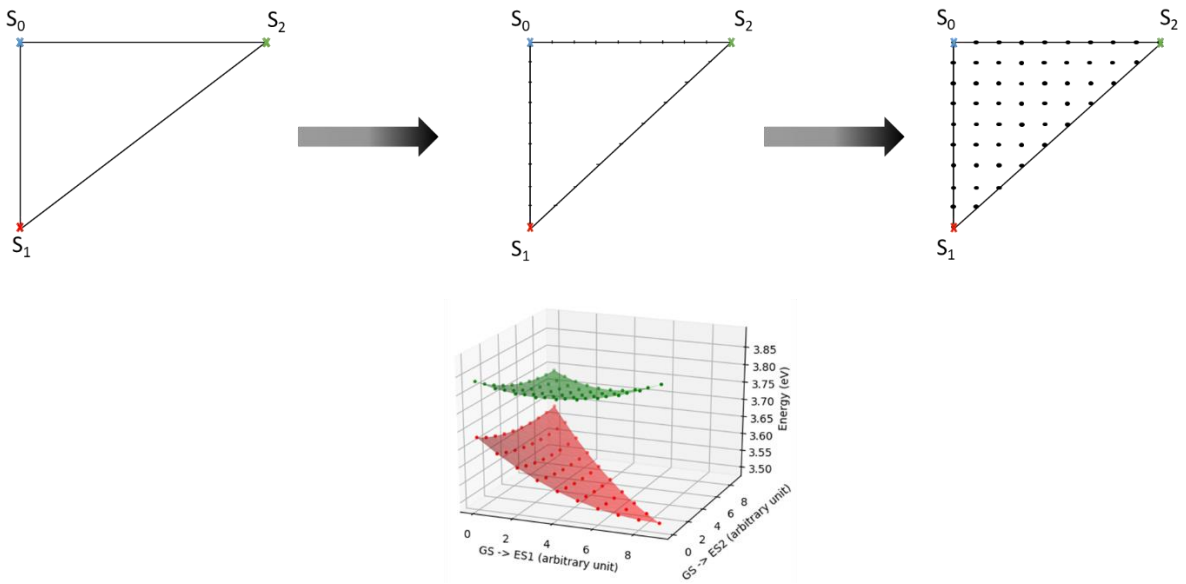

Figure 74 Concept of linking the ground state, first excited state and second excited state and the calculation of single points over the whole surface (on the top) and the 3D energy surfaces of the first and second excited states (on the bottom; pyrene in this case)

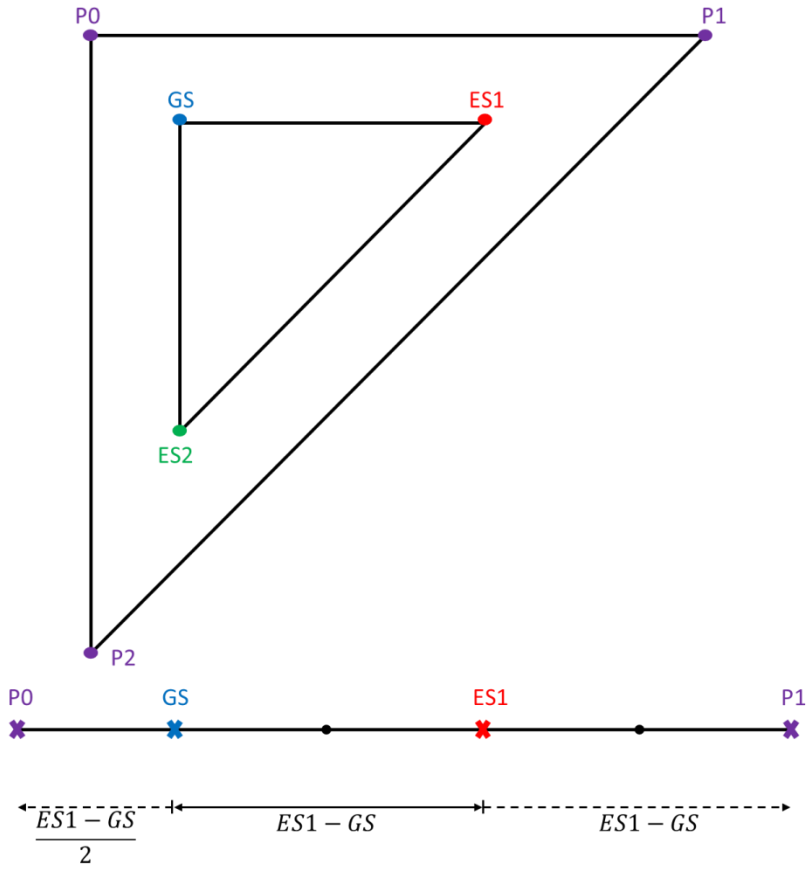

Figure 75 Enlargement of the surface connecting the ground state, first excited state and second excited state as well as the description of how each side was extended

The next step consisted in finding a relationship linking P0, P1 and P2 separately to GS, ES1 and ES2 to determine the coordinates of each geometry along the potential energy surface. The steps applied to generate the equations of P0, P1 and P2 are illustrated in Figure 76. In the equation of this figure, the label of the points and their Cartesian coordinates (seen as a spatial vector) are designed with a same notation to have equations as light as possible.

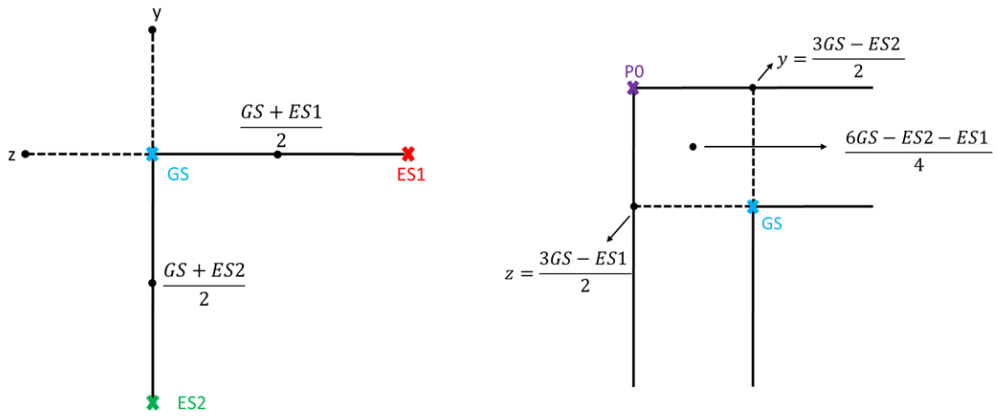

$$y+\frac{(GS+ES2)}{2}=GS$$

$$y=\frac{3GS-ES2}{2}$$

$$z+\frac{GS+ES1}{2}=GS$$

$$z=\frac{3GS-ES1}{2}$$

Figure 76 Mathematical resolution of the determination of the coordinates of the corners of the *triangle*

From the coordinates of y and z, we can find an equation to calculate P0 and we end up with Equation 1.

$$\mathrm{P0}=\left(\frac{3\mathrm{GS}-\mathrm{ES1}}{2}\right)+\left(\frac{3\mathrm{GS}-\mathrm{ES2}}{2}\right)-\mathrm{GS}$$

$$P0=\frac{4GS-ES1-ES2}{2} \qquad \textit{Equation 1}$$

If we refer back to Figure 75, we can find a relation between P0 and P1. Since P0 can be known through Equation 1, P1 can easily be defined.

$$\mathrm{P1}=\mathrm{P0}+\frac{5}{2}\left(\mathrm{ES1}-\mathrm{GS}\right)$$

$$\mathrm{P1}=\left(\frac{4\mathrm{GS}-\mathrm{ES1}-\mathrm{ES2}}{2}\right)+\frac{5}{2}\left(\mathrm{ES1}-\mathrm{GS}\right)$$

$$P1 = \left(\frac{4GS - ES1 - ES2 + 5ES1 - 5GS}{2}\right)$$

$$P1 = \frac{-GS + 4ES1 - ES2}{2} \qquad \textit{Equation 2}$$

The same procedure can be applied to find the coordinates of P2.

$$P2 = \frac{-GS - ES1 + 4ES2}{2} \qquad \textit{Equation 3}$$

With the P0, P1 and P2 coordinates defined, the *triangle* can, henceforth, be expanded from 55 single point to 351 single point energy calculations.

Figure 77 depicts the 3D graphical representation of the first two excited states of perylene and benzo[e]pyrene (the PES for the other molecules will be given later on). These two molecules were shown here because they represent two distinct cases. On one side, it can be seen that the two excited states of perylene are quite far from each other, explaining the absence of dual fluorescence. On the other side, the energy gap of the excited states for benzo[*e*]pyrene is very small and a crossing can clearly be observed.

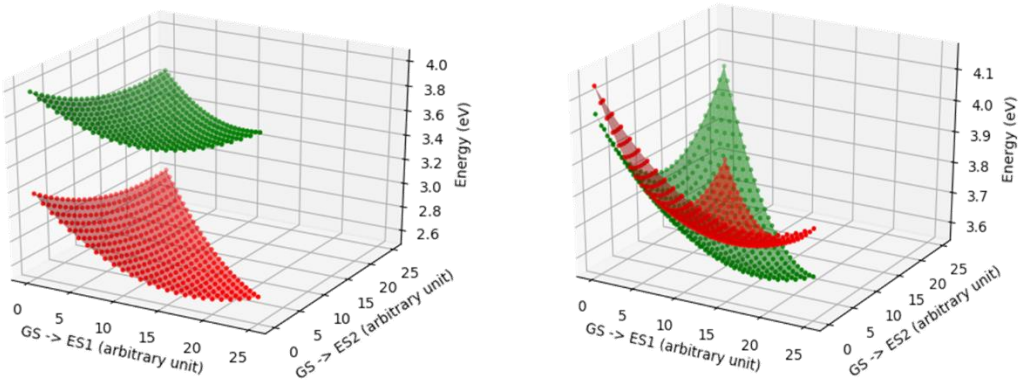

Perylene Benzo[*e*]pyrene

Figure 77 First two excited states of perylene and benzo[*e*]pyrene

3.3 Evaluation of plural reaction coordinates

Primarily, the energy of the molecule was computed at each point on the *triangle* to create the potential energy surface. In parallel, the reaction coordinates were calculated at the same coordinates as the energy single points. As expected, it can be quite tedious to do the calculations for all the 351 points required to form the triangle manually. For the data treatment to be successful, an additional file, specific to each molecule, was created. This file contained important parameters related to each PAH. Characteristic to the latter, they can be decomposed into several rings. The carbon numbers forming the different rings were noted in the file (one line contains all the carbon numbers corresponding to one ring). After describing all the rings, the last line contains the numbers of the carbon atoms forming the perimeter of the molecule. Figure 78 shows an example of this file for pyrene. The file enabled the calculation of the reaction coordinates detailed below.

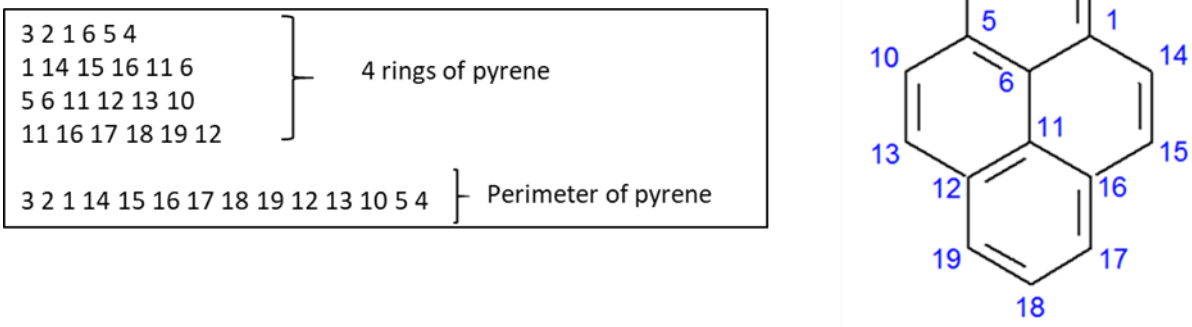

Figure 78 File containing some structural information about pyrene (on the left) and the corresponding molecule (on the right) showing the numbering of the carbon atoms.

3.3.1 Perimeter and Surface (RC1)

The first form factor to be tested was the one concerning the perimeter, *p* and the surface area, *s* of each PAH. The retained definition for this parameter is written below as Equation 4. It has been defined to reach 1 for a circle.

$$\mathrm{RC1} = \frac{4\pi \cdot s}{p^{\,2}} \qquad \textit{Equation 4}$$

To calculate the surface area of a polycyclic aromatic hydrocarbon, the molecule was divided into hexagons, then, the hexagons, in turn, were broken up into four triangles (the carbon atoms bearing an odd number were linked together). The sum of the surfaces of the triangles is computed to obtain the surface of a hexagon. Finally, the addition of the surfaces of the hexagons was done to have the surface area of the PAH. As for the perimeter, all the bond lengths around each molecule were summed up. From there, RC1 can easily be computed. Figure 79 shows the separate 3D plot of the single point energies and that of RC1 (left). Then, these two graphical representations are merged to a 2D plot (right) that shows the evolution of the energies with respect to RC1 for the first two excited states.

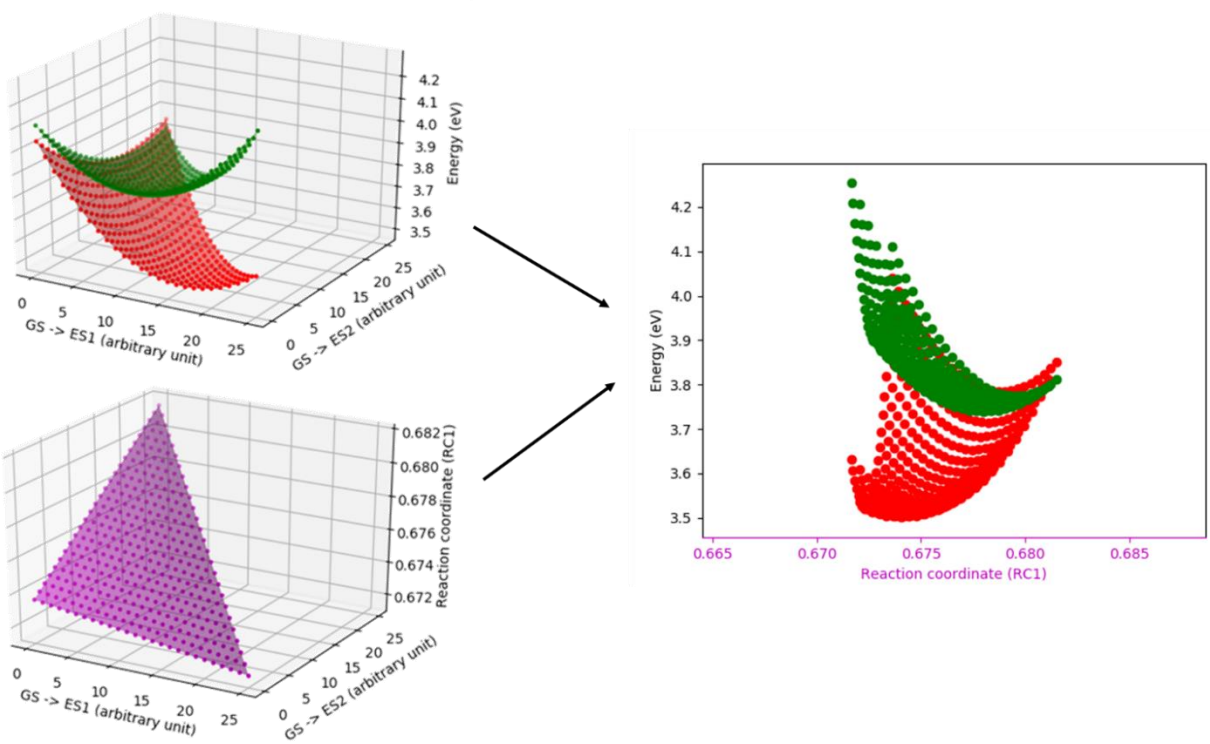

Figure 79 The 3D plot of the two energy surfaces of the lowest excited states (top left), the 3D plot showing the evolution of the reaction coordinate, RC1 (bottom left) and the merging of both 3D plots to obtain the 2D plot (on the right) of the energy with respect to RC1 for the pyrene molecule

The lowest state (in red) does not exactly represent any tendency and it is hard to interpret how the PES is varying as the points are spread in all directions. However, for the higher state (in green), the plot of the energy with respect to the first reaction coordinate enables us to visualise the progression of RC1. The points organised themselves quite regularly around a curve that illustrates a trend. Thus, RC1 can be considered as a reaction coordinate that gives a better description of the evolution of energy of the second excited state than the first one. The same procedure is applied to the other compounds and the transformations are illustrated in Figure 80. If a trend had been observed with the other PAHs, RC1 would have been a good reaction coordinate to characterise the second lowest energy state, but when RC1 is applied on the other molecules, the results obtained are not satisfactory (Figure 80).

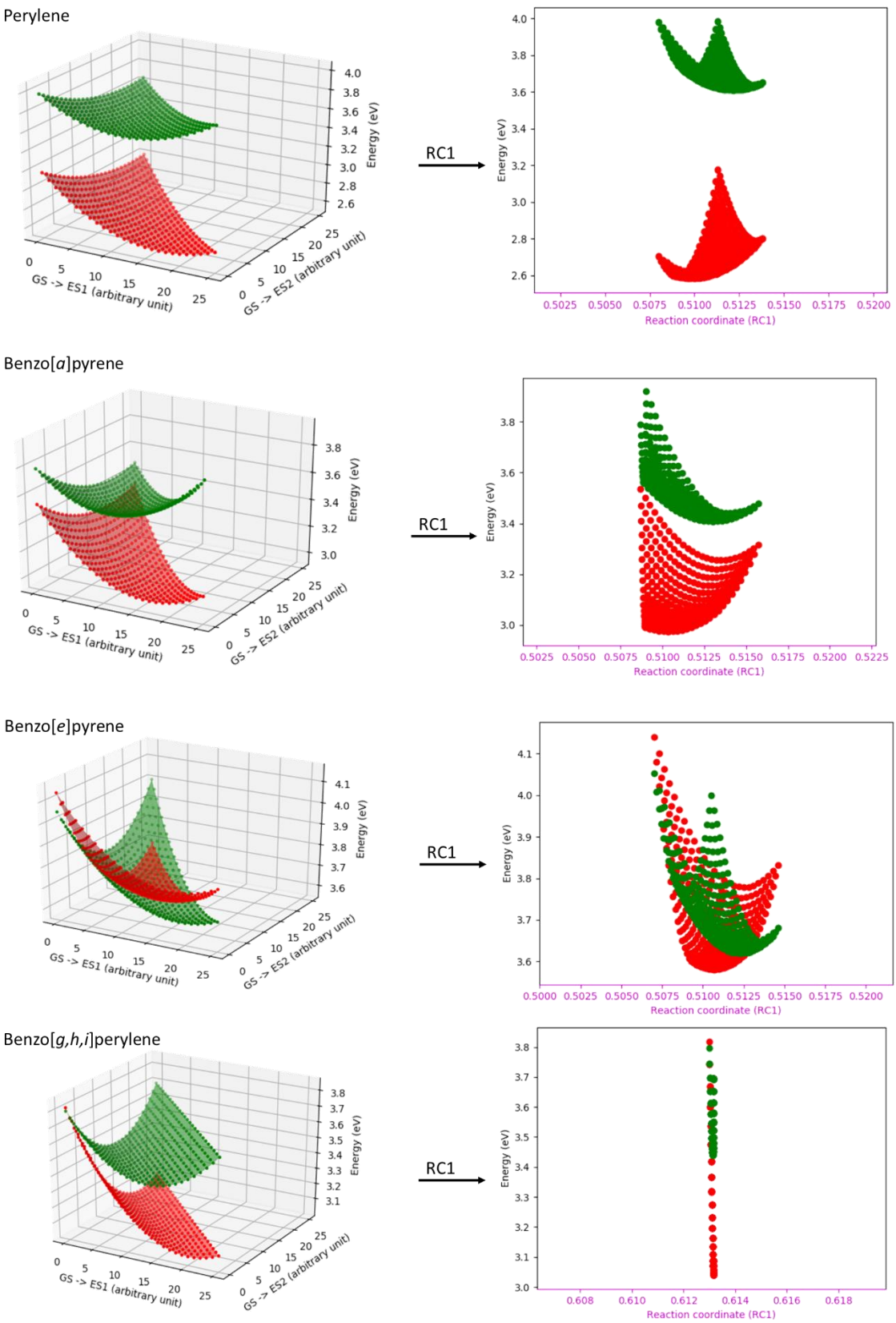

Figure 80 Two excited energy surfaces of perylene, benzo[*a*]pyrene, benzo[*e*]pyrene and benzo[*g,h,i*]perylene and their corresponding 2D plots with respect to RC1

Starting with perylene, no apparent trend is observed since the 2D plot does not help to visualise the evolution of the energy. The same observation is made with benzo[*e*]pyrene. The points are too scattered to obtain a good tendency. Concerning benzo[*a*]pyrene, the motion of the points in green characterising the second excited state is guessed even if it is not perfectly described. Unfortunately, the red points (first excited state) gave a bad result with RC1. Finally, for benzo[*g,h,i*]perylene, the variation of RC1 with the structure is so small that it is not visible on the plot, giving a very bad description of the PES. Therefore, based on the results depicted in Figure 80 are not as promising for the second lowest state as those obtained with the pyrene. Hence, it is not possible to use it as it is representative of all the compounds under study.

3.3.2 Singular Value Decomposition - SVD (RC2)

Singular Value Decomposition (SVD) is a method of sorting out data from a large set of intrinsically-ordered data. It can be applied based on different criteria. In this case, to define a form factor, there are three Singular Values (SVs, numbered by decreasing value): the first one is related to the length of the molecule, the second one is associated to the width of the molecule and the third one concerns the depth of the molecule. Since the PAHs are planar, SV3 is almost equal to zero. Hence, RC2 was calculated as the ratio of SV1 and SV2 (Equation 5). Once again, in the case of a circle, RC2 would yield 1.

$$RC2 = \frac{SV1}{SV2} \qquad \textit{Equation 5}$$

Figure 81 shows the results of the 2D graph of the motion of RC2 along the potential energy surface for each PAH.

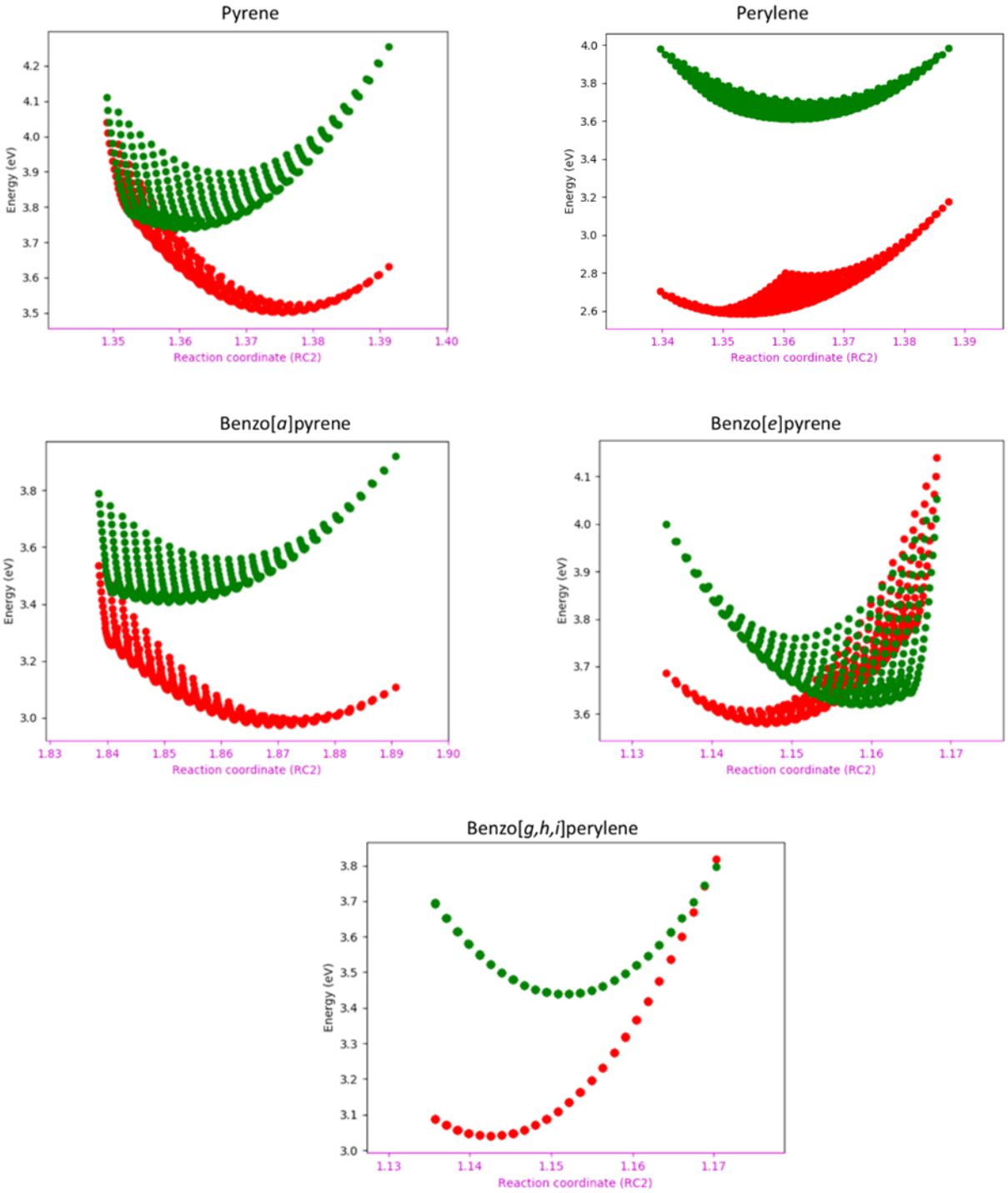

Figure 81 2D plots of pyrene, perylene, benzo[*a*]pyrene, benzo[*e*]pyrene and benzo[*g,h,i*]perylene showing the evolution of the energy with respect to RC2

In comparison with RC1, the reaction coordinate RC2 gave much better results. Concerning the pyrene molecule, a neat trend showing the evolution of energy with increasing RC2 is illustrated for the ES1 in red. However, the ES2 in green is not well represented since the values are too scattered. The use of RC2 on perylene was a little difference from that of

pyrene. In this case, both ES1 and ES2 are correctly described because the trend is obvious for both excited states. Benzo[*e*]pyrene and benzo[*a*]pyrene behaves the same way with respect to RC2. The lowest excited state is well described with the reaction coordinate even though the points are a little spread on the plot. However, the scattering of the points representing the second lowest excited state's plot does not allow to establish a good trend of the PES. As a matter of fact, the green plot for these two molecules is very similar to the one observed for pyrene. When RC2 is applied on benzo[*g,h,i*]perylene, a perfect characterisation of the first and second excited state is identified. The crossing point of the two PES is easily distinguished. This behaviour is what is expected from all the molecules when a reaction coordinate is used. Figure 81 enabled us to report that, for the studied molecules, RC2 is a good reaction coordinate for defining the lowest excited state, ES1. However, it is not appropriate for the second lowest excited state, ES2.

3.3.3 Optimised ellipse around the molecule (RC3)

The third form factor calculated was related to the creation of an ellipse that can be optimised around each PAH. In this case, each ellipse will have parameters that are proper for each molecule. An ellipse is defined as a closed plane curve generated by a point moving in such a way that the sum of its distances from two fixed points, known as the foci, is a constant. Figure 82 shows the representation of an ellipse. The orange dots are the carbon atoms of pyrene that are positioned on the perimeter of the molecule and the two blue dots are the focal points of the fitted ellipse. The parameters that interest us the most are the semi-major axis, *a* and the semi-minor axis, *b* in such a way that, by doing the ratio of both values, we end up with a plausible form factor, RC3 as shown by Equation 6.

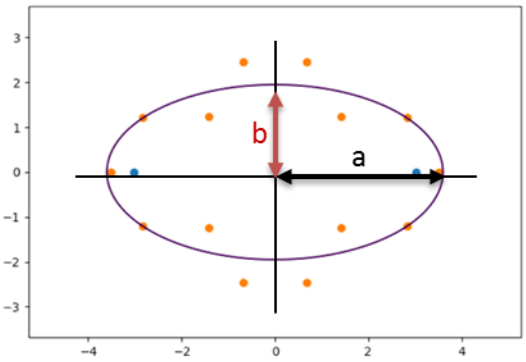

Figure 82 Optimisation of an ellipse around the pyrene molecule (described by the orange dots corresponding to the carbon atoms on the perimeter of the molecule)

$$RC3 = \frac{Semi - axis\ a}{Semi - axis\ b} \qquad \textit{Equation 6}$$

The values of the semi-axes can be obtained through various ways. Unlike for a circle, there is no canonical way to define the best ellipse. In this work, we proceeded as follows. From the coordinates of the molecule, the two focal points were placed arbitrarily on the x-axis and were defined from the SVD. An arbitrary atom of carbon on the compound was chosen and the distances from the point to each of the focal points are calculated and summed up. Afterwards, we sweep through all the carbon atoms that are present on the perimeter and the sums of the distance to the focal points are calculated. Following that, the mean sum of the distance is computed. The optimisation criterion is to decrease the value of the square of the differences between the sum of the distances for each individual bond and the mean value. An ellipse is thus obtained by a simple minimisation procedure and the a and b values obtained for each structure are used to compute RC3. The script used for this calculation is available in the Appendix (SI.1). Figure 83 shows the 2D plot of all the PAHs under the influence of RC3.

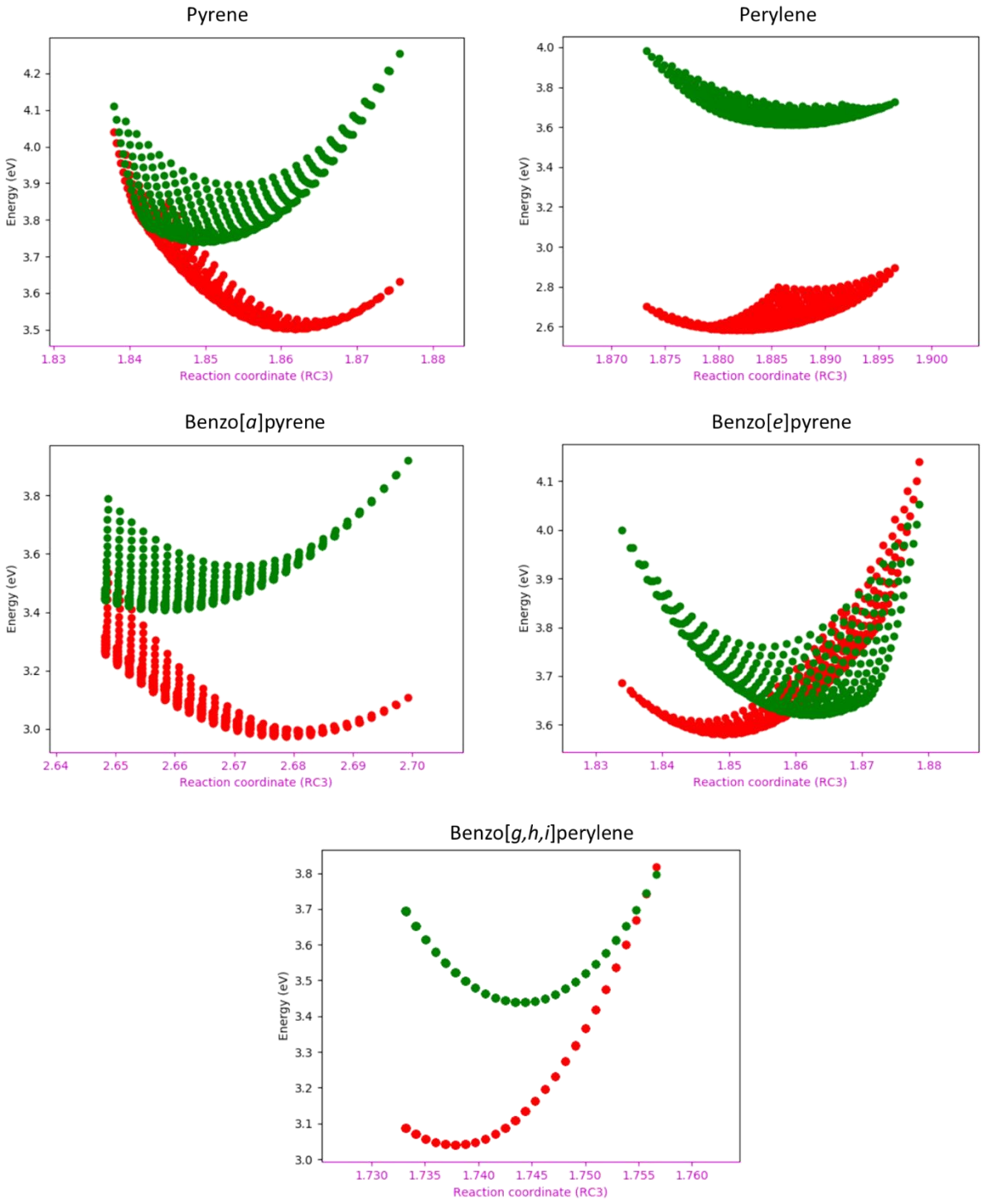

Figure 83 2D plots of pyrene, perylene, benzo[*a*]pyrene, benzo[*e*]pyrene and benzo[*g,h,i*]perylene showing the evolution of the energy with respect to RC3

One observation about Figure 83 is the striking resemblance that the 2D plots have with respect to those obtained with RC2 (Figure 82). This is not that surprising because the origins of the two quantities are very close to one another. First of all, for the pyrene molecule, RC3 gives a good description of the lowest excited state but it is not the case for the second excited

state, where the scattering effect is too obvious. Moving on to perylene, although the trend along the PES is not that perfect, the evolution of the energy values with RC3 is correctly described for both ES1 and ES2. For the benzo[*a*]pyrene, in general, both tendencies present an apparent spreading of the points. However, the lowest excited state seems to better describe the motion of the molecule. It is even more obvious with benzo[*a*]pyrene where the points are 'packed' for ES1 and are unevenly distributed for ES2. At last, RC3 with benzo[*g,h,i*]perylene shows an excellent evolution of both excited states without any outlying values. From these observations, it can be deduced that RC3 is an excellent reaction coordinate for the description of the lowest excited state (red plot). Unfortunately, based on Figure 83, it cannot be used describe the second lowest excited state.

The three form factors selected (RC1, RC2 and RC3) did not allow us to describe the two potential energy surfaces of the studied polycyclic aromatic hydrocarbons. While RC1 gave bad results for some of the molecules, making it a non-useful reaction coordinate for the description of the excited states, RC2 and RC3 gave more satisfactory results. They successfully showed the evolution of the lowest excited state along the potential energy surface. Since both form factors gave similar results, one of them can be chosen as one of the reaction coordinates. We choose RC3 that leads to a little more satisfactory results. The unsuccessful attempt to describe the second lowest excited state led us to look for other parameters that are not form factors. We would have preferred a single RC to characterise both states, but it would be nevertheless considered as a first step towards our objective.

3.3.4 Aromaticity and anti-aromaticity aspect (RC4)

Aromaticity is a term that is often used to characterise cyclic molecules with alternating π-conjugated bonds. Considering the molecules under study, it could be a good parameter to describe PAHs and potentially act as a reaction coordinate, as it combines several structural parameters. However, aromaticity is a property that is very hard to define. A basic rule related to this property is Hückel's rule, which stipulates that if the number of π electrons of a planar hydrogeno-carbonated cyclic compound is equal to 4n + 2 (n should be a non-negative whole number), then the molecule is aromatic. Unfortunately, this rule has its limitations as it is not

reliable for large systems (the coronene is a well-studied exception to this rule) and does not allow us to quantify the aromaticity. Several criteria are considered as basic rules that an aromaticity index must fulfil to be considered. Aromaticity, being a complicated notion that intricates many aspects, these criterions are linked to various aspects of chemistry. Among the many properties that a well-designed aromaticity index should account for[252]:

- The bond lengths in an aromatic ring are intermediate between a single and a double bond lengths (structrural criterion).
- Double bonds included in an aromatic ring are more stable than isolated double bonds (thermodynamic criterion).
- Aromatic compounds usually hold on to their π-electron structure and one way to achieve that is for the molecules to undergo substitution chemical reactions rather than addition reactions (reactivity criterion).
- The compounds induce a diatropic ring current by an external magnetic field (magnetic criterion).

Although polycyclic aromatic hydrocarbons are constituted of several benzene rings, the latter do not have the same degree of aromaticity[253]. Some of the benzene rings in the PAH are even considered to be anti-aromatic. In order to characterise and quantify aromaticity, different indexes have been suggested such as: Nucleus-Independent Chemical Shifts (NICS), aromatic FLUctuation index (FLU) and Harmonic Oscillator Model of Aromaticity (HOMA) amongst others[254,255,256,257].

---

[252] Krygowski, T. M., Szatylowicz, H., Stasyuk, O. A., Dominikowska, J., & Palusiak, M. (2014). Aromaticity from the Viewpoint of Molecular Geometry: Application to Planar Systems. *Chemical Reviews*, *114*(12), 6383–6422.

[253] Randić, M. (2003). Aromaticity of Polycyclic Conjugated Hydrocarbons. *Chemical Reviews*, *103*(9), 3449–3606.

[254] Fallah-Bagher-Shaidaei, H., Wannere, C. S., Corminboeuf, C., Puchta, R., & Schleyer, P. v. R. (2006). Which NICS Aromaticity Index for Planar π Rings Is Best? *Organic Letters*, *8*(5), 863–866.

[255] Matito, E., Duran, M., & Solà, M. (2005). The aromatic fluctuation index (FLU): A new aromaticity index based on electron delocalization. *The Journal of Chemical Physics*, *122*(1), 014109.

[256] Bultinck, P., Ponec, R., & Van Damme, S. (2005). Multicenter bond indices as a new measure of aromaticity in polycyclic aromatic hydrocarbons. *Journal of Physical Organic Chemistry*, *18*(8), 706–718.

[257] Simion, D. V., & Sorensen, T. S. (1996). A Theoretical Computation of the Aromaticity of (Benzene)Cr(CO) $_3$ Compared to Benzene Using the Exaltation of Magnetic Susceptibility Criterion and a Comparison of Calculated and Experimental NMR Chemical Shifts in These Compounds. *Journal of the American Chemical Society*, *118*(31), 7345–7352.

The method chosen for the calculation of the aromaticity is the NICS(0) method[258] that computes the magnetic shielding at the barycentre of the ring considered. A different index can therefore be computed for each ring, revealing subtle differences in the local aromaticity. This method requires that a ghost atom is placed in the barycentre of each six-membered ring of a polycyclic aromatic hydrocarbon. Therefore, four ghost atoms are added to pyrene, five ghost atoms for perylene, benzo[*a*]pyrene and benzo[*e*]pyrene and six ghost atoms for benzo[*g,h,i*]perylene. Following that, an NMR calculation is run on each molecule. The outcome of the calculation will give an isotropic value of the shielding, which will give a measure of the nature of the aromaticity of the ring. It should be noted that the value of the NICS of a ring is the negative integer of the value of the shielding. This means that, according to the NICS(0) method, a ring is considered to be aromatic if the shielding value is positive or if the chosen index is negative.

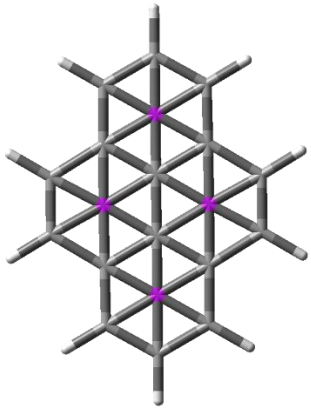

Figure 84 Pyrene molecule with the four ghost atoms (in pink) at the barycentre of each ring

Based on the computed data, three reaction coordinates were envisaged. Each compound can be described based on the most aromatic ring (highest isotropic value, noted RC4aro) but also on the most anti-aromatic one (lowest isotropic value, noted RC4antiaro). A third factor can also be the median isotropic value (noted RC4med). To separate the close values and compare more easily the trends, the values obtained for these index were linearly constrained to vary

[258] Aihara, J. (2002). Nucleus-independent chemical shifts and local aromaticities in large polycyclic aromatic hydrocarbons. *Chemical Physics Letters*, *365*(1–2), 34–39.

between 0 and 1. The 2D plots of the energy with respect to these three parameters are depicted in Figure 85, Figure 86 and Figure 87 for the five PAHs.

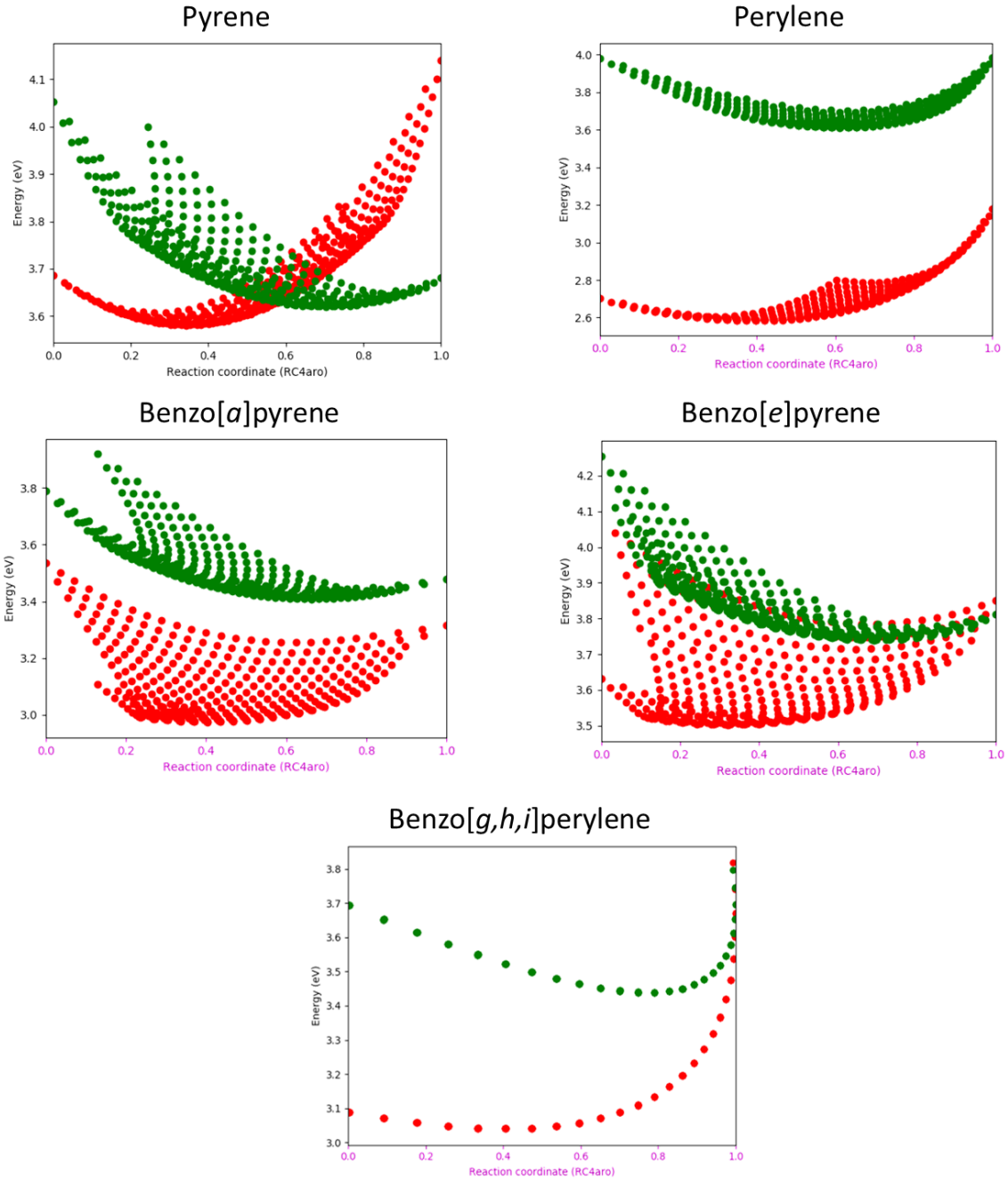

Figure 85 2D plots of pyrene, perylene, benzo[*a*]pyrene, benzo[*e*]pyrene and benzo[*g,h,i*]perylene showing the evolution of the energy with respect to RC4aro

Figure 85 illustrates the evolution of the energy for pyrene, perylene, benzo[*a*]pyrene, benzo[*e*]pyrene and benzo[*g,h,i*]perylene with respect to the aromaticity index of each molecule, named as RC4aro. If we focus on pyrene, the second lowest excited state mostly

decreases with increasing RC4aro but the points on the 2D plot are too scattered. The results are more promising for the lowest excited state where the evolution of the energy with respect to RC4aro is more regular. Concerning perylene, both lowest and second lowest excited states are well described by RC4aro, with a weak scattering of the points. It is unfortunate that for benzo[*a*]pyrene, the points are not well stacked, thus, none of the two excited states can be characterised by this reaction coordinate. A fair trend is observed for the second lowest excited state of benzo[*e*]pyrene with a spreading of the points but the general trend is still visible, however the same optimistic deduction cannot be made for the lowest excited state. The case of benzo[*g,h,i*]perylene is more debatable: a clear trend is recovered for both excited states without any scattering effect, but for high value of this reaction coordinate, a reversal point seems to be present. These observations lead us to say that RC4aro might be a starting point to determine a good reaction coordinate in describing the second lowest excited state of the polycyclic aromatic hydrocarbons. This parameter should be improved with the aim to decrease the scattering of the single points and to eliminate the reversal points observed.

Contrary to Figure 85, Figure 86 shows the evolution of the energy values for pyrene, perylene, benzo[*a*]pyrene, benzo[*e*]pyrene and benzo[*g,h,i*]perylene with respect to the anti-aromaticity character of each compound, RC4antiaro. The latter gave excellent trends for benzo[*g,h,i*]perylene for both excited states. As for benzo[*e*]pyrene, only the energy of the lowest excited state is seen to be increasing along with the reaction coordinate that could be convenient to describe this state. Unfortunately, these above observations for RC4antiaro are the only favourable features that could be found since this reaction coordinate is not at all convenient for the remaining molecules and excited states. If the pyrene and benzo[*a*]pyrene molecules are taken into account, a wide dispersion of the points for both states is seen without any noticeable trend. The same remark can be made for perylene with the addition of a reversal point to the scattering effect: RC4antiaro is unable to characterise any of the states. Based on these observations, RC4antiaro cannot be used as a reaction coordinate.

The last candidate as possible reaction coordinate in the series of aromaticity index is the median between the most aromatic ring and the least one, called RC4med as shown on Figure 87. Starting with the pyrene molecule, it can clearly be seen that RC4med is not adequate for

this molecule. No clear tendency is observed for both the lowest excited state and the second lowest excited state as the points are too spread arbitrarily on the plot. Perylene, on the other side, is the only molecule that is well described by RC4med. Concerning benzo[*a*]pyrene, a reversal point is observed for the second lowest excited state and together with that the points are scattered. As for benzo[*e*]pyrene, the red points are shown a very good evolution of the reaction coordinate. The green ones, however, do not display an excellent trend. Finally, for the benzo[*g,h,i*]perylene, an excellent tendency is observed for both excited states at the beginning, but the presence, once again, of a reversal point, makes it unable for the purpose of a good description of the second excited state. Unfortunately, RC4med has to be cast out since it is not appropriate for all the molecules.

From the interpretations done, it was seen that only RC4aro was able to give somewhat satisfactory results for the studied molecules, but this reaction coordinate needs to be further improved in order to be adequate for the description of the energy of all the studied polycyclic aromatic hydrocarbons.

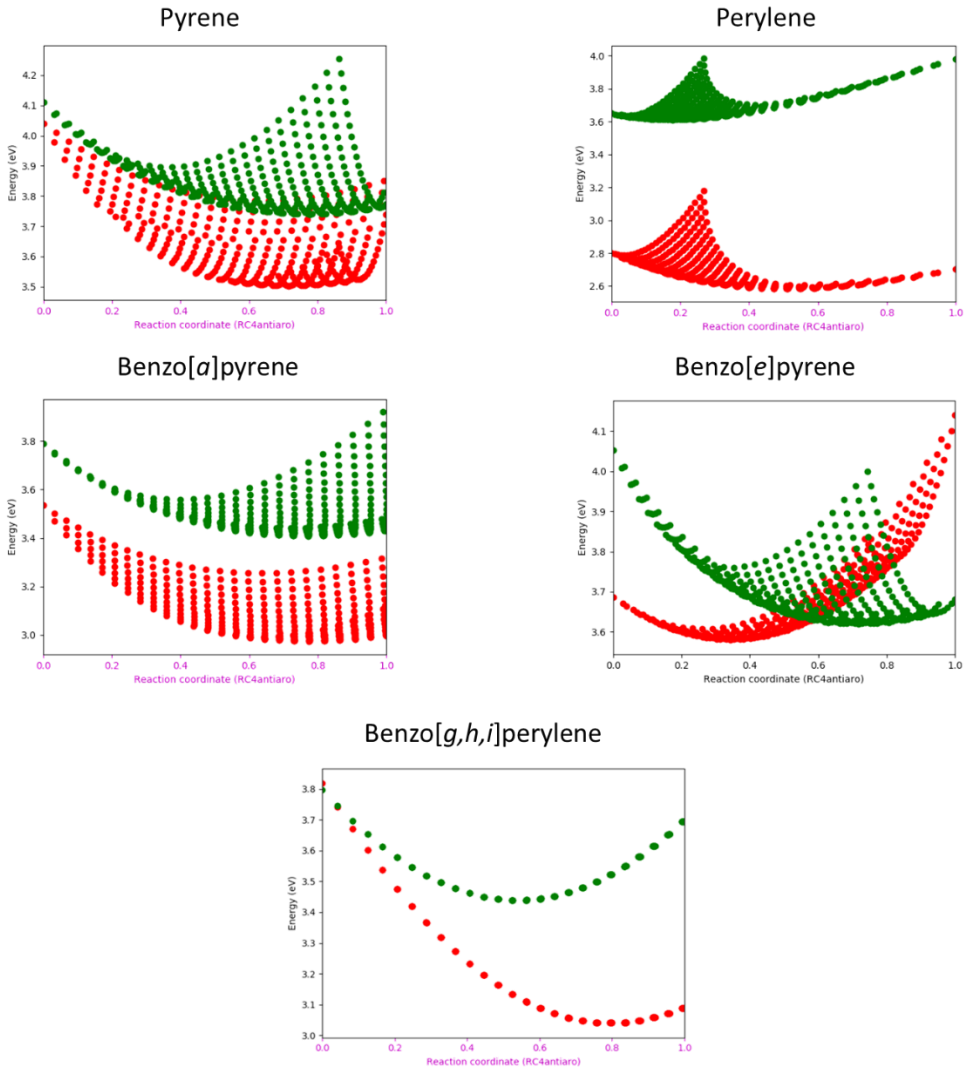

Figure 86 2D plots of pyrene, perylene, benzo[*a*]pyrene, benzo[*e*]pyrene and benzo[*g,h,i*]perylene showing the evolution of the energy with respect to RC4antiaro

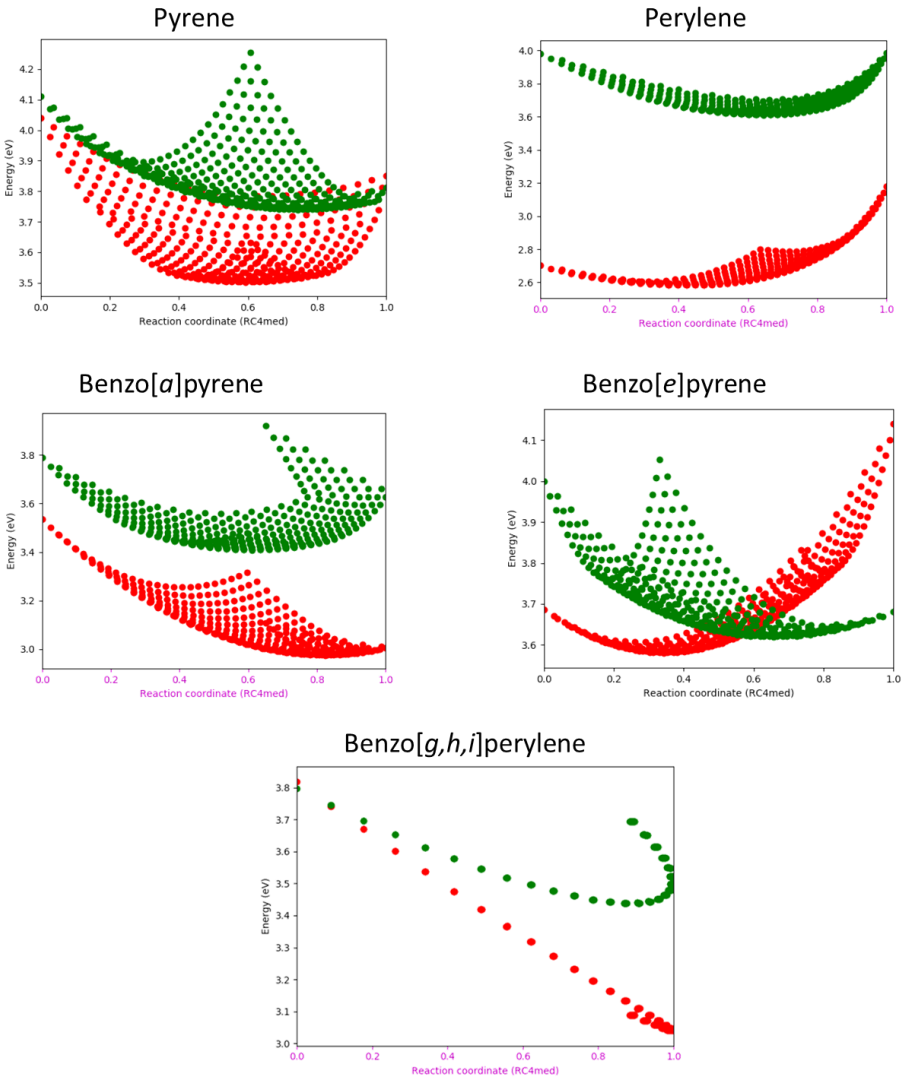

Figure 87 2D plots of pyrene, perylene, benzo[*a*]pyrene, benzo[*e*]pyrene and benzo[*g,h,i*]perylene showing the evolution of the energy with respect to RC4med

3.3.5 *Charge transfer index - D_{CT} (RC5)*

Usually, when a molecule is excited, a transfer of electron density happens from one region of the molecule to another one. There is a factor called the charge transfer index, denoted as D_{CT} that enables the quantification of the length of the electron transfer corresponding to an electron transition during excitation[259]. As quoted from this article: "The charge transfer index is a parameter that allows the characterisation of the spatial magnitude associated to a given transition along with the associated fraction of electrons transferred". The authors showed

[259] Le Bahers, T., Adamo, C., & Ciofini, I. (2011). A Qualitative Index of Spatial Extent in Charge-Transfer Excitations. *Journal of Chemical Theory and Computation*, *7*(8), 2498–2506.

how the D_{CT} may be applied to donor acceptor groups in push-pull systems to describe the amount of electron transfer from the ground state to the excited states. More recently, this index has been shown to be useful to describe the closeness of excited states[251].

In the case of this study, we are more focused on the characterisation of some polycyclic aromatic hydrocarbons to comprehend why some of them emit a dual fluorescence. Therefore, it was thought that it would be more adequate to compute the charge transfer index between the first two excited states to have an idea of the length of electron transfer from these two states and to have an idea on the energy gap that separates them.

In order to run D_{CT} calculations, the cube files containing the electron density data for the required states are generated for all the 351 single points. One main difficulty that we had to face was that some of the selected PAHs are symmetric, hence, the D_{CT} index computed was equal to zero. To remedy to this problem, the cube files were modified in such a way that the space containing electron density was divided in four for pyrene and perylene that possess two symmetry planes, in two for the benzo[*e*]pyrene and benzo[*g,h,i*]perylene that possess one symmetry plane. The result is depicted on Figure 88. By doing so, the symmetry of the molecule is broken and a non-negative value can be obtained for D_{CT}. The cube files corresponding to benzo[*a*]pyrene were not modified as the molecule does not have any axe of symmetry.

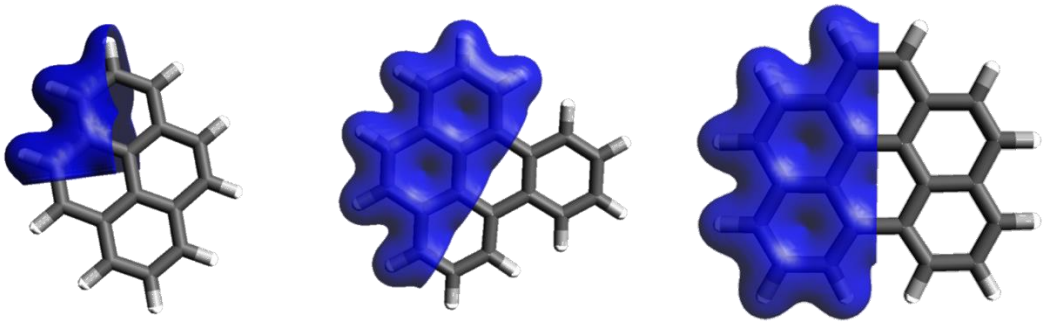

Figure 88 The segmentation of the electron density planned for pyrene (cut in 4), benzo[*e*]pyrene (cut in 2) and benzo[*g,h,i*]perylene (cut in 2)

However, the results obtained for perylene were not satisfactory, therefore, the cube files were divided into two instead. A similar problem arose for benzo[*e*]pyrene because the cutting of the electron density did not go as we thought it would, as it can be clearly seen in Figure 88. Hence, the remaining calculations were done without the modification of the cube files (it was made sure that the D_{CT} values were not equal to zero). Concerning the benzo[*g,h,i*]perylene, Figure 88 shows that the modification of the electron density was correctly done but the 2D plot of the energy values of the molecule with respect to RC5 presented a discontinuity as illustrated in Figure 89. Initially, it gives the impression that the points are arbitrarily spread but when a closer look is taken, the evolution is seen to have been cut into two. Due to this behaviour, the cube files were not modified for benzo[*g,h,i*]perylene.

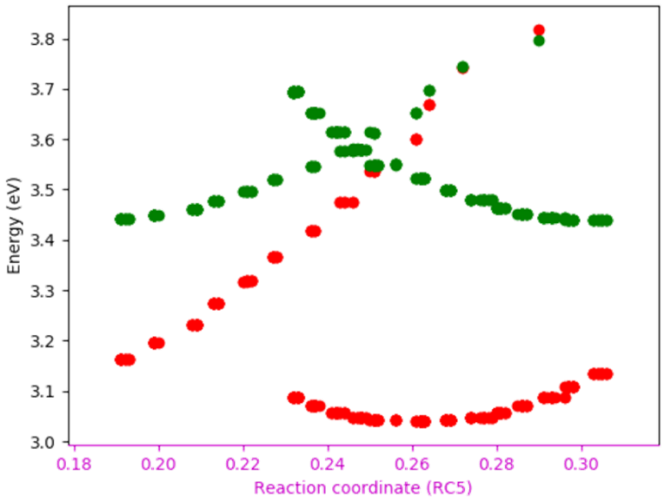

Figure 89 2D plot of benzo[*g,h,i*]perylene showing the evolution of the energy with respect to RC5 when the electron density is cut in half

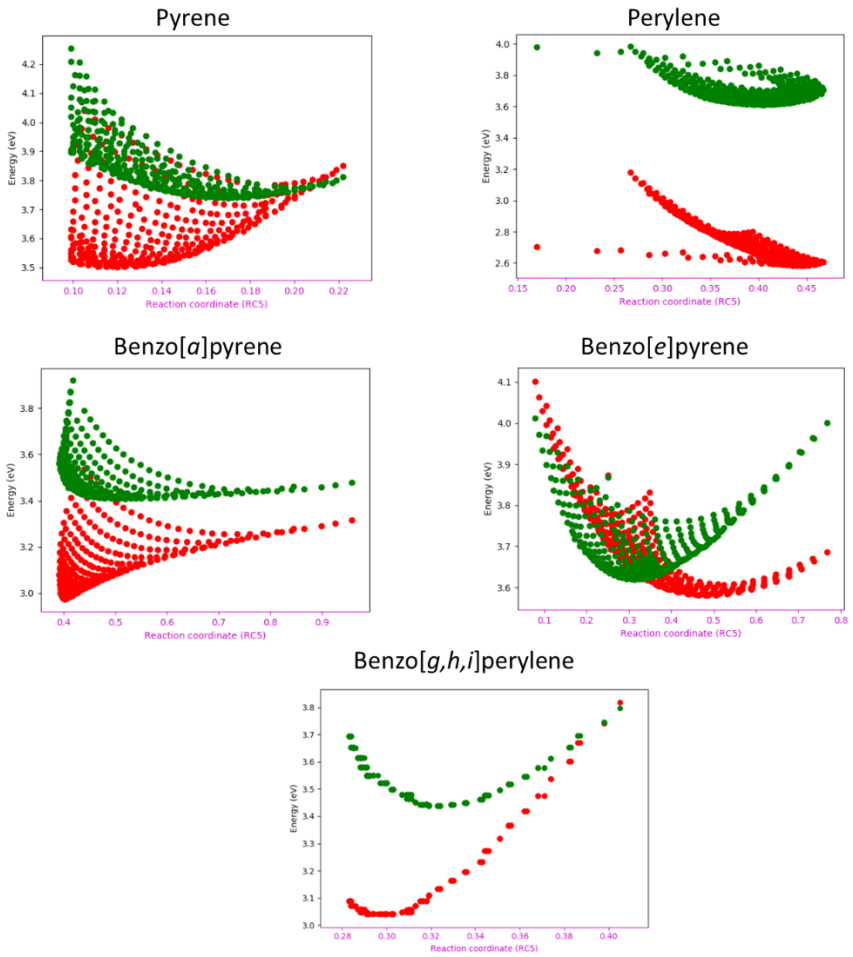

Figure 90 2D plots of pyrene, perylene, benzo[*a*]pyrene, benzo[*e*]pyrene and benzo[*g,h,i*]perylene showing the evolution of the energy with respect to RC5

Figure 90 represents the evolution of the PES with respect to RC5 for pyrene (cube files cut in four), perylene (cube files in two), benzo[*a*]pyrene (full cube files), benzo[*e*]pyrene (full cube files) and benzo[*g,h,i*]perylene (full cube files). Only the second lowest excited state is well described for pyrene. The points representing the lowest excited state are too scattered to show any trend. For perylene, even though the results obtained with the surfaces divided in half were the only ones exploitable, they are not at all adequate since no tendency is observed with a clear reversal point. The results obtained with benzo[*a*]pyrene show a too big spread of the points albeit the presence of a small trend. A similar observation is noticed with benzo[*e*]pyrene, further putting the emphasis on the fact the RC5 is not appropriate for this family of molecules. Benzo[*g,h,i*]perylene, similar to most of the reaction coordinates used, show a very good evolution of RC5 along the PES for both excited states. Therefore, form the observations, the charge transfer index is not an acceptable reaction coordinate for the chosen polycyclic aromatic hydrocarbons.

CONCLUSION AND PERSPECTIVES

This part of the work dealt with the study of polycyclic aromatic hydrocarbons. It was reported that only some of these compounds exhibit a dual fluorescence. In order to understand how each excited state is positioned with respect to each other and understand the mechanism behind the phenomenon of dual fluorescence, some molecules were selected to investigate their behaviour at the excited states. The chosen molecules were: pyrene, perylene, benzo[*a*]pyrene, benzo[*e*]pyrene, benzo[*g,h,i*]perylene and coronene and their absorption and emission spectra were measured.

Prior to the study of the PES of each excited states, a benchmark was carried out to find the adequate functional and basis set and PBE0/6-311+G** was considered appropriate for all the molecules because these computational conditions allow a good fit between the experimental and calculated data. During the computations, it was observed that the first two low-lying excited states, close to one another, had their oscillator strengths null and non-null, which can lead us to say that the AK 1 mechanism is conceivable.

A sampling of the PES for the two lowest excited states of each molecule was carried out. It evidenced two typical cases: the first one is a neat separation between these two energy levels (such as in perylene) and the second one is an obvious crossing of the surfaces (in the case of benzo[*e*]pyrene). These features illustrating the continuum between the two compounds (perylene that has a normal fluorescence and benzo[*e*]pyrene that has a dual fluorescence) lead to believe that the AK 1 mechanism is favoured.

Several reaction coordinates have been tested with the aim to find one coordinate that will be able to successfully describe both low lying excited states for all the selected molecules. Unfortunately, it was not possible to obtain a single reaction coordinate that can do that. However, it was shown that RC2 and RC3 involving form factors may be used to describe the lowest energy excited state.

From what has been exposed in the study of the polycyclic aromatic hydrocarbons, only a tiny proportion of the subject was investigated. The determination of a reaction coordinate that can help describe the second excited state or even one that can describe both states is still an ongoing work. A single reaction coordinate to characterise both states would have been preferable, nevertheless, the reduction to two reaction coordinates would yet be a huge step forward.

There are several routes that can be considered. One of them can be to introduce the concept of molecular dynamics and to apply the principle of surface hopping to understand how to follow the population distribution between the first two excited states[260]. If an AK 1 mechanism were to be confirmed, this method could be a solution to quantify the emission from both excited states individually. The temperature dependency could also be recovered by this way.

In addition to that, we are aware that the computational method used is appropriate for the small molecules that have been studied. However, another long term objective is to cope with more complex systems. A first possibility is to study bigger molecules, either with a larger PAH core like ovalene or with substituents that could alter the properties of the compounds (addition of carboxy or methoxy groups for instance). A second possibility is to replace some carbon atoms by other elements to check the sensibility of the studied properties. In both cases, it is less certain that the single configurational approach would still be adequate and a multi-configurational scheme will need to be thought of.

[260] Wang, L., Akimov, A., & Prezhdo, O. V. (2016). Recent Progress in Surface Hopping : 2011–2015. *The Journal of Physical Chemistry Letters*, *7*(11), 2100-2112.

APPENDIX

SI.1: Part of the script done to optimise the ellipse around the molecule and to calculate RC3

```
""" DEFINITIONS

    Calcule la distance entre deux atomes numérotés
    Attention à la numérotation de liste"""


def distance(structure, atome1, atome2):
    distance = np.sqrt((structure[atome1][1] - structure[atome2][1])**2 +
(structure[atome1][2] - structure[atome2][2])**2 + (structure[atome1][3] -
structure[atome2][3])**2)
    return distance

""" Calcule la surface d'un triangle
    Attention à la numérotation de liste"""


def surface_triangle(structure, atome1, atome2, atome3):
    a = distance(geoms[i1][i2],atome1,atome2)
    b = distance(geoms[i1][i2],atome2,atome3)
    c = distance(geoms[i1][i2],atome3,atome1)
    p = (a + b + c)/2
    return np.sqrt(p*(p-a)*(p-b)*(p-c))

""" Calcule la surface d'un hexagone
    Attention à la numérotation de liste"""


def surface_hexagone(structure, atome1, atome2, atome3, atome4, atome5,
atome6):
    s1 = surface_triangle(structure, atome1, atome2, atome3)
    s2 = surface_triangle(structure, atome3, atome4, atome5)
    s3 = surface_triangle(structure, atome5, atome6, atome1)
    s4 = surface_triangle(structure, atome1, atome3, atome5)
    return s1 + s2 + s3 + s4


# fit du périmètre par une ellipse
## calcul de la somme des distances entre un point et les deux foyers
# utiliser la notation de liste

def distance_centres(structure, atome, foyer1, foyer2):
    distance1 = np.sqrt((structure[atome][1] - foyer1[0])**2 +
(structure[atome][2] - foyer1[1])**2 + (structure[atome][3] -
foyer1[2])**2)
    distance2 = np.sqrt((structure[atome][1] - foyer2[0])**2 +
(structure[atome][2] - foyer2[1])**2 + (structure[atome][3] -
foyer2[2])**2)
    return distance1 + distance2


## liste de la moyenne des distances

def liste_distance(structure, carbones, foyer1, foyer2): # carbones sera la
dernière ligne de hexagones
    sortie = []
    for indice, atome in enumerate(carbones):
```

```
        sortie.append(distance_centres(structure, int(atome)-1, foyer1,
foyer2))
    return sortie


## objectif à minimiser

def cout_ellipse(structure, carbones, foyer1, foyer2):
    liste = liste_distance(structure, carbones, foyer1, foyer2)
    moyenne = np.mean(liste)
    liste_e = [(valeur-moyenne)**2 for valeur in liste]
    return sum(liste_e)


## on utilise les routines précédentes pour la minimisation

def format_cout(foyers,*arguments):
    return cout_ellipse(arguments[0], arguments[1], foyers[0:3],
foyers[3:6])


for i1 in range(taille):
    for i2 in range(taille):
        if len(geoms[i1][i2]) != 0:
            liste_x = []
            liste_y = []
            liste_z = []
            liste_x.append([geoms[i1][i2][i][1] for i in
range(len(geoms[i1][i2]))])
            liste_y.append([geoms[i1][i2][i][2] for i in
range(len(geoms[i1][i2]))])
            liste_z.append([geoms[i1][i2][i][3] for i in
range(len(geoms[i1][i2]))])


            # tracé molécule
            # recherche SVD
            ## ne conserver que les C du périmètre

            perim = [int(i) for i in hexagones[-1]]
            liste_x_perim = [ liste_x[0][i-1] for i in perim ]
            liste_y_perim = [ liste_y[0][i-1] for i in perim ]
            liste_z_perim = [ liste_z[0][i-1] for i in perim ]
            liste_x_perim_n = [ valeur - np.mean(liste_x_perim) for valeur
in liste_x_perim ]
            liste_y_perim_n = [ valeur - np.mean(liste_y_perim) for valeur
in liste_y_perim ]
            liste_z_perim_n = [ valeur - np.mean(liste_z_perim) for valeur
in liste_z_perim ]
            coordonnees = [liste_x_perim_n, liste_y_perim_n,
liste_z_perim_n]
            svd = np.linalg.svd(coordonnees)[1]
            svd_value = svd[0]/svd[1]
            svd_cr.append(svd_value)


            ## tracé molécule
            ## molécule dans le bon repère
            ### on aligne en fonction du premier vecteur selon la première
coordonnée, du troisième selon la troisième
```

```
            ### (qui pour une molécule plane sera toujours orthogonal) et
on remplace le deuxième par l'opposé du produit
            ### vectoriel des autres

            mat_passage =
np.array([np.linalg.svd(coordonnees)[0].T[0],np.cross(np.linalg.svd(coordon
nees)[0].T[2],np.linalg.svd(coordonnees)[0].T[0]),np.linalg.svd(coordonnees
)[0].T[2]])
            coordonnees_bis = np.dot(mat_passage,coordonnees)


            ## on positionne des foyers arbitraitement sur l'axe principal

            xf10b = max(coordonnees_bis[0])/2
            yf10b = 0
            zf10b = 0
            xf20b = -max(coordonnees_bis[0])/2
            yf20b = 0
            zf20b = 0


            ## recherche des bornes

            liste_x = [coordonnees_bis.T[i][0] for i in
range(len(coordonnees_bis.T))]
            liste_y = [coordonnees_bis.T[i][1] for i in
range(len(coordonnees_bis.T))]
            liste_z = [coordonnees_bis.T[i][2] for i in
range(len(coordonnees_bis.T))]
            x_min = min(liste_x) + (max(liste_x) - min(liste_x))*0
            y_min = min(liste_y) + (max(liste_y) - min(liste_y))*0
            z_min = min(liste_z) + (max(liste_z) - min(liste_z))*0
            x_max = max(liste_x) - (max(liste_x) - min(liste_x))*0
            y_max = max(liste_y) - (max(liste_y) - min(liste_y))*0
            z_max = max(liste_z) - (max(liste_z) - min(liste_z))*0


            ### nécessaire d'ajouter une colonne aux coordonnées pour les
numéros atomiques, attention aux carbones à renuméroter car on a enlevé ce
qui n'était pas dans le périmètre

            from scipy.optimize import minimize
            resultat =
minimize(format_cout,np.array([xf10b,yf10b,zf10b,xf20b,yf20b,zf20b]),args=(
np.c_[np.ones(len(coordonnees_bis.T)),coordonnees_bis.T],[i+1 for i in
range(len(coordonnees_bis.T))]),bounds =
((x_min,x_max),(y_min,y_max),(z_min,z_max),(x_min,x_max),(y_min,y_max),(z_m
in,z_max)))


# method='Nelder-Mead',
            ### les valeurs optimisées s'affichent avec la méthode x
            ## tracé de l'ellipse et calcul des paramètres # attention si
les foyers ont trop bougés : dans ce cas, l'ellipse ne sera pas
correctement centrée
            a_f =
0.5*np.mean(liste_distance(np.c_[np.ones(len(coordonnees_bis.T)),coordonnee
s_bis.T], [i+1 for i in range(len(coordonnees_bis.T))], resultat.x[0:3],
resultat.x[3:6]))
```

```
            c_f = 0.5*np.sqrt((resultat.x[0]-
resultat.x[3])**2+(resultat.x[1]-resultat.x[4])**2+(resultat.x[2]-
resultat.x[5])**2)
            b_f = np.sqrt(a_f**2 - c_f**2)


            #calcul de la coord reactionnelle F3 en fonction des semi axes
de l'ellipse optimises autour de la molecule

            result = float(a_f)/float(b_f)
            coord_centre =
[(resultat.x[0]+resultat.x[3])/2,(resultat.x[1]+resultat.x[4])/2,(resultat.
x[2]+resultat.x[5])/2]
            abscisse = np.linspace(1.5*x_min,1.5*x_max,1000)
            ordonnee = np.linspace(1.5*y_min,1.5*y_max,1000)
            abscisse,ordonnee = np.meshgrid(abscisse,ordonnee)

            x.append(float(i1))
            y.append(float(i2))
            z_rc3.append(result)


# représentations graphiques

## surface 3D deux premiers états excités

fig = plt.figure()
ax = fig.gca(projection='3d')
ax.scatter(np.array(x), np.array(y), np.array(z_ee1), s=5, color='r')
ax.plot_trisurf(np.array(x), np.array(y), np.array(z_ee1), color='r',
alpha=0.5)
ax.scatter(np.array(x), np.array(y), np.array(z_ee2), s=5, color='g')
ax.plot_trisurf(np.array(x), np.array(y), np.array(z_ee2), color='g',
alpha=0.5)
ax.set_xlabel('GS -> ES1 (arbitrary unit)')
ax.set_ylabel('GS -> ES2 (arbitrary unit)')
ax.set_zlabel('Energy (eV)')
ax.view_init(elev=25,azim=-60)
plt.show()


## 2D énergies des deux premiers états excités en fonction de RC3

fig = plt.figure()
ax = fig.add_subplot(111)
ax.scatter(z_rc3,z_ee1,color="r")
ax.scatter(z_rc3,z_ee2,color="g")
ax.spines['bottom'].set_color('m')
ax.set_xlabel('Reaction coordinate (RC3)')
ax.set_ylabel('Energy (eV)')
ax.xaxis.label.set_color('m')
ax.tick_params(axis='x', colors='m')
plt.show()
```

SI.2: Emission wavelengths for pyrene, perylene, benzo[*a*]pyrene, benzo[*e*]pyrene, benzo[*g,h,i*]perylene

PYRENE		LOWEST EXCITED STATE		SECOND LOWEST EXCITED STATE	
Functional/ Basis set	State	Wavelength, λ (nm)	Oscillator strength, *f*	Wavelength, λ (nm)	Oscillator strength, *f*
PBE0/ cc-pvdz	ES 1	369	0.532	348	0.421
	ES 2	333	0.001	339	0.002
PBE0/ 6-31+G**	ES 1	373	0.576	351	0.461
	ES 2	334	0.002	339	0.002
PBE0/ cc-pvtz	ES 1	371	0.542	348	0.424
	ES 2	333	0.002	338	0.003
PBE0/ 6-311+G**	ES 1	373	0.567	351	0.449
	ES 2	335	0.002	340	0.003
B3LYP/ cc-pvtz	ES 1	380	0.512	358	0.396
	ES 2	341	0.001	347	0.002
M06-2X/ cc-pvtz	ES 1	355	0.648	327	0.501
	ES 2	322	0.003	327	0.003
ωB97X-D/ cc-pvtz	ES 1	358	0.642	331	0.484
	ES 2	324	0.001	329	0.001

PERYLENE		LOWEST EXCITED STATE		SECOND LOWEST EXCITED STATE	
Functional/ Basis set	State	Wavelength, λ (nm)	Oscillator strength, f	Wavelength, λ (nm)	Oscillator strength, f
PBE0/ cc-pvdz	ES 1	504	0.501	469	0.506
	ES 2	347	0.000	346	0.000
PBE0/ 6-31+G**	ES 1	514	0.505	478	0.509
	ES 2	349	0.000	349	0.000
PBE0/ cc-pvtz	ES 1	512	0.485	474	0.489
	ES 2	350	0.000	350	0.000
PBE0/ 6-311+G**	ES 1	517	0.494	480	0.497
	ES 2	352	0.000	351	0.000
B3LYP/ cc-pvtz	ES 1	526	0.466	487	0.471
	ES 2	360	0.000	360	0.000
M06-2X/ cc-pvtz	ES 1	481	0.550	435	0.553
	ES 2	330	0.000	327	0.000
ωB97X-D/ cc-pvtz	ES 1	479	0.564	431	0.567
	ES 2	326	0.000	323	0.000

BENZO[*A*]PYRENE		LOWEST EXCITED STATE		SECOND LOWEST EXCITED STATE	
Functional/ Basis set	State	Wavelength, λ (nm)	Oscillator strength, f	Wavelength, λ (nm)	Oscillator strength, f
PBE0/ cc-pvdz	ES 1	441	0.473	410	0.418
	ES 2	366	0.012	372	0.018
PBE0/ 6-31+G**	ES 1	442	0.517	411	0.453
	ES 2	368	0.017	373	0.024
PBE0/ cc-pvtz	ES 1	443	0.466	410	0.412
	ES 2	366	0.018	371	0.025
PBE0/ 6-311+G**	ES 1	444	0.498	412	0.437
	ES 2	368	0.021	374	0.029
B3LYP/ cc-pvtz	ES 1	455	0.437	422	0.385
	ES 2	377	0.015	383	0.022
M06-2X/ cc-pvtz	ES 1	418	0.582	380	0.501
	ES 2	347	0.021	353	0.033
ωB97X-D/ cc-pvtz	ES 1	419	0.613	379	0.514
	ES 2	347	0.012	353	0.021

BENZO[*E*]PYRENE		LOWEST EXCITED STATE		SECOND LOWEST EXCITED STATE	
Functional/ Basis set	State	Wavelength, λ (nm)	Oscillator strength, f	Wavelength, λ (nm)	Oscillator strength, f
PBE0/ cc-pvdz	ES 1	331	0.001	353	0.393
	ES 2	328	0.305	345	0.001
PBE0/ 6-31+G**	ES 1	333	0.001	357	0.431
	ES 2	331	0.340	346	0.001
PBE0/ cc-pvtz	ES 1	330	0.001	343	0.002
	ES 2	328	0.311	304	0.379
PBE0/ 6-311+G**	ES 1	332	0.001	357	0.424
	ES 2	331	0.331	346	0.002
B3LYP/ cc-pvtz	ES 1	341	0.001	363	0.373
	ES 2	338	0.290	354	0.001
M06-2X/ cc-pvtz	ES 1	307	0.001	330	0.494
	ES 2	301	0.369	321	0.002
ωB97X-D/ cc-pvtz	ES 1	307	0.000	330	0.475
	ES 2	301	0.347	321	0.001

BENZO[*G,H,I*]PERYLENE		LOWEST EXCITED STATE		SECOND LOWEST EXCITED STATE	
Functional/ Basis set	State	Wavelength, λ (nm)	Oscillator strength, f	Wavelength, λ (nm)	Oscillator strength, f
PBE0/ cc-pvdz	ES 1	428	0.394	395	0.341
	ES 2	371	0.000	377	0.000
PBE0/ 6-31+G**	ES 1	433	0.406	400	0.356
	ES 2	372	0.001	378	0.001
PBE0/ cc-pvtz	ES 1	433	0.387	397	0.335
	ES 2	370	0.001	376	0.000
PBE0/ 6-311+G**	ES 1	436	0.397	400	0.346
	ES 2	372	0.001	378	0.000
B3LYP/ cc-pvtz	ES 1	446	0.367	410	0.316
	ES 2	382	0.001	389	0.000
M06-2X/ cc-pvtz	ES 1	406	0.465	365	0.399
	ES 2	347	0.000	354	0.000
ωB97X-D/ cc-pvtz	ES 1	403	0.474	363	0.386
	ES 2	347	0.000	353	0.000

Abstract

This manuscript deals with two independent topics: complexation of flavonoids with metal cations and the study of the excited states of polycyclic aromatic hydrocarbons.
Morin is a flavonoid that bears multiple fixation sites. Largely present in the vegetal kingdom, it is often in close proximity to metal cations. The complexation reactions of the zinc, manganese and calcium cations with morin were investigated to determine the preferential fixation site of the compound and also, to assess its complexation power with respect to other well-known flavonoids: quercetin and luteolin. The association of electronic spectroscopies, DFT and TD-DFT calculations is a robust method to elucidate the regio-selectivity of the reaction.
Polycyclic aromatic hydrocarbons are organic molecules constituted of several aromatic rings. It was highlighted that some of them exhibit a rare phenomenon, known as dual fluorescence. For the purpose of understanding the mechanism taking place when a compound possesses two emission bands, a study of the excited states was carried out theoretically using DFT and TD-DFT methods to determine any remarkable changes in the geometry of the selected PAHs. In addition, a sampling of the potential energy surfaces was done and energies were calculated with respect to different reaction coordinates to obtain a suitable description of the entanglement of the excited states. Eventually, it may enable us to explain the dual fluorescence of some PAHs.

Résumé

Cette thèse traite deux sujets indépendants: la complexation de flavonoïdes avec des cations métalliques et l'étude des états excités d'hydrocarbures aromatiques polycycliques.
La morine est un flavonoïde qui comporte plusieurs sites de fixation. Largement présent dans le règne végétal, il se trouve souvent à proximité de cations métalliques. Les réactions de complexation des cations zinc, manganèse et calcium avec la morine ont été étudiées pour déterminer le site préférentiel de fixation du composé et également pour évaluer son pouvoir complexant par rapport à d'autres flavonoïdes bien connus: la quercétine et la lutéoline. L'association des spectroscopies électroniques et des calculs DFT et TD-DFT est une méthode robuste pour élucider la régiosélectivité de la réaction.
Les hydrocarbures aromatiques polycycliques sont des molécules organiques constituées de plusieurs cycles aromatiques. Il a été mis en évidence que certains d'entre eux présentent un phénomène rare, appelé fluorescence duale. Afin de comprendre le mécanisme qui se produit lorsqu'un composé possède deux bandes d'émission, une étude théorique des états excités a été réalisée en utilisant les méthodes DFT et TD-DFT afin de déterminer les changements importants dans la géométrie des HAP sélectionnés. De plus, un échantillonnage des surfaces d'énergie potentielle a été effectué et les énergies ont été calculées en fonction de différentes coordonnées réactionnelles afin d'obtenir une description appropriée de l'intrication des états excités. À terme, cela pourrait nous permettre d'expliquer la fluorescence duale de certains HAP.